LOW MASS STAR AND BROWN DWARF FORMATION IN THE ORION B MOLECULAR CLOUD

By

JOANNA LISA LEVINE

A DISSERTATION PRESENTED TO THE GRADUATE SCHOOL
OF THE UNIVERSITY OF FLORIDA IN PARTIAL FULFILLMENT
OF THE REQUIREMENTS FOR THE DEGREE OF
DOCTOR OF PHILOSOPHY

UNIVERSITY OF FLORIDA

2006

This work is lovingly dedicated to:

Oma and Opa, Grandma and Grandpa, Mom, Dad, Sara, Jonathan, and Tim:

"*Call it a clan, call it a network, call it a tribe, call it a family. Whatever you call it, whoever you are, you need one.*"

-Jane Howard

Alora, Alberto, Sonia, and everyone else along the way who has encouraged me to dance while writing this dissertation:

"*Great dancers are not great because of their technique, they are great because of their passion.*"

-Martha Graham

The memory of Richard J. Elston (1961-2004):

"If you pretend you're playing a computer game, data reduction can be really fun!"

-Richard Elston

ACKNOWLEDGMENTS

First and foremost, I would like to thank all of the members of the University of Florida Astronomy Department. In your own way, each of you have contributed to my finishing this dissertation. Special thanks go to my adviser, Dr. Elizabeth Lada, who was an inspiration from the beginning, consistently providing many opportunities to explore independent research and, best of all, gave me the freedom to pursue my own path to the finish. Thank you also to my committee members (both current and former) – Drs. Richard Elston, Jonathan Williams, Steve Detweiler, Steve Eikenberry, and especially Ata Sarajedini whose office door was always open for me to ask even the most mundane photometry questions. Finally, thank you to Aaron Steinhauer, Andrea Stolte, Nick Raines and the other members of the FLAMINGOS team. Without this amazing group of people I would still be reducing data and classifiying spectra. Large pink birds and UF star formation postdocs are a special breed indeed!

My friends and fellow students in the Astronomy Department kept me sane during my time in graduate school. I owe many thanks to Sue Lederer (my first ever big sister), Lauren “shocked gas” Jones and Karl Haisch (officemates and local ISM gurus), Dave and Jo Osip (tarot players extraordinaire), David Dahari (board and video game master), Aaron Grocholski (my “gainesville boyfriend” and general partner in crime), Margaret Moerchen and Lauren Davis (shopping buddies), Ashley Espy (sister in knee problems caused by our respective obsessions), Audra Hernandez (fellow Starbucks addict and friendly neighbor), Leah Simon (the other astro-dancer who rock climbs), and the real NO DOUBT (a.k.a. the best graduate student office EVER).

I am also deeply grateful for the love and support I received from my friends in the dance world. Jessica Mayhew, Blair Litaker, Heather Collier, Heather Banes, Stacey

Readout, and the other members of the Dance Theatre of Santa Fe Community College (DTSF) accepted me as one of their own, keeping me young and happy and reminding me what it means to dance. Rachel Everett kept me company, both in and out of ballet class, proving to be a true kindred spirit who understands the beauty of a good friendship and the agony of dancing in pointe shoes past age 30. Tari Kendall always provided encouragement, even when I was taking up her office space, and Sonia Calero-Alonso always uplifted me with her smile. Alberto Alonso, Brian Brooks, Janis Brenner, and Peter Kalivas gave the gift of choreography, making me a part of their legacy and allowing me to share my art with the world – for that I will be eternally in their debt.

There are a few additional, extraordinary people who deserve special mention. My officemate of five years, Carlos Román-Zúñiga, played many roles including collaborator, comedian, philosopher, counselor, coffee brewer (or re-brewer), life coach, and Sith lord. However, first and foremost, he is, was, and always will be a great friend. I could not have chosen a better person with whom to share graduate school.

Doug Ratay and Catherine Garland redefined the meaning of friendship. Even though I was the first to start and the last to finish, they stood by and commiserated and/or cheered me on every step of the way. It's not every day you find friends who are willing to listen to a rough draft of your dissertation over the phone, one paragraph at a time.

Alora Haynes, co-director of DTSF, provided me with a place to go when I had nowhere else. Her kind nature and encouraging words both in and out of the studio were a constant source of inspiration and motivation as well as a strong reminder that there was in fact a light at the end of the tunnel. By taking me into the DTSF community she afforded me the opportunity to reawaken my passion and recapture the joy of dancing. As a result, my final years in graduate school were the most fulfilling. There are not enough stars in the sky to express my gratitude.

Finally, I could not have finished this dissertation without the love, encouragement, and support of my family. Mom always listened and tried her best to understand graduate

student life. If that didn’t work (or even if it did), I could always count on a little bit of home (whether it was fall maple leaves, fresh apples, blueberry muffins, or Belgian waffles) to arrive in the mail. Dad always reminded me that science should be fun; his enjoyment of all things astronomical is an ongoing inspiration. I thank Sara for showing me that the world is not a scary place and for always making me laugh. I thank Jonathan for always being my voice of reason and for keeping me company in the world of science.

Last but by no means least, I will be forever grateful to my fiancé, Tim Spahr, for supporting me wholeheartedly from day one in a way that no one else in the world ever could. His endless love, unwavering support, and above all, extreme patience during my tenure in graduate school made him a true prince charming.

Many people have been with me on this journey and I would not have had it any other way.

TABLE OF CONTENTS

LIST OF TABLES

LIST OF FIGURES

Figure page

Abstract of Dissertation Presented to the Graduate School
of the University of Florida in Partial Fulfillment of the
Requirements for the Degree of Doctor of Philosophy

LOW MASS STAR AND BROWN DWARF FORMATION IN THE ORION B MOLECULAR CLOUD

By

Joanna Lisa Levine

December 2006

Chair: Elizabeth A. Lada
Major Department: Astronomy

I present an extensive near-infrared imaging and spectroscopic survey of young, low mass objects in the Orion B molecular cloud. Results of this survey are used to investigate the shape of the low mass initial mass function (IMF) and examine the stellar and substellar populations of three young clusters in Orion B, ultimately placing observational constraints on models of brown dwarf formation.

Classical star formation theory predicts that the minimum mass required for the birth of a star is roughly one solar mass. However, studies of Galactic field stars have revealed many smaller objects, including significant populations of sub-solar mass stars (M$\simeq$0.2-0.3$M_{\odot}$) and brown dwarfs (M$<$0.08$M_{\odot}$). The origin of these objects remains an unsolved problem in modern astrophysics. Using FLAMINGOS on the Kitt Peak National Observatory 2.1 and 4 meter telescopes, I have completed a new *J*, *H*, and *K*-band imaging survey of $\sim$6 square degrees of Orion B and compiled a new library of $\sim$200 *JH* spectra of M stars in the young clusters NGC 2024, NGC 2068, and NGC 2071. I combine the photometry and spectroscopy to construct Hertzsprung-Russell diagrams, inferring masses and ages for cluster members using pre-main sequence evolutionary

models. Median ages, substellar disk frequencies, IMFs, and the abundance of brown dwarfs (R_{ss}) are determined and the spatial distribution of M stars is discussed.

The results show the IMF peaks for the Orion B clusters ($M_{peak} \simeq 0.2\text{-}0.3\,M_{\odot}$) are consistent with each other but different from isolated star forming regions such as Taurus. There is also evidence for a dependence of the peak mass on local gas density. A significant fraction of brown dwarfs are shown to have an infrared excess, indicative of circumsubstellar disks. Finally, I find that the R_{ss} is not universal but varies from region to region. After examining the dependence of R_{ss} on local physical properties, I find no clear trend with cluster mass, but some dependence on stellar and gas density and the spectral type of the most massive star in each region. I conclude that the outcome of the brown dwarf formation process appears to be dependent on the local star-forming environment.

CHAPTER 1
INTRODUCTION

1.1 Why Study Low Mass Star Formation?

Stars are the basic units of structure in our universe. Individual stars are home to planetary systems, providing life-sustaining energy and heat. The disk of our galaxy is comprised of expanding populations of stellar clusters which play a key role in galactic structure and dynamics. The death of massive stars enriches the interstellar medium (ISM) with heavy elements thus stellar evolution is a direct influence on the chemical evolution of galaxies. Finally, the net abundance of stars determines the mass-to-light ratio of galaxies, affecting dynamics and evolution on a universal scale. Clearly, if astronomers are to understand how the universe and its components formed and evolved, we must begin by quantifying the life histories of stars.

During the past century astronomers have made great progress towards this goal by developing detailed theories of stellar structure and evolution. However, a complete picture of the star formation process still eludes us. For example, there is currently no single theory which can predict the observed distribution of stellar masses at star birth (otherwise known as the initial mass function or IMF). In addition, while the birth and evolution of isolated, solar-type stars is reasonably well constrained, there are large gaps in our understanding of the physical processes governing star formation at the high and low mass ends of the mass spectrum. Further, it is unclear how these processes at either end are affected by the local star-forming environments.

The goal of this dissertation is to investigate the low mass star formation process. (In this context, the phrase "low mass star" refers to objects with masses less than one solar mass, $M<1\ M_{\odot}$.) In particular, I seek to determine the shape of the initial mass function below the hydrogen-burning limit (HBL, $M<0.08\ M_{\odot}$). This regime is

especially important because it defines a class of objects (called *brown dwarfs*) whose masses bridge the gap between stars ($M > 0.08\ M_{\odot}$) and planets ($M < 0.012 M_{\odot}$). Unfortunately, unlike stars which are known to form from the collapse of molecular cloud cores (§1.2.1) and planets which are thought to form via accretion in a circumstellar disk, the formation of brown dwarfs currently has no widely accepted explanation. This dissertation combines photometry and spectroscopy of low mass stars and brown dwarfs to a) place observational constraints on the possible mechanisms driving brown dwarf formation and b) examine how the brown dwarf formation process relates to that of low mass stars.

1.2 The Current Paradigm for Low Mass Star Formation

When looking at the Milky Way on a clear moonless night, the sharp-eyed observer will notice that the bright band of stars extending across the sky is interrupted by a number of dark patches through which no visible starlight pentrates. These regions, known as Giant Molecular Clouds (GMCs), are the sites of star and planet formation in our galaxy.

GMCs are composed primarly of very cold (T$\sim$10-50 K) molecular hydrogen gas (H_2) and interstellar dust. Their sizes range from 20-100 pc and their total masses range from 10^4-$10^6\ M_{\odot}$, yielding mean densities of 50-100 cm^{-3} (Lada, 2005). The star formation process converts the molecular material contained in these large and cold clouds into much smaller and hotter hydrogen-burning stars.

1.2.1 Formation of a Single Low Mass Star

According to the theory developed by Shu and collaborators (Shu, 1977; Shu et al., 1987), neglecting the influences of cloud rotation and magnetic fields, the star formation process begins when the molecular cloud begins to collapse due to its internal gravity. As the cloud collapses, the density increases non-homogeneously, allowing the cloud to fragment and form regions with extremely high local densities (n(H_2)$\sim 10^{4-5}$ cm^{-3}). If the density is high enough, these *cloud cores* become gravitationally unstable and

collapse isothermally until their increased densities cause the cores to become optically thick to their own radiation (e.g. radiation is absorbed and acts to increase the central temperature of the cores). At this point a protostar (a quasi-static stellar core) is born. Note that classical star formation theory predicts that there is a minimum mass required for the collapse of a dense core into a protostar (Jeans, 1902) and that for a typical star forming cloud this mass is on the order of a solar mass (Larson, 1995). As I will discuss in upcoming sections, this is a problem when considering the formation of objects with masses significantly smaller than 1 $M_{\odot}$.

The protostar is surrounded by an infalling envelope of gas and dust. To conserve angular momentum, the infalling envelope forms a disk around the embryonic core. The protostar continues to gain mass through the accretion of material from the disk. At this point, protostellar luminosities are dominated by an accretion luminosity which effectively dissipates the gravitational potential energy lost during infall and collapse. When the mass of the protostar increases such that the central temperature reaches 10^6K, deuterium burning begins, adding a new component to the protostar's luminosity. At the onset of deuterium burning, accretion typically slows down, the remnants of the protostellar envelope disperse, and the protostar becomes visible. This definines the start of the pre-main sequence (PMS) phase of stellar evolution.

Pre-main sequence stars burn their primordial deuterium rather quickly. Without significant accretion to replenish their fuel stores, nuclear reactions cease and the luminosity begins to decrease. The lack of radiation pressure in the core allows gravity to take over and the PMS star will again begin to contract. During this second epoch of contraction planet formation is thought to occur within the remnants of the circumstellar accretion disk. PMS evolution ends when the gravitational contraction has caused the central temperature to increase to 10^7K. At this point, the nuclear hydrogen burning that defines a star begins, the star's luminosity stabilizes, and the star is said to be on the main sequence (MS).

1.2.2 Star Formation in Clusters

The scenario above describes the formation of a single, isolated low mass star. However, we have learned that most stars are not born in isolation but rather form in dense clusters embedded in the largest and most massive cores of GMCs (Lada et al., 1991b; Carpenter, 2000; Lada & Lada, 2003; Porras et al., 2003). If we wish to truly understand the star formation process, we need to examine the embedded cluster population of GMCs.

Star clusters of any sort are important laboratories for astrophysical research. They contain a statistically significant ($N \gtrsim 50$) number of stars with a wide range of masses in a relatively small volume of space. Their members share a common origin, having formed from the same parent GMC. Additionally, cluster stars are at roughly uniform distances with similar ages and chemical compositions. The embedded phase of a cluster's evolution typically lasts around 3 Myr (Lada, 2005). At these ages, even the low mass cluster population is fairly bright (e.g. §1.2.1 and 1.2.4) and more readily observable than later in the cluster's lifetime. Further, embedded clusters are too young to have lost significant numbers of stars to stellar evolution and/or dynamical evaporation. Observations of embedded clusters therefore provide snapshots of stars *in their natal environments*. Consequently, embedded clusters are extremely useful tools for star formation studies.

1.2.3 The Initial Mass Function

A good example of the power of embedded clusters is the role they play in determining the initial mass function (IMF). The IMF is defined as the distribution of stellar masses at star birth (Salpeter, 1955) and it is a powerful tool used to constrain formation and evolution theory across the entire spectrum of astrophysics. In particular, determining the shape of the IMF, including the locations of the turnover and minimum masses, is vital to our understanding of the physical processes that control star and planet formation. However, in most cases the IMF is not a readily observable quantity. N-body simulations

show that older open clusters ($\tau \sim$100 Myr) contain a mere 20-30% of the stars in the original embedded clusters (Kroupa et al., 2001). These clusters require corrections for dynamical evolution and mass loss in any attempt to determine their IMFs. In contrast, the observed mass distribution in an embedded cluster *is* its IMF. The IMF of massive stars has been studied in this manner for many years and is reasonably well constrained (see Massey, 1998, for a review). The IMF of low mass stars, on the other hand, is far less certain due in part to the relatively recent (within the last $\sim$10 years) addition of brown dwarfs.

1.2.4 Brown Dwarfs

Brown dwarfs (BDs) are low mass ($M < 0.08\ M_{\odot}$), low luminosity objects characterized by their inability to sustain nuclear hydrogen burning. Rather, they shine brightly for the first few million years of their lives via the transformation of gravitational potential energy into heat. However, while full-fledged stars achieve core temperatures high enough to ignite hydrogen, the core temperatures of brown dwarfs remain below the HBL ($T_{core} \approx 10^7$K). Without a stable internal energy source, brown dwarfs spend the remainder of their lives cooling and fading from view (Burrows et al., 1997).

The identification of brown dwarfs poses an interesting observational challenge, neatly illustrated by the long amount of time that elapsed between the first theoretical mention of "black dwarfs" by Kumar (1963) and the first confirmed detection of such an object (GL 229B, Oppenheimer et al., 1995; Nakajima et al., 1995). This long time interval between theory and observation was due in part to the lack of appropriate detector technology. The most massive middle-aged brown dwarfs (M=0.08$M_{\odot}$, age$\sim$1 Gyr) have absolute magnitudes $V \sim$19 (Baraffe et al., 1998). Placing these objects at the distance of the nearest star-forming regions (d$\sim$100 pc) yields apparent magnitudes $v \sim$24, well below the limit of standard optical detectors on mid-size telescopes. At near-infrared (NIR) wavelengths, however, brown dwarfs are much brighter. In the $K-$band (2.2 μm) our example middle-aged brown dwarf would have a magnitude $K \sim$15 and a

corresponding young brown dwarf in the nearby star forming region ($\tau \sim 1$ Myr) would be blazing away at $K \sim 10$, easily detectable on a 1 m class telescope with the infrared detectors available today.

With the advent of deep, large-scale surveys such as the Deep Near-Infrared Survey (DENIS, Epchtein et al., 1994), the 2 Micron All Sky Survey (2MASS, Skrutskie et al., 1997), and the Sloan Digital Sky Survey (SDSS, York et al., 2000), the field of brown dwarf research has undergone rapid expansion over the past decade, resulting in the detection of numerous field brown dwarfs and the definition of two new spectral classes (e.g. Delfosse et al., 1997; Kirkpatrick et al., 1999; Leggett et al., 2000). Analysis of these observations has led to the conclusion that brown dwarfs constitute a significant fraction of the stellar population in the solar neighborhood and may comprise as much as 15% of the galactic disk mass (Reid et al., 1999; Chabrier, 2002).

A robust theory of star and planet formation must therefore take brown dwarf formation into account. However, as mentioned earlier in this chapter, classical star formation theory has trouble explaining the formation of objects with masses significantly smaller than a solar mass. Consequently, the origin of brown dwarfs is still unclear. Do brown dwarfs form in a manner similar to their stellar counterparts or more akin to their planetary cousins? What mechanism drives brown dwarf formation and does it depend on the star forming environment? What is the shape of the brown dwarf IMF? Recently many theories of brown dwarf formation have been proposed, including turbulent fragmentation of a molecular cloud (Padoan & Nordlund, 2002), ejection of protostellar embryos (Reipurth & Clarke, 2001), protostellar disk collisions (Lin et al., 1998), and photo-erosion of prestellar cores (Whitworth & Zinnecker, 2004). Studies of young brown dwarfs in their birth environments are needed to distinguish between these scenarios.

Figure 1–1. Optical image of Orion B: North is up and East is left. The brightest star in the field is ζ Ori, the easternmost star in Orion's Belt. NGC 2024 (the Flame Nebula) lies just east of ζ Ori. NGC 2023 is the blue reflection nebula south of NGC 2024, with IC 434 and the Horsehead Nebula slightly to the southwest. NGC 2068 (M78) and NGC 2071 are in the northeast corner of the image. Photo: W. H. Wang (IfA, U. Hawaii)

1.3 Orion B: An Ideal Testbed for Star Formation Studies

This dissertation is a study of young brown dwarfs and low mass stars in the natal environments of the Orion B molecular cloud. Historically, Orion B (or Lynds 1630) has long been known to be an extensive locale of active star formation, even prior to its

identification as a dark cloud by Lynds (1962). Early studies detected a number of H α emission line stars east and north of Orion's belt (Haro & Moreno, 1953; Herbig & Kuhi, 1963), and the region's colloquial namesake, Orion "B" (the second strong radio source detected in the Orion region), was found to be a compact H II region (NGC 2024) more than 50 years ago (Hepburn et al., 1954). Practically, Orion B lends itself to the study of young, low mass objects as it is one of the nearest regions of ongoing star formation and the nearest region of massive star formation. Distance estimates to the cloud range from 390-415 pc (Anthony-Twarog, 1982) although Brown et al. (1994) point out that there may be a gradient across the region with the near cloud edge at 320 pc and the far edge at 500 pc. Assuming a median distance of 400pc, the proximity of Orion B implies that an unrededdened 1 Myr brown dwarf will have a *K* magnitude of ∼13 – easily observable with today's telescopes and NIR instruments. In addition, Orion B is conveniently located out of the plane of the galaxy (l=206°, b=-15°), reducing foreground and background contamination by the general galactic stellar population.

Orion B contains many spectacular objects known for more than a century to both amateur and professional astronomers alike: the reflection nebulae NGC 2068 (M78), NGC 2071, and NGC 2023, the H II regions NGC 2024 (The Flame Nebula) and IC 434, and the small dark cloud of the Horsehead Nebula (B33) seen in silhouette. All of these regions can be seen in the optical image shown in Figure 1–1. However, optical images do not show the whole picture. Recall that the visible hallmark of a GMC is a broad, dark swath of sky with little to no optical starlight. In actuality, GMCs are not devoid of stars at all. It is the large concentrations of dust within a GMC that absorb and scatter the light from background stars causing the region to *appear* dark. In order to truly unlock the secrets of star formation contained in a GMC, longer wavelength observations are needed to penetrate the dust.

Radio observations (λ=2.6 mm) of the Orion B region by Tucker et al. (1973) revealed a large complex of extended CO emission (indicating the presence of molecular

hydrogen) coinciding with the optical dark cloud. The optical nebulae described above were found not to be singular sources of CO emission but rather maxima located within a much larger region of molecular line emission. The full extent of Orion B was subsequently delineated by the higher sensitivity CO observations of Maddalena et al. (1986) who found that the cloud subtends approximately 19 deg^2 on the the sky and contains nearly 10^5 $M_\odot$ of gas (Figure 1–2).

Lada et al. (1991a) carried out a systematic search for dense gas (n$>10^4$cm^{-3}) in Orion B using the J(2-1) transition of CS as a tracer and found that only a small fraction ($<$19%) of the total cloud mass is located in the dense cores and is thus involved in the star formation process (recall §1.2.1). In a companion 2.2 μm survey, Lada et al. (1991b) unexpectedly discovered that 60-90% of the young stellar population resides in 3 populous clusters (NGC 2024, NGC 2068, and NGC 2071) embedded in the most massive dense molecular cores. This result was confirmed by Carpenter (2000) using data from 2MASS. However, the completeness limits of both the Lada survey (K $<$13.0) and 2MASS (K_s $\sim$14.0) were too bright to probe very far below the hydrogen burning limit. This dissertation extends the current body of work in Orion B beyond the limits of the previous surveys, specifically focusing on the contribution of young brown dwarfs to the overall embedded cluster population.

1.4 A NIR Spectroscopic Study of Young Brown Dwarfs in Orion B

Many recent studies of the low mass populations in young clusters have detected significant numbers of brown dwarfs using deep near-infrared (NIR) photometry (e.g. Hillenbrand & Carpenter, 2000; Luhman et al., 2000; Muench et al., 2002 in the Orion Nebula Cluster and Muench et al. 2003 in IC 348). However, stellar and substellar mass functions derived from photometry alone can only be studied in a statistical sense. Individual mass estimates remain ambiguous due to uncertainties in the age, extinction, and membership status of any given source. A determination of effective temperatures using NIR spectroscopy alleviates some of these uncertainties and, with the help of

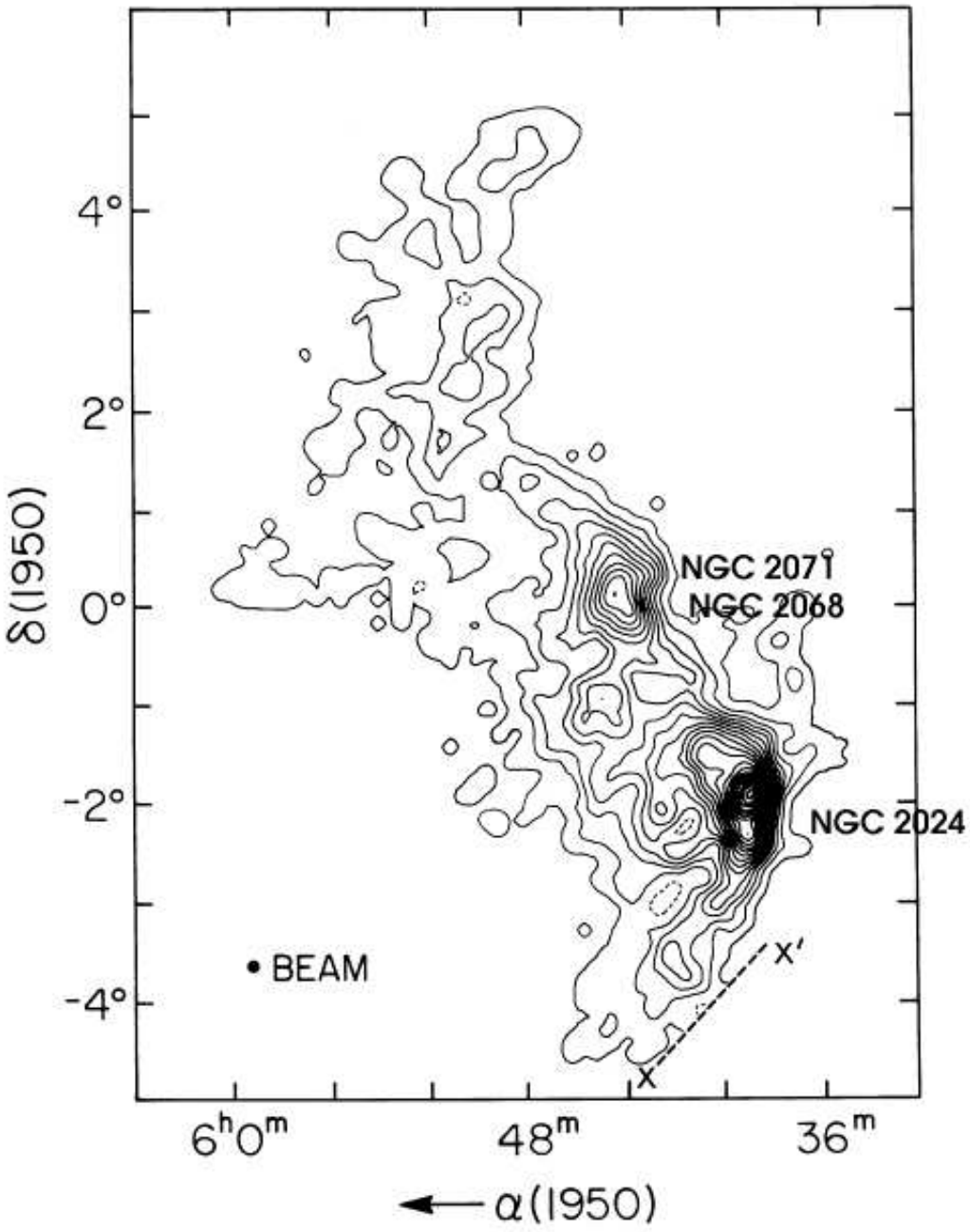

Figure 1–2. CO map of Orion B adapted from Maddalena et al. (1986). The cloud subtends 19 square degrees on the sky and contains $\sim 10^5$ $M_\odot$ of molecular gas (Maddalena et al., 1986). The three most prominent star forming regions are indicated.

pre-main sequence models, allows for more accurate mass estimates for each individual source.

For my dissertation, I am using a combination of NIR photometry and spectroscopy to characterize the brown dwarf populations in the dominant star forming regions in Orion B. I will use the results of this study to assess current theories of brown dwarf formation in the context of the observations, ultimately examining the relationship between the formation processes of brown dwarfs and low mass stars. Chapter 2 describes all data acquisition and reduction. This includes the planning, execution, and reduction of a large-scale NIR imaging survey of Orion B, the use of this survey to select the spectroscopic sample, and all spectroscopic observations and reductions. Chapter 3 describes our methods for the classification of young M star and brown dwarf spectra and includes a discussion of surface gravity. Chapter 4 presents the results of our study of NGC 2024. Chapter 5 presents the results for NGC 2068 and NGC 2071. Chapter 6 examines these results and their implication for brown dwarf formation in Orion B. Chapter 7 investigates the star-forming history of the region and Chapter 8 presents my conclusions and plans for future work.

CHAPTER 2
NEAR-INFRARED IMAGING AND SPECTROSCOPY OF ORION B

2.1 FLAMINGOS: The FLoridA Multi-object near-INfrared Grism Observational Spectrometer

All imaging and spectroscopic data included in this work were taken using FLAMINGOS, the Florida Multi-Object Imaging Near-Infrared Grism Observational Spectrometer (Elston, 1998). Conceived by Richard Elston and built at the University of Florida, FLAMINGOS is a combination of a wide-field NIR imager and the world's first fully cryogenic NIR multi-object spectrometer.

FLAMINGOS employs a 2048×2048 pixel HgCdTe HAWAII-2 infrared array with 18 micron pixels. On the Kitt Peak National Observatory (KPNO) 4 meter (4 m) telescope this corresponds to a plate scale of 0.318″/pixel and a 10.8′×10.8′field of view. On the KPNO 2.1 m telescope, the plate scale is 0.608″/pixel, yielding a field of view of 20.5′× 20.5′. The imaging filters include standard broadband J (1.25 μm), H (1.65 μm), and K (2.2 μm) filters roughly equivalent to the Caltech (CIT) system, as well as a K_s (2.12 μm) filter. For spectral observations, FLAMINGOS offers both a JH and HK grism and filter set which provide spectra across two bands (J and H or H and K) simultaneously. Spectral resolutions are low (typically R=1000-1800 depending on the filter and grism combinations chosen).

The large detector area and wide field of view of FLAMINGOS, particularly on the KPNO 2.1m, makes FLAMINGOS a very efficient instrument for imaging large regions of the sky: an entire square degree can be observed in nine fields. Further, the multi-object spectrometer (MOS) of FLAMINGOS makes it possible to obtain spectra of 25-50 objects simultaneously. These qualities make FLAMINGOS an excellent instrument for

large-scale, multi-dimensional NIR surveys. This dissertation is one of the first broad applications of FLAMINGOS as a survey instrument.

2.2 Surveying the Stellar and Substellar Content of GMCs with FLAMINGOS

In the year 2000, the National Optical Astronomy Observatories (NOAO) approved the long-term survey project *Toward a Complete Near-Infrared Spectroscopic and Imaging Survey of Giant Molecular Clouds* (NOAO Survey Program 2000B-0028, P.I.: E. A. Lada). The main goals of the survey were to use FLAMINGOS imaging and spectroscopy to determine the number and spatial extent of young stars in six of the nearest GMCs and to measure their ages and masses. When data acquisition, reduction, and analysis for all clouds are complete, the data will also be used to study the IMF of each region and to address issues such as the variations of star formation efficiency and rate from cloud to cloud, the formation of clusters and sequential star formation. The clouds selected for study were Orion B, Perseus, Rosette, and Monoceros. The contribution of my dissertation is a broad imaging survey of Orion B and an in-depth analysis combining both imaging and spectroscopy of the most active star forming regions in the cloud.

2.3 FLAMINGOS Imaging of Orion B

2.3.1 Survey Strategy and Observations

As discussed in Chapter 1, earlier studies of Orion B have shown that the majority of star formation in the cloud occurs within the dense cores (Lada et al., 1991a,b; Carpenter, 2000). The FLAMINGOS survey region was therefore chosen to coincide with the densest gas as indicated by the CO map of Maddalena et al. (1986). In addition, the survey region encompasses nearly the entire CS survey of Lada et al. (1991a) (Figure 2–1).

Initial observations of the 50 FLAMINGOS fields shown in Figure 2–1 as well as three off-cloud control fields were obtained during the 2001-2002 winter observing season on the KPNO 2.1 m telescope. All fields were observed in the *J*, *H*, and *K* filters

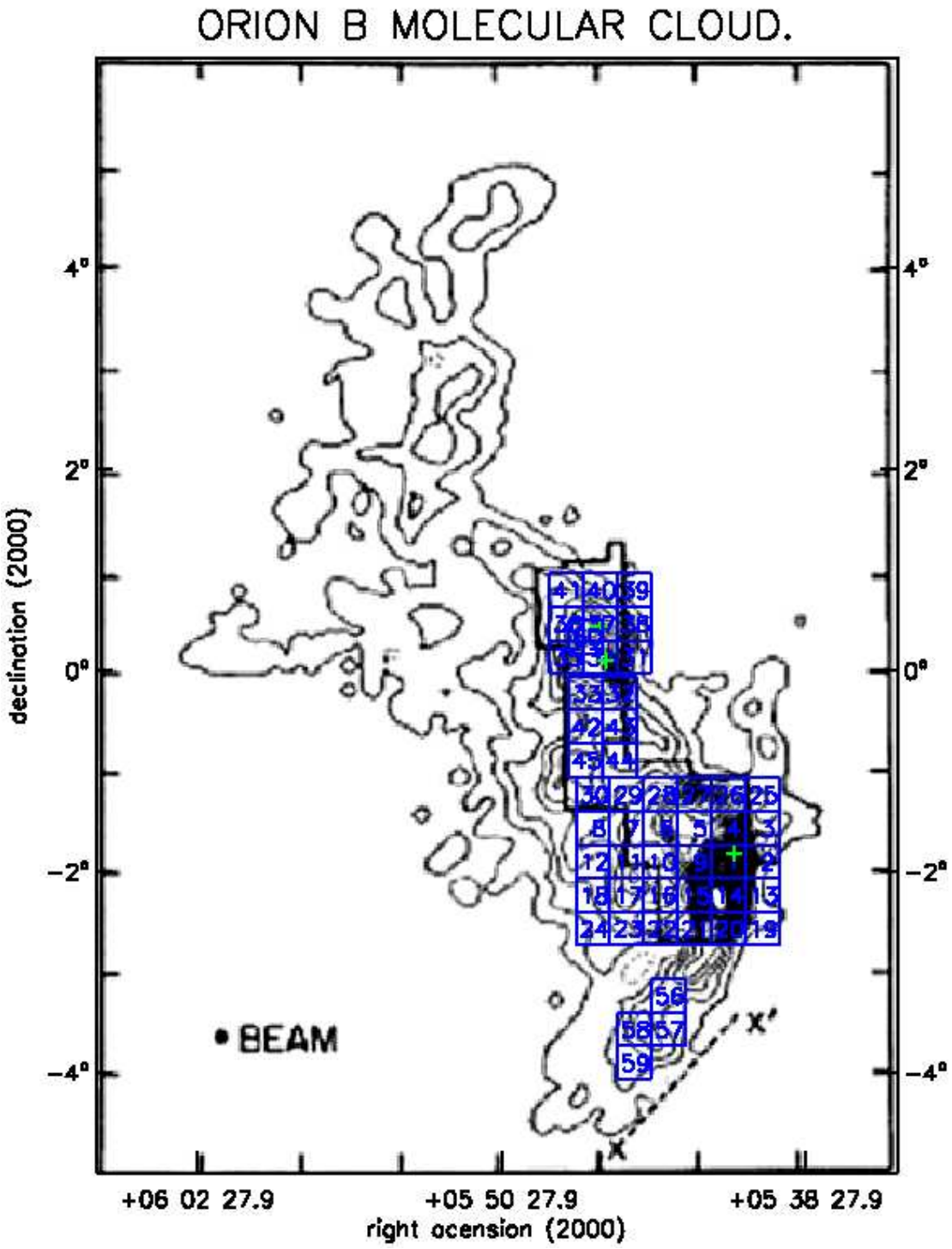

Figure 2–1. CO map of Orion B (Maddalena et al., 1986) shown with the observed FLAMINGOS/KPNO 2.1m survey fields. Each FLAMINGOS field is 20′ on a side to allow for some overlap from field to field. The thick black line outlines the CS survey of Lada et al. (1991a).

using a 9-point dither pattern to allow for the creation and subtraction of a background sky frame. The integration time at each point was 35 seconds in all bands, yielding a total of $\sim$5 minutes on source and a targeted depth of $J = H = K \geq 18$. Typical seeing was 1.″5-1.″9 as indicated by the full width at half maximum (FWHM) of the stellar profiles. Dome flats at all wavelengths and dark frames were also observed for calibration purposes.

Occasionally, due to poor weather conditions, instrument/telescope problems, or observer error, the image quality and/or depth was much worse than expected (e.g. seeing $\gg$ 2.″0 and/or $J = H = K \ll$18.0 as indicated by preliminary data reduction). These fields were marked as re-takes and re-observed during the winters of 2002-2003 and 2003-2004. In addition, during the 2003-2004 and 2004-2005 observing seasons four more off-cloud control fields and 6 "gap" fields in the vicinity of NGC 2024, NGC 2068, and NGC 2071 were observed to ensure full coverage of that region of the map. A complete observing log for the Orion B fields can be found in Appendix A.

Over the course of the entire survey, a total of $\sim$360 individual Orion B images were taken covering nearly 6 square degrees of sky and yielding $\sim$6 gigabytes of data. It was impractical to reduce and photometer such a large amount of data by hand; thus, two automated processing pipelines were designed to complete these tasks. The first pipeline, dubbed *LongLegs* and authored by Carlos Román-Zúñiga, takes care of preliminary processing, basic data reduction, and construction of a final image (Román-Zúñiga, 2006). The second pipeline, called *Pinkpack* and written by this author, incorporates source extraction, photometry, astrometry, and the combination of multi-wavelength data into a single catalog. Both pipelines were constructed using a combination of pre-existing Image Reduction and Analysis Facility (IRAF) tasks and custom C and FORTRAN routines written by the authors. Each pipeline is typically run on one night of data (300-500 raw data frames, 16Mb each) at a time. The detailed functionality of these pipelines is described in the following sections.

2.3.2 LongLegs: The Data Reduction Pipeline

A standard infrared image does not just contain flux from the desired targets. Rather, background emission from the atmosphere, telescope, and instrument all contribute to the total flux incident on the detector. In the NIR, the sky background dominates, often rendering even the brightest science targets nearly invisible in the raw data frames (Figure 2–2). In addition, most infrared detectors suffer from varying sensitivity across

Figure 2–2. Raw $K-$band image of an Orion B control field (oribcf6) taken with FLAMINGOS in November 2004. Note that there are hardly any stars visible.

the array, non-linearity in the detector response, and various dead, hot, or excessively noisy pixels. All of these effects must be removed prior to any study of the astronomical target. *LongLegs* (Román-Zúñiga, 2006) was written to accomplish this task for all FLAMINGOS images. Aside from its ability to complete the data reduction process for large volumes of data, *LongLegs* is innovative in that it includes a two-pass sky subtraction routine which effectively creates and removes the local sky background while leaving the science target fluxes intact. The remainder of this section provides the details of the *LongLegs* data reduction process.

2.3.2.1 Cleanflamingos

The first step in the *LongLegs* pipeline is cleanflamingos. Beginning with raw data frames such as the one shown in Figure 2–2, cleanflamingos takes care of all preliminary data processing for an entire night of data, one science target at a time. Bad pixels (pixels having counts $>$60000 or $<$-60000) are identified and set to have values of 0.0. Images are grouped according to type (e.g. object, flat, dark) and the mean and standard deviation are calculated; frames having mean values which differ by more than 2 sigma from the mean of the group are rejected. A third-degree polynomial correction is then applied to the good data to correct the integrated counts in each pixel for the non-linear response of the detector. Dark frames are median combined to create a master dark for the science images as well as a dark for the flat fields. A master flat field is created by median combining and normalizing the dark-subtracted dome flats. Finally, a bad pixel mask (BPM) is created by identifying all anomalous pixels in the master dark and the master flat.

2.3.2.2 Crunchflamingos

The main data reduction engine in *Longlegs* is crunchflamingos, which completes two separate passes through the reduction process. Pass 1 begins by subtracting the master dark from all science frames, removing the dark current and bias voltage from the images. A local sky frame is created for each individual science image by scaling

and median combining the 8 adjacent dark-subtracted frames. This local sky is then subtracted from the science images to remove the sky background. The resulting data are divided by the master flat to account for the pixel-to-pixel sensitivity variations in the detector.

In theory, a single pass through the reduction process would be sufficient to create science quality images. However, in many cases the object removal during sky creation is imperfect and large negative residuals are left in the final images. Consequently, pass 2 of crunchflamingos recreates the background sky with the astronomical objects masked out. The IRAF source detection program daofind is run on all frames in a dithered set, the frame offsets are calculated, and a preliminary combined frame is constructed. All sources with fluxes larger than a user-specified sigma threshold are masked out from the individual images and local skies are re-created from the "starless" data frames. These new sky frames are subtracted from the object images and used to create a night sky flat which is subequently used to flatten the data The output of crunchflamingos is an improved set of reduced images ready for final combination.

2.3.2.3 Smoothflamingos

The last task in the *LongLegs* pipeline is smoothflamingos. Smoothflamingos creates the final, science-grade images according to the following steps: First, a 6th order Chebyshev polynomical correction is applied to all flat-fielded data frames and BPMs using the IRAF task geotran to correct for geometric distortion (caused by imperfections in the FLAMINGOS optical system). Note that the exact coefficients of the polynomial depend on the observing season since the correction was redetermined using images of a 20×20 pinhole grid array each time the array or filter positions were disturbed. Once all data have been geotranned, the frame offsets for each dither set are recalculated, the pixels are resampled to half of their original size, and the dither set is average combined to create a final image (Figure 2–3). All final images are trimmed to be 4096×4096 pixels and are then ready for photometry, astrometry, or any other analysis.

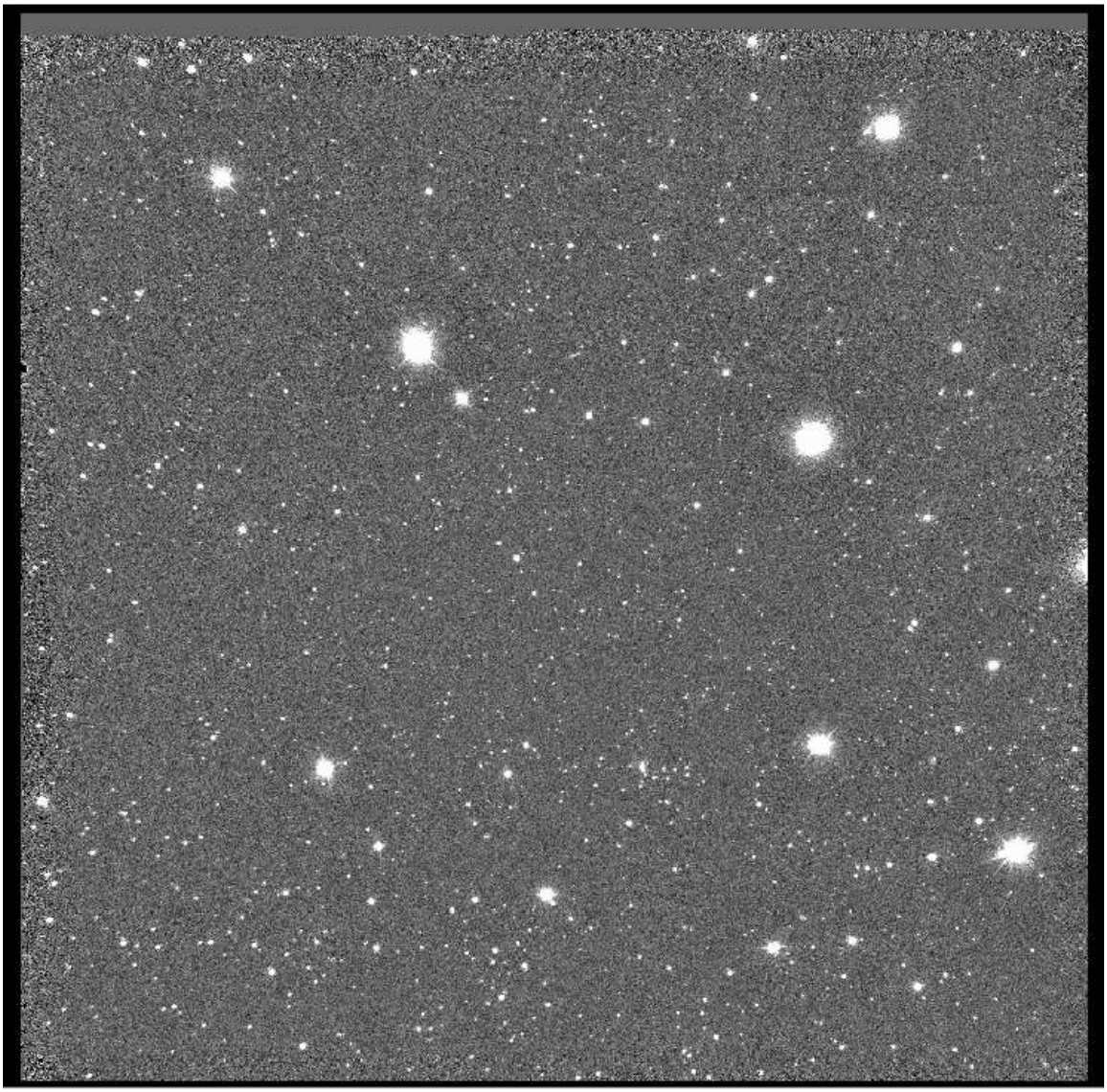

Figure 2–3. The final LongLegs product for the image shown in Figure 2–2. This image has been linearized, dark-subtracted, sky-subtracted, flat-fielded, corrected for geometric distortion, combined with other images in the dither set, re-sampled and trimmed to have 4096×4096 pixels. Note the plethora of stars revealed by the reduction process.

2.3.3 Pinkpack: The Photometry and Astrometry Pipeline

Pinkpack, written and tested by this author in 2001 and updated in 2002 and 2003, is the FLAMINGOS photometry and astrometry pipeline. Once a night of data has been fully reduced using *LongLegs*, *Pinkpack* tasks can be used to generate image statistics, detect all sources in the images, obtain calibrated aperture and point spread function

photometry for detected objects, solve for the astrometric solution of each image, complete preliminary data assessment, and combine multi-wavelength data into a single catalog.

2.3.3.1 Pinkphot

The first major task in the *Pinkpack* pipeline is pinkphot, the FLAMINGOS photometry task. Pinkphot detects sources and derives both aperture and profile fitting photometry on an image-by-image basis for as many images as the user chooses to place in the input list. The task begins by running the source extraction program SExtractor (Bertin & Arnouts, 1996) to generate a preliminary source list for the current image. This list is passed through a detection filter which employs the BPM to remove any objects falling on bad regions of the chip where their photometry will be compromised. The filtered source list is then passed through two additional routines which remove saturated objects and select stars suitable for defining the image point spread function (PSF). PSF stars must be relatively bright, isolated (no other objects within 5 FWHM), at least 100 pixels from the image edges, be roughly evenly distributed across the image and above all exhibit a typical stellar profile. Thus, objects flagged by SExtractor as elongated and objects having a FWHM more than 1.5 times the mean or less than 0.5 times the mean are automatically eliminated from the PSF star list.

After creation of the final source catalog and PSF star list, pinkphot begins its photometry routines. The sky background estimated and subtracted by *LongLegs* is typically a decent representation of the true local sky, however, for very nebulous and/or crowded fields their will still be some element of contamination in large apertures by flux from nearby neighbors or nebulosity. Pinkphot circumvents this problem by applying an aperture correction. Aperture photometry of the PSF stars is obtained using the IRAF phot task over twelve apertures with radii ranging from 0.5FWHM to 3.25FWHM. An aperture correction from apertures 3-12 (aperture radii from 1-3.25FWHM) is then calculated from the PSF star photometry using the IRAF task mkapfile. All sources in the

image are photometered using the small aperture (r=FWHM) and subsequently corrected out to the larger aperture (r=3.25FWHM), yielding contaminant-free large aperture photometry for all objects. Note that at this point all photometry is uncalibrated with the zero point set at 0.0.

Once the corrected aperture photometry is obtained, pinkphot derives PSF photometry for all sources using two passes through the IRAF DAOPHOT routines (Stetson, 1987). In the first pass, a model PSF is created from the PSF stars using a second order variable Moffat function with the β parameter set to 2.5. This PSF is fit to each object in the complete source catalog using the large aperture photometry as input. The fitted stars are then subtracted from the original image, revealing any close companions. The second pass repeats the initial aperture photometry and PSF fitting process on the newly detected sources using the aperture correction and model PSF derived in pass one.

The net output from pinkphot is a catalog containing the x and y pixel coordinates, the small aperture radius in pixels, the flux in that aperture, the phot magnitude using the small aperture, the large aperture radius in pixels, the aperture-corrected magnitude and its associated error, the PSF magnitude and its error, and detection flags indicating whether an object is potentially saturated and/or elongated. It should be noted that while the aperture photometry is included for completeness and its potential usefulness in determining the magnitudes of non-stellar sources, all survey magnitudes discussed from this point forward are derived from PSF photometry, due to its improved ability to handle extremely crowded or nebulous fields and variations in stellar PSFs across an image (refer to §2.3.4 for further discussion of this effect).

2.3.3.2 Pinkastrom

At this point in the pipleline, objects are identified only by their x and y positions on the detector. These coordinates, while useful when looking at the image itself, yield no information regarding an object's true position in the sky. However, each image is a two-dimensional projection of a portion of the three-dimensional celestial sphere. Using

standard spherical geometry it is therefore possible to derive a transformation between the two. This transformation, known in astronomical terms as the plate solution, defines the image world coordinate system (WCS), linking each image pixel to a specific location on the celestial sphere. Pinkastrom employs the pixel and celestial coordinates of known objects in the field to derive a plate solution and WCS for each image, subsequently applying the solution and deriving astronomical coordinates for all pinkphot detections. Note that pinkastrom uses the standard equatorial coordinates of Right Ascension (R.A.) and Declination (Dec.) to describe object positions on the celestial sphere. The epoch of all equatorial coordinates is J2000.

Pinkastrom begins by obtaining the coordinates of the image center (R.A. and Dec.) from the image header. Pinkastrom then calls out to an online catalog repository and downloads the equatorial coordinates and magnitudes of all sources within a 15 arcminute radius of this point. Here the user has the option of employing the most recent U. S. Naval Observatory all sky catalog (USNO B1.0) or the 2 Micron All Sky Survey (2MASS). For the purposes of the FLAMINGOS GMC survey, we have found that the 2MASS catalog consistently yields a higher number of matches per field (likely because it is also an infrared survey), providing a better sampled grid of points from which to calculate the solution. Consequently, all plate solutions and celestial coordinates quoted in this dissertation were derived using 2MASS. Once pinkastrom has a catalog of celestial coordinates corresponding to objects in the field, these coordinates are converted to rough x and y pixel positions using estimated WCS information provided in the image header and matched to objects in the pinkphot catalog using the IRAF task xyxymatch. The IRAF task ccmap is then used to calculate a rough plate solution using a second order polynomial fit to the matched list. The downloaded 2MASS catalog and the FLAMINGOS catalog are subsequently rematched with the IRAF task ccxymatch using the transformation given by the rough plate solution. A final fourth order polynomical solution is calculated from the re-matched lists.

The catalogs are matched a third time using the new plate solution. At this point, the final number of matches and the astrometric residuals are checked, and if they are satisfactory (n_{match} >50, residuals < 0.″25) the image WCS is updated and all pinkphot pixel positions are converted to J2000 R.A. and Dec. The output from pinkastrom is a new catalog containing both pixel and celestial coordinates for each object, a database file containing the plate solution, and a logfile containing the precise plate scale in arcseconds per pixel, image rotation in degrees, and rms values of the astrometry in arcseconds for all images in the input list. As indicated by Figure 2–4, typical rms values for the final positions are $\lesssim$0.″25.

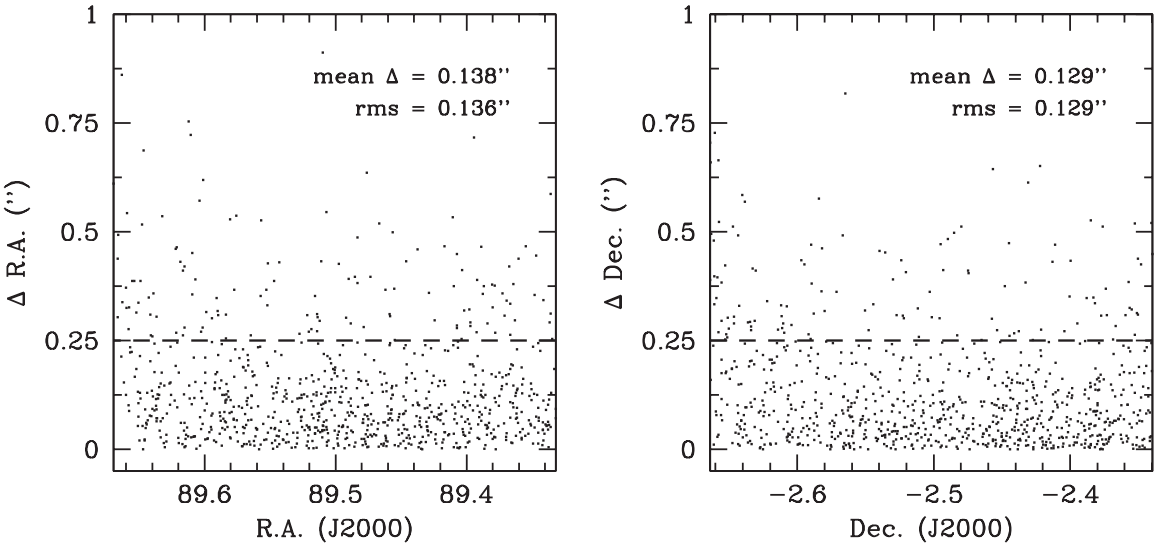

Figure 2–4. The deviations (Δ) in arcseconds of pinkastrom coordinates from 2MASS positions for 863 objects in the image shown in Figure 2–3. Both the mean deviations and the rms values for R.A. and Dec. are less than 0.″25.

2.3.3.3 Massmatch

The third major task in the *Pinkpack* pipeline is massmatch. As indicated by its name, massmatch matches FLAMINGOS detections to their 2MASS counterparts (if they haven't already been matched in the previous step) and calculates a photometric zero point for each FLAMINGOS image using 2MASS photometry. Note that this task is wavelength-dependent and must be run separately for the *J*, *H*, and *K* band images in each night.

The task begins by assessing whether a matched 2MASS/FLAMINGOS catalog exists. If not, source matching is accomplished using ccxymatch in the same manner described above. The matched catalog is then passed through a filtering routine which removes stars outside the acceptable magnitude range for zero point calculation. Stars used in the zero point calculation must be fainter than the FLAMINGOS saturation limit, conservatively estimated at $J = H = K$ =11.0, and brighter than J=15.5, H=15.0, and K=14.0. The faint limits were set to be slightly brighter than the 2MASS completeness limits ($J \simeq 15.8$, $H \simeq 15.1$, and $K \simeq 14.3$, Carpenter, 2000). Once an appropriate sample has been identified, the differences between the FLAMINGOS and 2MASS magnitudes are calculated for each object in the list. massmatch then creates a histogram of these differences and takes the centroid. Because the FLAMINGOS photometry was initially derived using a zero point set to 0.0, the centroid of this difference histogram is the photometric zero point (Figure 2–5).

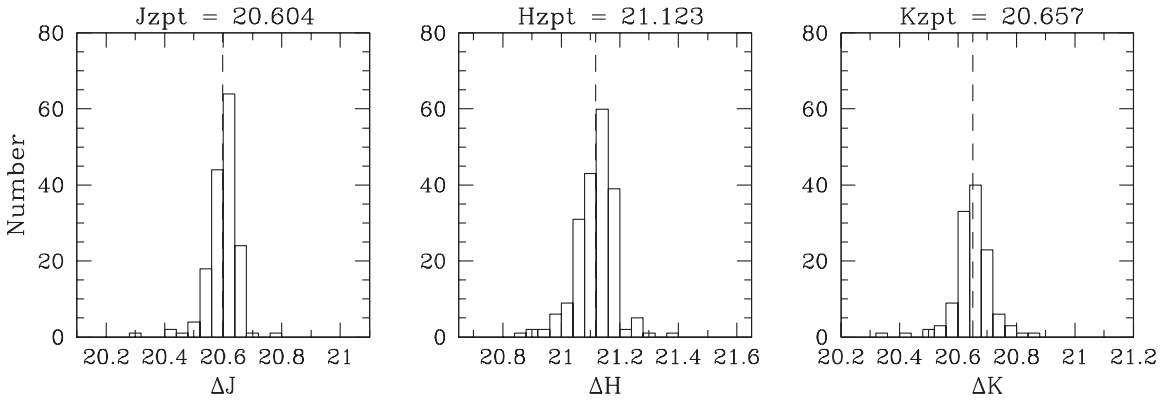

Figure 2–5. Sample difference histograms (Δ=M_{2MASS} - M_{FLMN}) used by massmatch to determine the zero point. These data are from the *JHK* image set of orib-07, taken on 2001 Dec 18. The dashed line in each histogram is the location of the centroid, the corresponding zero points are labelled atop each plot.

After calculating the zero point, massmatch uses this value to correct the photometry, updating the pinkastrom catalog so that it now contains calibrated photometry. In addition, massmatch also generates a number of data assessment tools. These include: a

calibrated luminosity function, magnitude comparison files, and magnitude scatter data. These tools will be discussed further in the quality assessment section below (§2.3.5).

2.3.3.4 Jhkmatch

Jhkmatch is the final step in the *Pinkpack* pipeline. The task uses the plate solutions determined with pinkastrom coupled with the IRAF matching task ccxymatch to merge the calibrated data from individual images into a single, multi-wavelength catalog for each field. In addition, jhkmatch uses the celestial coordinates of each object to assign a unique catalog identifier. The output from jhkmatch is a single catalog for each field containing object ids, celestial coordinates (J2000), pixel coordinates, *JHK* magnitudes and errors derived from aperture photometry, *JHK* magnitudes and errors derived from PSF photometry, and the informational data flags discussed above.

2.3.4 Positional Zero Point Correction

The presence of small misalignments and/or fabrication errors in the FLAMINGOS optical system does cause some noticeable PSF degradation in our images, particularly at the field edges. This PSF variation is present in survey data from all epochs. In addition, during the summer of 2005, it was noticed that stars located in the upper right quadrant of FLAMINGOS had pinkphot magnitudes which were systematically fainter than their 2MASS counterparts by $\sim$0.5 magnitudes. A comparison of flat fields taken in 2004 and 2005 revealed a small but significant flux loss ($\sim$5%) in this portion of the chip for the more recent data. A working theory by members of the FLAMINGOS team attributes the flux loss to a deterioration of the coating on the “field lens” (which is effectively the entrance window to the camera dewar). Because the stripping of the lens coating is highly structured, the net result is that the PSFs in affected region vary rapidly with position. This effect worsened over time: data taken in the 2001/2002 observing season are only minimally affected (e.g. Figure 2–5, presenting data taken in 2001 December) while the strongest effects are seen in data from the 2004-2005 observing season (e.g. Figure 2–7, presenting data taken in 2004 November).

Aperture photometry cannot account for variations in stellar PSFs across an image. PSF photometry as derived from pinkphot does attempt to compensate for some variation in the PSF, however the model used is a smooth function which cannot handle the amount of PSF degradation present in the FLAMINGOS images affected by the deterioration of the lens coating. In particular, sources in the southeast corner of recent (2004-present) FLAMINGOS images have wide, coma-shaped halos containing a significant portion of the stellar fluxes (Figure 2–6).

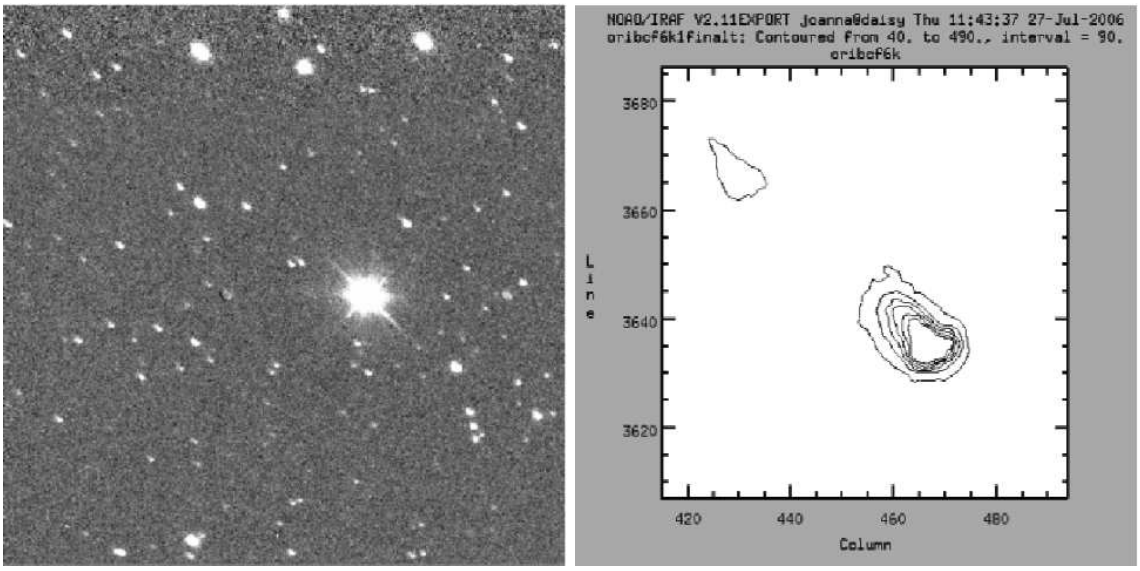

Figure 2–6. (a) Southeast corner of the reduced *K*-band image of control field 6 (orib-cf6-k1) taken in November of 2004. (b) Contour plot of two of the stellar profiles. The PSFs are clearly elongated and exhibit strong coma shaped halos which increase in size towards the edge of the image.

The model PSFs used in the pinkphot fitting routines cannot account for the flux in these halos. Consequently, the fitted magnitudes of objects in the affected regions are systematically too faint compared to their 2MASS counterparts, with the severity of this effect dependent on radial distance from the optical center (Figure 2–7a).

In addition, if enough sources are affected this problem has the additional consequence of skewing the central zero point for the image. In other words, if the observed magnitudes are too faint, the value of Δ (2MASS - FLAMINGOS magnitude) will be

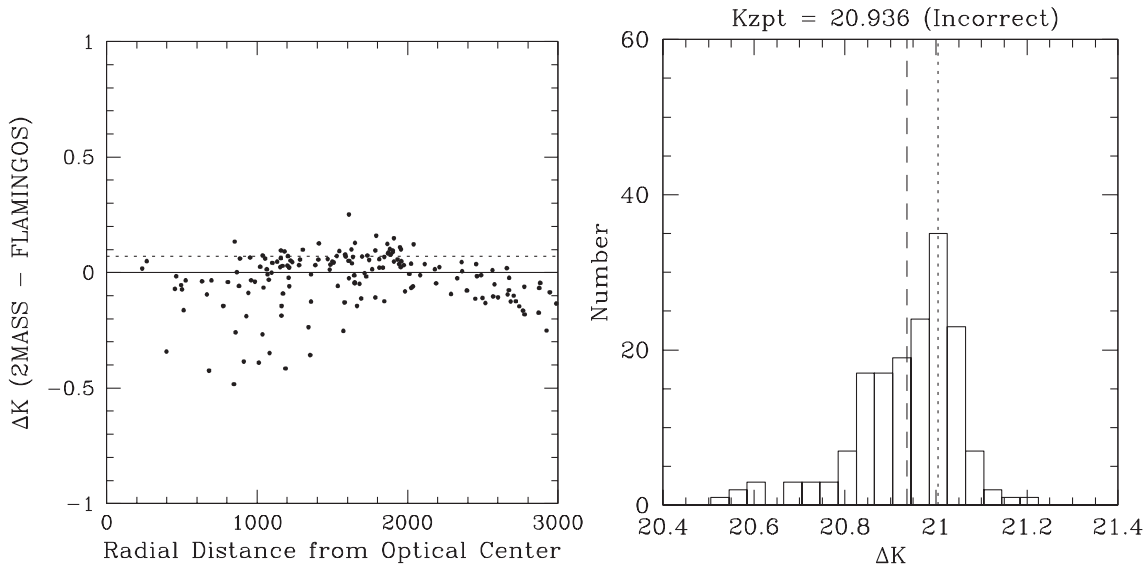

Figure 2–7. (a) Radial dependence of the photometric deviation from 2MASS for orib-cf6-k1 data after a first pass zero point has been applied. (b) Skewed zero point caused by the optical distortions shown in Figure 2–6. The dashed line in (b) is the centroided zero point calculated by massmatch. The dotted line in both (a) and (b) is the correct zero point for the image.

smaller than it should be and the centroided zero point will in turn be too bright since the offset distribution is now asymmetric with a bright tail (Figure 2–7b).

These effects would appear to have catastrophic implications for pipelined FLAMINGOS photometry, however, as it turns out, they are correctable. Andrea Stolte has devised a routine which both adjusts the skewed zero point and corrects the magnitudes affected by the lost flux. The routine operates by fitting a 6th order Legendre polynomical to the deviation between calibrated FLAMINGOS and 2MASS magnitudes as a function of position on the detector (Figure 2–8a). Based on the fit, we then apply this polynomical correction one band at a time to the zero point to obtain final, *correct* calibrated photometry (Figure 2–8b). The details of calculating and applying the fit can be found in Román-Zúñiga (2006).

The polynomial zero point correction was applied to all imaging data. The results of this correction include a reduction in the overall photometric scatter (see §2.3.5 for a discussion on how this value is calculated) and assurance that the final photometry is in

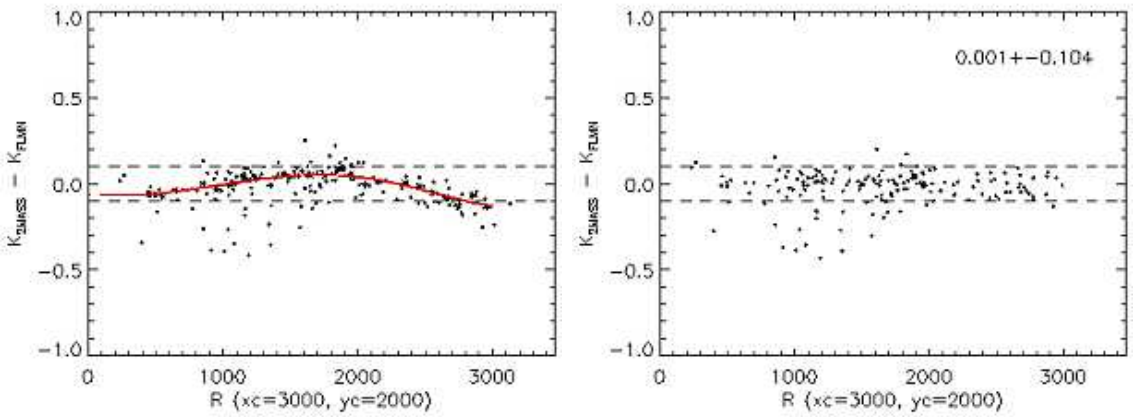

Figure 2–8. (a) Uncorrected *K*-band photometry for Ori B control field 6 shown with the 6th order polynomial fit to the data. (b) Corrected photometry for the same image shown with the new median ΔK and the standard deviation of this value.

agreement with 2MASS to within 0.1 magnitudes for a typical image. Note that since the PSF distortion effects worsened with time, the amount of improvement in the photometry is also time dependent: a typical improvement in photometric scatter was 0.01-0.02 magnitudes for data taken prior to fall 2003 and 0.03-0.04 magnitudes for fields observed November 2003-present. Fortunately, the majority of the Orion B survey data were taken during the 2001-2002 observing season, only requiring a small correction.

2.3.5 Imaging Data Quality and Completeness

2.3.5.1 Accuracy of the Photometry

Once the zero point correction was applied, photometric quality was assessed using the difference between the final FLAMINGOS photometry and the 2MASS database. The 1 σ rms values of the deviation from 2MASS were calculated in 0.5 mag bins and plotted as a function of the FLAMINGOS magnitude in each band (Figure 2–9). The overall photometric scatter for each image was derived by taking the mean of all rms values in the magnitude range from the FLAMINGOS saturation magnitude to the conservative 2MASS completeness estimates stated above. The final scatter values for each field can be found in Table A–2.

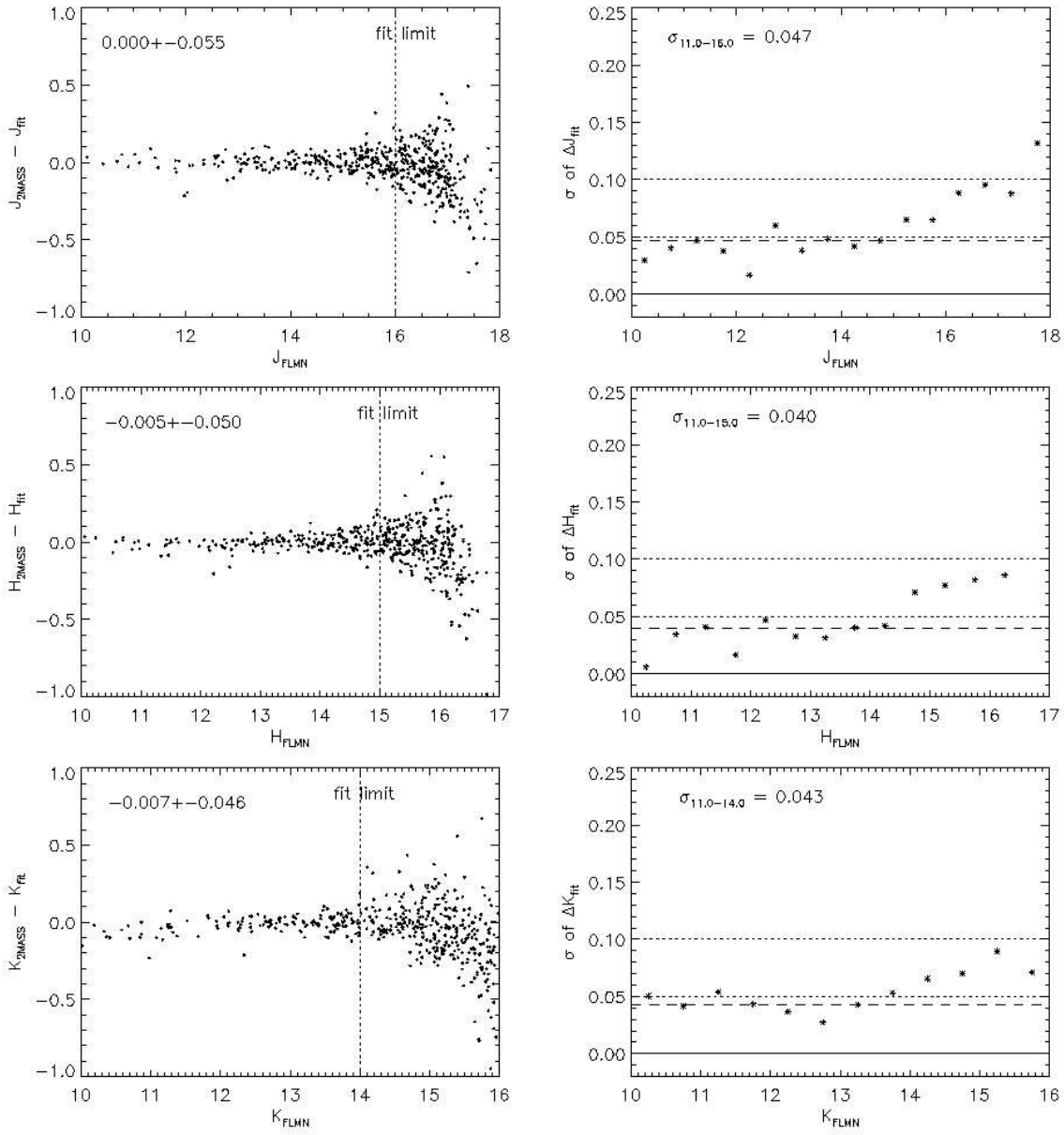

Figure 2–9. Sample scatter plots for data taken during the 2001-2002 observing season (orib-08, observed 2001 Dec 20) after application of the zero point correction. The left-hand panels plot the deviation between 2MASS and FLAMINGOS magnitudes as a function of FLAMINGOS magnitude. The dotted line indicates the faint limit for fitting the polynomial zero point correction. The right-hand panels show the calculated rms values as a function of magnitude. Dotted lines are plotted at limits of 0.05 and 0.10 magnitudes. The dashed line is the mean of the rms values down to the fit limit (the numerical value is indicated at the top of the plot).

The median scatter values for the entire Orion B survey (excluding extremely nebulous frames) are σ_J=0.05, σ_H=0.04, and σ_K=0.05. Consequently, in regions with little to no nebular emission, we estimate the bulk of our photometry is accurate to within 0.05 magnitudes. For images with large amounts of nebula (e.g. orib-01, orib-14, orib-34, and orib-37 which are centered on NGC 2024, NGC 2023, NGC 2068, and NGC 2071 respectively) the scatter with respect to 2MASS is much larger ($\gtrsim$0.1 magnitudes) than that expected from pure photometric noise. A similar effect has been noted by other authors studying young clusters with significant nebular emission (e.g. Muench et al., 2003 in IC 348 and Muench et al., 2002 and Slesnick et al., 2004 in the Trapezium) and is usually attributed to the large size of the 2MASS pixels ($\sim$2.0″), intrinsic variability of young objects, and variations in aperture size coupled with the strong nebular background. Finally, it should also be noted that for data taken in 2001-2002 the scatter with respect to 2MASS is also larger ($\sim$0.1 mag) for objects on the edge of detector where the data rapidly degrade due to a delamination of the engineering array.

2.3.5.2 Sensitivity Limits

The sensitivity limits of the survey were derived through an analysis of the photometric errors, following procedures similar to those employed by 2MASS. Simply put, there is a theoretical limit to the photometric precision at every signal to noise ratio (SNR) which takes into account the contribution from all internal noise sources in a digital, sky-subtracted image. This limit (σ_{lim}) is given by the equation

$$\sigma_{lim} \simeq 1.0857(S/N)^{-1}, \tag{2.1}$$

derived fully by Newberry (1991). If we wish to find the 10σ detection limit, we simply need to locate the magnitude at which the errors agree with the value of σ_{lim} at a SNR of 10: $\sigma_{10} \simeq 0.109$. Figure 2–10 shows the median photometric error (estimated in 0.2 magnitude bins) as a function of magnitude in each band for the entire FLAMINGOS/Orion

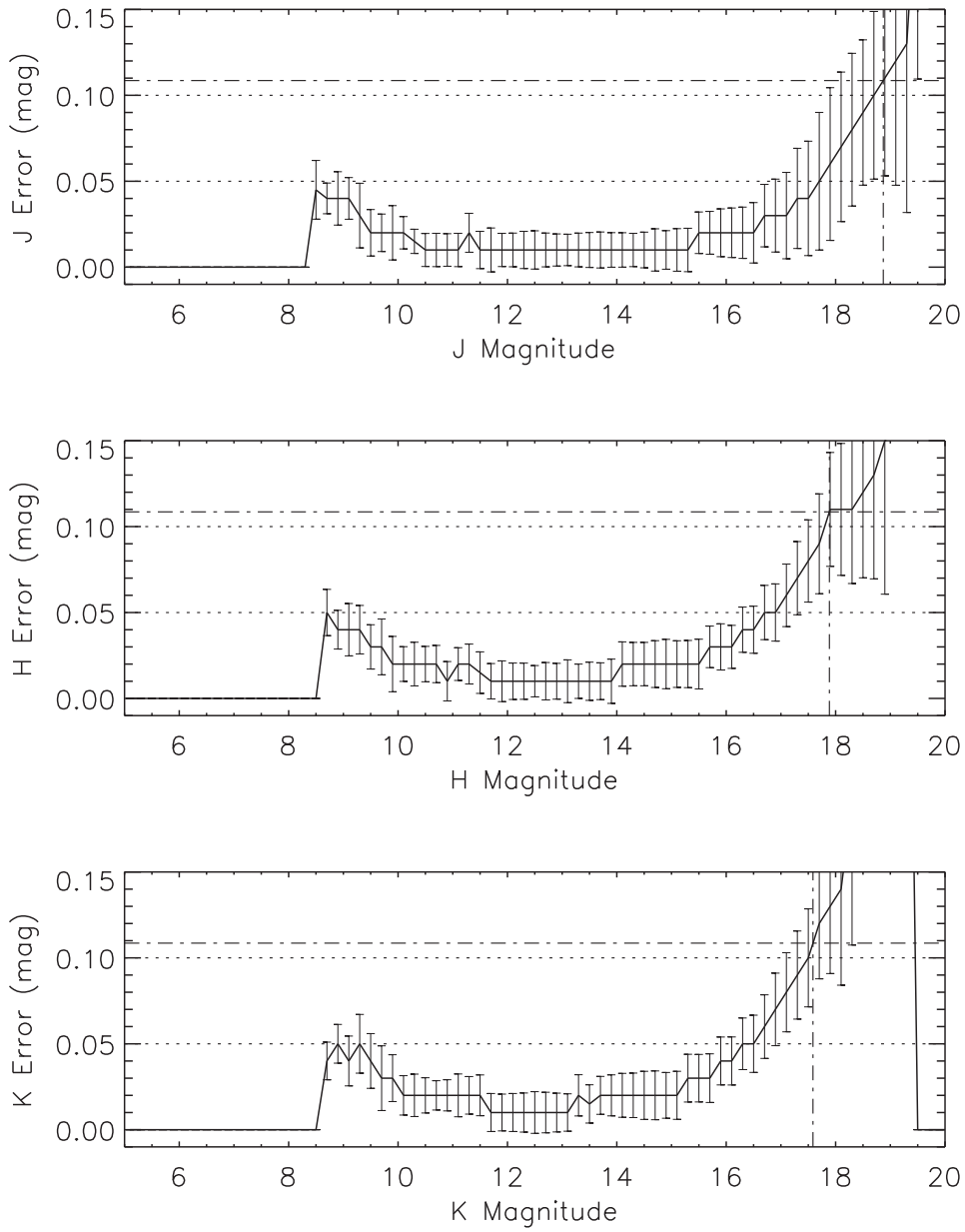

Figure 2–10. Error plots constructing using data from the entire FLAMINGOS/Orion B imaging survey. In each band, the median errors (calculated in 0.2 magnitude bins) are plotted as a function of magnitude (solid line). Error bars are the rms in each bin. The dotted lines are plotted at fiducial values of 0.05 and 0.10 magnitudes. The horizontal dot-dashed lines indicate the limiting error for 10σ magnitudes and the vertical dot-dashed lines show the location of the 10σ limits for this survey.

B imaging survey. The 10σ detection limits (where the error function crosses the limiting value) indicated by the figure are J=18.9, H=17.9, and K=17.6.

2.3.5.3 Completeness

For the purpose of this dissertation, the immediate function of the imaging survey is to provide a photometric catalog deep enough to select spectroscopic targets down to and below the HBL ($K \sim$13.0 at the distance of Orion B), subsequently using this photometry to place spectroscopically observed and classified objects on the Hertzprung-Russell diagram. Consequently, I am only concerned with ensuring that the photometric completeness limits are deeper than the magnitude limits for spectroscopic observations (H=15.0 on the KPNO 4 m telescope, H=13.0 on the KPNO 2.1 m telescope).

Completeness limits at the 90% level are canonically estimated using the turnover magnitude of a field's luminosity function. As mentioned above, massmatch outputs calibrated luminosity functions (LFs) for each image (e.g. Figure 2–11) and writes the peak of this function to the image headers. The LF peaks for all survey images can be found in Table A–3. I estimate the 90% completeness limits of the survey to be the median of these values for each band: J_{lim}=18.5, H_{lim}=17.75, and K_{lim}=17.5, which are certainly below the spectroscopic limits (§2.4.1).

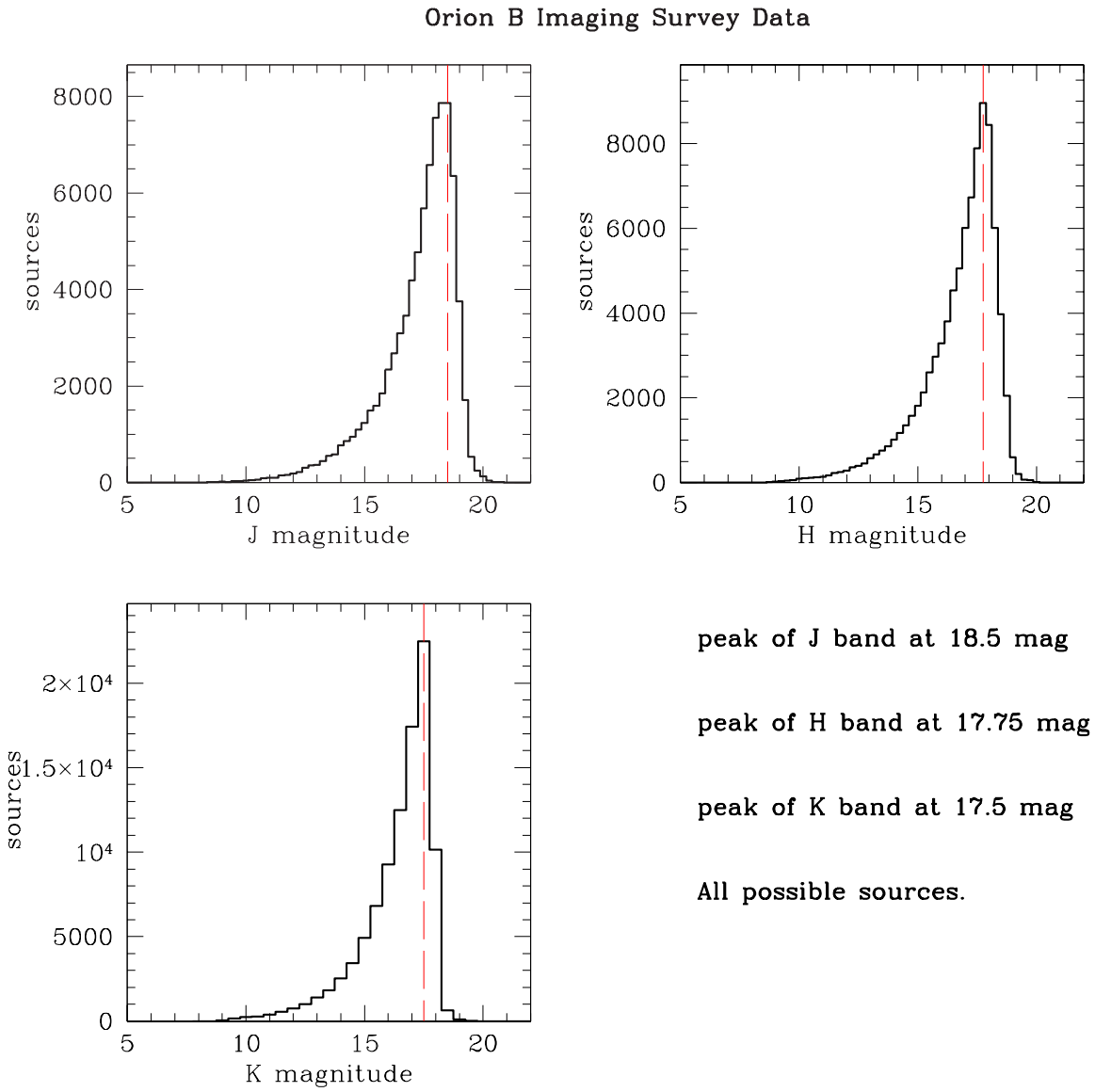

Figure 2–11. *J*, *H*, and *K*-band luminosity functions for the entire combined Orion B imaging survey. The dashed lines indicate the peak of each LF as well as the estimated 90% completeness limits for each band.

2.4 FLAMINGOS Spectra of Orion B

As mentioned in Chapter 1, infrared photometry alone is not sufficient to estimate masses for individual objects. Rather, by combining photometry with NIR spectra we can derive effective temperatures and stellar luminosities, ultimately using theoretical PMS evolutionary models to identify young brown dwarfs. In this section I discuss the design of the spectroscopic observing program, the details of the spectroscopic observations, and our data reduction techniques.

2.4.1 Spectroscopic Sample Selection and Mask Design

The FLAMINGOS/Orion B imaging survey contains more than 100,000 individual sources. Clearly, even with FLAMINGOS' multi-object capabilities it would be impractical to obtain a spectrum for every source. Rather, a more realistic course of action is to define an intelligent subsample suitable for MOS observations on the KPNO 4 m and/or 2.1 m telescopes which includes both candidate brown dwarfs and young stars representative of the general population in Orion B.

The first step in the sample selection process was to identify broad regions of interest in the cloud. Recall that the stated goal of this project is to characterize the brown dwarf populations in the most active areas of star formation in Orion B. Thus, the bulk of the regions chosen for spectroscopic observation are either the locations of known clusters or dense cores, with a few off-cluster/off-core regions added for comparison. Figure 2–12 shows the areas originally chosen (indicated by boxes representing the $10' \times 10'$ field of view of FLAMINGOS on the 4 m) and their relationship to the dense gas. Center coordinates for each field as well as the corresponding 2.1 m imaging survey region and any indications of known star formation activity are listed in Table 2–1.

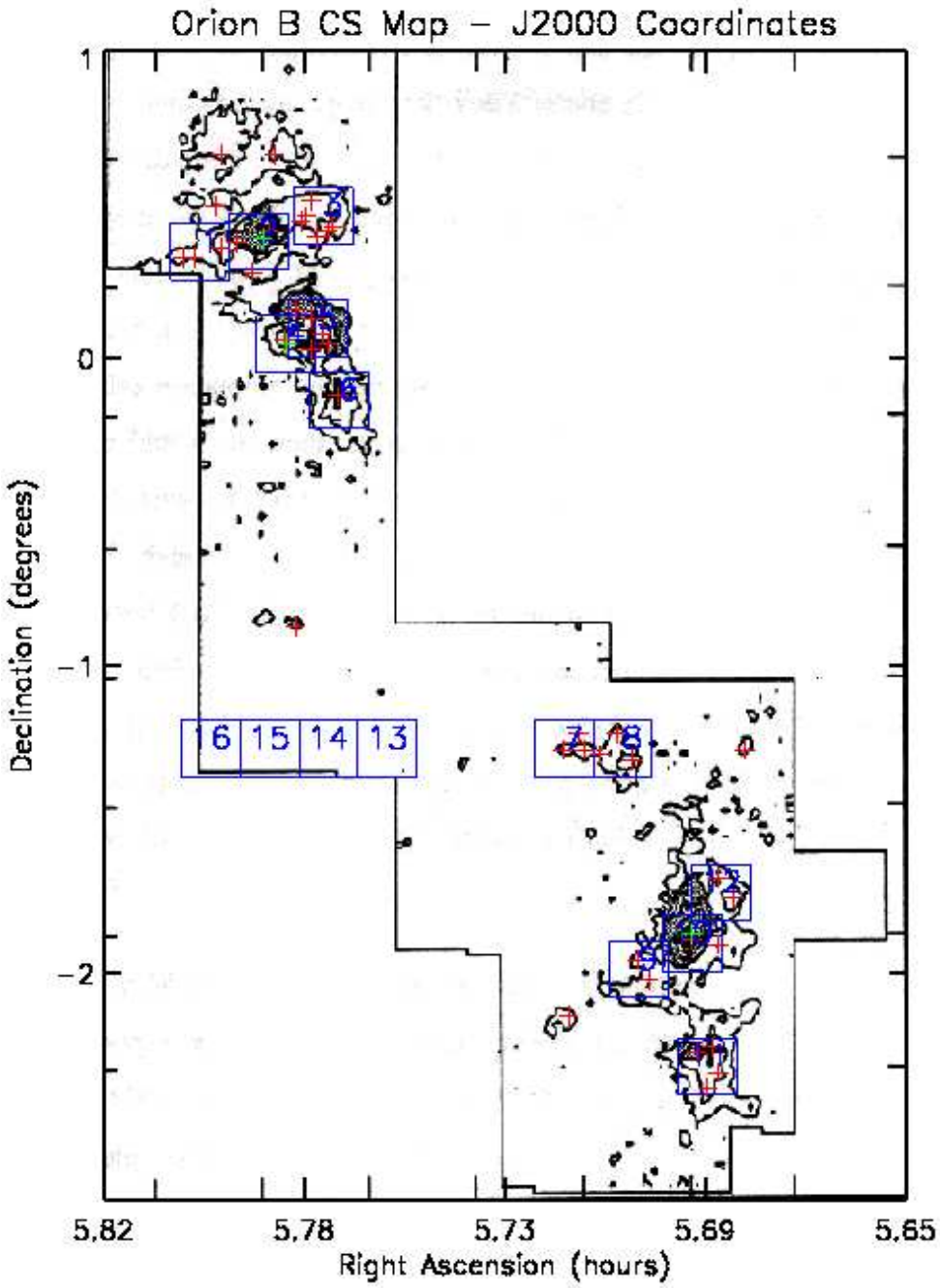

Figure 2–12. Regions of the Orion B cloud targeted for spectroscopic observations shown with the CS contours of Lada et al. (1991a). (Recall that Figure 2–1 shows the outline of this CS map in reference to the FLAMINGOS imaging survey and the CO map of Maddalena et al. (1986).) Boxes are 4 m FLAMINGOS fields (10'×10') and crosses indicate the 5σ CS clumps identified by Lada et al. (1991a). Note that the spectroscopic survey predominantly targets the regions of dense gas affiliated with known star formation, however, a few regions devoid of dense gas are also targeted.

Table 2–1. Regions Targeted for Spectroscopic Observation

ID	R.A. (J2000)	Dec.(J2000)	Imaging Field	Comments[a]
1	05:47:51.54	+00:20:43.3	orib-36	LBS 1,2,5
2	05:47:07.54	+00:22:43.3	orib-37	NGC 2071
3	05:46:19.54	+00:27:43.3	orib-37	LBS 13-15,18,20,22
4	05:46:47.54	+00 02 43.3	orib-34	NGC 2068
5	05:46:23.54	+00:05:43.3	orib-32/33	LBS 10
6	05:46:07.54	-00:08:16.7	orib-32	LBS 23
7	05:43:19.54	-01:16:16.7	orib-27	LBS 26-28
8	05:42:35.54	-01:16:16.7	orib-28	LBS 29,30
9	05:42:23.54	-01:59:16.7	orib-09	LBS 31,32
10	05:41:43.54	-01:54:16.7	orib-01	NGC 2024
11	05:41:31.54	-02:18:16.7	orib-14	NGC 2023
12	05:41:21.54	-01:44:16.7	orib-04	LBS 37,40
13	05:45:31.54	-01:16:16.7	orib-29	no dense gas
14	05:46:15.54	-01:16:16.7	orib-29	no dense gas
15	05:46:59.54	-01:16:16.7	orib-30	no dense gas
16	05:47:43.54	-01:16:16.7	orib-30	no dense gas

[a]A designation of LBS indicates the region was identified as a 5σ dense core by Lada et al. (1991a).

Once the fields were chosen, specific sources needed to be targeted for spectroscopic observation. This was a slightly more complex procedure due to the restrictions imposed by multi-object observations. MOS mode with FLAMINGOS is provided by a grism inside the camera dewar and a slit mask (a rectangular stainless steel plate with slits lasered into it) placed at the telescope focal plane. Each slit in the mask corresponds to a single position on the detector; unique slit masks must therefore be designed for each field, with accurate positions of the desired targets known a priori. Sample selection thus becomes a two step process; the first step is to compile a list of desired targets and the second step is to design slit masks which maximize the number of these targets on the mask.

The final consideration in the selection and design process is the choice of telescope. As part of the NOAO GMC survey, we had the option of carrying out FLAMINGOS MOS observations on either the KPNO 2.1 m or 4 m telescopes. Due to the intrisic faintness of the low mass population of Orion B, the majority of objects targeted in

this study were placed on masks designed for observation on the KPNO 4 m telescope, making use of the increased sensitivity (1 hour limiting magnitude, K$\sim$15.0) to maximize the number of brown dwarf spectra obtained. However, selected bright sources were targeted for observation on the 2.1 m telescope (1 hour limiting magnitude, K$\sim$13.0).

2.4.1.1 4 m Target Selection

Making use of either the images, photometry, and astrometry output from the 2.1 m imaging survey or a 4 m image with photometry and astrometry also generated by *Pinkpack*, target lists for 4 m spectroscopy were constructed according to the following guidelines: During the 2002-2003 observing season priority was given to brown dwarf candidates having $K < 16.5$. These objects were identified by comparing source positions in $H/H-K$ color-magnitude diagrams with a theoretical 1 Myr isochrone. All objects located below the reddening vector extending from the isochrone positioned at $M = 0.08 M_{\odot}$ (corresponding to the HBL) are candidate brown dwarfs (e.g. Figure 2–13, left). During the 2003-2004 observing season priority was given to infrared excess (IRX) sources (a common indicator of youth, e.g. Chapter 4, §4.3.2.3) having magnitudes brighter than K=16.5. In this case, IRX targets were identified using $J-H$ vs $H-K$ color-color diagrams (Figure 2–13, right). In either case, once a target list was compiled with the available IRX sources or brown dwarf candidates, a secondary list was created containing all available objects having K magnitudes 12.0$<K<$16.5 irrespective of their IRX or brown dwarf candidate status. Finally, during the 2004-2005 and 2005-2006 observing seasons target lists were compiled using a simple magnitude-limited selection including as many sources as possible with H magnitudes brighter than 15.5.

2.4.1.2 2.1 m Target Selection

The brighter sources (10.0$<K<$13.0) were targeted for observation on the 2.1 m telescope as part of a parallel survey to characterize the intermediate mass population of Orion B (Hernandez, 2006). I include discussion of the bright population in this study

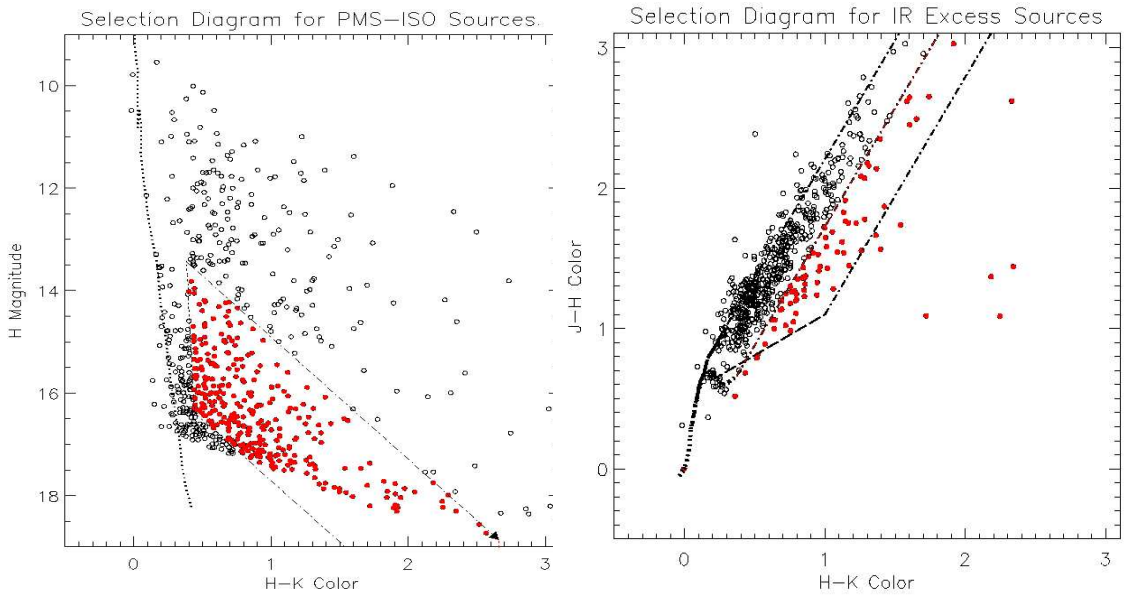

Figure 2–13. Sample selection diagrams for spectroscopic targets in NGC 2071: a) Color-magnitude diagram (CMD) for all sources down to K <16.5. The leftmost dotted line is the main sequence from Bessell & Brett (1988). The shorter dotted line is an abbreviated 1 Myr isochrone of D'Antona & Mazzitelli (1997). The dot-dashed lines are reddening vectors using the extinction law of Cohen et al. (1981) placed at 0.08 and 0.02 $M_{\odot}$. Selected brown dwarf candidates are shown as solid red dots. b) Color-color diagram (CC) for all sources down to K <16.5. The solid lines are the giant colors of Bessell & Brett (1988) coupled with a combination of Bessell & Brett (1988) dwarf colors for spectral types down to K7 and Leggett (1992), Leggett et al. (1996), and Dahn et al. (2002) for spectral types from M0 to M6 (Refer to Ch. 4.4.1 for an explanation of dwarf color choice). The dot-dashed lines are the reddening vectors of Cohen et al. (1981) and the dashed line is the classical T Tauri locus of Meyer et al. (1997). Selected IRX sources are shown in red.

since a few of the observed objects may be extremely young M stars and statistics of the brighter sources will aid in assessing our overall completeness in the region.

All 2.1 m targets were selected solely on the basis of a magnitude limit. Sources selected during the 2003-2004 observing season had magnitudes K <13.0 and sources selected during the 2004-2005 observing season had H <14.0.

2.4.1.3 Mask Design and Fabrication

Once suitable target lists were assembled, slit masks were designed using *Maskdesign*, a custom C program written by Matthew Horrobin. *Maskdesign* takes an input

catalog and an associated image as well as a user specified field center (the MOS field of view on FLAMINGOS is $\sim$1/3 of the full imaging field) and places as many slits as possible in the MOS field down to a specified magnitude limit. It is up to the user to adjust the selections to ensure that the desired sources are targeted and also to keep track of sources which have been placed on previous masks. In addition, the user must also select at least three bright stars distributed across the field to be used as setup stars. These stars are required to align the mask at the telescope - without the setup stars, it is impossible to center the science targets in their slits. Finally, it is important to note that for *Maskdesign* to run properly, the image used to design the masks must have the plate scale and field of view corresponding to the FLAMINGOS field at the telescope where the MOS observations will be taken. The 2.1 m survey images and catalogs thus required resampling and trimming prior to their use in mask design - this was accomplished using the IRAF task `geotran`. In addition, in a few cases (particularly for the 2001-2002 observing season) select fields were "pre-imaged" with FLAMINGOS at the 4 m. These images were also run through the pipelines and the output could then be directly used for mask design.

All slitmasks for the Orion B spectroscopic survey were designed as follows: first a maximum number of the priority objects discussed above were placed on the mask. Once this was completed, any available magnitude-limited "filler" objects were added to maximize the total yield from the multi-object observations. In all cases, the total number of objects targeted on each mask was limited by the spatial distribution of sources in the regions being targeted. Typically we were able to place 20-30 objects per mask for fields targeting the densest portions of the clusters and 10-20 objects per mask in the non-clustered regions. Figure 2–14 shows the region file output by *Maskdesign* indicating the location of the slits and acquisition stars for a sample mask (n2071a2) targeting the eastern (low stellar density) region of NGC 2071.

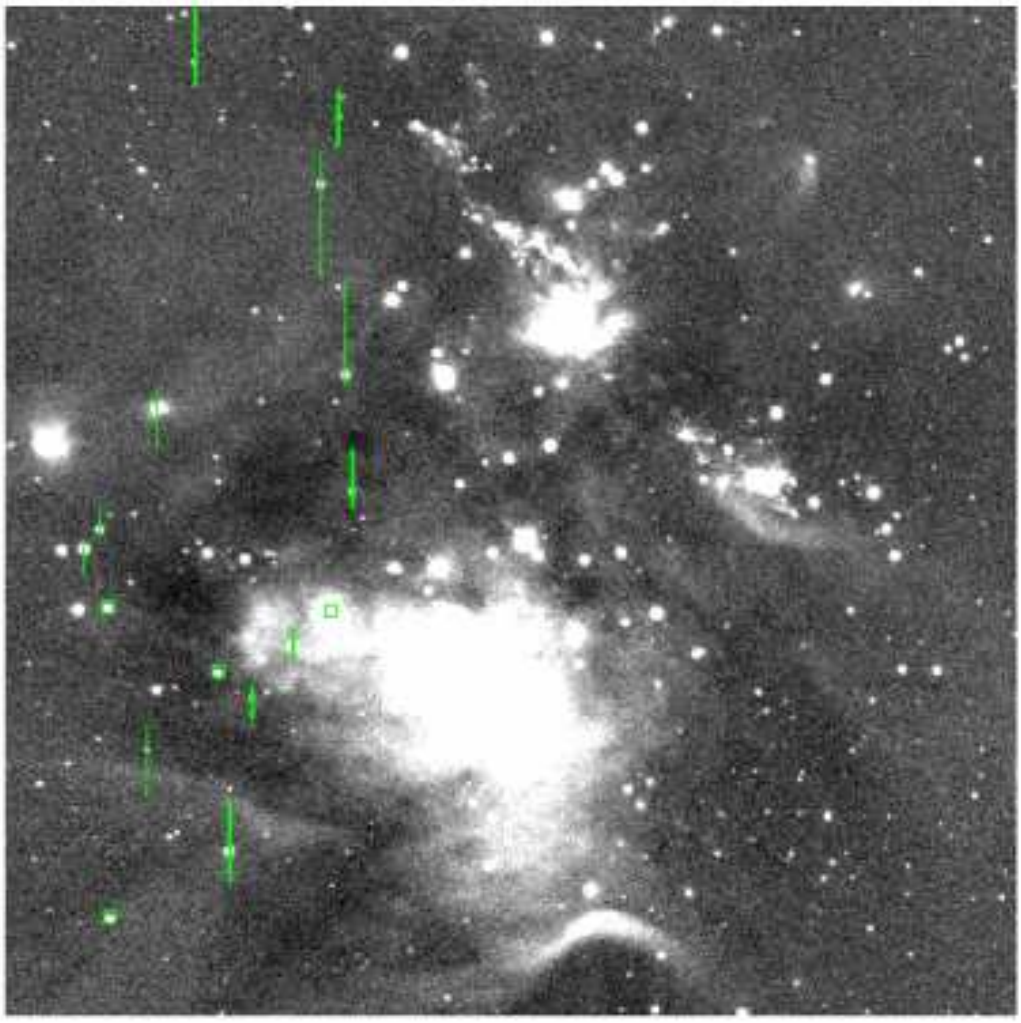

Figure 2–14. *K*-band image of NGC 2071 (North is up and East is left) taken with FLAMINGOS on the KPNO 2.1 m telescope on 2002 Dec 31 and transformed to the 4 m field of view using geotran. The green regions on the image indicate the slit positions for the mask n2071a2, designed in fall 2004 and targeting 11 objects with $H<15.5$ and one filler target with $H<16.0$. The bright stars enclosed in boxes are the acquisition stars.

Slit masks designed for the FLAMINGOS GMC survey were fabricated using an on-site laser in the University of Florida's Infrared Instrumentation lab and either sent or taken by the observers to the telescopes.

2.4.2 Spectroscopic Observations

MOS spectra of young sources in Orion B were taken with both the KPNO 2.1m and 4m telescopes. For the most part the data acquisition procedures were the same on

both telescopes, however, there were a few differences, thus I have chosen to discuss them separately. A complete observing log for the masks observed on both telescopes can be found in Table B–1 in Appendix B.

2.4.2.1 4-m Data Acquisition

Slit masks identified in Table B–1 as 4 m masks were observed on the KPNO 4 m telescope during four consecutive winter observing seasons from January 2003 through December 2005 using the following procedure: First, the field in question was imaged using a short exposure time (typically 10-30s) in the K or K_s filter. If the resultant image was suitably centered with the setup stars visible, a guide star was acquired, and the MOS mask was put into place. At this point the field was re-imaged (with the slit mask in) to check mask alignment. A perfectly aligned field will have stars centered in all of the alignment boxes and some of the slits (Figure 2–15). On the other hand, if the alignment stars were not centered in their boxes, the IRAF task xbox was used to determine small correctional offsets to the telescope position. These offsets were applied, the field was reimaged, and this process was repeated until acceptable mask alignment was achieved.

All spectra were taken using the JH filter (0.9-1.8 μm) coupled with the JH grism, providing complete spectral coverage in both the J and H bands simultaneously. The slit width in all cases was 3 pixels or $0\farcs95$ on the 4m, yielding a spectral resolution, R $\sim$ 1300. For each mask, 300s or 600s exposures were taken in sets of four, dithering between two positions on the chip in a standard ABBA pattern to allow for background sky subtraction. The separation between positions A and B was $4''$along the long dimension of the slitlets. Total exposure times for each mask typically ranged from 40-80 minutes and are detailed in Table B–1.

Once the science exposures were completed, internal quartz lamp flat fields and HeNeAr arc lamp spectra were taken for calibration purposes. Short exposure, long slit spectra of a nearby G dwarf at similar airmass were also taken immediately following the science observations to correct for telluric absorption.

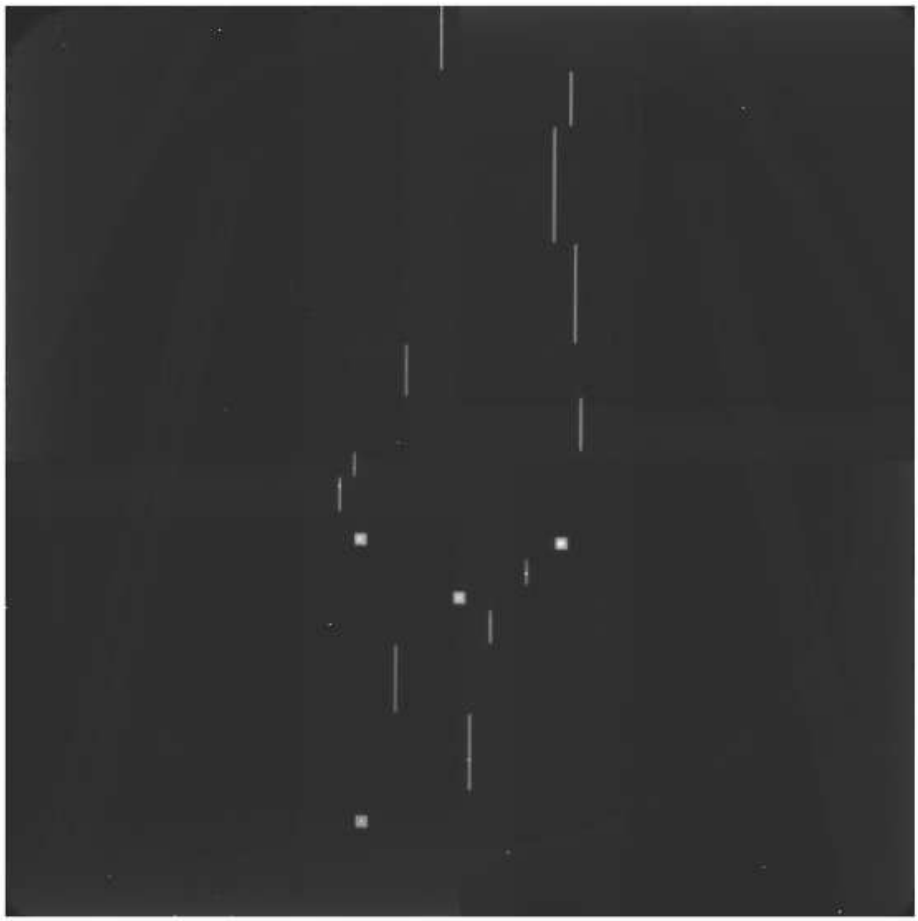

Figure 2–15. Image of a properly aligned MOS plate. The plate shown is n2071a2 (*c.f.* Figure 2–14) with North up and East left. Note that all of the setup boxes contain reasonably centered stars.

2.4.2.2 2.1-m Data Acquisition

Data acquisition for the 2.1 m spectra proceeded in much the same way as for the 4 m spectra, but with slight differences in the guiding and calibration procedures. The guider at the 2.1 m is not a moveable guide probe (as at the 4 m) but rather a fixed off-axis mirror which feeds into the guide camera. Consequently, the first step in the 2.1 m observation procedure was to ensure that a suitable guide star was present in the FOV of the guide camera and would remain so for the entire ABBA dither pattern. If this was the case, then the observations could proceed as above.

Spectra of the brighter targets were obtained with FLAMINGOS on the KPNO 2.1m telescope during the 2003-2004 and 2004-2005 winter observing seasons. As with the 4 m spectra, all sources were observed using the combination of the *JH* filter and the *JH* grism. Individual 300s exposures were taken in sets of four, yielding typical total integration times of $\sim$1 hour (see Table B–1 for precise exposure times per mask). All slits were again 3 pixels wide, which on the 2.1 m corresponds to a width of $1\farcs82$ and results in a spectral resolution of R $\sim$ 1300. Flat fields were taken using an illuminated white screen mounted on the inside of the telescope dome. Due to the lack of internal arc lamps at the 2.1 m, no designated wavelength calibration frames were obtained - wavelength calibration would be determined using the atmospheric OH emission lines intrinsic to all NIR spectra. Finally, as with the 4 m data acquisition, a nearby G star was observed to correct for telluric absorption.

2.4.3 Data Reduction

All FLAMINGOS spectra taken for this study (both 2.1m and 4m data) were reduced using a combination of standard IRAF procedures and custom FLAMINGOS routines. Spectra taken prior to fall 2004 were run through all reduction procedures by hand. Spectra taken after this point were reduced using the FLAMINGOS spectral reduction pipeline, dubbed *Shrimpeater* and authored by Aaron Steinhauer. Either way, the reduction procedure is outlined below.

We determined that a linearization correction was not necessary as the size of the correction was $<$1% of the raw flux levels for usable data and the high order function needed would likely introduce larger errors. Consequently, the raw data were first dark subtracted and subsequently divided by a normalized flat field created by averaging a number of dark subtracted quartz flats (4 m) or dome flats (2.1 m). A pairwise subtraction of adjacent exposures was then employed to remove background sky emission. The sky subtracted images were aligned and combined using imcombine to create a single image containing all spectra for each slit mask or standard star (e.g. Figure 2–16).

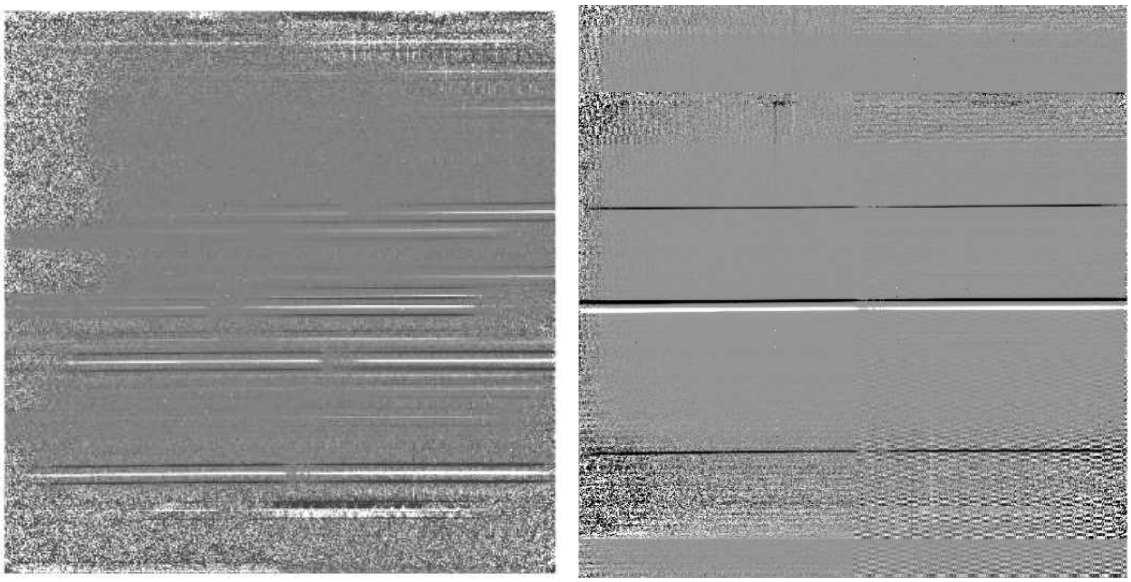

Figure 2–16. Reduced (but not extracted) spectra for n2071a2 (left) and the telluric standard HD 23050 (right) both observed on 2004 Nov 26. The negative regions are byproducts of the pairwise subtraction

Once basic reductions were complete, the two-dimensional images were converted to one-dimensional spectra as follows: The long slit (e.g. standard star) spectra were extracted immediately, using the IRAF task apall to identify and trace the aperture and extract the flux. The same aperture trace was then employed to extract arc lamp spectra (4 m data) or background sky spectra (2.1 m data) for wavelength calibration. The positions of known lines in these spectra were identified and used to derive the dispersion correction (to convert pixel numbers to wavelengths). The correction was subsequently applied using the IRAF task dispcor.

Extraction of the multi-slit data was accomplished by first cutting a two-dimensional image of each slitlet from the final combined image described above (Figure 2–17).

Figure 2–17. Two-dimensional image of a single reduced MOS slitlet prior to extraction of the one-dimensional spectrum. The image shown is n2071a2_06 - the sixth slitlet on n2071a2.

Each spectrum was then traced and extracted separately using apall. The dispersion solutions for the multi-slit data were derived using background OH emission lines local to each slitlet. Once the wavelength calibration was applied, target spectra were divided by the telluric standard to correct for atmospheric absorption. Features introduced by this division were removed by multiplying the resultant spectra by the solar spectrum, thereby yielding the final product ready for spectral classification (Figure 2–18).

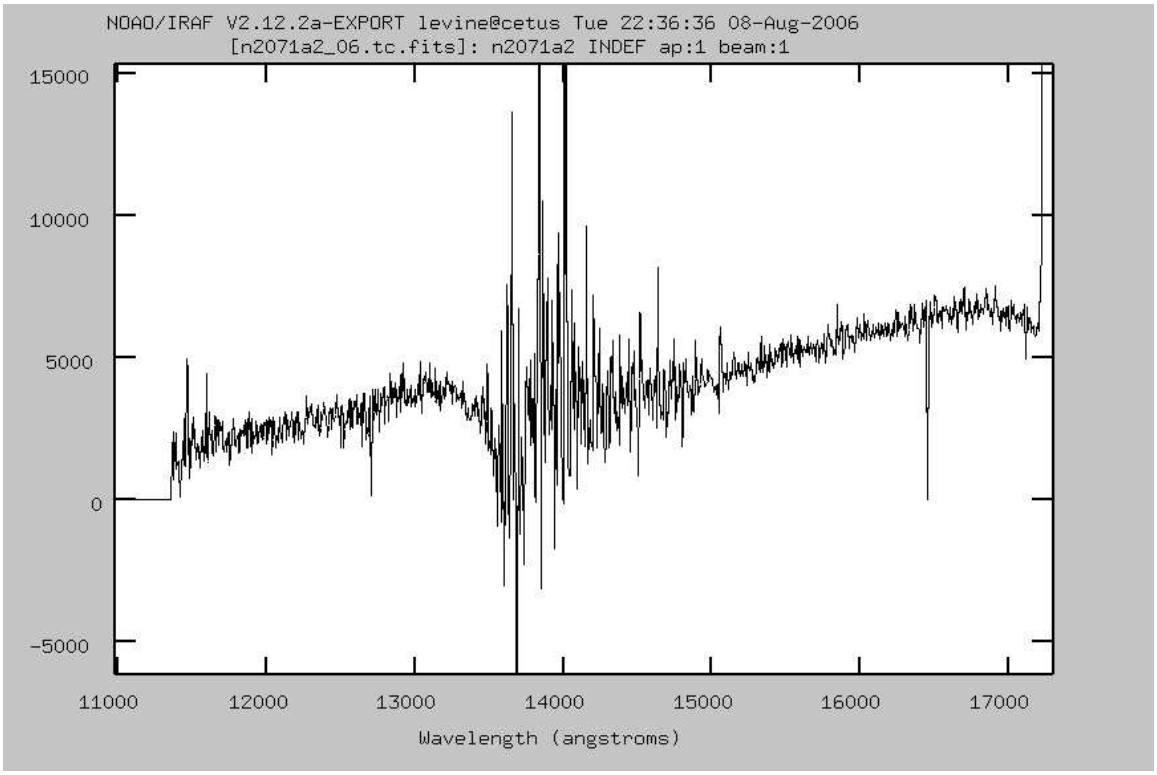

Figure 2–18. The final reduced and calibrated spectrum for n2071a2_06.

2.4.4 Final Spectroscopic Sample

Although sixteen fields were originally targeted for spectroscopic observations, as can be seen from Table B–1, only fields 2 (NGC 2071), 4 (NGC 2068), 6 (dense core), 8 (dense core), 9 (dense core), 10 (NGC 2024), and 13 (no dense gas) were observed. In part this was a choice made after the first observing season to increase the overall number of sources observed (and hence the statistical significance) in the cluster regions. Unfortunately, in the end, the limited off-cluster data taken proved to be

insufficient for analysis, largely due to low signal-to-noise values (SNR$<$20 as compared to SNR$\sim$30-100 for the cluster spectra) reducing the overall number of extractable and/or classifiable sources in these regions. Reasons for these poor SNR values include weather, large extinction in the cores, and poor plate alignment. Consequently, in the remaining chapters, I focus solely on the imaging and spectra of the three Orion B clusters: NGC 2024, NGC 2068, and NGC 2071.

CHAPTER 3
SPECTRAL CLASSIFICATION OF YOUNG M STARS

3.1 Classification Strategy

In order to determine the spectral types of the late-type objects in our Orion B sample, it is necessary to develop a classification scheme using standard stars of similar spectral class. Over the past decade, the astronomical community has assembled a large library of NIR spectra of field dwarfs (e.g. Cushing et al., 2005; McLean et al., 2003; Reid et al., 2001; Leggett et al., 2001, 1996; Jones et al., 1994). The most prominent features in low-moderate resolution NIR spectra of these late-type stars are the narrow atomic lines of Al I, Na I, K I, and Mg I and broad absorption bands due to steam (H_20), iron hydride (FeH), titanium oxide (TiO), and carbon dioxide (CO). The strength of these features is strongly dependent on spectral type (e.g. the molecular absorption in Figure 3–1.

The water absorption bands are ideal for classifying M dwarfs (e.g. Wilking et al., 1999; Reid et al., 2001; Jones et al., 2002; Slesnick et al., 2004) as they produce a very distinct continumm shape which becomes even more pronounced for later spectral types, even at very low spectral resolutions (Figures 3–1 and 3–2). However, steam absorption is significantly stronger in the NIR spectra of young objects than in field dwarfs of the same optical spectral type (e.g. §3.4 and Lucas et al., 2001; McGovern et al., 2004). Consequently, if we use field dwarf standards to type our young cluster members, the derived spectral types will be systematically too late. Rather, we must use optically classified young objects to make an accurate comparison.

3.2 FLAMINGOS Late-Type Spectroscopic Standards

Due to the large amount of dust absorption in the region, there is a dearth of objects with published optical spectral types in Orion B. Consequently, to define a set of young

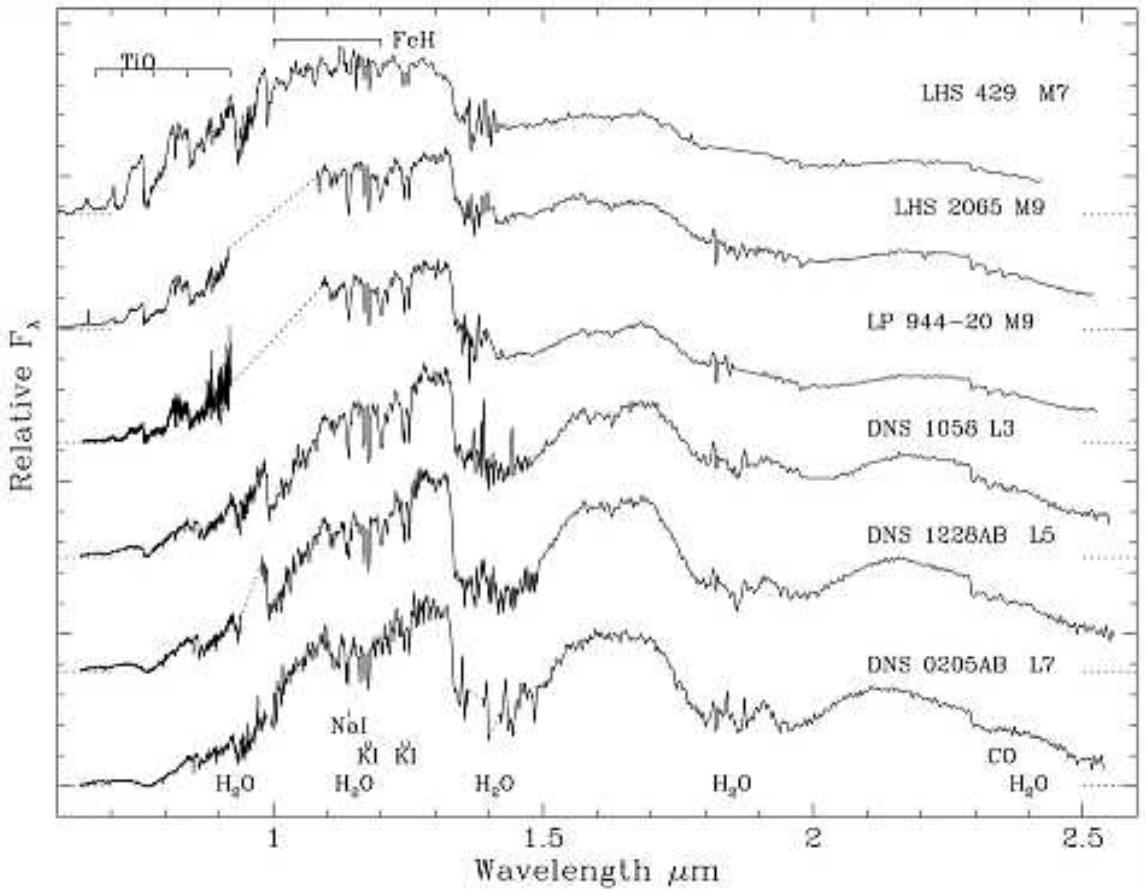

Figure 3–1. A sample of low resolution near-infrared spectra (R $\sim$ 600) for late-type field dwarfs adapted from Leggett et al. (2001). Note the increase in water absorption for later spectral types.

spectral standards, we turned to the nearby Perseus molecular cloud and the young cluster IC 348. IC 348 is a partially embedded young cluster which has been extremely well studied by multiple authors (e.g. Luhman et al. 2003b; Muench et al. 2003 and refererences therin). The relatively low extinction in the region has allowed for a number of known members with established optical classifications. Further, the youth of the cluster (mean age $\sim$ 2 Myr, Herbig 1998) implies that spectral template stars taken from IC 348 membership lists will be similar in age and surface gravity to our Orion B program objects (see §3.4 for further discussion of surface gravity effects). Table 3–1 lists the identifications, positions, and optical spectral types of the IC 348 standards as taken from Luhman et al. (2003b).

Table 3–1. Young Spectral Standards

ID	R.A.	Dec.	Optical Spectral Type
I348-052	03:44:43.53	+32:07:43.0	M1
I348-122	03:44:33.22	+32:15:29.1	M2.25
I348-207	03:44:30.30	+32:07:42.6	M3.5
I348-095	03:44:21.91	+32:12:11.6	M4
I348-266	03:44:18.26	+32:07:32.5	M4.75
I348-230	03:44:35.52	+32:08:04.5	M5.25
I348-298	03:44:38.88	+32:06:36.4	M6
I348-329	03:44:15.58	+32:09:21.9	M7.5
I348-405	03:44:21.15	+32:06:16.6	M8
I348-603	03:44:33.42	+32:10:31.4	M8.5
KPNO-Tau4	04:27:28.01	+26:12:05.3	M9.5

Note. — Spectral types for the IC 348 objects are the spectral types adopted by Luhman et al. (2003b) and found in table 2 of that work. The spectral type for KPNO-Tau4 was determined by Briceño et al. (2002).

FLAMINGOS spectra of these standards were obtained on the nights of 2004 October 04 and 05 on the KPNO 4 m telescope and reduced according to the procedures described in Chapter 2 as part of a parallel survey to classify new members of IC 348 Luhman et al. (2005a, hereafter L05). In addition, we also obtained a spectrum of the young Taurus member KPNO-Tau 4 to provide a very late type template (M9.5, Briceño et al., 2002). The entire FLAMINGOS M star standard sequence can be seen in Figure 3–2.

3.3 A Reddening-Independent Procedure for Classifying Late-Type Spectra

The deeply embedded nature of our spectroscopic targets guarantees that there will be significant amounts of extinction towards most sources (The A_V in these regions is typically 5-10 magnitudes and can sometimes be as high as 20-30 magnitudes, *c.f.* Table 4–2). Consequently, the resultant spectra will be highly reddened, altering both the continuum slope and the depth of any absorption features. This is a problem for traditional M star classification schemes which employ spectral indices based on

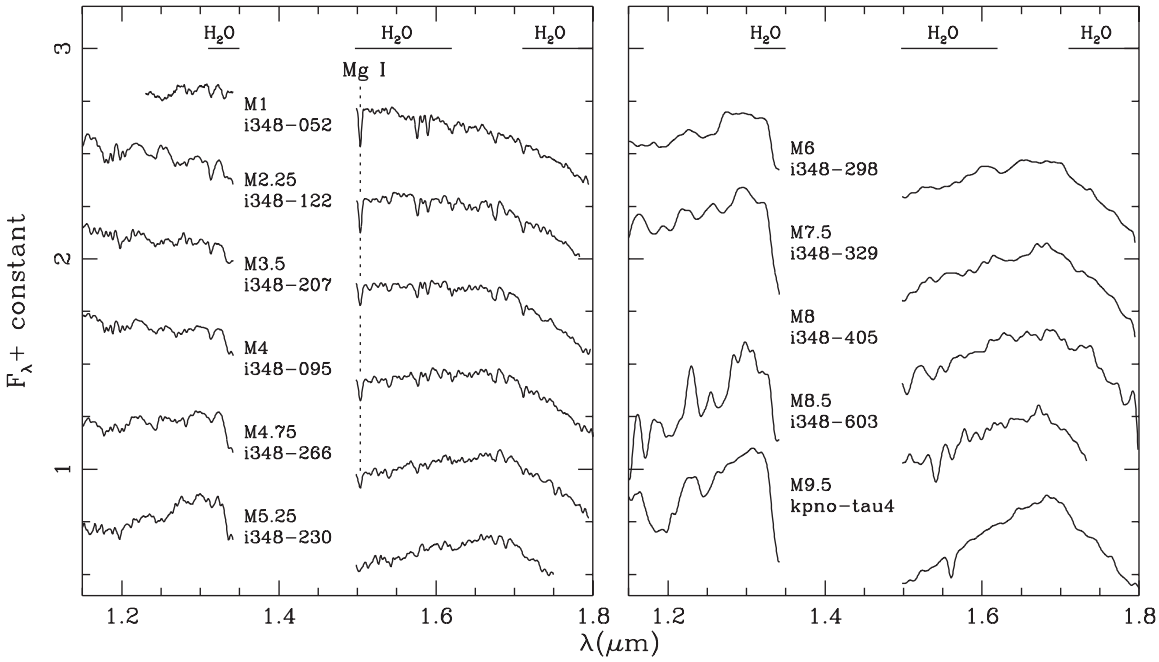

Figure 3–2. FLAMINGOS M star spectral sequence compiled using young ($\tau \sim$1-2 Myr) members of IC 348 and Taurus (Luhman et al., 2003b; Briceño et al., 2002). Prominent features in these low resolution spectra are indicated. Note that objects with spectral types earlier than M6 are displayed at R=500 and objects later than M6 are shown with R=200 for the reasons discussed below (§3.3). The central regions of the spectra are blocked out for display purposes because in most cases the signal to noise in these regions is very low due to the overwhelming telluric absorption.

continuum ratios to determine spectral type. In these cases, the extinction towards an object is usually derived photometrically and the spectrum is then "dereddened" by that amount. The spectral index is subsequently determined from the dereddened spectrum, implying that the final classification is dependent on the calculated extinction (see Figure 3–3).

This dependence of spectral classification on knowing the actual exctinction to an object can be dangerous. As we will show in Chapter 4, photometrically derived A_V values can sometimes be off by as much as 3-4 magnitudes, which will most certainly alter the derived spectral type. For example, Slesnick et al. (2004) found that an uncorrected spectrum with A_V=5 magnitudes was enough to cause one to mis-classify an object by 2 spectral types using a spectral index based on the depth of the *J*-band water feature.

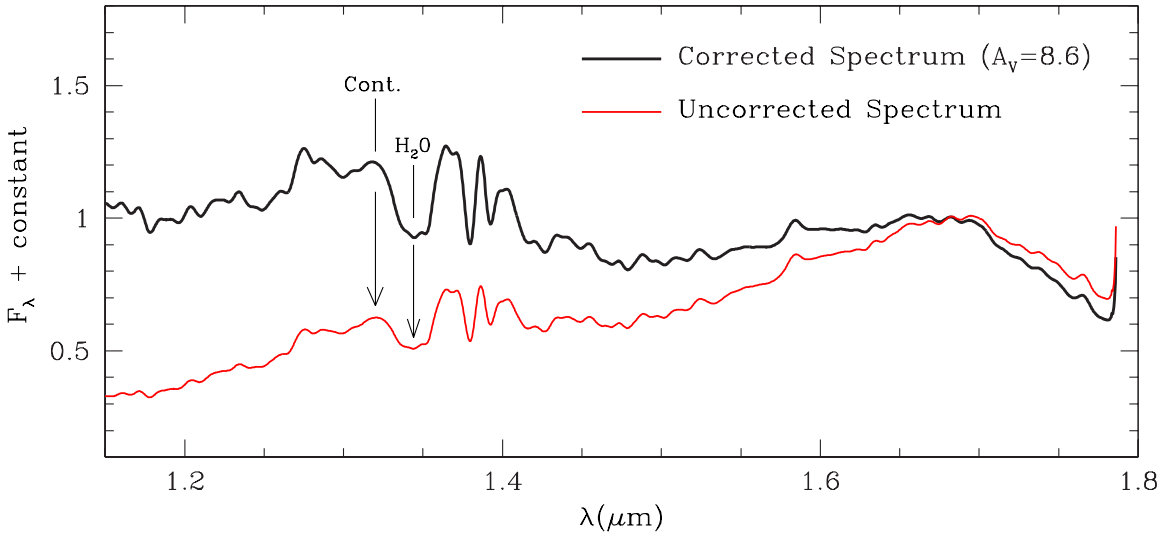

Figure 3–3. Reddened and dereddened FLAMINGOS spectra of an M6.25 object in NGC 2068. The *J*-band H_2O absorption feature and nearby continuum peak are indicated on both spectra. It is clear that the continuum/line ratio for this absorption feature will depend on the applied reddening correction.

Following the work of L05, we have elected to use a visual method to classify our spectra. Generally, this method involves a "pseudo-dereddening" procedure which dereddens the spectra by arbitrary amounts until all objects have uniform continuum slopes. These "dereddened" spectra are then compared to the spectra of the IC 348/Taurus standards shown in Figure 3–2. The major advantage to this method is that it is largely *independent* of the true line-of-sight extinction towards an object and the effect noted by Slesnick et al. (2004) and discussed in the caption to Figure 3–3 does not apply. Whether or not the reddening value determined visually is accurate, because all spectra and standards have the same J-band flux values (see below) we can use the RELATIVE depths of the water feature to classify objects without worrying about the accuracy of photometrically determined reddening values. Put another way, the visual method of classification we use here is a robust way to determine spectral types without requiring a true extinction correction. The details of this visual method are as follows:

1. All reduced spectra (including the standards) are smoothed to a resolution R $\sim$ 500 and normalized such that the peak flux in the *H*-band, located at 1.68 μmhas a

value of 1.0. Note that because we are using a visual classification process based on broad absorption profiles we are not losing any critical information by lowering the resolution – rather, the increase in S/N makes the continuum shape easier to discern, facillitating spectral classification.

2. The slopes of the standard spectra are adjusted (if necessary) using the IRAF *deredden* task until they have uniform *J*-band flux values (flux$\simeq$1.21) at 1.32 μm (*cf.* Figure 3–2). The points at 1.32 and 1.68 μm were chosen because they represent the regions least affected by the stellar absorption features and are therefore closest to the true continuum levels.

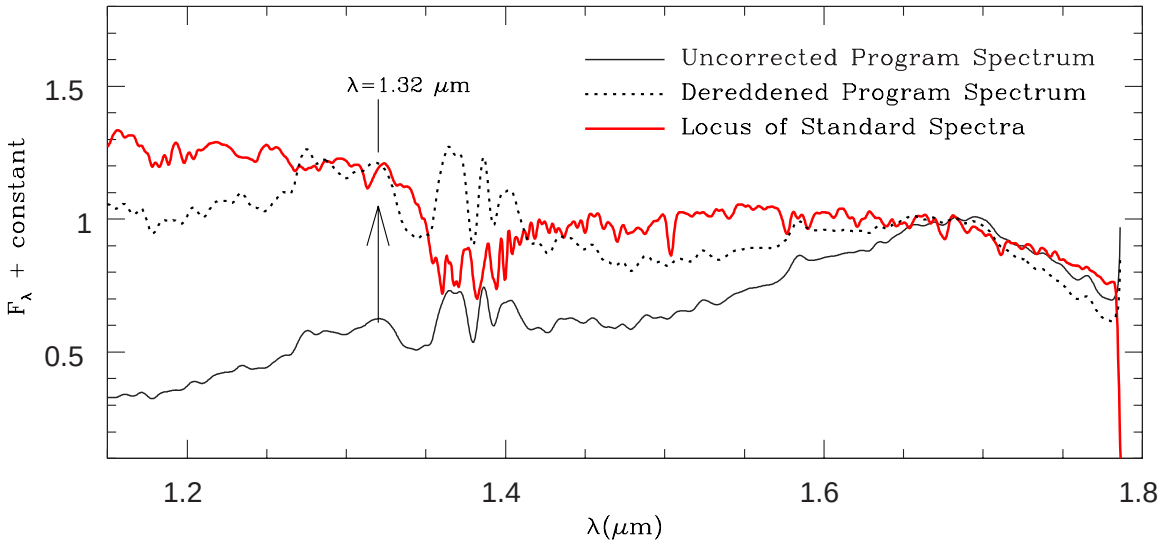

Figure 3–4. Example of the visual dereddening process. Objects are dereddened and overplotted with the standard spectra until their flux values at 1.32 μmmatches the standard template flux, irrespective of spectral type.

3. The IRAF ”deredden” task is then used to *visually* redden or deredden the program spectra until the flux value at 1.32 μm matches the flux of the standard templates (Figure 3–4). Note that although a nominal value of extinction is generated via this process, it is not necessarily reflective of the true extinction toward program objects as this ”dereddening” is simply an aritificial mechanism to ensure that all objects have a relatively uniform appearance.

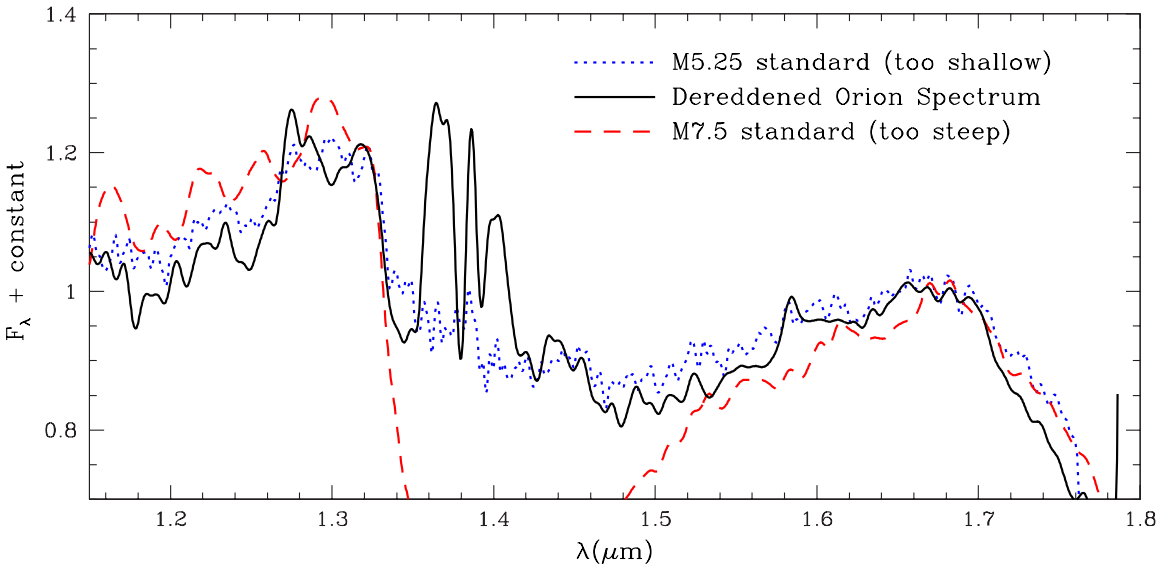

Figure 3–5. Example of the visual classification process. In this case, the *J*-band fall-off of the blue spectrum (M5.25) is shallower than the Orion object while the same water absorption feature in the red spectrum (M7.5) is too deep. The same effect can be seen in the *H*-band in the region from 1.5-1.7 μm. Consequently, the true spectral type of this object must be somewhere in between. (In the end, after plotting this object with the M6 standard and against similarly classified Orion spectra, we estimate its spectral type to be M6.25$\pm$0.75 subclasses.)

4. A spectral type for each object is determined by visually comparing the program spectra to the individual standards until a best fit match is determined. Particular attention is paid to the slope and depth of the *J*-band fall-off at 1.35 μm, the strong absorption features in the H-band on either side of 1.68 μm, and if present, the strength of the Mg I line (Figure 3–5). If the object appears to be late-type ($\geq$M6), the spectrum is smoothed to R$\sim$200 to further increase the S/N, making the exact spectral type more obvious. Finally, once all objects have been assigned a first-pass spectral type, classifications are fine-tuned by placing the spectra in order of their M subclasses and adjusting the sequence to ensure that the strength of the water absorption monotonically increases with spectral type.

We estimate this method of spectral classification to be quite robust, with typical errors in spectral type of $\pm$0.5-1 subclasses.

Table 3–2. Surface Gravity Standards

ID	R.A.	Dec.	SpT[1]	Gravity	Obs.Date	Telescope/Obs.Type[2]	τ_{exp}	N_{exp}
HD 39045	05:51:25.0	+32:11:09	M3 III	very low	2004 Dec 18	2.1m/slit	3s	7
I348-207	03:44:30.3	+32:07:43	M3.5 IV	low	2003 Jan 16	4m/mos	600s	12
GL 388	22:28:00.3	+57:40:06	M3 V	high	2004 Oct 08	4m/slit	10s	7
HD 196610	20:37:55.6	+18:20:24	M6 III	very low	2004 Dec 31	2.1m/slit	2s	9
I348-298	03:44:38.9	+32:06:36	M6 IV	low	2003 Jan 16	4m/mos	600s	12
GJ 1111	08:29:48.9	+26:48:32	M6 V	high	2004 Dec 12	2.1m/slit	20s	10
KPNO-Tau4	04:27:28.0	+26:12:05	M9.5 IV	low	2004 Oct 07	2.1m/slit	300s	12
LHS 2065	08:53:36.4	-03:27:32	M9.5 V	high	2004 Dec 13	2.1m/slit	60s	15

[1]Spectral Type for each object, including luminosity class.

[2]Indicates whether data were taken at the KPNO 2.1m or 4m telescope and whether the data were taken in mulit-object (mos) or single slit (slit) mode.

3.4 Surface Gravity

In addition to their obvious usefulness in general spectral classification, the low resolution NIR spectra of M stars can also be employed to yield rough estimates of an object's surface gravity (e.g. Gorlova et al., 2003; McGovern et al., 2004). In particular, certain narrow absorption features as well as the broad water absorption bands discussed above are especially sensitive to surface gravity effects. This sensitivity provides a natural method for distinguishing young sources (which have intermediate surface gravities) from relatively high surface gravity field dwarfs or low gravity background giants. In order to evaluate the surface gravity of the Orion sources and ultimately assist with membership assessment (see Chapters 4 and 5), I have assembled a small selection of surface gravity standards observed with FLAMINGOS. The sources and observing log are listed in Table 3–2 and the reduced spectra are shown in Figure 3–6.

Figure 3–6 illustrates the progression of the strongest gravity sensitive features visible in our data–the broad water absorption features in both the J and H bands and a narrow potassium doublet at 1.243/1.252 μm–as a function of both surface gravity and spectral type. For the M3 objects both the J and H-band H_2O induced fall-offs are steepest for the young star. This effect becomes more dramatic for the M6 and M9 objects where the field dwarf continuum profiles have broad H-band plateaus versus a distinct triangular shape for the young objects. (The same effect was also noted by Lucas et al. (2001) and L05). Looking at the M6 and M9.5 objects, the field stars have

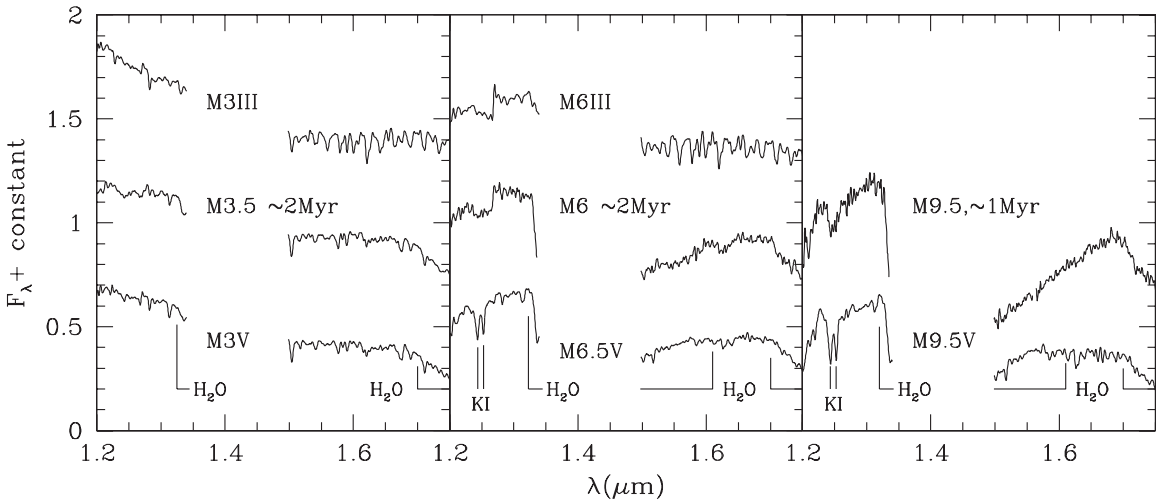

Figure 3–6. FLAMINGOS spectra of the young objects I348-207 (M3.5), I348-298 (M6), and KPNO-Tau4 (M9.5), shown with spectra of the field dwarfs GL 388 (M3V), GJ 1111 (M6.5V), LHS 2065 (M9.5V) and the M Giants HD 39045 (M3III) and HD 196610 (M6III). The most prominent gravity sensitive features at R∼500 are labeled. The spectra of both giants appear to have a much higher H-band line frequency than the young objects or field dwarfs. In addition, water absorption causes the younger objects to have a much more triangular H-band shape which can be used to distinguish field stars from young cluster members.

a strong potassium doublet which is weak or absent in the lower gravity atmospheres of the young stars and giant. Finally, it is also apparent that the two giants have a flatter continuum profile and a much higher frequency of H-band absorption lines. Consultation of the literature (e.g. the low resolution infrared spectral libraries of Lancon & Rocca-Volmerange (1992)) confirms that this is a hallmark of giant stars and is likely caused by overtones of CO and OH as well as blended molecular lines only visible at very low surface gravities.

These trends in spectral shape and line frequency will be used in upcoming chapters to assess the surface gravity of each Orion spectrum. As in Table 3–2, sources will be assigned a designation of low (indicating a low surface gravity young object), high (indicating a field dwarf), and very low or giant (indicating a very low gravity giant). The results of this gravity assessment will then be used to assist in establishing the membership status for each object.

CHAPTER 4
M STARS AND BROWN DWARFS IN NGC 2024

4.1 Introduction

In this Chapter I present results from FLAMINGOS photometry and spectroscopy of the young cluster NGC 2024. Specifically, I characterize the individual spectra, subsequently combining them with the photometry to construct Hertzprung-Russell diagrams for the region. With the aid of PMS evolutionary models, I derive a new age and IMF for the low mass cluster population and examine the properties of the substellar population. In forthcoming chapters these results will be compared with those in other regions of low mass star formation both within and outside the boundaries of Orion B.

NGC 2024 is a young ($<$1 Myr) HII region that is deeply embedded in the cloud material of Orion B. The distance to the region is estimated to be 415pc (Anthony-Twarog, 1982). Optical images show a spectacular, flame-shaped nebula with a dark dust lane at the center obscuring the heart of the cluster and most of the stars in the region (Figure 4–1).

The center of the optical nebula is a bright radio source which exhibits both radio continuum emission and recombination lines, indicating the presence of a massive star (spectral type $\sim$O9) responsible for the ionizing radiation (§1.3, Kruegel et al., 1982; Barnes et al., 1989). Due to the large amount of dust in the region, this ionizing source was only recently identified to be the late O to early B star IRS2b (Bik et al., 2003). The full extent of the cluster assiciated with the HII region was revealed by the *K*-band imaging survey of Lada et al. (1991b) who detected $\sim$300 sources down to $K<14.0$. Multi-wavelength infrared photometric studies of the cluster show that majority of detected objects exhibit near-infrared excess emission indicative of hot circumstellar material (Comeron et al., 1996; Haisch et al., 2000). The proximity, extreme youth, and

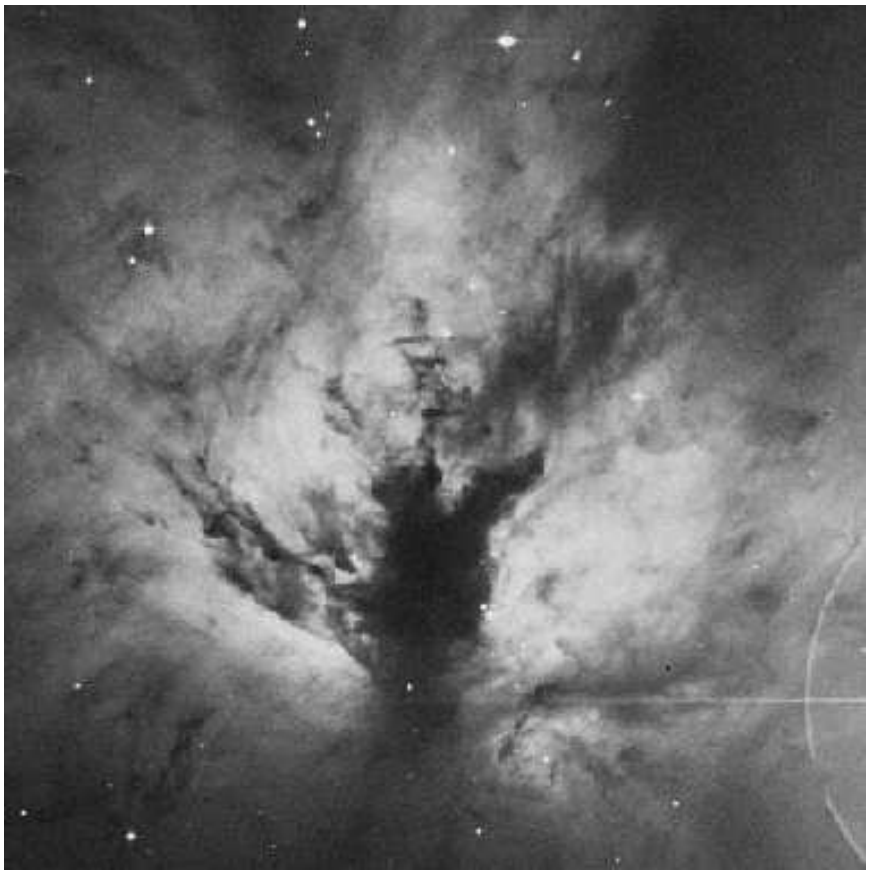

Figure 4–1. Optical image of NGC 2024 (The Flame Nebula) taken from the digital sky survey. North is up, East is left, and the field of view is $20' \times 20'$.

indicators of active star formation in NGC 2024 combine to make this an ideal region to study the young, low mass population.

4.2 New Photometry for NGC 2024

In addition to the survey photometry described in Chapter 2, *J*, *H*, and *K*-band images of NGC 2024 were obtained on 2001 November 19 using FLAMINGOS on the KPNO 4m telescope. The data were taken using a 16-point dither pattern with individual exposure times of 60s for *J* and *H* and 30s for *K*, yielding total exposure times of 16 minutes in *J* and *H* and 8 minutes in *K*. Typical seeing at all wavelengths was $1\farcs1$-$1\farcs2$ FWHM and the 10σ detection limits are *J*=19.4, *H*=18.8, and *K*=17.8.

These images were reduced and assessed using the pipelines and routines described in §2.3.2 and 2.3.3.1. The JHK photometry for ∼400 sources having color errors <0.1

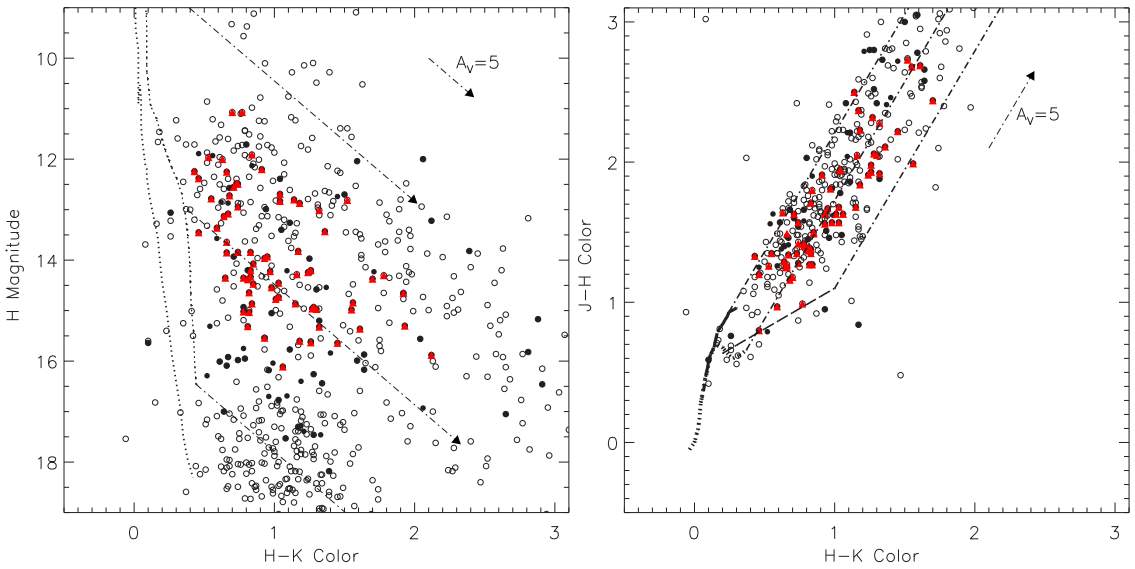

Figure 4–2. Color-magnitude (left) and color-color (right) diagrams for all classified objects in NGC 2024. In the CMD, the leftmost dotted line is the main sequence from Bessell & Brett (1988) and to the right is the 1 Myr isochrone of D'Antona & Mazzitelli (1997). The dot-dashed lines are reddening vectors using the extinction law of Cohen et al. (1981) placed at 3, 0.08, and 0.02 $M_{\odot}$. In the color-color diagram, the dotted lines are the giant colors of Bessell & Brett (1988) combined with Bessell & Brett (1988) dwarf colors for spectral types down to K7 and Leggett (1992), Leggett et al. (1996), and Dahn et al. (2002) dwarf colors for spectral types from M0 to M6. The dot-dashed lines are the reddening vectors of Cohen et al. (1981) and the dashed line is the classical T Tauri locus of Meyer et al. (1997). Open circles are general photometric catalog sources, filled circles are spectroscopic targets, and the red triangles represent the final classified sample.

magnitudes is shown in Figure 4–2. In regions with little to no nebular emission, the photometric accuracy (as indicated by a comparison to 2MASS) is estimated to be 0.03 magnitudes. For regions with large amounts of nebula, as in the center of NGC 2024, the scatter with respect to 2MASS was much larger ($\sim$0.15 magnitudes) than that expected from purely photometric noise. Reasons for this difference are discussed in §2.3.5. The scatter with respect to 2MASS was also larger for objects on the edge of detector where the data rapidly degrade due to a delamination of the engineering array. For objects in this region (generally non-nebular), the 2.1 m photometry from the imaging survey was used. The survey field corresponding to NGC 2024 is orib-01. Given that the sources requiring

Table 4–1. Slit Masks Observed in NGC 2024

Mask ID	Telescope	Target Selection Method	N_{slits}	$N_{extracted}$ [a]	$N_{classified}$ [b]	$N_{duplicates}$ [c]
n2024bd1	4m	Brown Dwarfs	23	22 (+1)	8	0
oc24mf11	4m	IRX Sources	27	22	16	0
oc24mf21	4m	IRX Sources	22	19 (+3)	17	0
n2024f31	2.1m	*K* magnitude	23	11 (+1)[d]	5	1
n2024b2	4m	*H* magnitude	25	19	9	0
n2024b3	4m	*H* magnitude	28	22 (+2)	19	4
Totals:			148	115 (+7)	74	5

[a]In cases where multiple sources fell on a single slit it was possible to extract stars in addition to those originally targeted. These objects are indicated in the $N_{extraction}$ column by (+n).

[b]$N_{classified}$ refers to the number of M stars classified in each mask in the 4 m field of view. In other words, stars with spectral types earlier than M are not counted.

[c]This column indicates the number of independently classified duplicate sources on the given mask

[d]Of the 23 slits on the 2.1 m plate, only 11 fell within the 4 m field of view.

this photometry are in predominantly non-nebular regions, the mean survey scatter value of σ=0.05 magnitudes applies. The field-specific statistics (which include the extremely nebular portions of the cluster) can be found in Appendix A.

4.3 Spectroscopy of NGC 2024

4.3.1 Sample and Observations

The spectroscopic sample for NGC 2024 was selected according to the guidelines described in Chapter 2. In the end, 148 sources were targeted for observation on 6 different slit masks. The targeting breakdown can be found in Table 4–1 and the photometry is shown by filled circles in Figure 4–2. The spatial distribution of these targets can be seen in Figure 4–3.

FLAMINGOS observations of the 4m slit masks were taken on the nights of 2003 January 19, 2003 December 06, 2003 December 10 and 2004 December 01. Spectra from the 2.1 m slit mask were obtained with FLAMINGOS on the night of 2003 November 29. The full details of the observing procedures at both telescopes can be found in §2.4.2. The specific integration times by mask can be found in Appendix B. All spectroscopic

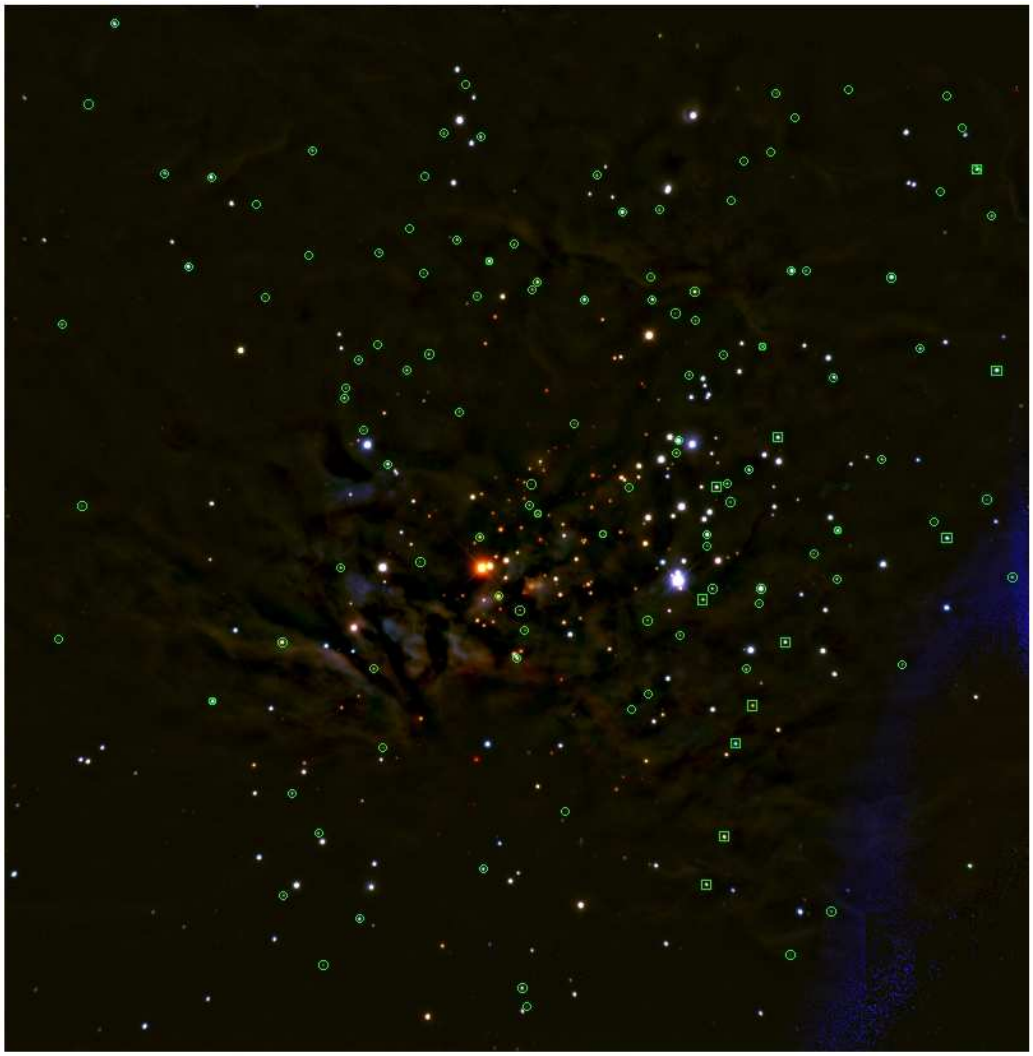

Figure 4–3. Three-color image of NGC 2024 taken with FLAMINGOS on the KPNO 4m telescope. North is up, East is to the left, and the field is approximately 10’ on a side. Circled objects are all 4m spectroscopic targets and rectangles enclose the 2.1m targets.

data were reduced using the procedures detailed in §2.4.3 and classified according to the methods developed in Chapter 3. Totals by mask of the number of sources targeted, extracted, and classified are listed in Table 4–1.

4.3.2 Results

4.3.2.1 Spectral Classification

The final classifications yielded 65 unique objects from the 4m sample with identifiable M type spectra (ranging from M1 to >M8) and 2 sources with spectral

types earlier than M0. In addition, 4 duplicate sources were also extracted which when independently classified yielded spectral types in agreement with the original source to within 0.25 subclasses. Of the ∼40 4m extracted objects which were not classfied, 14 were filler targets with K magnitudes > 15.0 which are typically too faint to classify with our current exposure times. The remaining unclassified sources while bright at K, were typically highly reddened objects with poor signal to noise in the J and H bands after dereddening. The 2.1m sample yielded 4 new M type objects, 6 sources with spectral types earlier than M0, and one duplicate classification (which agreed with the 4m source to within 0.5 subclasses). All classified spectra are shown in Figure 4–4 along with selected objects from the FLAMINGOS M star standard sequence (§3.2). Objects with spectral types <M6 are plotted with R∼500 and objects with spectral types ≥ M6 have been further smoothed to R∼200 to aid in the classification process.

4.3.2.2 Surface Gravity Assessment

Applying the surface gravity diagnostics discussed in Chapter 3, §3.4 to the NGC 2024 spectra, I find the majority of sources display the distinct triangular continuum profiles indicative of youth and are thus assigned *low* gravity designations. I also find that strong J-band potassium lines are absent from all spectra. Two sources (60 and 64) display enhanced absorption in the H-band and may be background M giants.

Results of the assessment for each individual object are noted in Table 4–2. An ellipsis in the gravity column indicates that the gravity assessment was not completed, typically because the spectral type was too early to exhibit a distinct triangular profile. However, for all uncertain cases the H-band was sufficient to rule out background giants and the relatively large values of A_V imply that these sources are not foreground objects (refer to §4.5.1).

4.3.2.3 Infrared Excess and Spectroscopic Veiling

The presence of excess flux in the near infrared is commonly taken to be an indicator of thermal emission by warm dust in a circumstellar disk. This type of emission can result

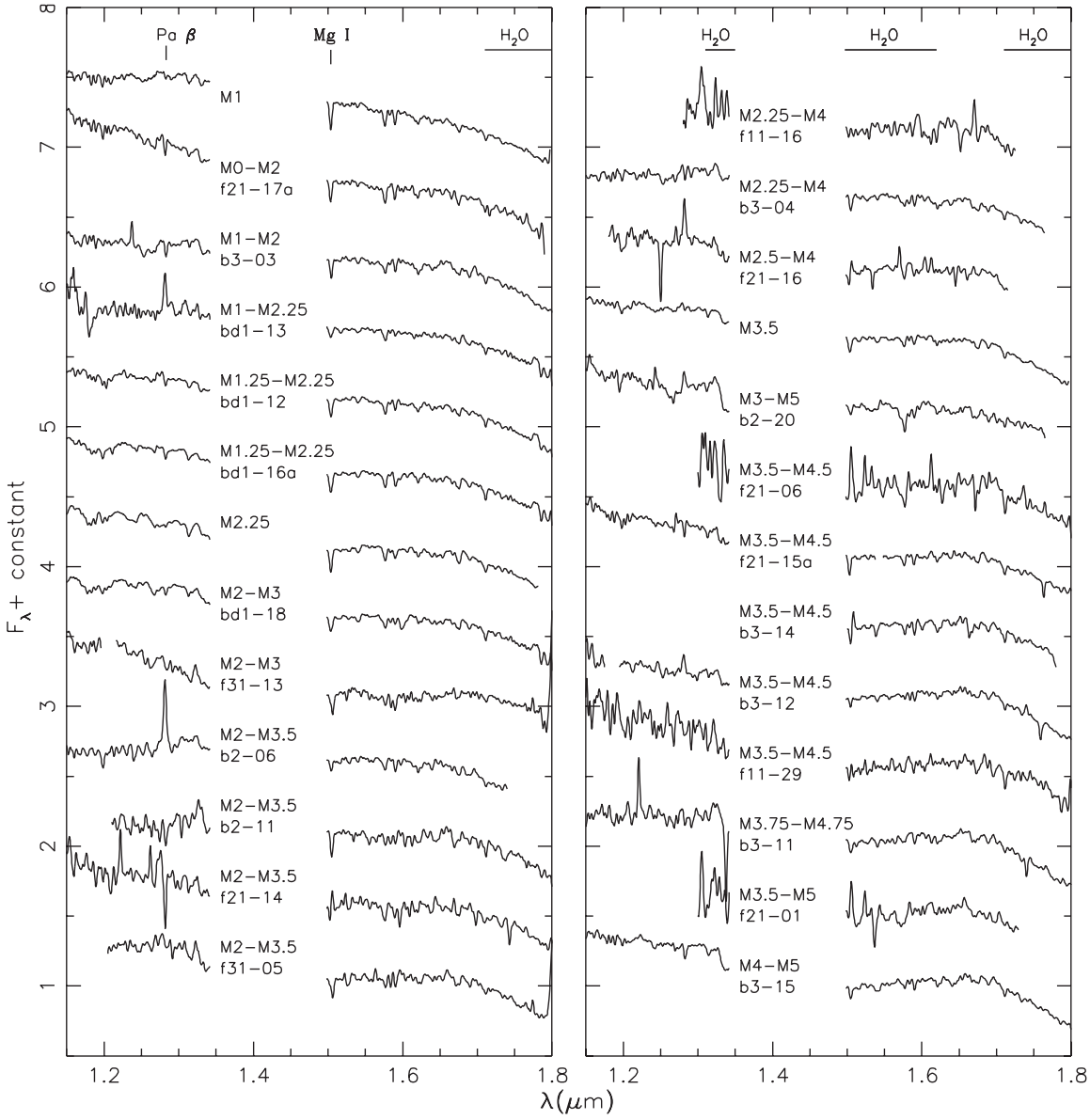

Figure 4–4. NIR spectra of all classified M stars in NGC 2024 (labeled with both spectral type and ID) shown with the IC 348 optically classified young standards (labeled with spectral type only). Prominent spectral features are identified at the top. Objects having spectral types $<$M6 have been smoothed to R$\sim$500 and objects $\geq$M6 have been smoothed to R$\sim$200 to aid in the classification process. The central regions of the spectra are blocked out for display purposes because in most cases the signal to noise in these regions is very low due to the overwhelming telluric absorption. In some cases, the *J*-band has also been blocked - these spectra were particularly noisy and classified using their *H*-band continuum shape only.

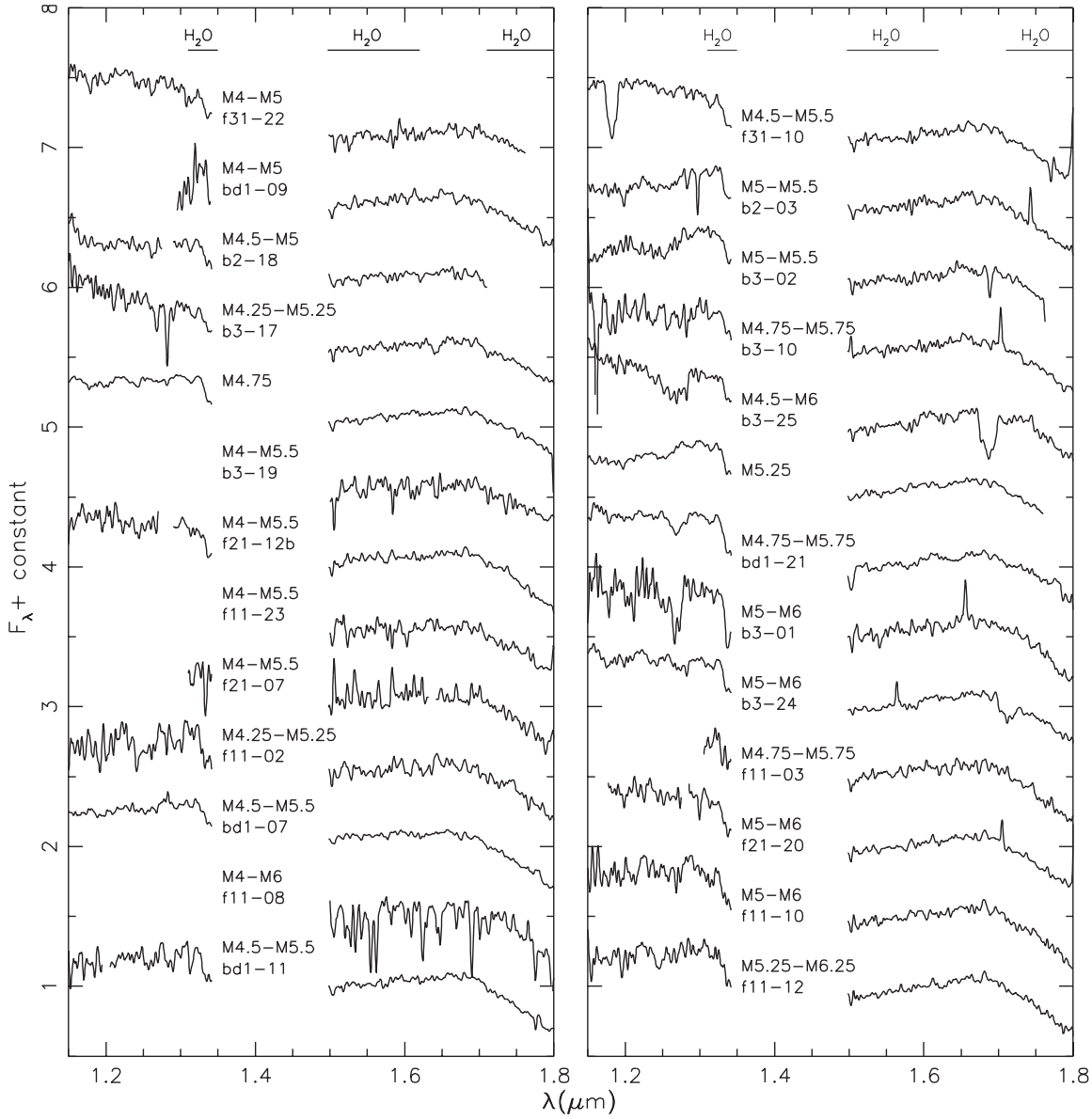

Figure 4–4. continued

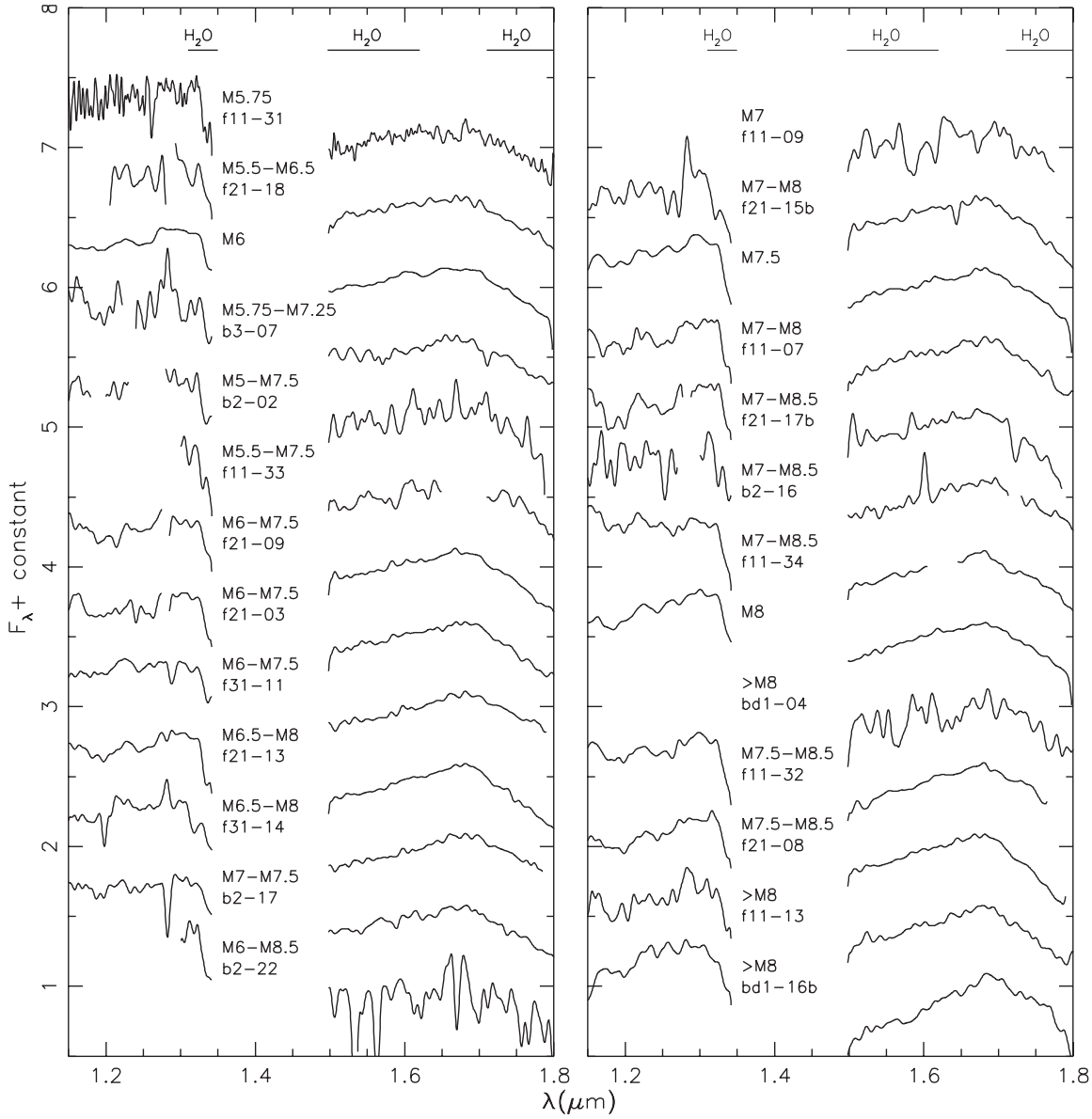

Figure 4–4. continueds

in the weakening or *veiling* of both narrow and broad-band spectral lines. If the amount of veiling is significant, it can affect spectral classification causing an object to appear earlier than its true spectral type. In this section I attempt to quantify the effect of veiling on our classification process by visually inspecting our sample and examining its infrared excess (IRX) properties.

Visual inspection of the spectra yielded one object (source 5, M1.75) with obviously weak Mg I absorption likely caused by veiling. In addition, excluding the possible giants (see above), 27 out of 67 objects or 40%±9% of our classified M star sample exhibit an IRX as determined via a comparison of each object's expected intrinsic $H-K$ color (inferred from spectral type) with its dereddened observed $H-K$ color. (The reader is referred to §4.4.1 for an explanation of intrinsic color choice and dereddening methods.) What fraction of IRX sources can be expected to have significant veiling? To answer this question I have calculated r_k, the K-band veiling index for each source.[1] The typical errors on r_k are ±0.08 magnitudes, implying that we should not place too much weight on individual values of r_k which are close to zero. However, since the primary purpose of this r_k analysis is to identify the sources with veiling strong enough to bias our spectral classification, this error is acceptable. As can be seen from Table 4–2, only source 38 (r_k=0.62) exhibits an amount of veiling near r_k=0.6, the median value for Classical T Tauri stars (Meyer et al., 1997). Consequently, I note the potential bias towards an earlier spectral type for this object.

4.4 The Hertzsprung-Russell Diagram

In this section I combine spectral types and infrared photometry to derive visual extinctions, effective temperatures and bolometric luminosities for all classified objects. I

[1] The veiling index r_λ is defined as $F_{\lambda_{ex}}/F_{\lambda_*}$. Converting to photometric K-band excess yields $r_k = [(1+r_H)10^{((H-K)-(H-K)_0-0.065A_v)/2.5} - 1]$. Note that because I am dereddening to intrinsic dwarf colors our values for r_k are lower limits since r_h is assumed to be zero (Meyer et al., 1997).

then place these data on the Hertzprung-Russell (H-R) diagram and use theoretical PMS evolutionary models to infer masses and ages for the sample.

4.4.1 Extinction

Because NGC 2024 is so deeply embedded in its natal cloud, there is a large and variable amount of extinction in the region which acts to differentially redden source magnitudes. In order to properly estimate physical parameters and infer masses and ages, this reddening must be accounted for. The amount of extinction towards a given source is typically derived by dereddening its broadband colors, however, care must be taken when choosing passbands. The redder infrared bands are less sensitive to variations in extinction but may also be contaminated by infrared excess emission arising from a circumstellar disk. Optical bands suffer from contamination due to UV excess emission from the stellar photosphere. It is generally agreed upon that bands between R and J are most sensitive to extinction while minimizing the effects of excess emission (*cf.* Meyer et al. 1997; Luhman et al. 2003b). As I do not have reliable optical photometry for NGC 2024, I elected to use the bluest infrared bands to derive extinction estimates for each source.

Extinction estimates were determined by comparing our observed $J-H$ colors with the empirically determined intrinsic M dwarf colors of Leggett (1992); Leggett et al. (1996) and Dahn et al. (2002) and then converting the color excess to an A_V measurement using the reddening law of Cohen et al. (1981). The choice of both the intrinsic colors and the reddening law was based primarily on photometric system. FLAMINGOS filters closely approximate the CIT system (Elston et al. (2003) and the FLAMINGOS web pages) thus I opted for a reddening law and intrinsic color set derived in the same system. I opted against using theoretical PMS colors since at young ages these are highly dependent on model input physics. For the one source lacking J-band photometry, an extinction estimate was derived using $H-K$ colors. It should be noted that for comparison I also estimated visual extinctions for all sources using $H-K$ intrinsic colors

and by dereddening objects to a model isochrone in both $J/J-H$ and $H/H-K$ color magnitude diagrams. These methods yielded A_V values which deviated from the $J-H$ intrinsic color estimates by as much as 1-2 magnitudes for $J/J-H$ and 3-4 magnitudes for $H/H-K$. Effects of this deviation will be discussed in §§4.4.2 and 4.5.2.

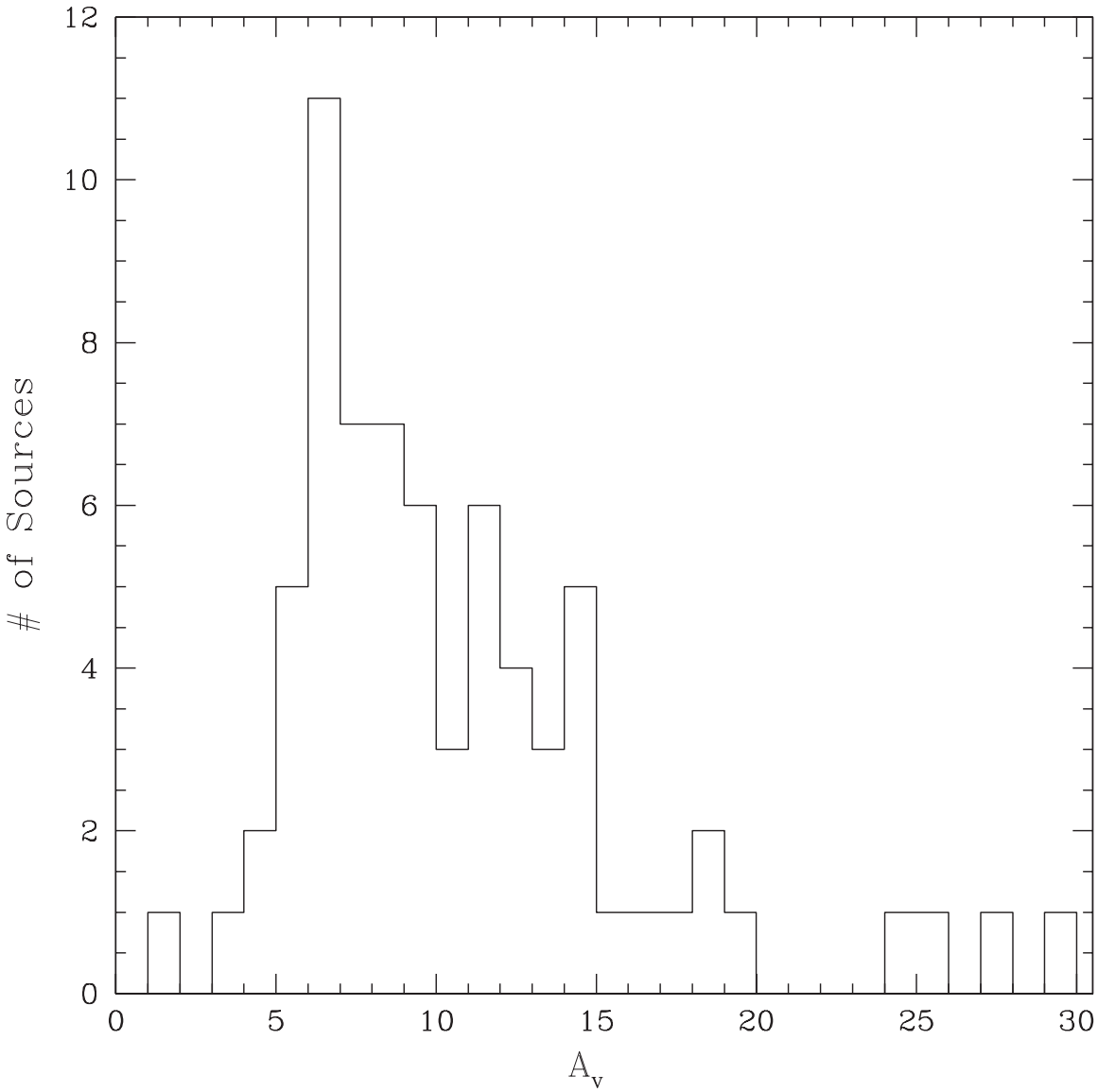

Figure 4–5. Distribution of A_V for the NGC 2024 spectroscopic sample. A_V values were derived by comparing observed $J-H$ colors with the intrinsic $J-H$ colors of Leggett (1992); Leggett et al. (1996); Dahn et al. (2002).

Figure 4–5 shows the distribution of visual extinctions derived from $J-H$ intrinsic colors. Values range from ∼1-30 visual magnitudes with a mean A_V of 10.7 magnitudes.

This is in good agreement with the survey of Haisch et al. (2000), who find a range of A_V from roughly 0-30 visual magnitudes and a mean A_V of 10.4.

4.4.2 Effective Temperatures and Bolometric Luminosities

Spectral types were converted to effective temperatures using a linear fit to the adopted temperature scale of Luhman et al. 2003. This temperature scale, derived from the young quadrouple system GG Tau, falls between dwarf and giant temperature scales and is thus appropriate for the intermediate surface gravity objects studied here. Absolute magnitudes were calculated by dereddening K magnitudes (see below) using the A_V derived in §4.4.1 and applying a distance modulus of 8.09 (Anthony-Twarog, 1982). Bolometric magnitudes and luminosities were derived using the bolometric corrections of Leggett (1992); Leggett et al. (1996) and Dahn et al. (2002) as they were observationally determined using CIT photometry.

While *J*-band is typically the preferred wavelength for deriving bolometric luminosities as contaminating excess effects are minimized (Luhman, 1999, see also §4.4.1), I have elected to use the *K*-band since luminosities derived from *K* magnitudes are far less sensitive to errors in dereddening. As discussed above, photometrically derived extinction values can have errors as large as 3-4 magnitudes. A change in A_V of 3 magnitudes corresponds to nearly a magnitude of uncertainty in dereddened *J*-band magnitudes but yields a much smaller ΔK ($<$0.3 mag). Although *K* magnitudes are more sensitive to excess emission from a warm circumstellar disk, this effect is small in log-Luminosity space (average $\Delta logL$ $\sim$0.06 dex). Even when combined with the A_V uncertainty, the net uncertainty in *K*-derived bolometric luminosities ($\pm$ 0.17 dex) remains smaller than the corresponding uncertainty using *J*-band to derive bolometric luminosities ($\pm$ 0.32 dex).

4.4.3 H-R Diagram

Figure 4–6 shows H-R diagrams for the classified sources in NGC 2024 along with the PMS evolutionary models of D'Antona & Mazzitelli (1997) and Baraffe et al. (1998). The triangular points represent 2.1m classifications and sources with diamonds were

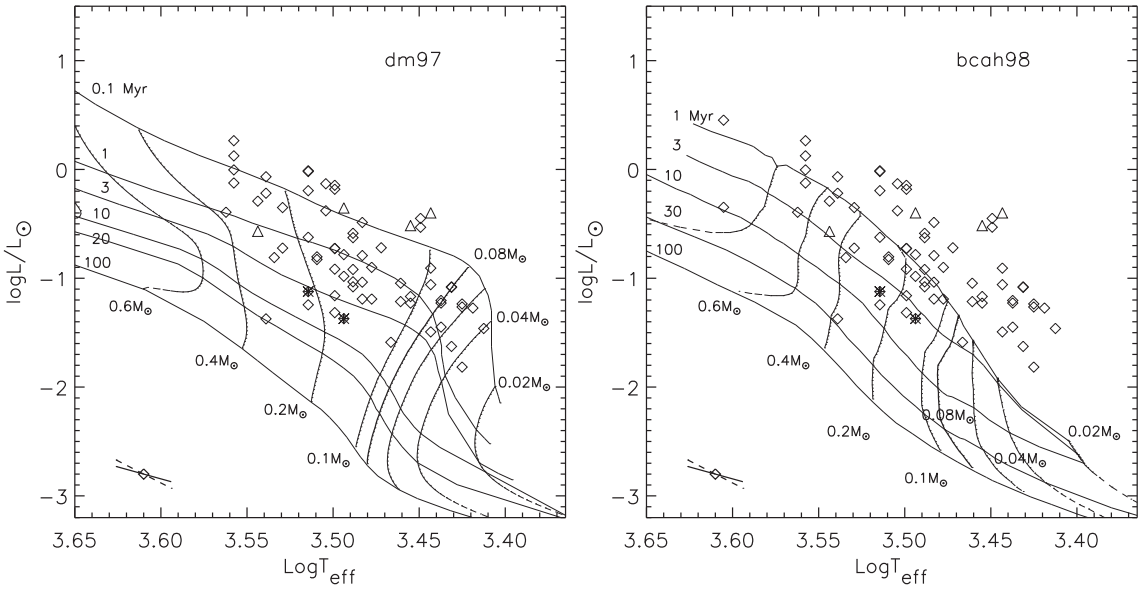

Figure 4–6. H-R Diagrams for NGC 2024 shown with the pre-main sequence models of D'Antona & Mazzitelli (1997) (left) and Baraffe et al. (1998) (right). The diamonds represent points with 4m spectra and the triangles are sources classified with 2.1m spectra. Asterixes are potential background giants. Representative error bars for an M5 object are shown. The solid line accounts for errors in derived spectral type, distance modulus, and photometry and the dashed line incorporates an additional error of ± 3 magnitudes of visual extinction (see §4.4.1).

classified using 4m spectra. The two asterixes represent the possible background giants (see §4.3.2.2). Individual object data are tabulated in Table 4–2. Two typical error bars for an M5 dwarf are shown in the lower left corner. The solid line was derived by classically propagating the measured errors in the photometry, spectral type (0.75 subclasses), and distance modulus. In this case, the error in luminosity is dominated by error in the distance to NGC 2024. The dashed line incorporates an additional error of $\pm$ 3 magnitudes (corresponding to $\pm$0.2 dex) in the reddening estimate (refer to §4.4.1) which dominates the error bar and leads to a larger uncertainty in the calculated luminosity.

Table 4–2. Data for Classified Sources in NGC 2024

Source	J	H	K	M Subclass[a]	Gravity	A_V	r_K	$\log T_{eff}$	$\log(L/L_\odot)$	Mass ($M_\odot$)
01	12.06	11.07	10.30	<M	...	...	...	...	...	...
02	12.25	11.07	10.37	1.75	...	4.73	0.19	3.558	0.125	0.72
03	13.71	11.91	11.07	4.00	low	10.82	-0.11	3.514	-0.012	0.29
04	14.11	12.20	11.29	1.75	...	11.36	-0.03	3.558	-0.004	0.72
05	15.54	12.81	11.29	1.75	...	18.82	0.09	3.558	0.264	0.72
06	13.64	12.00	11.37	1.75	...	8.91	-0.13	3.558	-0.124	0.70
07	13.22	11.96	11.43	2.50	low	5.59	-0.05	3.544	-0.292	0.55
08	14.64	12.69	11.65	3.50	low	12.18	-0.01	3.524	-0.195	0.29
09	15.30	12.80	11.66	4.00	low	17.18	-0.20	3.514	-0.019	0.29
10	15.10	12.87	11.69	4.75	low	14.70	-0.06	3.499	-0.146	0.17
11	15.29	13.01	11.69	2.75	low	14.93	0.12	3.539	-0.067	0.54
12	14.06	12.49	11.75	4.50	low	8.64	-0.09	3.504	-0.380	0.20
13	14.77	12.83	11.79	2.75	low	11.84	0.04	3.539	-0.218	0.54
14	13.57	12.24	11.81	1.50	...	6.09	-0.14	3.562	-0.393	0.68
15	14.18	12.55	11.84	2.75	low	9.32	-0.12	3.539	-0.350	0.44
16	13.58	12.38	11.92	5.25	low	5.48	-0.17	3.488	-0.587	0.13
17	14.36[b]	12.94	12.20	5.25	low	7.48	-0.05	3.488	-0.627	0.13
18	14.13	12.78	12.23	2.75	low	6.73	-0.13	3.539	-0.623	0.28
19	14.42	13.08	12.41	4.75	low	6.61	-0.04	3.499	-0.725	0.17
20	14.42	13.13	12.49	5.50	low	6.36	-0.08	3.483	-0.791	0.12
21	17.57	14.30	12.52	4.50	low	24.09	-0.06	3.504	-0.131	0.20
22	16.19	13.82	12.65	<M	...	...	...	...	...	...
23	16.81	14.37	12.67	5.50	low	16.82	0.30	3.483	-0.487	0.12
24	18.04	14.65	12.73	4.75	low	25.25	-0.01	3.499	-0.182	0.17
25	14.33	13.36	12.77	7.75	low	3.49	-0.05	3.431	-1.084	0.03
26	16.18	14.20	12.94	4.75	low	12.43	0.16	3.499	-0.727	0.17
27	14.91	13.64	12.98	5.00	low	6.05	-0.03	3.494	-0.982	0.17
28	15.60	13.93	12.98	7.25	low	10.25	-0.10	3.443	-0.907	0.04
29	14.25	13.45	12.99	8.00	low	1.15	-0.05	3.425	-1.264	0.03
30	16.15	14.24	13.00	3.25	low	11.86	0.24	3.529	-0.723	0.35
31	15.55	13.84	13.01	4.25	low	9.95	-0.08	3.509	-0.828	0.25
32	15.59	13.96	13.03	5.75	low	9.59	-0.02	3.478	-0.900	0.10
33	15.12	13.84	13.10	5.25	low	6.20	0.03	3.488	-1.033	0.15
34	16.33	14.28	13.12	5.00	low	13.14	0.01	3.494	-0.783	0.15
35	15.10	13.85	13.19	5.25	low	5.93	-0.03	3.488	-1.078	0.15
36	15.57	14.07	13.22	7.25	low	8.70	-0.10	3.443	-1.059	0.04
37	16.03	14.22	13.25	5.25	low	11.02	-0.05	3.488	-0.919	0.13
38	16.83	14.84	13.28	3.00	low	12.36	0.62	3.534	-0.810	0.37
39	18.86	15.30	13.37	7.00	low	27.05	-0.18	3.449	-0.450	0.04
40	15.55	14.20	13.37	8.00	low	6.16	-0.01	3.425	-1.236	0.03
41	16.13	14.45	13.42	5.50	low	9.91	0.06	3.483	-1.036	0.12
42	17.66	14.98	13.43	6.00	low	19.27	-0.04	3.472	-0.720	0.09
43	15.71	14.33	13.50	7.50	low	8.00	-0.09	3.437	-1.205	0.03
44	16.11	14.54	13.56	6.75	low	8.98	0.02	3.455	-1.168	0.05
45	15.77	14.38	13.57	5.50	low	7.27	0.02	3.483	-1.191	0.13
46	15.75	14.35	13.57	5.75	low	7.50	-0.03	3.478	-1.191	0.11
47	15.96[b]	14.47	13.62	4.75	low	7.98	0.04	3.499	-1.160	0.19
48	16.99	14.93	13.65	7.75	low	13.40	-0.01	3.431	-1.079	0.03
49	17.02	14.97	13.67	6.50	low	13.36	0.07	3.461	-1.045	0.06
50	17.28	14.96	13.69	4.75	low	15.52	-0.03	3.499	-0.916	0.20
51	15.60	14.35	13.70	4.00	low	5.82	0.01	3.514	-1.244	0.23

Table 4–2—Continued

Source	J	H	K	M Subclass[a]	Gravity	A_V	r_K	logT_{eff}	log(L/L$_\odot$)	Mass ($M_\odot$)
52	16.30	14.73	13.70	6.50	low	9.00	0.08	3.461	-1.215	0.06
53	16.54	14.86	13.71	8.25	low	9.12	0.10	3.419	-1.274	0.03
54	18.05	15.36	13.75	4.25	low	18.86	0.11	3.509	-0.803	0.24
55	...	15.88	13.76	7.00	low	29.11	-0.14	3.449	-0.531	0.04
56	16.40	14.77	13.76	6.75	low	9.52	0.02	3.455	-1.228	0.05
57	15.91	14.64	13.82	8.50	low	5.36	0.01	3.412	-1.461	0.02
58	17.24	15.32	14.00	7.50	low	12.91	0.07	3.437	-1.228	0.03
59	16.13	14.86	14.02	7.50	low	7.00	-0.02	3.437	-1.449	0.03
60	17.86	15.64	14.19	4.00	giant	14.64	0.24	3.514	-1.123	0.24
61	16.40	15.03	14.21	2.75	low	6.66	0.16	3.539	-1.373	0.37
62	16.44	15.02	14.24	7.25	low	7.98	-0.12	3.443	-1.493	0.04
63	17.56	15.63	14.37	4.75	low	11.98	0.19	3.499	-1.316	0.16
64	17.44	15.60	14.42	5.00	giant	11.23	0.15	3.494	-1.371	0.14
65	16.68	15.31	14.50	6.25	low	7.27	-0.01	3.466	-1.588	0.07
66	17.10	15.54	14.61	7.75	low	8.85	-0.06	3.431	-1.626	0.03
67	17.74	16.11	15.05	8.00	low	8.70	0.05	3.425	-1.816	0.03
68	13.74[b]	12.25	11.59	5.00[c]	low	8.05	-0.14	3.494	-0.399	0.15
69	13.83	12.48	11.75	6.75[c]	low	6.98	-0.09	3.455	-0.516	0.05
70	13.88	12.72	12.04	2.50[c]	low	4.68	0.16	3.544	-0.568	0.47
71	15.54	13.43	12.07	7.25[c]	low	14.25	0.03	3.443	-0.399	0.04

[a]Spectral types are listed as M subclasses, thus a table entry of 0.0=M0.0, 7.50=M7.50, etc.

[b]Sources 17, 47, and 68 have J magnitudes derived from FLAMINGOS imaging on the 2.1m telescope.

[c]Sources 68-71 have spectral types derived from 2.1m spectroscopy.

4.4.4 Masses and Ages

In order to derive mass and age estimates for young objects, sources must be placed on an H-R diagram and their positions compared with pre-main sequence evolutionary models. The most frequently used models for low mass stars and high mass brown dwarfs (rather than planetary mass objects) are those of D'Antona & Mazzitelli (1997, hereafter DM97) and Baraffe et al. (1998, hereafter BCAH98). The primary differences between these two models are their treatment of convection (mixing-length theory for BCAH98 and full spectrum turbulence for DM97) and the assumption of grey atmospheres in DM97 vs. non-grey in BCAH98. BCAH98 and references therein argue that the grey atmosphere approximation is inappropriate for stars whose effective temperatures fall

below ∼4500-5000 K as molecules present in the atmospheres will introduce strong non-grey effects. There is some evidence supporting this claim as both White et al. (1999) and Luhman et al. (2003b) used empirical isochrones definined with low mass members of IC 348 and Taurus and the young quadrouple system GG TAU to show that the BCAH98 models agree better with observational constraints. Consequently, while I present H-R diagrams using both sets of tracks, for the remaining discussion we will focus primarily on results derived from the BCAH98 models.

Mass and age estimates were derived from the BCAH98 models by interpolating between the isochrones and mass tracks shown in Figure 4–6. Sources falling above the youngest isochrone (1 Myr) were assumed to have an age <1 Myr and were dropped down to the 1 Myr isochrone along a line of constant effective temperature to derive a mass estimate. In this manner, I derived masses spanning a range from 0.02 to 0.72 $M_{\odot}$ (with 23 objects falling below 0.08 $M_{\odot}$) and ages ranging from <1 to ∼30 Myr.

4.5 Properties of the Low Mass Cluster Population

4.5.1 Cluster Membership

Prior to drawing any conclusions regarding the age of NGC 2024 or its substellar population, it is necessary to evaluate the membership status of sources in our sample. In the absence of proper motion data, we must rely on other diagnostics to determine whether objects are bona fide cluster members or foreground or background sources projected on the cluster area. The discussion of surface gravity effects in §4.3.2.2 rules out foreground or background dwarf contamination in our spectroscopic sample as there are no potassium lines present in our spectra. In addition, NGC 2024 is deeply embedded in a core of dense gas (Lada et al., 1991a, 1997) which will obscure background field stars, limiting the number of field contaminants in the photometric sample. The average column density of hydrogen in a 0.6 pc clump centered on NGC 2024 has been estimated from $C^{18}O$ emission to be $N(H_2)$=4.6×10^{22} cm^{-2} (Aoyama et al., 2001). Given that a molecular hydrogen column density of 10^{21} cm^{-2} corresponds to 1 magnitude of

visual extinction (Bohlin et al., 1978), background sources in this region will be viewed through 46 magnitudes of visual extinction, or ∼4.1 magnitudes of *K*-band extinction. The spectroscopic sample includes sources down to $K \simeq 15$. Background objects contaminating this sample are seen through the cloud and thus will have unreddened magnitudes $K \leq 11$. Looking at the distribution of sources in an off-cloud FLAMINGOS control field as well as a similar area from the 2MASS database, I estimate that there are no more than 5 background sources with $K \leq 11$. As this is a relatively insignificant contribution to the total photometric luminosity function, I conclude that a background correction is unnecessary. I do note the possibility of giant contamination for two spectroscopic sources (60 and 64) which display enhanced absorption in the H-band, thus these objects are excluded from further analysis.

4.5.2 Cluster Age

Sources in the H-R diagrams in Figure 4–6 do not fall along a single isochrone but rather show a scatter in age ranging from $\ll$1 Myr to ∼30 Myr, irrespective of the PMS models used. This type of width in the evolutionary sequence of young clusters is common and is usually attributed to a variety of effects including: real age differences between sources, errors in luminosity derived from uncertainties in the derived reddening, photometric uncertainty (these effects are represented by the error bars in the figure), as well as distance variations between sources, variability due to accretion and rotation of young objects, and unresolved binaries. The median age of the entire sample however should be representative of the median age of the cluster population in the mass range detected here.

Using the models of BCAH98 the majority of sources fall above the 1 Myr isochrone. Consequently, the median age of the cluster can only be constrained to $<$1 Myr. However, the DM97 models extend to younger ages than those of BCAH98. Even though I have elected to place more weight on results derived with the BCAH98 models (see §4.4.4), the DM97 models provide us with additional information on the age

of the cluster population as well as a means to compare our results with previous surveys of NGC 2024 and other regions where authors have used the DM97 models to derive an age. Using the DM97 models we derive a median age of 0.5 Myr. If we factor in errors in the distance modulus (8.09±0.17, Anthony-Twarog, 1982), this leads to a possible age range of 0.4-0.6 Myr. Including a 3 magnitude shift in reddening (refer to §4.4.1) yields a larger range of 0.2-0.9 Myr. All of these results remain consistent with the age derived from the BCAH98 models, placing NGC 2024 at $<$1 Myr.

Our derived age of 0.5 Myr for NGC 2024 is in good agreement with ages found by previous surveys of NGC 2024. Both Meyer (1996, hereafter M96) and Ali et al. (1998) used infrared photometry and spectroscopy with the models of D'Antona & Mazzitelli (1997) to derive mean ages of 0.3 and 0.5 Myr respectively. Further, M96 used a distance modulus of 8.36 magnitudes. Increasing the distance to the cluster acts to increase the derived bolometric luminosity of sources, making objects appear younger. Indeed, using the larger distance modulus with the models of DM97, I derive a median age of 0.3 Myr which is in excellent agreement with the results of M96.

A few sources in our H-R diagrams appear to have ages which deviate significantly from the median. Using either set of PMS models there is a small, lower luminosity population with inferred ages $>$3 Myr. In order to attribute these low luminosities to general scatter caused by photometric errors and uncertainties introduced by variability (generally no more than ±0.2 mag at K), derived reddening (±0.3 mag, see above), and distance modulus (±0.2 mag), these effects would have to combine to produce at least a 1-2 magnitude shift at K. On the other hand, it has been noted by multiple authors (e.g. Luhman et al., 2003b; Slesnick et al., 2004; Wilking et al., 2004) that a circumstellar disk can act to occult the central source, resulting in an underestimate of the object's luminosity and thus an overestimate of the object's age. I have examined the infrared excess properties of the subsample in question and, irrespective of the model isochrones

used, all but one of the objects with an inferred age >3 Myr have excess flux, indicating the presence of circumstellar material.

Looking at Figure 4–6, it would appear that object age may be slightly mass dependent with the less massive sources appearing younger. To quantify this trend, I have divided our sample into two populations: objects with masses lower than the median mass and objects with masses higher than the median mass ($M_{median} \simeq 0.15\ M_{\odot}$). Using the BCAH98 models there does not seem to be an age difference between the low and high mass samples as both have median ages <1 Myr. However, the median ages indicated by the DM97 models are somewhat different from one population to the other. The low mass sample has an age of 0.3 Myr and the higher mass sample has an age of 0.9 Myr. There are a number of possible explanations for this effect. First, the trend may be an artifact arising from uncertainties in the evolutionary models at very young ages and low masses. No two sets of PMS tracks look alike in the brown dwarf regime thus it is a distinct possibility that the apparent age segregation is caused by a problem with the tracks. On the other hand, the observed mass dependence could be a selection effect caused by the intrinsic faintness of the older substellar population – according to the BCAH98 models even the highest mass brown dwarfs will be undetectable by our survey by the time they reach ages of 2-3 Myr and this limit becomes younger for lower mass objects. Finally, it is also possible that this effect is real. If so, this may be evidence for sequential formation as a function of mass where lower mass objects form later in the evolutionary sequence of a young cluster. Unfortunately, our data are not sensitive enough to distinguish between these possibilities – deeper spectroscopic observations are needed.

4.5.3 Spatial Distribution of Sources

Figure 4–7 presents the spatial distribution of all sources classified using FLAMINGOS spectra. Open circles are objects with $M > 0.08\ M_{\odot}$, filled triangles have masses $M < 0.08\ M_{\odot}$, and asterixes are the possible giants. The star at the center of the cluster represents IRS2b, the likely ionizing source for the region (see below). It can be seen

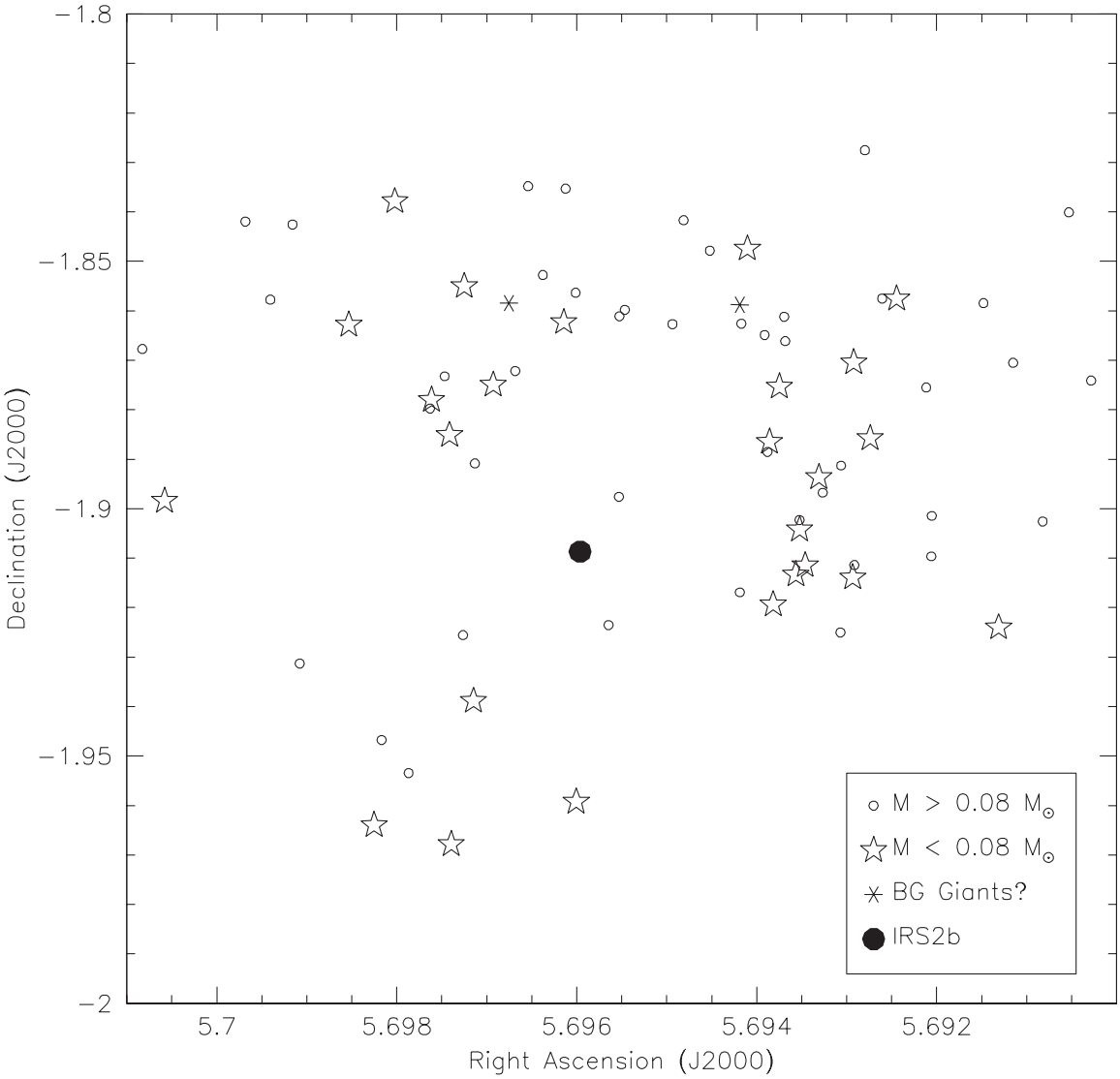

Figure 4–7. Spatial distribution of both stellar and substellar objects in NGC 2024. The open circles represent objects with masses M $>$ 0.08 $M_{\odot}$, stars are objects with M $<$ 0.08$M_{\odot}$, asterixes are possible background giants, and the large dot represents IRS2.

from this figure that the substellar objects are not localized to one region but rather appear to be distributed similarly to the stellar mass objects classified here. It should be noted that the dearth of classified objects (either stellar or substellar) in the center of the cluster is a selection effect caused by the high extinction in this region blocking much of the *J* and *H*-band flux.

4.5.4 Substellar Disk Frequency

As discussed in §4.3.2.3, the presence of an infrared excess is commonly taken to be an indicator of thermal emission from a circumstellar disk. Disks around brown dwarfs are of particular interest because their presence or absence has implications for the likelihood of planet formation (planets form within circumstellar dust disks) and the formation mechanism of brown dwarfs (accretion disks play an important role in the star formation process). Combining our spectral classifications with $H-K$ intrinsic colors we find 40%±9% of sources in our total sample have an $H-K$ color excess. This method of selecting excess sources has been shown by Liu et al. (2003) to be more sensitive to small IR excesses (as opposed to the traditional *JHK* color-color diagrams) and is thus well suited for investigating the disk properties of brown dwarfs, which are expected to have smaller excesses than their stellar counterparts. Approximately one third of the excess sources detected using the color-spectral type analysis have masses which place them below the hydrogen-burning limit (spectral types ≥M6). This yields a substellar *HK* excess fraction for NGC 2024 of 9/23 or 39%±15%, where quoted errors are derived from Poisson statistics.

Substellar excess fractions have been compiled for a number of other regions. For example, Muench et al. (2001) used *JHK* color-color diagrams to examine a set of photometrically selected brown dwarfs in the Trapezium cluster and found a substellar excess fraction of ∼65%±15%. In a follow-up L' study of the same region, Lada et al. (2004) find a $K-L'$ excess fraction of 52±20% for their spectroscopically selected brown dwarf sample and 67% using a *JHKL* color-color analysis for the larger photometric sample. More recently, Luhman et al. (2005b) used the Spitzer Space Telescope to obtain mid-infrared photometry for low mass members of the IC 348 and Chamaeleon I clusters, finding that 42%±13% of brown dwarfs in IC 348 and 50%±17% of brown dwarfs in Chamaeleon exhibit excess emission, consistent with our result for NGC 2024.

Based on the above results (placing more emphasis on studies with spectroscopic information), we can conclude that 40-50% of brown dwarfs are surrounded by circum(sub)stellar disks. Note though in many cases the quoted substellar excess fractions are deemed lower limits to the true substellar disk fraction (e.g. Lada et al., 2004; Luhman et al., 2005b). This is also true for NGC 2024. Disk modeling by Liu et al. (2003) shows that the *maximum* expected K-band excess for a disk with no inner hole is 0.42 magnitudes for an M6 dwarf and 0.31 magnitudes for an object classified as M9. However, the L' observations of Liu et al. (2003) are more consistent with disks having an inner hole $R_{in} \approx (2-3)R_*$. The K-band excess for these objects would be very small or undetectable using the $H-K$ analysis I present here.

The choice of intrinsic colors may also lead to an underestimate of the substellar disk fraction in NGC 2024. I have used an intrisic color set derived from observations of field dwarfs. Our targets are pre-main sequence objects which have lower surface gravities than field dwarfs (e.g. §3.4) and thus bluer $H-K$ intrinsic colors for a given spectral type (refer to the low surface gravity giant sequence plotted in Figure 4–2 as compared to the dwarf sequence plotted in the same figure). The assumption of the redder dwarf colors will preclude objects with a K-band excess similar to or smaller than the difference between PMS and dwarf colors from being counted as excess sources. Combining this effect with the fact that $H-K$ excess is a poor indicator of disk emission for substellar objects (see above), I conclude the true substellar disk fraction for NGC 2024 may be significantly higher than 39%. This yields further weight to the idea that the majority of brown dwarfs form through a disk accretion process similar to their stellar counterparts.

4.5.5 Low Mass IMF

Prior to constructing a mass function for NGC 2024, it is crucial to ensure that the subsample under consideration is representative of the overall cluster population. The left-hand panel of Figure 4–8 shows the uncorrected K-band luminosity function (KLF) for the photometric sample with the KLF of the final classified spectroscopic

sample. Without placing any limits on the data, it can be seen that our spectroscopic

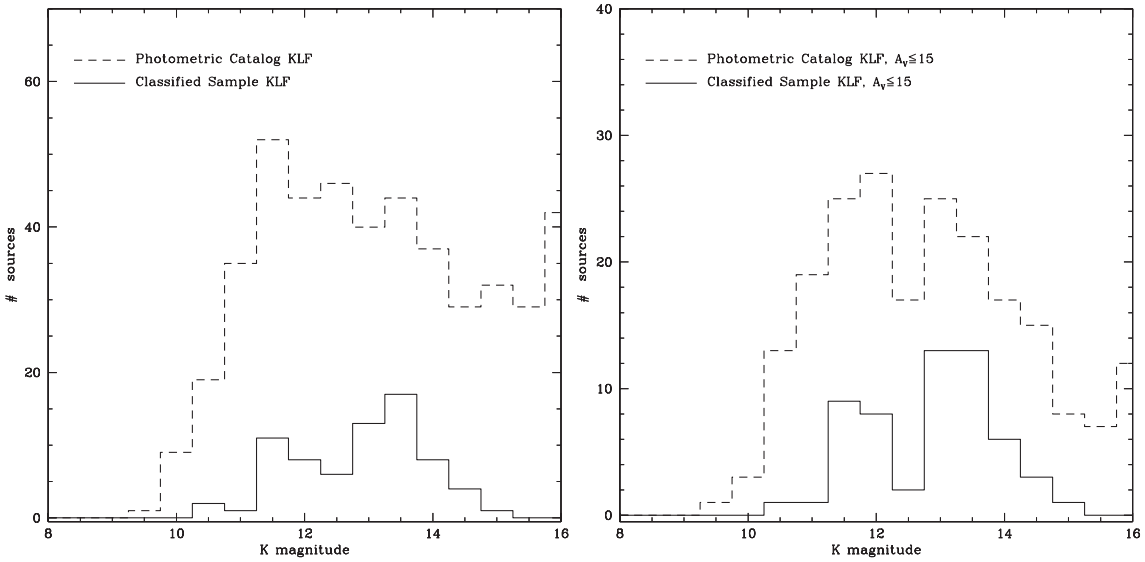

Figure 4–8. *Left: K*-band luminosity function for all classified objects in the spectroscopic sample (solid line) shown with the KLF for the photometric catalog (dashed line). *Right:* KLFs for both samples with an imposed extinction limit of $A_V \leq 15$. It can be seen from the figure that in the magnitude range $11.25 < K < 14.75$ the extinction-limited spectroscopic sample is representative of the extinction-limited main cluster population.

survey is typically only 10-20% complete in the magnitude range from K=10.5-15.0. As discussed in §4.5.1, correcting for background field stars will have little effect. Rather, much of our incompleteness is caused by high reddening within the molecular cloud itself (§4.4.1). Imposing an extinction limit on the data yields a higher completeness fraction and gives a more controlled sample from which an IMF can be constructed. The right-hand panel of Figure 4–8 shows the K-band luminosity functions for all sources having $A_V \leq 15$ in both the photometric catalog and the final sample of classified objects. Disregarding the bins on either end (as they contain only one object each), it now appears that the spectroscopic KLF is a good representation of the total photometric KLF in the magnitude range $11.25 < K < 14.75$. Further, with the exception of the bin centered on K=12.5, the completeness fraction in the same magnitude range now extends from ∼25-60% with a median value of 35%. Following the work of Slesnick et al. (2004),

I corrected for this incompleteness by adding sources to each deficient magnitude bin according to the object mass distribution in that bin.

Figure 4–9 shows the spectroscopically derived mass function for NGC 2024. The solid line is the mass function for all objects with spectral types ≥M0, excluding the two possible giants (§4.5.1). Error bars are derived from Poisson statistics. The dashed line shows the IMF for the same sample corrected for the incomplete magnitude bins down to K=14.75. We estimate that for our extinction-limited sample, this corresponds to a mass completeness limit of 0.04 $M_{\odot}$. The mass function rises to a peak at ∼0.2 $M_{\odot}$ before declining across the stellar/substellar boundary. There is an apparent secondary peak around ∼0.03 $M_{\odot}$ although the error bars are also consistent with a relatively flat IMF in this regime. The implications of this mass function will be discussed in Chapter 6.

It should be noted that the exact shape of the substellar IMF is somewhat dependent on the choice of bin centers and sizes. For a bin width of 0.3 dex, shifting the bin centers in increments of 0.05 dex shifts the location of both the primary and secondary peaks through a range of masses from ∼0.25-0.1 $M_{\odot}$ and ∼0.03-0.04 $M_{\odot}$ respectively. Additionally, in some cases the secondary peak disappears and the substellar IMF becomes flat. Decreasing the bin width by 30% emphasizes the secondary peak, however, the errors remain consistent with a flat IMF. Increasing the bin widths by 30% either preserves the secondary peak, flattens the substellar mass function, or causes it to decline throughout the brown dwarf regime depending on the choice of bin centers.

4.5.6 The Ratio of Brown Dwarfs to Stars

A more robust tool for quantifying the IMF is the ratio of brown dwarfs to stars as this quantity is independent of the detailed structure and exact shape of cluster mass functions. Briceño et al. (2002) define the ratio of the numbers of stellar and substellar objects as

$$R_{ss} = \frac{N(0.02 \leq M/M_{\odot} \leq 0.08)}{N(0.08 < M/M_{\odot} \leq 10)}. \quad (4.1)$$

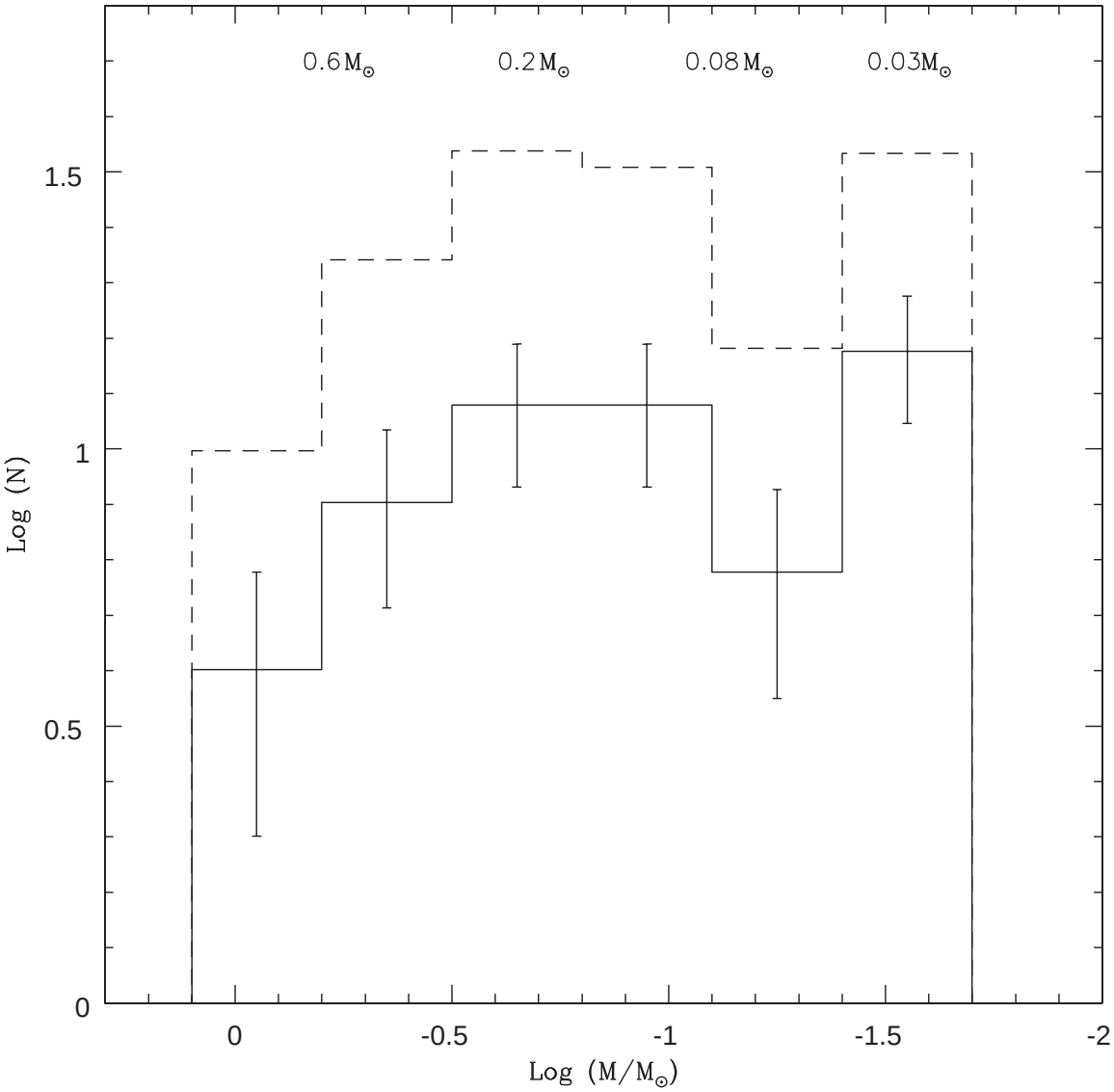

Figure 4–9. Mass function for all classified objects in NGC 2024 whose spectra indicate that they are cluster members with spectral types $\geq$M0. The solid line is the uncorrected raw mass function shown with Poisson error bars and the dashed line has been corrected for magnitude incompleteness in the range from $11.25 < K < 14.75$.

In our completeness-corrected, extinction-limited mass function for NGC 2024 there are 45 objects with masses $0.02M_{\odot}<M<0.08M_{\odot}$ and 103 objects with masses $M > 0.08M_{\odot}$. In addition, there are 36 sources in our photometric catalog with K magnitudes brighter than the bright limit of our mass function (K=11.25, §4.5.5). Since the youngest (and thus brightest) object classified as substellar has a K magnitude of 11.75 with the majority of brown dwarfs falling below K=12.75 it is reasonable to infer that all of these bright photometric sources have masses greater than 0.08 $M_{\odot}$. Finally, I include 9 sources from the 2MASS catalog with magnitudes brighter than the FLAMINGOS saturation limit which are also expected to be far more massive than the substellar limit. This yields a value of R_{ss}=45/148 or 0.30±0.05 assuming Poisson errors. A comparison of the R_{ss} for NGC 2024 with that of other low mass star forming regions can be found in Chapter 6.

4.6 Summary

This Chapter presents results from FLAMINGOS photometry and spectroscopy for 71 objects in NGC 2024. Derived spectral types yield 67 young M stars ranging from ∼M1 to >M8, excluding two sources with spectral types <M and two background giants. Spectral types for these 67 objects were then converted to effective temperatures and photometry was used to calculate extinctions and bolometric luminosities. Sources were then placed on H-R diagrams and masses and ages were inferred with the assistance of pre-main sequence evolutionary models.

The median age of M stars in NGC 2024 is 0.5 Myr using the evolutionary models of D'Antona & Mazzitelli (1997). This value is consistent with a median age <1 Myr as derived from the models of Baraffe et al. (1998). Estimated masses range from 0.02 $M_{\odot}$ to 0.72 $M_{\odot}$ using the Baraffe et al. (1998) models, with 23 of the 67 objects falling below the stellar/substellar boundary. The spatial distribution of sources indicates that the brown dwarfs appear to be evenly distributed relative to their stellar counterparts and thirty

nine percent of the classified brown dwarfs appear to have an infrared excess, possibly indicative of thermal emission from a warm disk.

Using an extinction limited subsample of the spectroscopic sources ($A_V < 15.0$), I constructed the low mass IMF for the region. The IMF for NGC 2024 peaks at $\sim$0.2 $M_\odot$ and then declines into the brown dwarf regime. There is a possible secondary peak around 0.035 $M_\odot$. Finally, the ratio of stellar to substellar objects in NGC 2024 is R_{ss}=0.30$\pm$0.05.

CHAPTER 5
M STARS AND BROWN DWARFS IN NGC 2068 AND NGC 2071

5.1 Introduction

In this Chapter I present results from FLAMINGOS photometry and spectroscopy of the young clusters NGC 2068 and NGC 2071. Both of these clusters are associated with prominent reflection nebulae located in the northern part of the Orion B cloud (Figure 5–1) and have long been known to be areas of active star formation. Early spectroscopic and photometric studies detected a number of Hα emission line stars and confirmed the

Figure 5–1. Optical Image of NGC 2068 and NGC 2071 from the Digital Sky Survey. North is up and east is left.

presence of a population of very young ($\tau \sim 0.1$ Myr) stars (e.g. Herbig & Kuhi, 1963; Strom et al., 1975). More recent work in the region includes the molecular line maps of Maddalena et al. (1986) in CO and Lada et al. (1991a) and Lada et al. (1997) in CS, the 2.2 μm survey of Lada et al. (1991b), and dust continuum mapping at 850 μm by Mitchell et al. (2001) and Johnstone et al. (2001). However, to date, there have been no detailed studies of the low mass cluster populations. This chapter presents an in-depth study of the M star population of NGC 2068 and NGC 2071, including new H-R diagrams, ages, and mass functions for both clusters.

5.2 Photometry of NGC 2068 and NGC 2071

J, *H*, and *K*-band images of NGC 2068 and NGC 2071 were obtained with FLAMINGOS on the KPNO 2.1 m telescope as part of the Orion B imaging survey (Chapter 2, §2.3) on the nights of 2002 January 13 and 2002 December 31. All data were taken using a single pass of the standard 9-point dither pattern described in §2.3.1, with the exception of the *H*-band for NGC 2068 which was observed twice to account for bad reads. The exposure time at each point was 35 seconds, yielding a total exposure of $\sim$8 minutes for the N2068 *H*-band dither set; the other image sets all had totals of $\sim$5 minutes on source. The seeing for NGC 2068 was 1.″7-1.″9 FWHM and the seeing for NGC 2071 was 1.″7-1.″8 FWHM.

All imaging data were reduced and photometered using the FLAMINGOS data reduction and analysis pipelines described in Chapter 2. The resultant zero point-corrected catalogs for the entire 2.1 m field of view ($20' \times 20'$) yielded $\sim$800 sources in N2068 and $\sim$700 sources in N2071 with PSF-fitting color errors less than 0.1 magnitudes. This photometry is shown in Figures 5–2 and 5–3.

Photometric quality was assessed in the standard manner for the survey (§2.3.5). The mean photometric scatter with respect to 2MASS in all bands is 0.06-0.07 magnitudes (e.g. Table A–2). The 10σ detection limits for the cluster data are J=19.3, H=18.8, and *K*=17.8 and the photometric catalog luminosity functions for both clusters turn over at

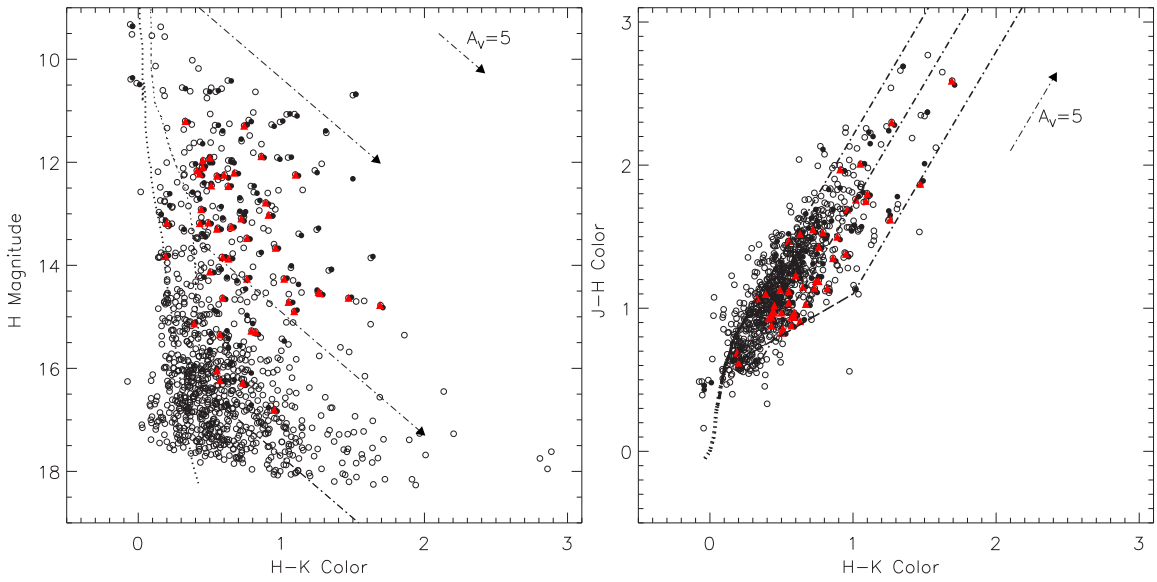

Figure 5–2. Color-magnitude (left) and color-color (right) diagrams for all objects in NGC 2068 with color errors <0.1 magnitudes. Symbol definitions are the same as in Figure 4–2, with open circles representing the general cluster population, filled circles representing the spectroscopic targets, and filled red triangles are the classified sources in NGC 2068.

or beyond 19.0, 18.25, and 17.5 magnitudes for *J*, *H*, and *K* respectively (Table A–3).

Using these turnovers as representative completeness limits (§2.3.5), it is clear that the

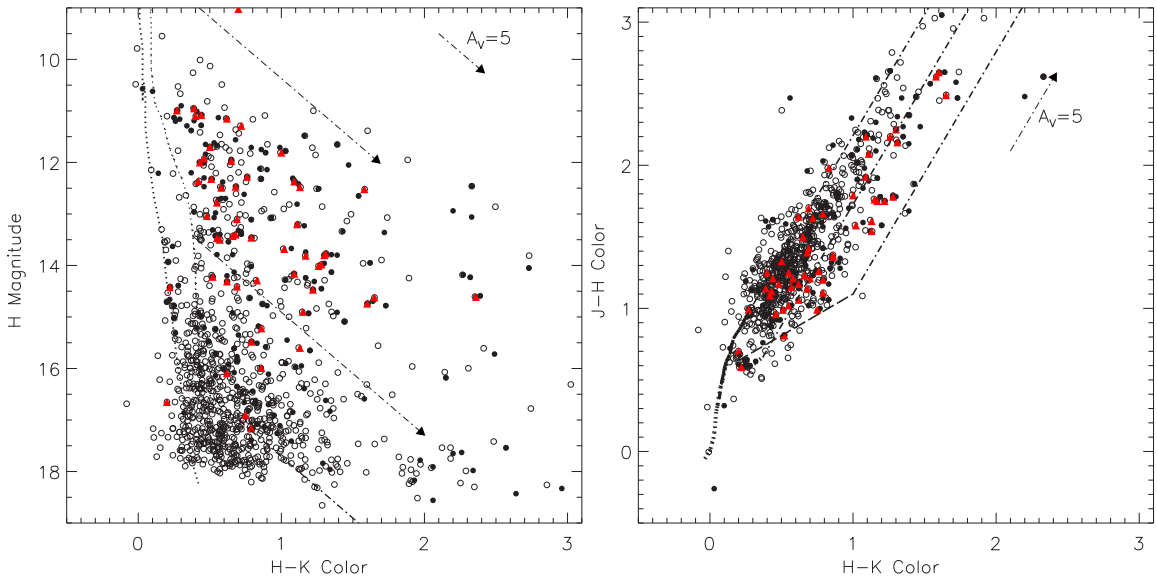

Figure 5–3. Same as Figure 5–2 but for NGC 2071.

Table 5–1. Detail of Slit Masks Observed in NGC 2068

Mask ID	Telescope	Target Selection Method	N_{slits}	N_{ext}[a]	$N_{<M}$[b]	$N_{\geq M}$[c]	N_{dups}[d]
ob4nm1	4m	Brown Dwarfs	22	17	4	9	0
n2068a1	4m	*H* magnitude	19	18	7	7	1
n2068a2	4m	*H* magnitude	17	17	1	12	2
n2068a4	4m	*H* magnitude	22	21	10	9	0
n2068f11	2.1m	*K* magnitude	22	20	15	1	0
n2068f21	2.1m	*K* magnitude	19	18 (+1)	9	7	1
n2068a31	2.1m	*H* magnitude	20	20 (+1)	20	1	0
Totals:			141	131(+2)	66	46	4

[a]Number of sources extracted

[b]Number of sources earlier than M0

[c]Number of new low surface gravity M stars

[d]Number of duplicate M stars

photometry for NGC 2068 and NGC 2071 is complete well beyond the *K*=16.5 targeted limit of the spectroscopic survey (§2.4.1).

5.3 Spectroscopy of NGC 2068 and NGC 2071

5.3.1 Sample Selection, Observations, and Data Reduction

The spectroscopic samples for NGC 2068 and NGC 2071 were selected from the above photometry according to the guidelines described in Chapter 2. In NGC 2068, a total of 141 sources were targeted, with 80 sources on four 4 m slit masks and the remaining 61 objects on three 2.1 m slit masks. In NGC 2071, we targeted a total of 234 sources: 176 objects on nine 4 m masks and 58 objects on three 2.1 m masks. The targeting breakdown by MOS plate can be found in Tables 5–1 and 5–2; the photometry of targeted sources is shown by filled circles in Figures 5–2 and 5–3, while the spatial distribution of these targets can be seen in Figures 5–4 and 5–5.

Spectra of the NGC 2068 4 m targets were obtained using FLAMINGOS on the nights of 2003 January 15 and 2004 December 01-03. Spectra of the NGC 2068 2.1 m targets were taken on 2003 November 30 and 2004 December 14. In NGC 2071, spectra of the 4 m targets were obtained on 2003 December 11, 2004 January 06-07, 2004 November 26, 2004 December 03, 2005 December 17, and 2005 December 20/21. The

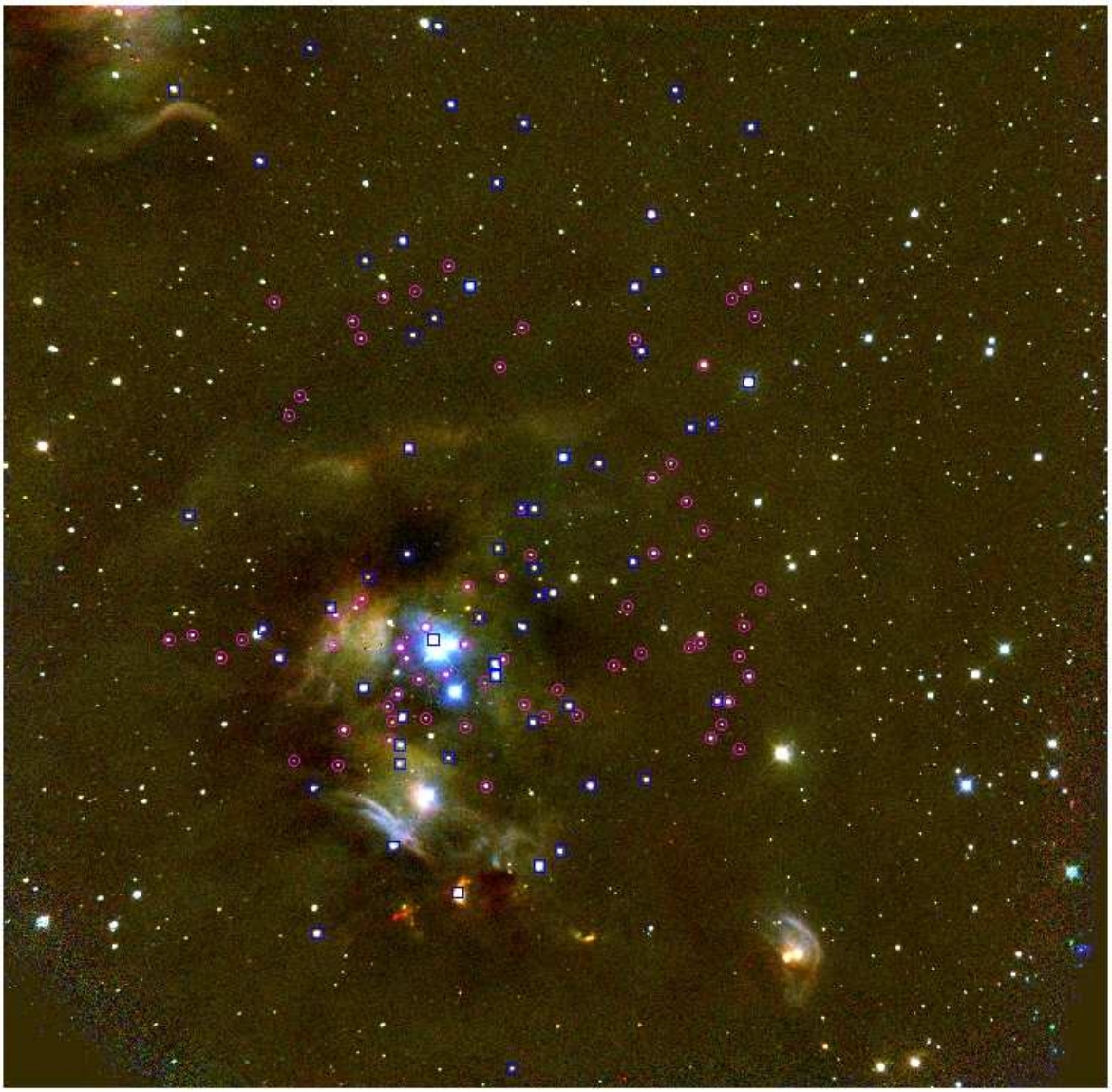

Figure 5–4. Three-color combined image of NGC 2068. The data were taken with FLAMINGOS on the KPNO 2.1 m telescope. North is up, East is to the left, and the field is approximately 20’ on a side. Objects enclosed in purple circles are the 4 m spectroscopic targets and blue rectangles enclose the 2.1 m targets.

Figure 5–5. Same as Figure 5–4 but for NGC 2071

Table 5–2. Detail of Slit Masks Observed in NGC 2071

Mask ID	Telescope	Target Selection Method	N_{slits}	N_{ext}[a]	$N_{<M}$[b]	$N_{\geq M}$[c]	N_{dups}[d]
oc34mf1a	4m	IRX sources	24	19	7	7	1
oc34mf2a	4m	IRX sources	17	11	1	3	0
oc44mf11	4m	IRX sources	21	14	0	7	2
oc44mf31	4m	IRX sources	24	14	4	4	0
n2071a2	4m	*H* magnitude	12	12	1	2	2
n2071a3	4m	*H* magnitude	15	14	3	3	3
n2071a4	4m	*H* magnitude	25	25	4	12	4
n2071a5	4m	*H* magnitude	20	18	6	5	4
n2071a6	4m	*H* magnitude	18	17	5	4	2
n2071f21	2.1m	*K* magnitude	21	21	17	4	0
n2071f22	2.1m	*K* magnitude	19	18	16	2	0
n2071a21	2.1m	*H* magnitude	18	18	17	1	0
Totals:			234	201	81	54	18

[a]Number of sources extracted

[b]Number of sources earlier than M0

[c]Number of new low surface gravity M stars

[d]Number of duplicate M stars

2.1 m targets in NGC 2071 were observed on 2003 November 28, 2003 December 01, and 2004 December 20. The full details of the observing procedures at both telescopes can be found in §2.4.2. The specific integration times by mask can be found in Appendix B, Table B–1.

All spectroscopic data were reduced using the procedures detailed in §2.4.3 and classified according to the methods developed in Chapter 3. Totals by mask of the number of sources targeted, extracted, and classified are listed in Tables 5–1 and 5–2.

5.3.2 Results

5.3.2.1 Spectral Classification

Figures 5–6 and 5–7 show the final sets of M star spectra in NGC 2068 and NGC 2071 respectively. In NGC 2068, 37 unique M stars were classified from the 4 m sample and 9 unique M stars were classified from the 2.1 m sample, yielding a total of 46 classified M stars. In NGC 2071, I classified 47 unique M stars from the 4 m spectra and 7 unique M stars from the 2.1 m spectra resulting in a total of 54 classified M stars. In

addition, I also extracted a total of 22 duplicate sources. When independently classified (without a priori knowledge of their duplicity), the spectral types for 12 of these objects matched the original source exactly or to within 0.25 subclasses. Spectral types for all but one (located on the edge of a plate) of the remaining 10 duplicates were within 1 subclass of the original object, thus, I am confident that all spectral types are accurate within the errors quoted (typically 1 subclass or less).

Considering the 48 extracted 4 m objects which were not classfied, 14 were filler targets with K magnitudes > 15.0 which we have learned are typically too faint to classify with our current exposure times. The remaining unclassified sources while bright at K, were typically highly reddened objects with poor signal to noise in the J and H bands after dereddening. Targets which were not extractable were simply too faint to achieve an accurate aperture trace.

5.3.2.2 Surface Gravity Assessment

As discussed in previous chapters, there are certain diagnostics in the NIR spectra of M stars which can be used as surface gravity indicators. The strongest of these visible in FLAMINGOS spectra are the J-band potassium absorption lines, the H-band line frequency, and the overall continuum shape as induced by the broad water absorption features in both J and H (§3.4). I have searched for these features in all of our spectra and use their relative strengths to assess the gravity of each source. Results of this assessment are noted in Tables 5.4.1 and 5.4.1. A designation of low indicates a source is a low surface gravity young object, high indicates a field dwarf, and giant is a very low gravity giant. An ellipsis in the gravity column indicates that I was unable to complete the gravity assessment, either because the J-band signal-to-noise was too low to distinguish the potassium lines or because the spectral type was too early and the high gravity indicators were not strong enough to be detected. However, for all uncertain cases the H-band was sufficient to rule out background giants.

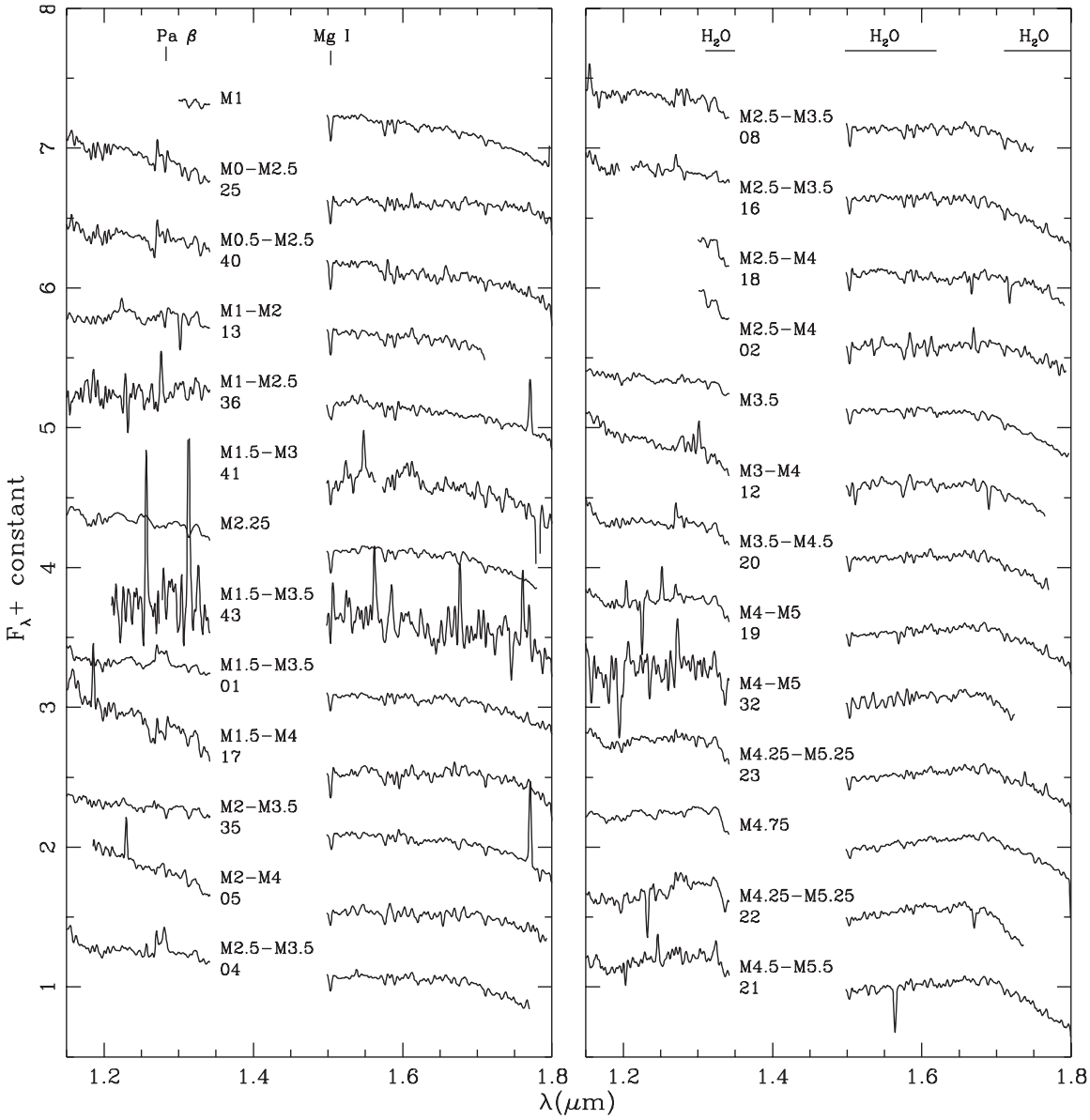

Figure 5–6. NIR spectra of all classified M stars in NGC 2068 (labeled with both spectral type and ID) shown with the IC 348 optically classified young standards (labeled with spectral type only). Prominent spectral features are identified at the top. As with NGC 2024, objects having spectral types $<$M6 have been smoothed to R$\sim$500 and objects $\geq$M6 have been smoothed to R$\sim$200 to aid in the classification process. The central regions of the spectra are blocked out for display purposes because in most cases the signal to noise in these regions is very low due to the overwhelming telluric absorption. In some cases, the *J*-band has also been blocked - these spectra were particularly noisy and classified using their *H*-band continuum shape only.

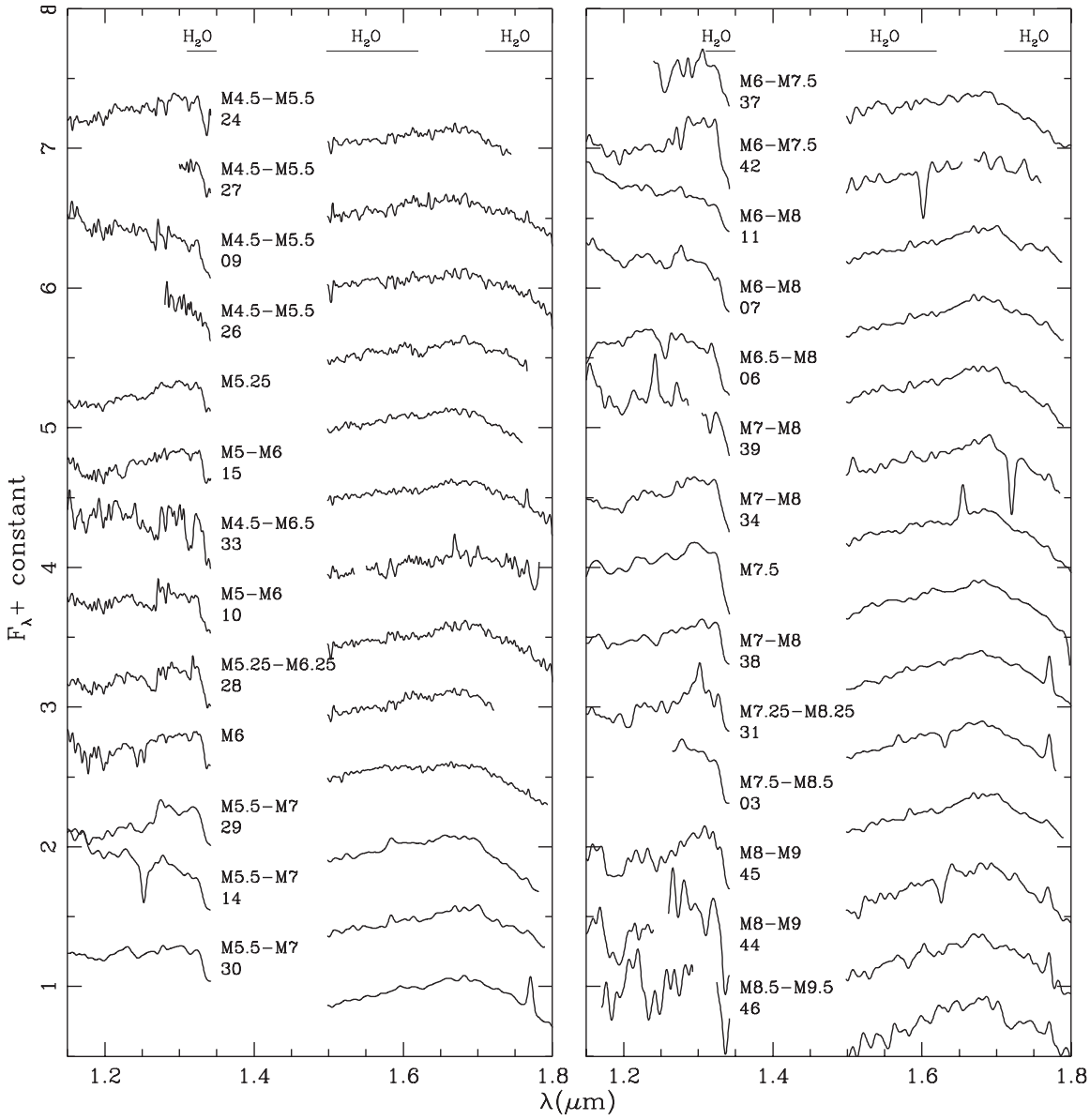

Figure 5–6. continued

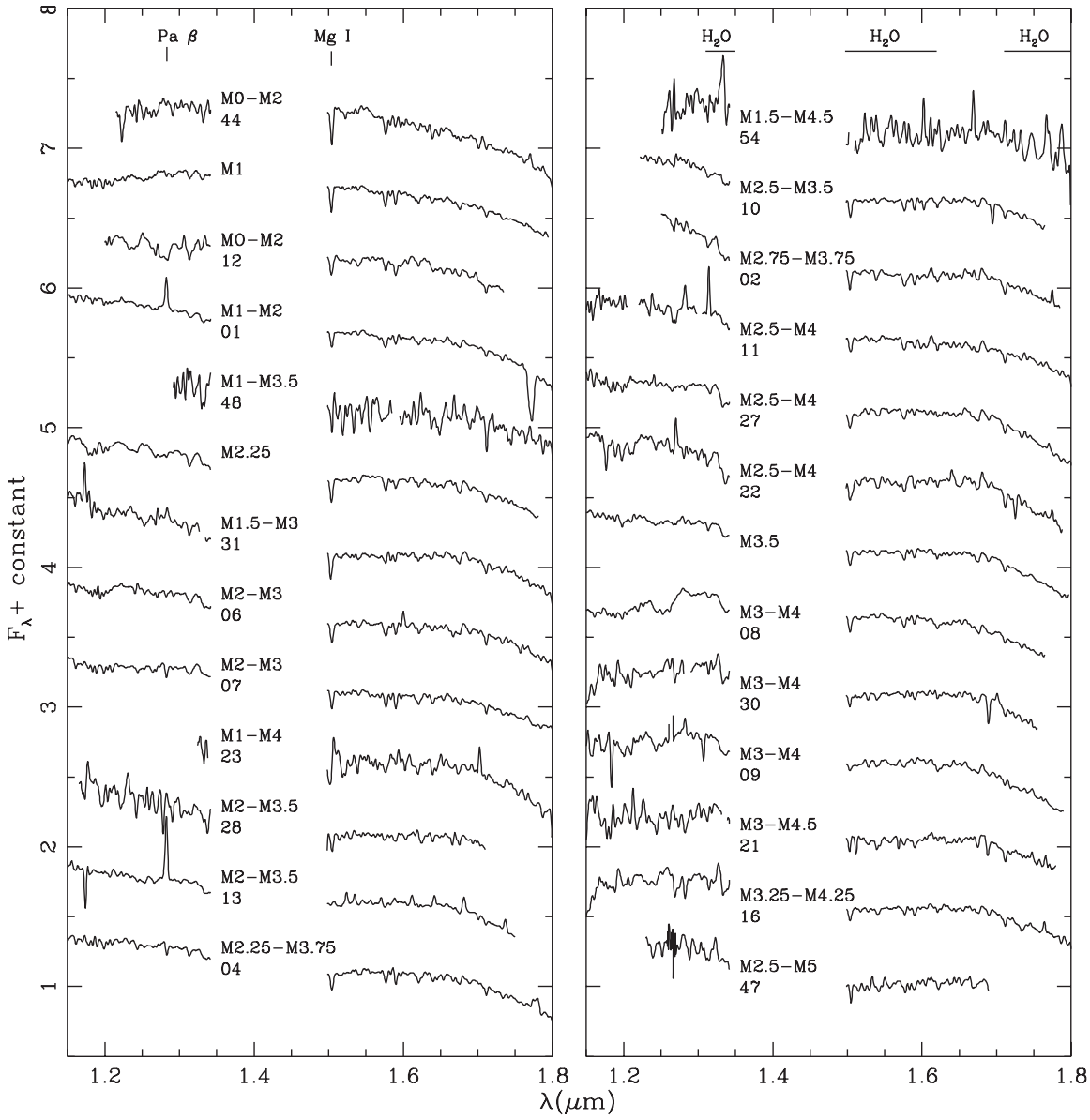

Figure 5–7. NIR spectra of M stars in NGC 2071.

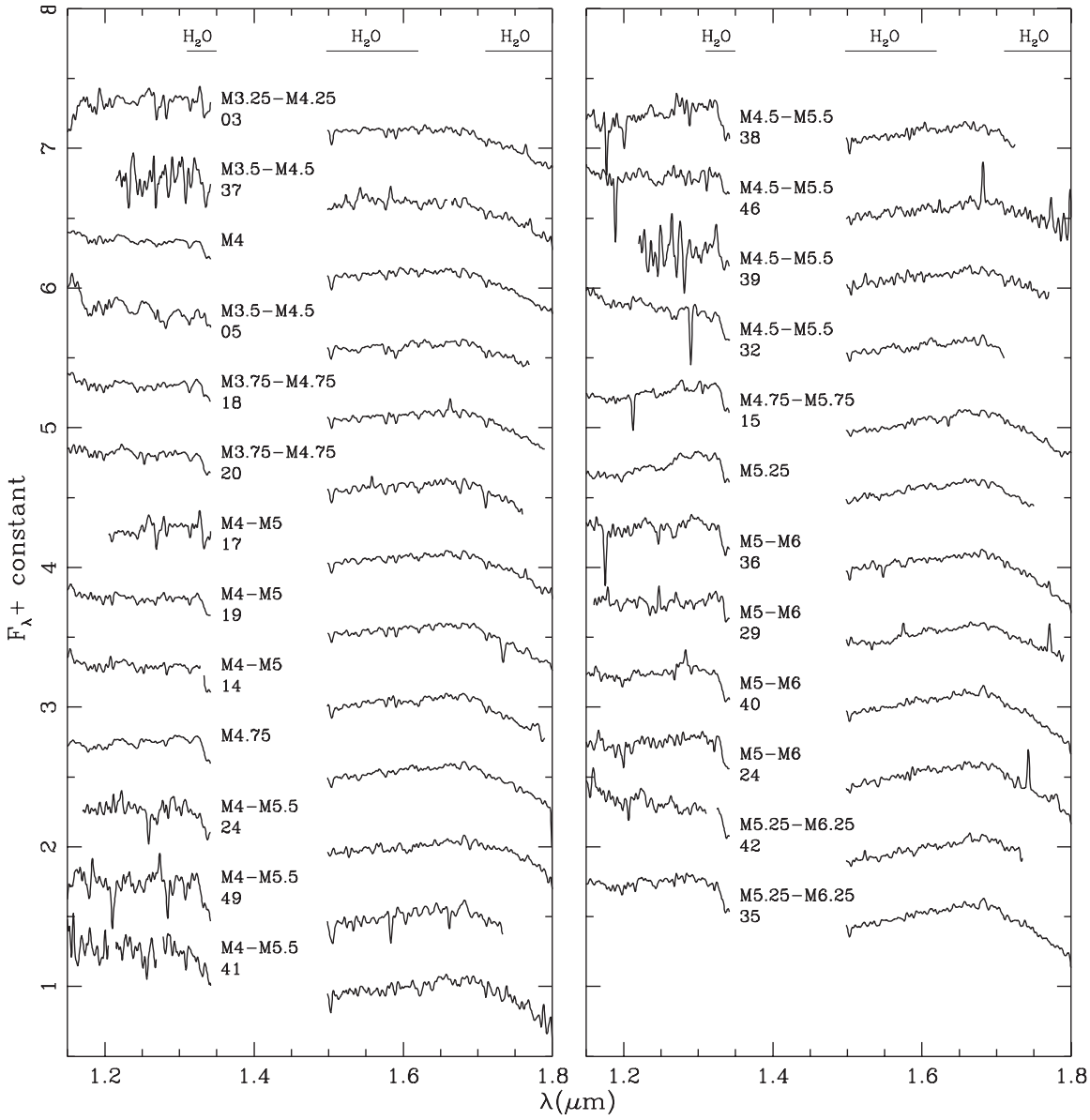

Figure 5–7. NIR spectra of M stars in NGC 2071 continued.

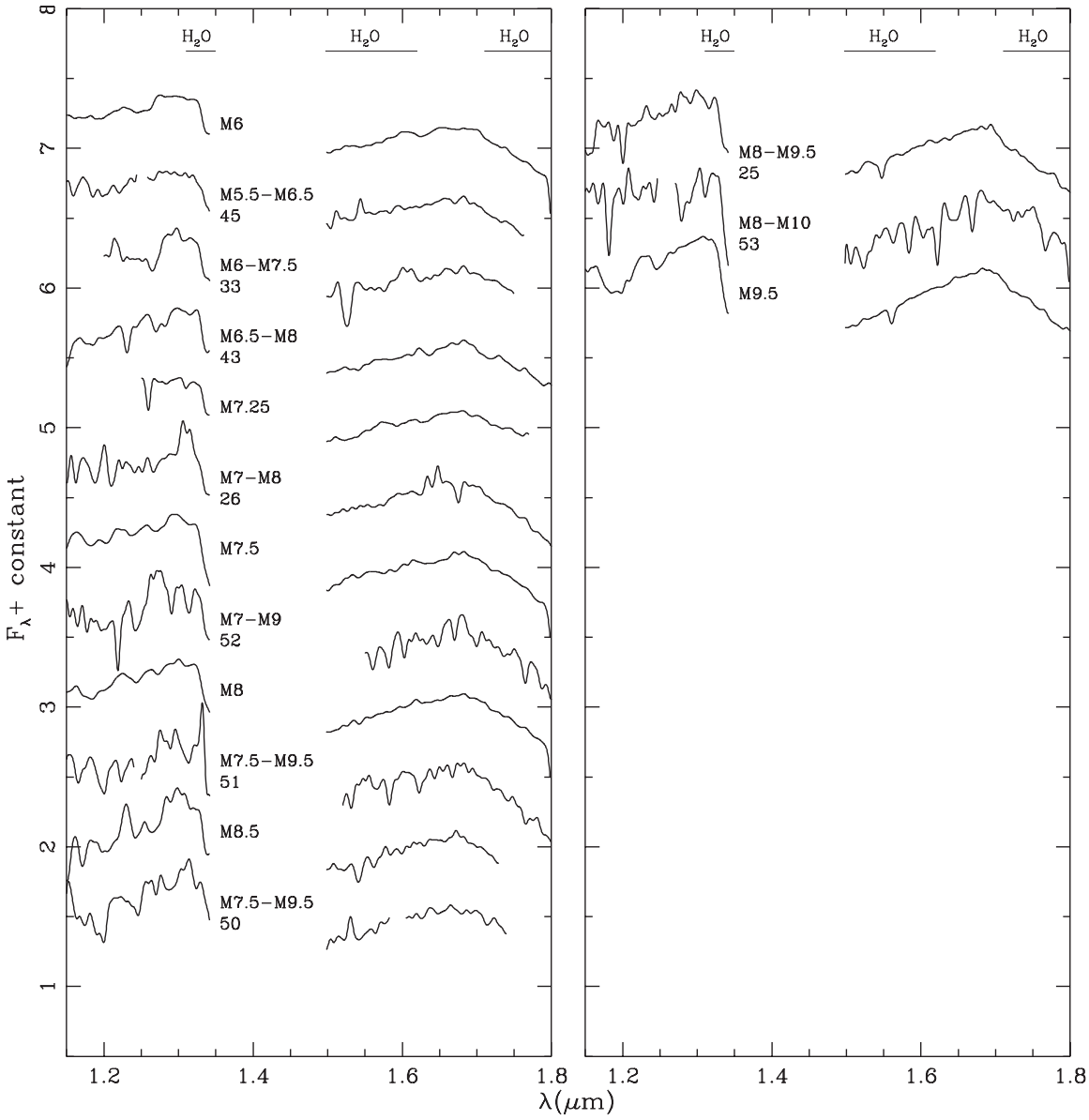

Figure 5–7. continued

Objects of particular interest in NGC 2068 include n2068-35 which exhibits relatively strong K I absorption as well as an *H*-band plateau consistent with a field dwarf, and n2068-41 and n2068-43 which both exhibit a large number of H-band lines and are likely background giants although these spectra are quite noisy due to the faintness of the objects. Source n2068-32 also shows some enhanced absorption features but the H-band profile remains triangular. Sources n2068-01, 05, 11, and 16 all exhibit weak potassium lines while simultaneously showing signs of youth (Paβ and/or triangular profiles). In NGC 2071, enhanced H-band absorption implies that n2071-48 and n2071-54 are likely background giants. Relative to all other objects, Sources n2071-46 and n2071-49 show significant potassium absorption, however, their KI lines are not quite as strong as expected for a true field dwarf. In addition, their H-band profiles remain somewhat triangular. I therefore classify these objects as having medium surface gravity – they may be foreground dwarfs or simply be older members of the cluster. Finally, I note that although it is classified as a low surface gravity object based on its H-band profile, n2071-14 does also exhibit weak K I absorption.

5.3.2.3 Spectroscopic Veiling and Comments on Individual Sources

A few sources require additional notes. The atomic absorption lines in n2071-01 and n2071-13 are weaker than expected based on the spectral types implied by the water absorption bands. This is usually taken to be evidence for continuum veiling by circumstellar material, which if strong enough can cause objects to appear earlier than their true spectral types. Consequently, the uncertainty in the spectral types for these two objects is larger than the rest of the sample, possibly by 1-2 subclasses (e.g. L05). In addition, n2071-01, n2071-09, n2071-11, n2071-13, n2071-31, and n2071-40 as well as n2068-01 all show a significant emission feature at 1.283μm. This feature is attributed to Paschen Beta (Paβ) emission and is indicative of ongoing disk accretion in these objects. Objects with Paβ emission are noted in Tables 5.4.1 and 5.4.1.

5.4 The Hertzsprung-Russell Diagram

In this section, I follow the procedures developed in Chapter 4 to derive extinction estimates, effective temperatures and bolometric luminosities for the 46 classified M stars in NGC 2068 and the 54 classified M stars in NGC 2071. I then place these objects on the H-R diagram and use pre-main sequence evolutionary models to infer masses and ages for all likely cluster members.

5.4.1 Extinction, Effective Temperatures, and Bolometric Luminosities

As in Chapter 4, extinctions towards each source were estimated using the intrinsic dwarf colors of Leggett (1992), Leggett et al. (1996), and Dahn et al. (2002) to calculate $E(J-H)$ and subsequently converting this color excess to A_V with the reddening law of Cohen et al. (1981). Spectral types were converted to effective temperatures using a linear fit to the temperature scale presented in Luhman et al. (2003b). Bolometric luminosities were derived by combining dereddened K-band magnitudes with a distance modulus of 8.0 (Anthony-Twarog, 1982) and the bolometric corrections of Leggett (1992), Leggett et al. (1996), and Dahn et al. (2002). These quantities are tabulated for each object in Tables 5.4.1 and 5.4.1.

Table 5–3. Data for Classified M Stars in NGC 2068

Source	J	H	K	A_V	M subclass	gravity	logT_{eff}	log(L/L$_\odot$)	Mass ($M_\odot$)	Comments
01	12.48	11.29	10.55	5.00	2.50	low	3.54	0.01	0.59	weak KI, Paβ emission
02	12.27	11.20	10.87	4.18	3.25	low	3.53	-0.18	0.44	
03	13.23	11.88	11.02	6.16	8.00	low	3.43	-0.33	0.03	
04	14.04	12.24	11.14	10.55	3.00	low	3.53	-0.05	0.49	
05	12.88	11.91	11.41	3.00	3.00	low	3.53	-0.43	0.45	weak KI
06	12.93	11.96	11.51	3.89	7.25	low	3.44	-0.58	0.04	
07	13.23	12.20	11.53	4.05	7.00	low	3.45	-0.57	0.04	
08	13.11	12.09	11.64	3.45	3.00	low	3.53	-0.50	0.42	
09	13.47	12.24	11.64	5.68	5.00	low	3.49	-0.49	0.15	
10	13.38	12.26	11.71	4.82	5.50	low	3.48	-0.57	0.12	
11	13.09	12.16	11.75	3.14	7.00	low	3.45	-0.69	0.04	weak KI
12	13.16	12.22	11.79	3.27	3.50	low	3.52	-0.59	0.36	
13	13.98	12.46	11.83	7.82	1.50	...	3.56	-0.37	0.68	
14	14.28	12.78	11.89	8.45	6.25	low	3.47	-0.53	0.07	
15	13.31	12.45	11.94	2.45	5.50	low	3.48	-0.74	0.12	
16	14.99	13.02	12.11	12.09	3.00	low	3.53	-0.38	0.46	weak KI
17	14.64	13.09	12.37	8.36	2.75	low	3.54	-0.61	0.43	
18	13.89	12.91	12.47	3.36	3.25	low	3.53	-0.85	0.34	
19	14.40	13.25	12.60	4.82	4.50	low	3.50	-0.89	0.22	
20	14.30	13.17	12.68	4.73	4.00	low	3.51	-0.91	0.26	
21	15.35	13.66	12.70	9.86	5.00	low	3.49	-0.76	0.15	
22	14.90	13.47	12.71	7.43	4.75	low	3.50	-0.85	0.20	
23	14.33	13.29	12.74	3.89	4.75	low	3.50	-0.99	0.20	
24	14.06	13.18	12.75	2.50	5.00	low	3.49	-1.05	0.17	
25	13.79	13.17	12.97	0.00	1.25	...	3.57	-1.10	0.58	
26	17.36	14.77	13.08	18.05	5.00	...	3.49	-0.62	0.15	
27	16.50	14.63	13.16	11.50	5.00	low	3.49	-0.89	0.16	
28	14.78	13.87	13.24	3.05	5.75	low	3.48	-1.25	0.10	
29	16.02	14.26	13.24	10.82	6.25	low	3.47	-0.99	0.07	
30	14.78	13.84	13.25	3.36	6.25	low	3.47	-1.26	0.07	
31	16.14	14.52	13.26	9.40	7.75	low	3.43	-1.10	0.03	
32	16.84	14.54	13.27	15.27	4.50	...	3.50	-0.78	0.22	
33	15.45	14.26	13.50	5.45	5.50	...	3.48	-1.26	0.12	
34	14.95	14.12	13.62	3.00	7.50	low	3.44	-1.46	0.03	
35	14.51	13.82	13.63	0.55	2.75	high	3.54	-1.40	...	KI present
36	16.72	14.71	13.66	12.27	1.75	...	3.56	-0.95	0.56	
37	16.64	14.89	13.80	10.61	6.75	low	3.46	-1.24	0.05	
38	15.60	14.63	14.04	4.27	7.50	low	3.44	-1.59	0.03	
39	16.43	15.29	14.47	5.82	7.50	low	3.44	-1.70	0.03	
40	16.80	15.27	14.48	7.91	1.50	...	3.56	-1.43	0.50	
41	16.23	15.13	14.74	4.09	2.25	giant	3.55	-1.69	...	
42	16.22	15.34	14.77	2.70	6.75	...	3.46	-1.91	0.05	
43	17.51	16.04	15.49	7.55	2.50	giant	3.54	-1.88	...	
44	17.42	16.28	15.55	4.18	8.50	low	3.41	-2.23	0.02	
45	17.17	16.23	15.66	2.36	8.50	low	3.41	-2.34	0.02	
46	18.18	16.80	15.85	6.09	9.00	low	3.40	-2.30	0.02	

Table 5–4. Data for Classified M Stars in NGC 2071

Source	J	H	K	A_V	M subclass	gravity	logT_{eff}	log(L/L$_\odot$)	Mass ($M_\odot$)	Comments
01[a]	10.23	9.02	8.32	5.00	1.50	...	3.562	0.932	0.77	Paβ emission, veiling
02	12.79	11.15	10.53	9.50	3.25	low	3.529	0.147	0.44	
03	12.09	10.95	10.56	4.95	3.75	low	3.519	-0.043	0.34	
04	12.92	11.29	10.57	9.00	3.00	...	3.534	0.128	0.49	
05	12.29	11.08	10.64	5.45	4.00	low	3.514	-0.065	0.29	
06	12.35	11.10	10.70	5.55	2.50	...	3.544	-0.036	0.59	
07	11.98	10.99	10.72	3.14	2.50	low	3.544	-0.130	0.59	
08	13.60	11.81	10.81	11.00	3.50	low	3.524	0.084	0.39	
09	15.14	12.52	10.94	18.55	3.50	low	3.524	0.303	0.39	Paβ emission
10	13.03	11.70	11.20	6.27	3.00	...	3.534	-0.222	0.49	
11	14.57	12.37	11.28	14.27	3.25	...	3.529	0.030	0.44	multiple emission lines
12	13.47	11.97	11.32	7.64	1.00	...	3.571	-0.157	0.82	
13	14.02	12.48	11.35	8.27	2.75	...	3.539	-0.208	0.54	multiple emission lines, veiling
14	12.88	11.92	11.46	3.09	4.50	low	3.504	-0.495	0.20	weak KI
15	13.54	12.28	11.52	6.02	5.25	low	3.488	-0.439	0.13	
16	13.12	12.00	11.57	4.77	3.75	low	3.519	-0.453	0.34	
17	13.86	12.47	11.79	7.00	4.50	low	3.504	-0.486	0.20	
18	13.31	12.32	11.81	3.41	4.25	low	3.509	-0.615	0.24	
19	13.70	12.49	11.91	5.36	4.50	low	3.504	-0.593	0.20	
20	13.45	12.36	11.94	4.32	4.25	low	3.509	-0.635	0.24	
21	15.28	13.20	12.09	13.36	4.00	low	3.514	-0.360	0.29	
22	14.03	12.78	12.23	5.82	3.25	low	3.529	-0.661	0.36	
23	18.79	14.61	12.25	32.18	2.50	...	3.544	0.302	0.59	
24	14.52	13.10	12.41	7.55	5.50	low	3.483	-0.749	0.12	
25	15.93	13.77	12.46	13.32	8.75	low	3.406	-0.675	0.02	
26	16.05	13.80	12.50	15.91	7.50	low	3.437	-0.552	0.03	
27	14.21	13.04	12.56	5.09	3.25	low	3.529	-0.819	0.34	
28	15.56	13.81	12.64	10.09	2.75	...	3.539	-0.655	0.44	
29	15.26	13.68	12.66	9.00	5.50	low	3.483	-0.796	0.12	
30	15.12	13.46	12.67	9.82	3.50	low	3.524	-0.703	0.33	
31	15.76	13.98	12.70	10.36	2.25	...	3.548	-0.657	0.51	Paβ emission
32	14.54	13.40	12.72	4.86	5.00	low	3.494	-0.952	0.17	
33	16.21	14.01	12.75	14.70	6.75	low	3.455	-0.670	0.05	
34	14.66	13.43	12.77	5.61	4.75	low	3.499	-0.937	0.20	
35	14.49	13.47	12.92	3.91	5.50	low	3.483	-1.084	0.12	
36	14.65	13.50	12.93	4.95	5.00	low	3.494	-1.033	0.17	
37	17.11	14.62	12.97	17.09	4.00	...	3.514	-0.578	0.30	
38	16.08	14.16	13.07	11.82	5.00	low	3.494	-0.837	0.15	
39	17.39	14.74	13.14	18.59	5.00	...	3.494	-0.626	0.15	
40	16.22	14.47	13.25	10.55	5.50	low	3.483	-0.977	0.12	Paβ emission
41	16.27	14.29	13.46	12.43	4.75	low	3.499	-0.967	0.20	
42	15.48	14.31	13.69	5.41	5.75	low	3.478	-1.346	0.10	
43	15.03	14.22	13.70	2.43	7.25	low	3.443	-1.508	0.04	
44	16.11	14.41	13.72	9.45	1.00	...	3.571	-1.051	0.62	
45	16.66	14.90	13.75	10.91	6.00	low	3.472	-1.181	0.09	
46	15.01	14.42	14.20	0.00	5.00	medium	3.494	-1.719	...	KI
47	16.59	15.22	14.36	7.05	3.75	...	3.519	-1.487	0.24	
48	17.21	15.60	14.47	8.73	2.25	giant	3.548	-1.421	...	
49	16.68	15.48	14.69	5.34	4.75	medium	3.499	-1.715	...	KI
50	17.35	15.99	15.13	6.18	8.50	low	3.412	-1.988	0.02	
51	17.15	16.09	15.47	3.45	8.50	low	3.412	-2.222	0.02	
52	17.89	16.90	16.15	2.88	8.00	low	3.425	-2.498	0.03	
53	18.27	17.16	16.37	3.64	9.00	low	3.400	-2.599	0.02	
54	17.35	16.65	16.45	0.55	3.00	giant	3.534	-2.529	...	

[a]Source 01 was saturated in the FLAMINGOS images. Consequently, we use photometry from the 2MASS source 2MASS_J054707+001931 for this object.

[b]Sources 46 and 49 have significant KI absorption, however, they also show triangular H-band profiles thus we hestitate to classify them as field dwarfs - rather we classify them as intermediate surface gravity objects.

5.4.2 H-R Diagrams for NGC 2068 and NGC 2071

H-R diagrams for NGC 2068 and NGC 2071 are shown in Figures 5–8 and 5–9. As with NGC 2024, I have elected to display two sets of diagrams for each cluster: the diagrams on the left in each figure are shown with the evolutionary models of DM97, diagrams on the right are shown with the models of BCAH98 and Chabrier et al. (2000, hereafter known collectively as the Lyon models). In all cases, diamonds are objects classified using 4 m spectra, triangles are objects classified from 2.1 m spectra, asterixes are sources identified as likely background giants and solid dots are potential foreground dwarfs. A representative error bar for an M5 object is shown in the lower left corner.

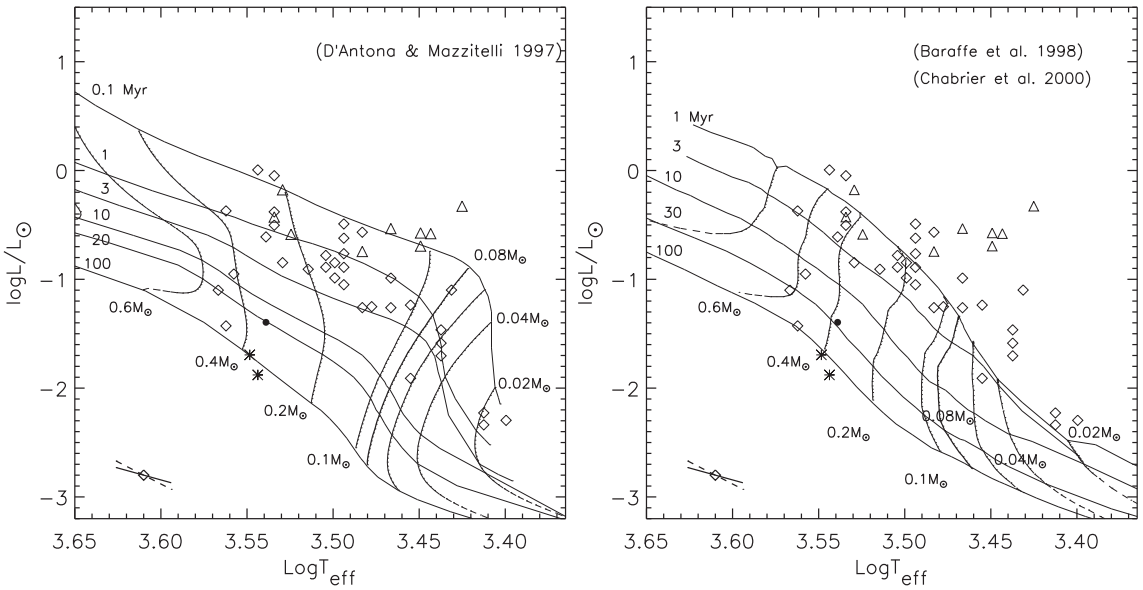

Figure 5–8. H-R diagrams for NGC 2068 shown with the pre-main sequence models of DM97 (left) and the Lyon models (right). The diamonds are objects classified using 4 m spectra and the triangles are sources classified from 2.1 m spectra. Asterixes represent background giants and the solid dot is a foreground dwarf. Representative error bars for an M5 object are shown. The solid line accounts for errors in derived spectral type, distance modulus, and photometry and the dashed line incorporates an additional uncertainty in A_V of ± 3 magnitude (§4.4).

Mass and age estimates are derived for all likely cluster members (see §5.5.1) by interpolating between the isochrones and mass tracks plotted in Figures 5–8 and 5–9. It has been shown that the Lyon group models are in better agreement with observational

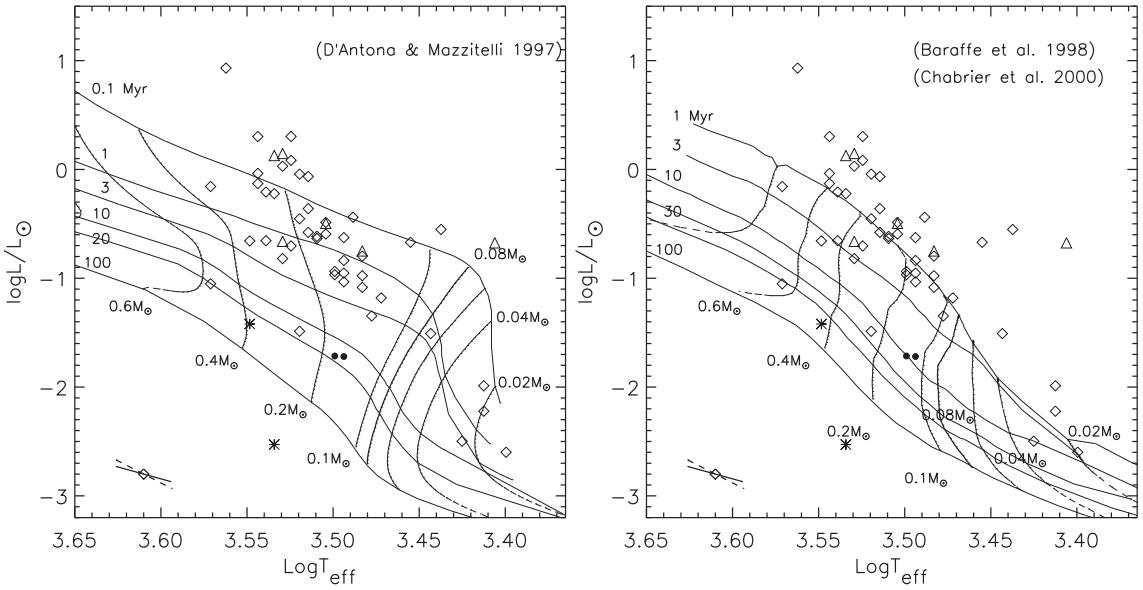

Figure 5–9. H-R diagrams for NGC 2071. Symbol definitions are predominantly the same as in Figure 5–8, however, in this case, the solid dots represent the medium surface gravity objects (§5.3.2.2)

constraints (Chapter 4 and references therein), thus, while I present diagrams using the DM97 models, for the remaining discussion I will focus primarily on results obtained using the Lyon tracks. In the H-R diagrams for both clusters, many objects fall above the youngest isochrone (1 Myr). These objects are assumed to have an age $<$1 Myr and are then dropped down to the 1 Myr isochrone along a line of constant effective temperature to derive a mass estimate. For all other objects, their actual positions on the H-R diagram are used to derive age and mass estimates. In this manner I derived masses spanning a range from 0.02 to 0.68 $M_{\odot}$ (with 16 objects falling below the HBL) and ages ranging from $<$1 to $\sim$100 Myr for NGC 2068. Masses derived for objects in NGC 2071 range from 0.02 to 0.82 $M_{\odot}$ (with 8 objects falling below the HBL) with ages ranging from $<$1 to $\sim$35 Myr.

5.5 Low Mass Populations of NGC 2068 and NGC 2071

5.5.1 Cluster Membership

Classified stars in both clusters must fall into one of three categories: foreground sources, cluster members, or background stars. Ultimately, in order to investigate the

properties of the star forming cluster populations, we must eliminate the objects which do not appear to be typical members of either NGC 2068 or NGC 2071.

In order to distinguish between cluster members and non-members, I have employed a combination of spectroscopic and photometric techniques. First, using the surface gravity assessment in §5.3.2.2, objects in 5.4.1 and 5.4.1 with gravity designations of *low* are taken to be cluster members. In addition, sources with significant Paβ emission are also assumed to be members. Sources with gravity designations of *high* or *giant* are assumed to be foreground or background sources and excluded from further analysis. Although, the two objects in NGC 2071 with gravity designations of *medium* may be young sources, upon examining their position in the H-R diagrams in Figure 5–9, it is clear that they are segregated from the bulk of the cluster population. Consequently, I have chosen to remove them from the general membership sample.

There are 8 sources in NGC 2068 and 9 sources in NGC 2071 with no spectroscopic indicators of membership. In these cases we turned to the photometrically derived extinction measurements (§5.4.1) to determine membership status. Figures 5–10 and 5–11 show the distribution of visual extinctions for the classified M stars in each cluster. The distribution for NGC 2068 peaks at $A_V \simeq 4.5$ with a mean value of 6.1 magnitudes; for NGC 2071 the peak is slightly higher at $A_V \simeq 5.5$ with an additional population having even larger extinctions as indicated by the mean value of 8.3 magnitudes. Indeed, looking at the histogram of A_V for NGC 2071, there is a secondary peak around $A_V \simeq 10$. At the distance of the clusters (d$\sim$400 pc, Anthony-Twarog, 1982), only objects with $A_V < 1$ can be foreground sources as the line of sight extinction to the molecular cloud is <1. This qualification rules out all but one of the 17 objects under consideration - source n2068-25 has an A_V of 0.0, making a likely candidate for a foreground object. Indeed, looking at the H-R diagrams, n2068-25 lies along the same isochrone as the spectroscopic field dwarf n2068-35 thus I exclude it from further analysis.

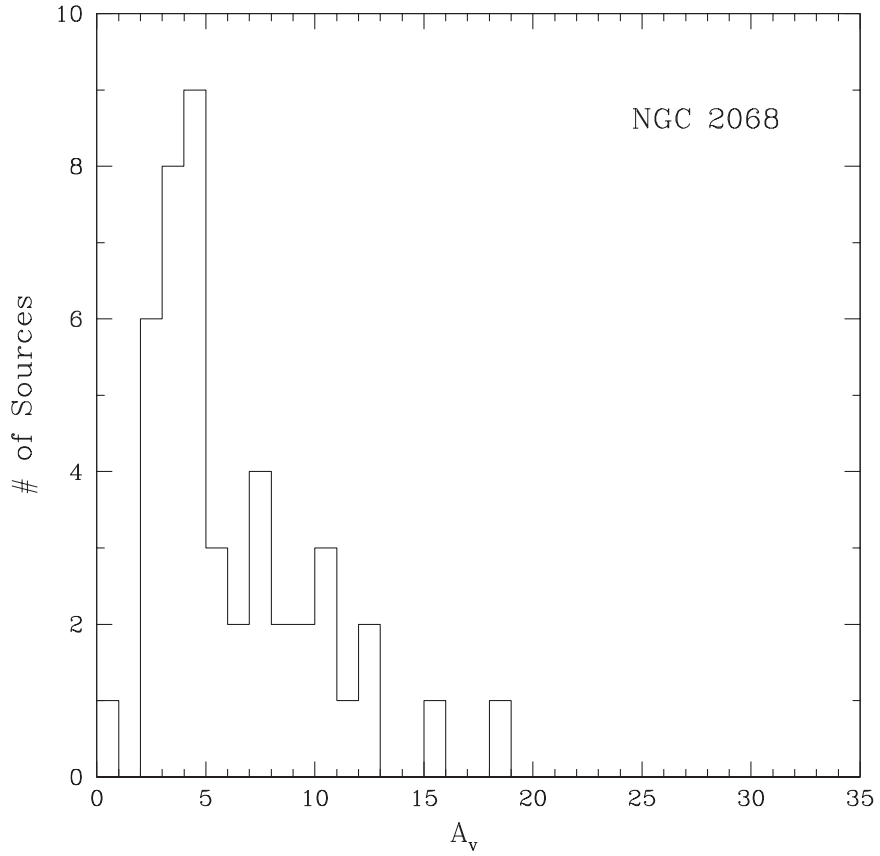

Figure 5–10. Distribution of A_V for M Stars in NGC 2068. All extinction values were derived photometrically using the methods described in Chapter 4, §4.4.1.

The remaining 15 sources must either be cluster members or background objects. Sources with extinctions >1 and a position above the main sequence in the H-R diagram cannot be background dwarfs since dwarf luminosities as seen through the cloud would place them below the main sequence. The only remaining possibility other than cluster membership is that these sources are background giants. However, as discussed in §5.3.2.2 I am confident that all of the objects with incomplete gravity assessments are not giants, therefore they must be cluster members. This yields a final sample of 42 likely members in NGC 2068 and 50 likely members in NGC 2071.

Finally, when looking at the positions of the classified sources in the color-magnitude and color-color (Figure 5–2 and 5–3), there are 2 objects in each cluster which appear to be on the main sequence rather than the 1 Myr isochrone in the CMDs

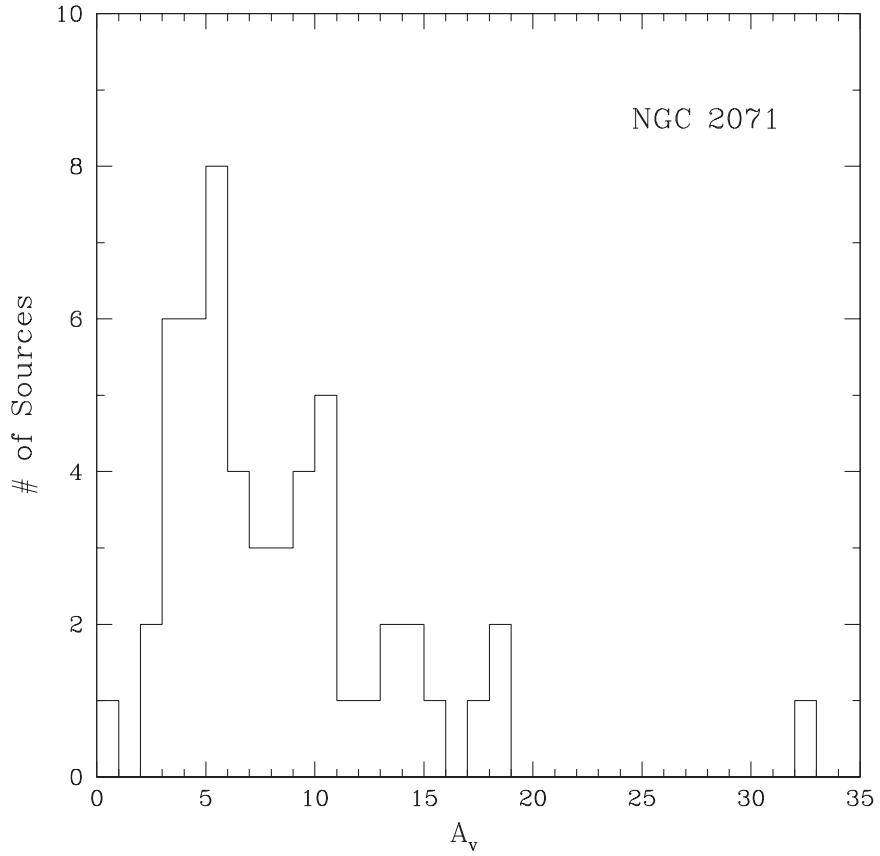

Figure 5–11. Distribution of A_V for M Stars in NGC 2071.

and lie on the unreddened dwarf/giant sequence in the color-color diagrams. In all cases, these are objects which I have already excluded from the membership samples: n2068-25, n2068-35, and n2071-46 are likely foreground dwarfs and n2071-54 was identified as a giant. Based on these results, I am confident that all objects remaining in the final sample are cluster members.

5.5.2 Cluster Ages

Taking the membership samples derived above, I now determine a median age for each cluster. As with NGC 2024, the H-R diagrams for NGC 2068 and NGC 2071 show a spread of ages ranging from $<$1 Myr to $>$30 Myr, however, the median age of the cluster members classified here should be representative of the true median age of the M star populations in these regions.

Using the Lyon group models (the right-hand diagrams in Figures 5–8 and 5–9), the median age of the classified members in both clusters is <1 Myr. Although the Lyon models are the preferred PMS tracks for deriving ages and masses (§5.4.2, these results do not allow for a comparison of young cluster ages since the ages of NGC 2024, NGC 2068, and NGC 2071 are all constrained to the same upper limit. Consequently, as in Chapter 4 I use the DM97 models to derive a detailed age estimate for all cluster members within the boundaries of the isochrones. The median age of NGC 2068 computed from the DM97 models is 0.9 Myr. The error on this value as indicated by a computation of the standard error of the median yields a possible range of ages from 0.6-1.2 Myr. For NGC 2071, the median age of the classified members is 0.4 Myr and the range of possible ages indicated by the standard error of the median is 0.3-0.6 Myr. Note that the standard errors of the median were computed in log space as the isochrones are logarithmic on the H-R diagram.

The DM97 ages for both clusters are consistent with the <1 Myr estimate derived from the Lyon models. In other words, both NGC 2068 and NGC 2071 appear to be very young. In addition, while it is only a 1 sigma effect, it is possible that N2071 is younger than NGC 2068 by ∼0.5 Myr. There is some concern that the apparent youth of the brown dwarf population in both clusters is a selection effect caused by our inability to detected older, low mass objects (e.g. Chapter 4, §4.5.2) and that these objects subsequently skew the median age estimates towards younger values. Consequently, I have also derived the median age for NGC 2068 and NGC 2071 excluding objects with masses M<0.08$M_{\odot}$. The median age of the stellar population in NGC 2068 remains at 0.9 Myr with a slightly larger error range from 0.6-1.3 Myr. The median age of stellar sources in NGC 2071 is surprisingly younger than the previous estimate, having a value of 0.3 Myr with 1 σ uncertainty range of 0.2-0.5 Myr. Myr.

Further discussion of these results and comparisons with other young clusters, including NGC 2024, can be found in Chapter 6.

5.5.3 Spatial Distribution of Sources

Figures 5–12 through 5–15 present the spatial distribution of all classified M stars in NGC 2068 and NGC 2071. Source positions as a function of age are shown in Figures 5–12 and 5–14. In these plots, open circles are sources with ages >1 Myr, filled triangles are sources with age <1 Myr and the crosses are objects identified in §5.5.1. In addition, the dotted line in Figure 5–12 represents the $10' \times 10'$ 4 m FLAMINGOS field centered on NGC 2068. The four sources which fall outside this boundary were classified from 2.1 m spectra. This subdivision is not necessary for NGC 2071 because all classified 2.1 m sources fell within the boundaries of the 4 m field. Source positions as a function of mass are shown in Figures 5–13 and 5–15. In these figures, open circles are objects with M>0.08 $M_{\odot}$, stars are objects with M<0.08 $M_{\odot}$, and the crosses are the non-members. The dotted region in Figure 5–13 is the 4 m field described above. Note that all ages and masses for this analysis are derived from the Lyon tracks (recall that these ages remain consistent with those of DM97).

In NGC 2068, the distribution of young sources in the southern part of the field appears to be slightly skewed towards the western part of the cluster. However, for the more extended cluster region the young sources appear to be randomly distributed with respect to the rest of the classified population. This is in contrast to NGC 2071 where the young population is extended across the entire region, with a slight elongation along the north-south direction. In addition, it is interesting to note that in NGC 2071 many of the young sources have extinctions in excess of 10 magnitudes. This is not the case for NGC 2068.

Looking at source positions as a function of mass, it would appear that in NGC 2068 the location of the brown dwarfs roughly follows the distribution of the youngest sources, with the brown dwarfs clustered towards the west. This effect can also be seen in the H-R diagram for NGC 2068 (Figure 5–8, right) where there is only one object classified as a brown dwarf with an age >1 Myr. In NGC 2071, on the other hand, there are far fewer

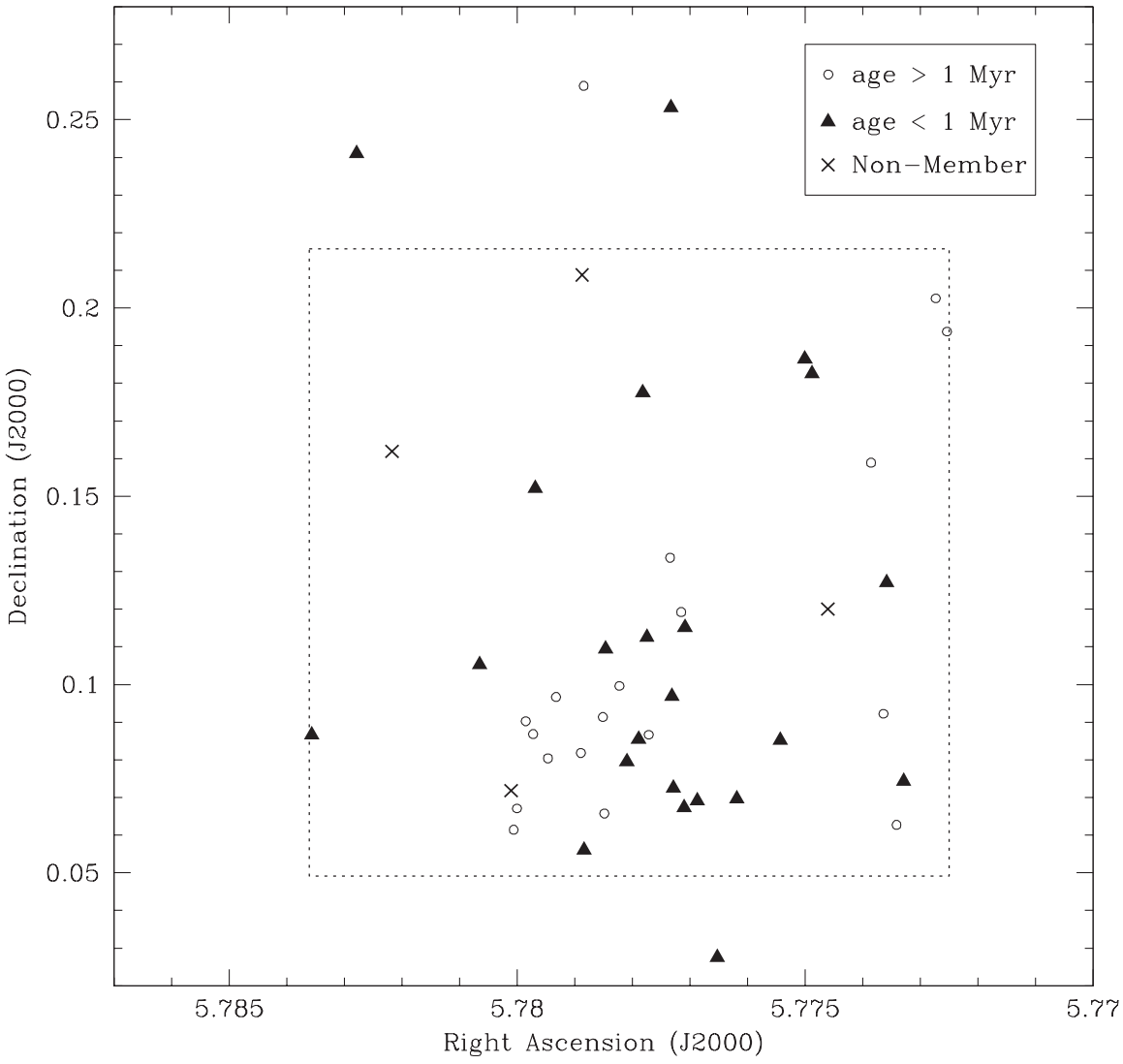

Figure 5–12. Location of classified sources in NGC 2068 as a function of age. Open circles are all sources with ages >1 Myr, filled triangles are sources with ages <1 Myr, and the crosses are the sources identified in §5.5.1 as non-members. The region enclosed by the dotted line represents the FLAMINGOS 4 m field centered on NGC 2068.

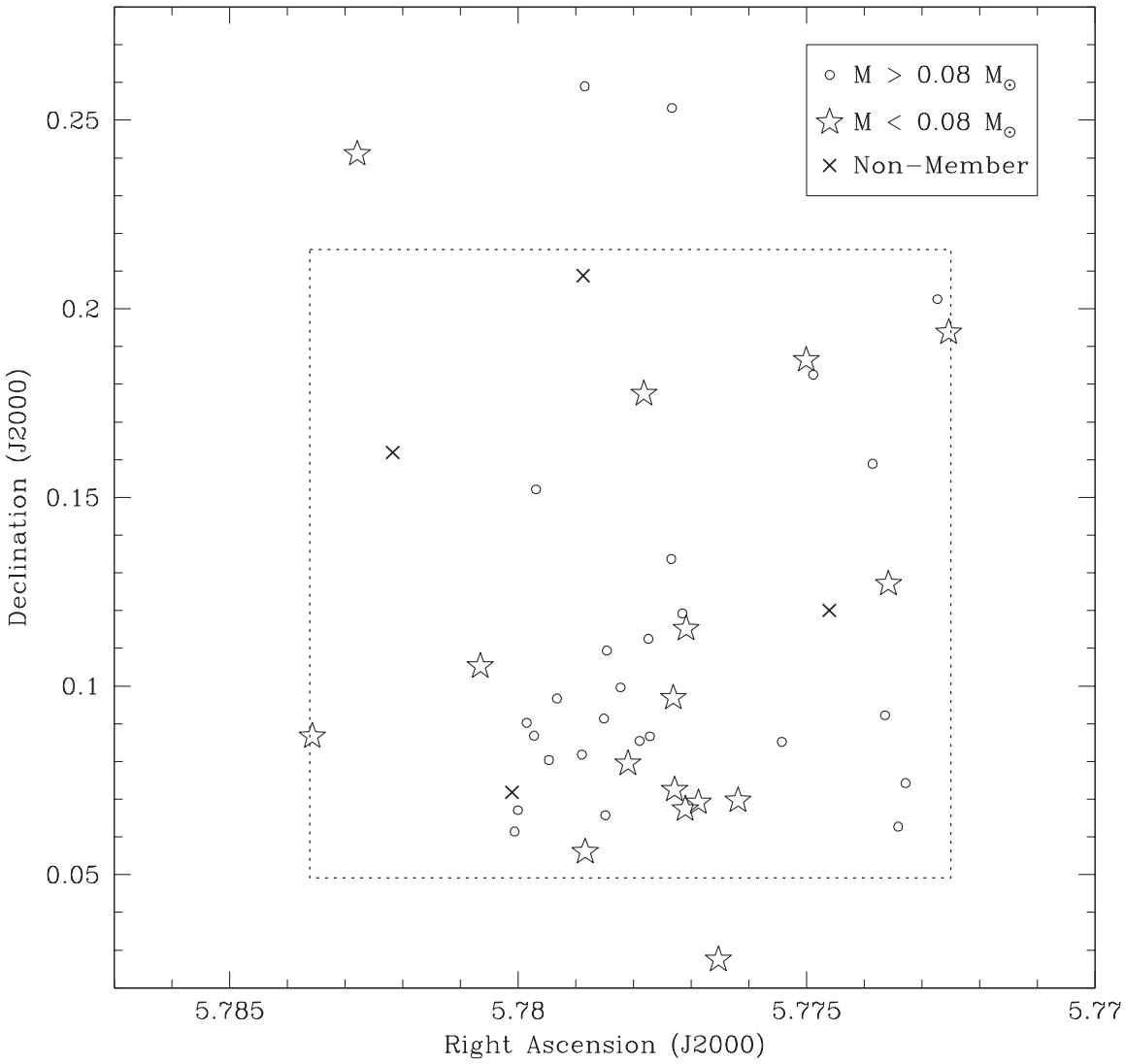

Figure 5–13. Location of classified sources in NGC 2068 as a function of mass. Open circles are all sources with masses M>0.08$M_{\odot}$, stars are sources with masses M<0.08$M_{\odot}$, and crosses represent the non-members. The dotted line is the FLAMINGOS 4m field centered on NGC 2068.

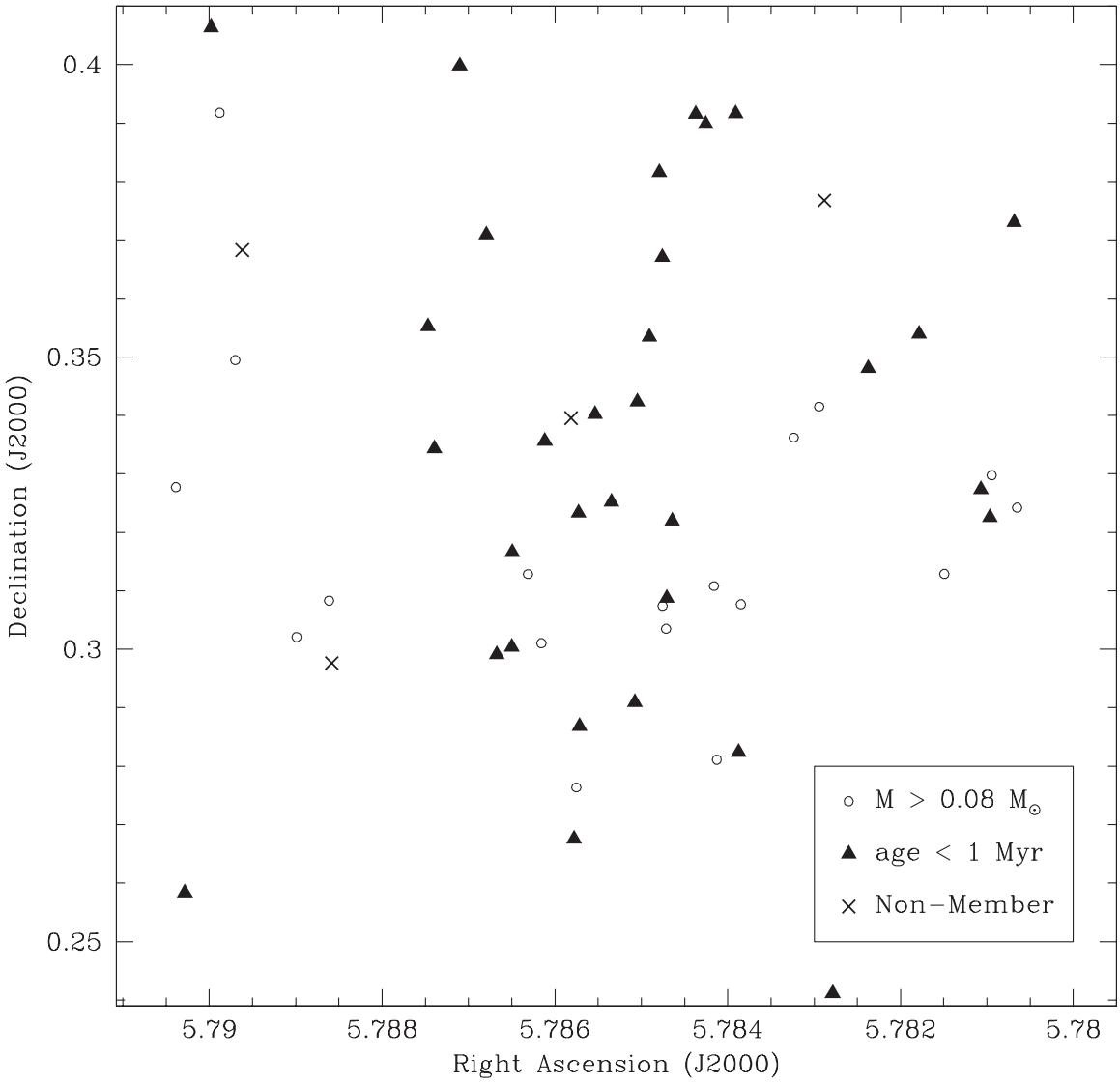

Figure 5–14. Location of classified sources in NGC 2071 as a function of age. Symbol definitions are the same as in Figure 5–12.

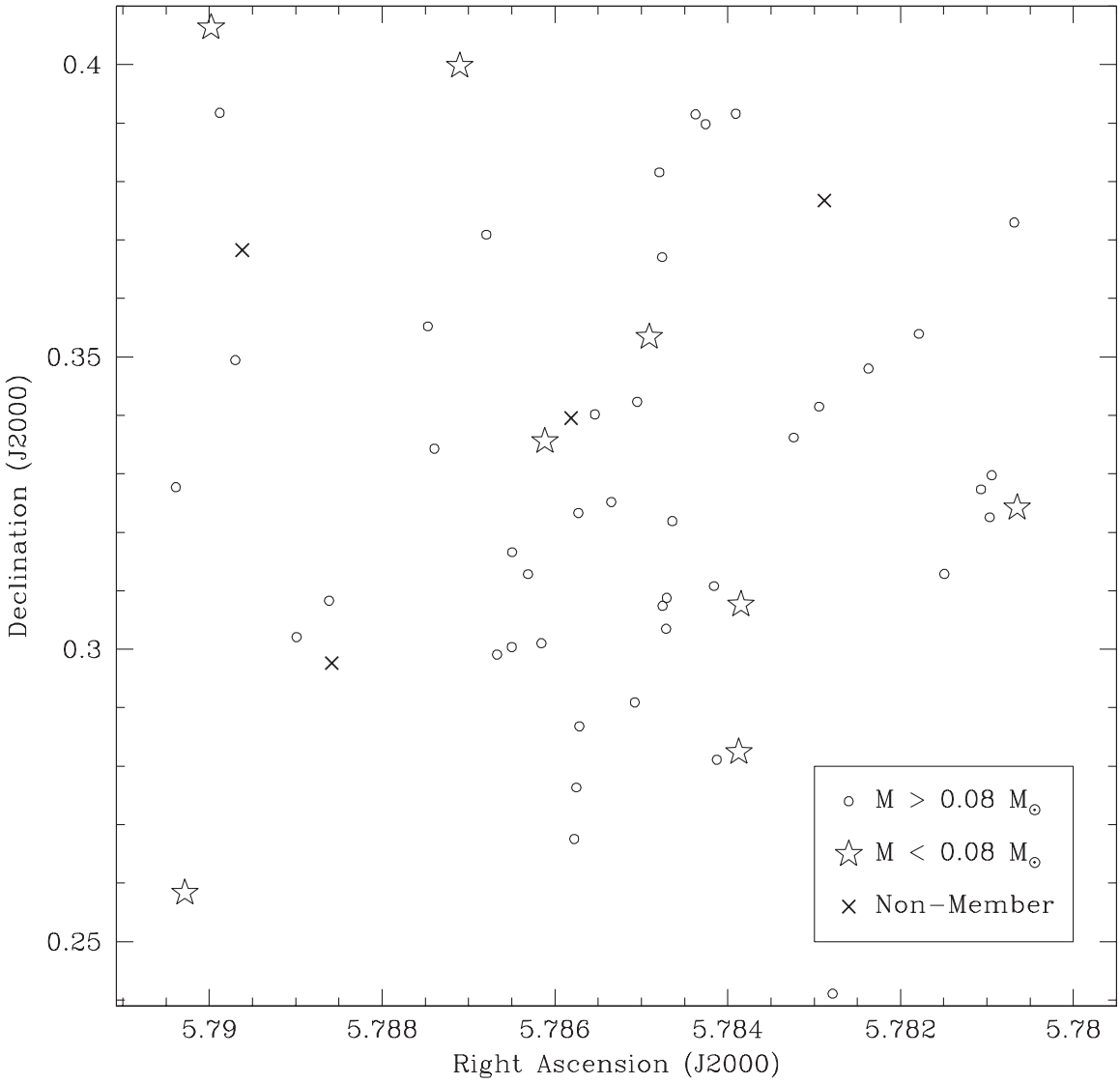

Figure 5–15. Location of classified sources in NGC 2071 as a function of mass. Symbol definitions are the same as in Figure 5–13.

brown dwarfs and those that are present are roughly evenly distributed throughout the region (although again, most of the brown dwarfs do have ages $<$1 Myr).

5.5.4 Infrared Excess and Substellar Disk Fractions

As discussed in Chapter 4, the presence of excess flux in the near infrared is commonly taken to be an indicator of thermal emission by warm dust in a circumstellar disk. In order to assess the the likelihood of disks around sources in NGC 2068 and NGC 2071, I have calculated the infrared excess fractions for both clusters in the same manner as for NGC 2024 (e.g. via a comparison of each cluster member's expected intrinsic $H-K$ color with its dereddened observed $H-K$ color). In NGC 2068, 21 out of 42 sources exhibit some level of excess, yielding an overall IRX fraction of 50%$\pm$13%. In NGC 2071, 20 out of 50 cluster members exhibit an infrared excess, yielding an IRX fraction of 40%$\pm$11%. Considering just the substellar population of each region, 8 out 16 brown dwarfs in NGC 2068 exhibit an *HK* excess and 2 out of 8 brown dwarfs in NGC 2071 exhibit an *HK* excess, yielding substellar IRX fractions of 50%$\pm$22% and 25%$\pm$20% for NGC 2068 and NGC 2071 respectively. Note that all quoted errors are derived from Poisson statistics. For comparison, the IRX fractions calculated in Chapter 4 for NGC 2024 were 40%$\pm$9% for the general cluster population and 39%$\pm$15% for the brown dwarfs. The implications of these disk fractions will be discussed further in Chapter 6.

5.5.5 Initial Mass Functions for M Stars in NGC 2068 and NGC 2071

In this section I derive the low mass initial mass functions for NGC 2068 and NGC 2071. This is accomplished by examining the photometric *K*-band luminosity functions of both clusters and correcting for the presence of background sources, assessing and correcting for the incompleteness of the spectroscopic samples, and constructing an M star mass function for each region.

5.5.5.1 Young Cluster Luminosity Functions and the Contribution of the Stellar Background

As discussed in Chapter 4, prior to determining the IMF of a young cluster it is important to ensure that the contributing sources are representative of the overall cluster population. Figure 5–16 shows both the spectroscopic and photometric *K*-band luminosity functions for the 4 m FOV in NGC 2068 and NGC 2071. While I am confident that all spectroscopic sources in the current samples are in fact cluster members, it is clear from both plots that neither spectroscopic sample is a complete census of its parent cluster. Thus, as with NGC 2024, a completeness correction from the photometry is required. However, there is a critical difference between the photometric KLFs presented here and the KLF of NGC 2024 (Figure 4–8) - namely the significance of the stellar background.

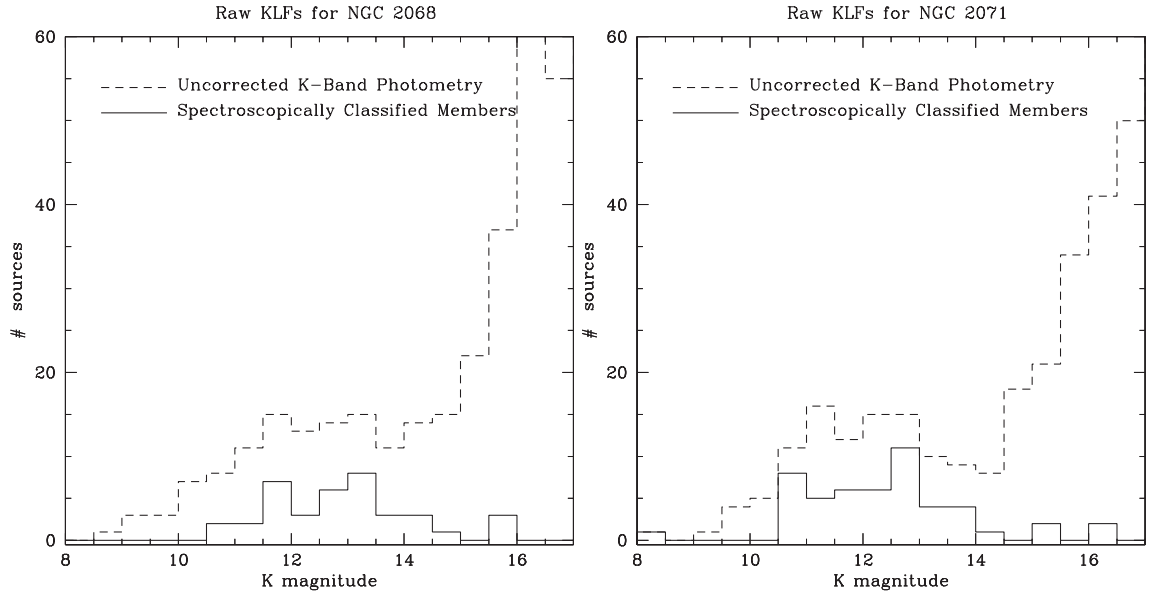

Figure 5–16. Uncorrected *K*-Band Luminosity Functions for NGC 2068 and NGC 2071, shown with the KLFs of spectroscopically classified M stars. Both KLFs are shown for the boundaries of the 4 m field only. In both clusters the number counts in the photometry shoot up between *K*=14-15, indicating the presence of a large background population.

Looking at the left-hand panel of Figure 4–8, the raw photometric luminosity function does not begin to rise steeply (indicating the presence of background sources)

until $K \simeq 16$. Once an extinction limit has been applied (Figure 4–8, right) the background contribution is further minimized and effectively negligible down to the spectroscopic limit of $K \simeq 15.0$. On the other hand, the photometric luminosity functions in Figure 5–16 both begin to rise in the vicinity of K=14.0-14.5, nearly two magnitudes brighter than in NGC 2024. This effect can be explained by the lower density of cloud material in the regions surrounding NGC 2068 and NGC 2071 (e.g. Lada et al., 1991a; Aoyama et al., 2001) allowing the light from background stars to shine through. The reduced amount of extinction in NGC 2068 and NGC 2071 coupled with smaller but deeper samples means that a simple application of an extinction limit will not suffice to remove the background contribution. Rather, this population must be accounted for *prior to* estimation of the spectroscopic completeness limits to avoid over-correction.

Recall that as part of the FLAMINGOS/Orion B imaging survey, data were obtained for a number of off-cloud control fields. The purpose of these data is to account for the specific distribution of background field stars at the galactic latitude of Orion B. Figure 5–17 shows the average K-band luminosity function for control fields 1-4 (thick histogram), scaled to the 4 m field size of 10 arcminutes. For comparison, the KLF for a 2MASS field centered on the coordinates of control field 1 is also shown (thin histogram) and the number counts agree to within 1 σ down to K=15.0, where 2MASS photometry becomes very uncertain and incomplete.

The distribution of background sources estimated from the control fields can theoretically be subtracted from the raw KLFs shown in Figure 5–16 to yield new KLFs containing only the statistical contribution from cluster members. However, without accounting for the reddening within the molecular cloud itself, direct subtraction of an unreddened background distribution will result in an over-correction. Given that the cloud material in Orion B acts as a screen in front of the background, before subtracting the background KLF from the cluster luminosity functions, this KLF must be reddened by the amount of extinction present in the specified region of the cloud. The mean A_V

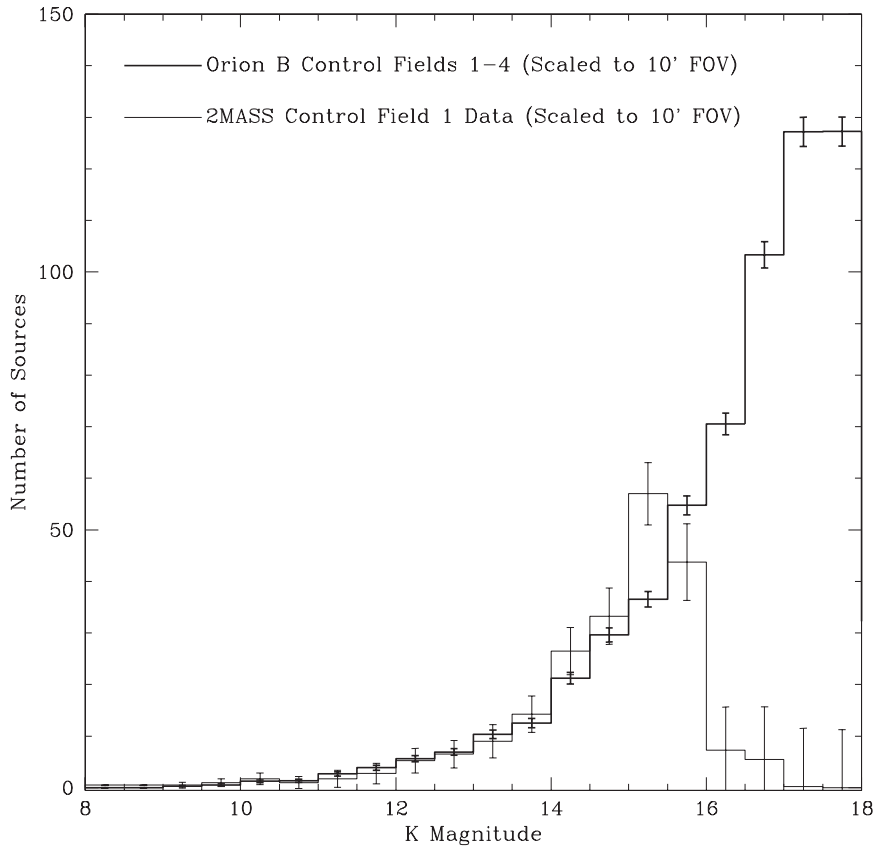

Figure 5–17. Average KLF for Orion B control fields 1-4 (thick line), scaled to 10 arcminutes, shown with the KLF for the 2MASS field centered on control field 1 (thin line). Error bars in both cases are Poisson errors propagated to account for the averaging and scaling of the histograms.

for the spectroscopic samples in NGC 2068 and NGC 2071 are 6.1 and 8.3 magnitudes respectively. However, recall that all classified spectra are relatively bright in J and H. Consequently, the reddest sources in each cluster are preferentially excluded from the mean A_V calculations, implying that these values are not necessarily representative of the true line-of-sight extinction through the cloud. A more appropriate extinction estimate is a mean value derived from longer wavelength photometry of all objects in the field, thereby allowing the entire range of A_V to be sampled.

I have recalculated the extinction values for each cluster using the H and K photometry from the imaging survey coupled with the NICE technique for determining extinctions (Lada et al., 1994). The basic idea of NICE is very similar to the methods used earlier in

this thesis (e.g. §4.4.1 and §5.4.1), where extinctions were calculated using the difference between observed and intrinsic $J-H$ colors to determine the color excess and then converting to A_V using a reddening law. The major difference is that NICE is a purely photometric technique, thus rather than using intrinsic colors based on spectral type, the intrinsic $J-H$ or $H-K$ colors are drawn from the control field photometry. Using the NICE technique and incorporating the H and K photometry for all possible sources in the 10 arcminute fields centered on each cluster yields new mean extinction estimates for NGC 2068 and NGC 2071 of 9.7 and 11.3 magnitudes, respectively. While these values are still single estimates for a patchy region in a molecular cloud, they are preferable to an estimate derived solely from J and H photometry.

Figures 5–18 and 5–19 show both the reddened control field histograms (reddened by the mean extinctions derived above) and the final background-subtracted luminosity functions along with the KLFs of the spectroscopically classified M stars. Error bars shown are the counting errors in both histograms. Looking at the background-subtracted KLFs it is clear that the completeness of both spectroscopic surveys is much improved, particularly at the faint end.

5.5.5.2 Completeness of the Spectroscopic Surveys

As mentioned above, prior to contructing the spectroscopic mass functions for each cluster it is critical to assess and correct for the incompleteness of the spectroscopic samples. Recall from Chapter 4 that this correction is calculated by examining the difference between the photometric and spectroscopic KLFs, adding sources to the incomplete magnitude bins according to the object mass distribution in those bins. Caution must be used, however, because if certain bins in the spectroscopic KLF are not well populated, it is possible to inadvertantly over-correct for the masses represented in those bins and under-correct for the masses not present. To minimize this problem, I have included an additional sample of sources in the spectroscopic luminosity function which are part of the bright star survey of Orion B (Chapter 2, §2.4.1 Hernandez, 2006).

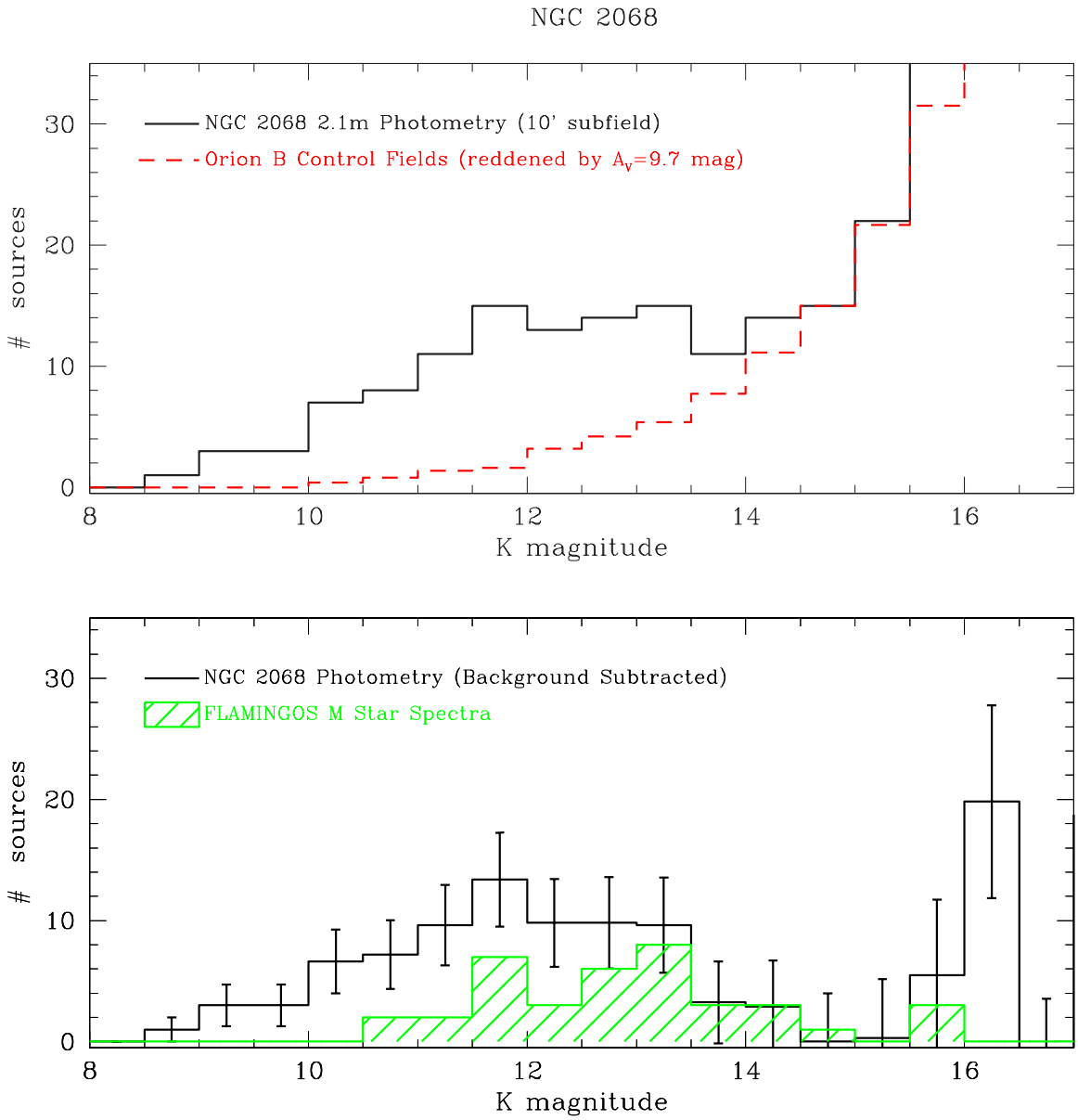

Figure 5–18. Background subtracted KLF for NGC 2068. The top panel shows the uncorrected luminosity function for the cluster (solid line) along with background distribution from Figure 5–17 (dashed line), reddened by 9.7 magnitudes of A_V. The bottom panel shows the background-subtracted photometry with Poisson error bars (solid line) and the KLF of the 42 classified members of NGC 2068 (shaded histogram).

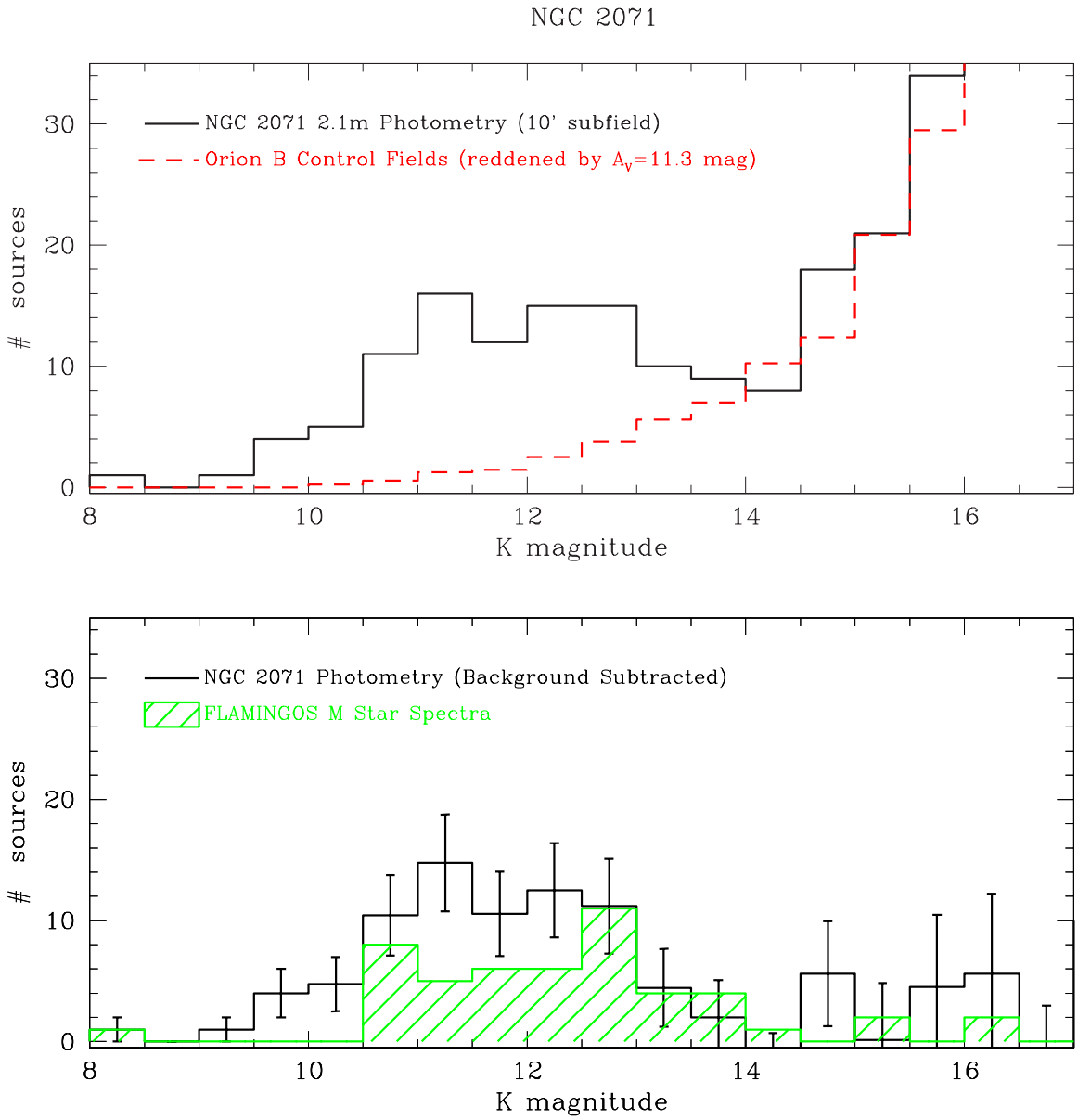

Figure 5–19. Background subtracted KLF for NGC 2071. The top panel shows the uncorrected luminosity function for the cluster (solid line) along with background distribution from Figure 5–17 (dashed line), reddened by 11.3 magnitudes of A_V. The bottom panel shows the background-subtracted photometry with Poisson error bars (solid line) and the KLF of the 50 classified members of NGC 2071 (shaded histogram).

Although these objects have not yet been classified, the spectra have been visually examined by multiple authors and assessed to be earlier than M. In addition, the bright magnitudes of these sources (the vast majority have $K<12.0$) makes it statistically unlikely for them to be background objects (*c.f.* the top panels of Figures 5–18 5–19), thus they are likely cluster members. Therefore, incorporating these sources into the spectroscopic KLFs will increase the overall completeness fractions (thereby reducing the size of the correction needed) without changing the statistics of the M stars or affecting the shape of the M star mass function.

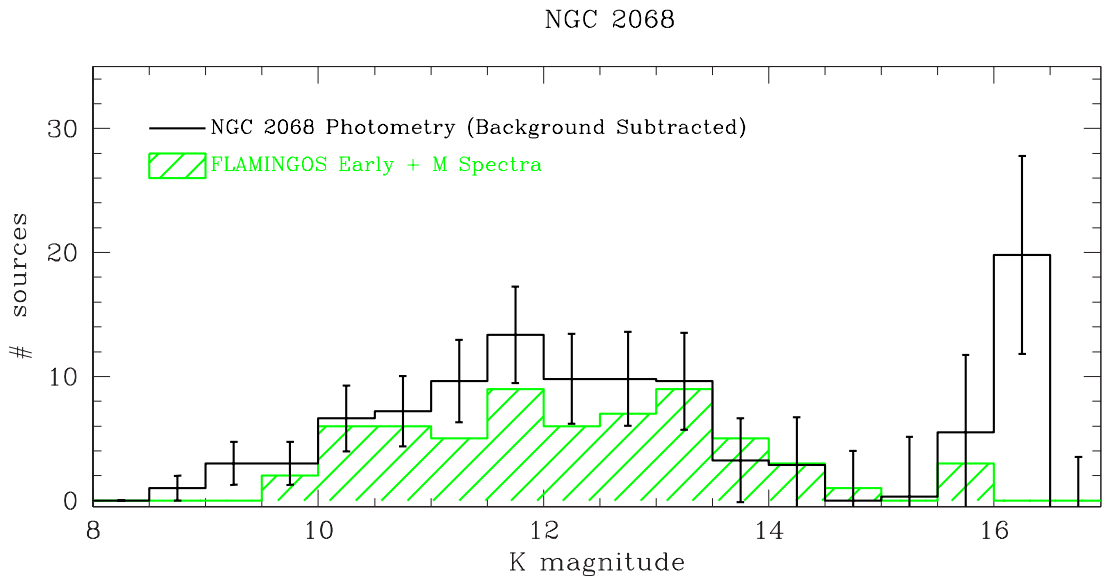

Figure 5–20. Completeness of NGC 2068 Spectra. The solid line is the background-subtracted KLF and the shaded histogram is the sum of the 24 early and 42 M star spectra.

Figures 5–20 and 5–21 show the background-subtracted luminosity functions for each cluster along with the newly combined spectroscopic KLFs. In NGC 2068, there are 38 classified members and 31 early-type spectra in the magnitude range $8.0<K<16.0$, with 24 early-type stars falling within the 4 m image boundaries for NGC 2068. Combining the two samples leaves only the bins from 8.5-9.5 and 11.0-13.0 with completeness fractions less than 80% down to K=15.0, however, only the bins having $K>10.5$ contain M stars. In NGC 2071, there are 50 classified members and 26 early-type

spectra in the magnitude range 8.0<K<16.5. Sixteen of the early-type stars fall within the boundaries of the NGC 2071 4 m field. Combining these sources with the M star KLF leaves only the bins from 9.5-10.5 and 11.0-12.5 with completeness fractions less than 90%, down to K=14.5. Once again, only the incomplete bins with K>10.5 contain M stars. Thus, to create the M star IMF for each cluster, I need only correct the NGC 2068 KLF in the range from 11.0<K<13.0 and NGC 2071 in the range from 11.0<K<12.5. In NGC 2068 this correction results in the addition of 16 sources to the mass function and in NGC 2071 the correction corresponds to the addition of 12 sources. Note that these corrections do not account for the incompleteness below K=14.5 (corresponding to a completeness limit of $\simeq$0.04 $M_{\odot}$for NGC 2071) or K=15.0 (mass completeness limit of $\simeq$0.035 for NGC 2068), however, this is a prudent course of action as the background subtraction at the faint ends of the KLFs is far more uncertain, as indicated by the size of the error bars associated with these bins. The effects of limiting the completeness correction will be discussed in the upcoming sections.

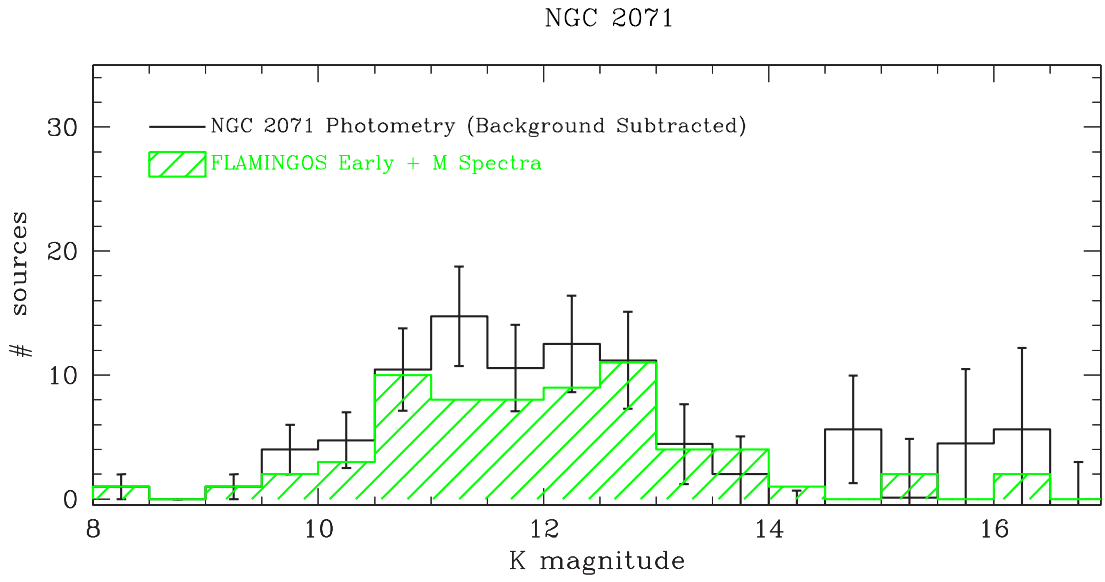

Figure 5–21. Completeness of NGC 2071 Spectra. The solid line is the background-subtracted KLF and the shaded histogram is the sum of the 26 early and 50 M star spectra.

5.5.5.3 Low Mass IMFs for NGC 2068 and NGC 2071

Figures 5–22 and 5–23 show the spectroscopically derived mass functions for NGC 2068 and NGC 2071, respectively. In both cases, the solid line is the IMF for all classified members of each cluster, shown with Poisson errors. The dashed lines represent the incompleteness-corrected mass functions using the small magnitude ranges specified above. The dotted lines, shown for comparison, are the mass functions corrected over the entire magnitude range of the spectroscopic samples.

The mass function for NGC 2068 peaks in the bin centered on Log(M/$M_{\odot}$)=-0.5, corresponding to a mass range of 0.2-0.5$M_{\odot}$. The IMF appears to slowly decline into the brown dwarf regime although the errors are also consistent with a flat IMF throughout the entire M star range. Neither incompleteness correction changes the overall shape of the mass function significantly, nor is there a significant difference between the two corrections until the mass range below $\sim$0.03 $M_{\odot}$is reached. At this point, the larger completeness correction (magnitude range from 9.5$<K<$16.0) increases the number of brown dwarfs present in the last bin. However, looking at Figure 5–20, the faint bins of the background-subtracted KLF have very large errors associated with them. The bin centered on K=15.75 is responsible for the bulk of the additional low mass correction and it is not clear that a correction should even be applied to this bin. Consequently, very little weight (if any) should be placed on the low mass end of the dotted IMF in Figure 5–22. Note that the same caveat applies to the dotted incompleteness-corrected IMF for NGC 2071.

The mass function for NGC 2071 peaks in the same bin as that of NGC 2068 (mass range from 0.2-0.5$M_{\odot}$), however, the peak is more pronounced for NGC 2071 and the incompleteness correction acts to increase its significance. In addition, the IMF for NGC 2071 exhibits a strong deficit of objects at or below the brown dwarf limit. Even if we ignore the cautions discussed above and apply the larger incompleteness correction

(dotted line), the deficit of low mass objects in NGC 2071 as compared to NGC 2068 remains significant.

Similar to the earlier discussion of the NGC 2024 mass function (§4.5.5), it should be noted here that the exact shapes of the mass functions for NGC 2068 and NGC 2071 are also somewhat dependent on the choice of bin centers and sizes. Consquently, as pointed out in Chapter 4 it remains true that the more robust choice for investigating the importance of brown dwarfs in a region is the relative numbers of stars and brown dwarfs in each cluster.

5.5.6 Ratio of Stars to Brown Dwarfs in NGC 2068 and NGC 2071

As discussed in Chapter 4, §4.5.6, the ratio of brown dwarfs to stars (R_{ss}) is an extremely useful tool for quantifying the IMF as it is independent of the detailed structure and exact shape of cluster mass functions. In the small range incompleteness-corrected mass function for NGC 2068 (dashed line in Figure 5–22) there are 16 objects with masses $0.02M_{\odot}<M<0.08M_{\odot}$ and 32 objects with masses $M > 0.08M_{\odot}$. Adding in the statistics for the early-type source (which are confirmed earlier than M and thus not brown dwarfs) adds an additional 30 objects with masses $M > 0.08M_{\odot}$. Finally, there are 7 sources in the background-subtracted photometric KLF with magnitudes brighter than K=11.0 which were not included in the completeness corrected mass function. Incorporating these sources yields a yielding a total of 69 stellar sources. (Recall that there are no substellar objects with K magnitudes brighter than 12.0, thus it is safe to assume that the 7 photometric sources are all stars.) This results in an R_{ss} for NGC 2068 of 16/69 or 0.23±0.06.

In NGC 2071, the incompleteness-corrected mass function contains 9 brown dwarfs and 50 stellar sources. Including the early-type stars adds an additional 20 objects with $M > 0.08M_{\odot}$. Finally, there are 4 sources with magnitudes $K<11.0$ in the photometric KLF and one additional source which was not in the FLAMINGOS catalog due to its extreme brightness (K=6.33, courtesy of 2MASS) but is quite obvious in the 4 m image,

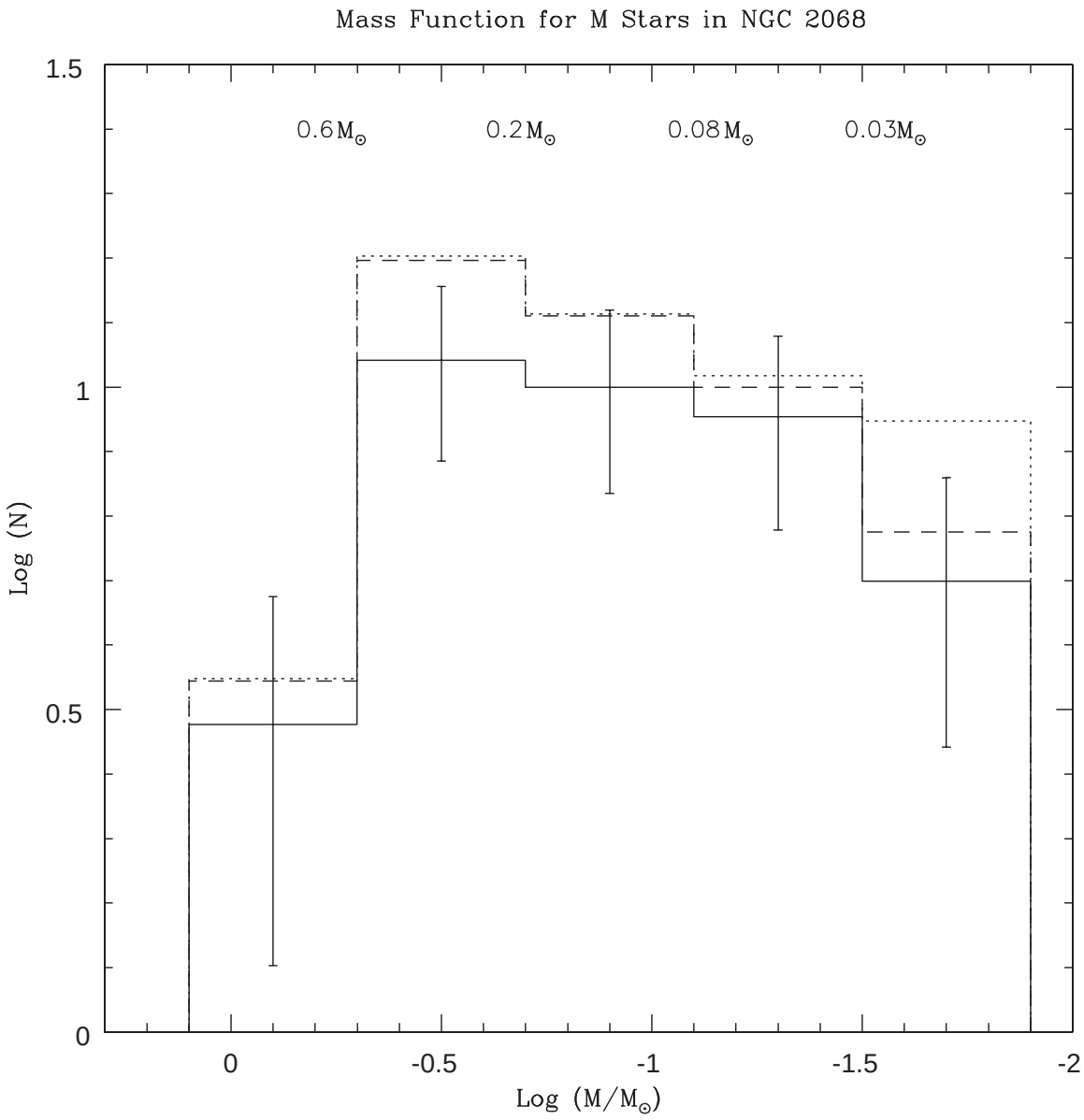

Figure 5–22. Mass function for M stars in NGC 2068. The solid line is the uncorrected, purely spectroscopic mass function for all classified members of NGC 2068. The dashed line is the spectroscopic mass function corrected for magnitude incompleteness in the range from $11.0<K<13.0$ and the dotted line has been corrected for magnitude incompleteness in the range $9.5<K<16.0$. Error bars shown are Poisson errors.

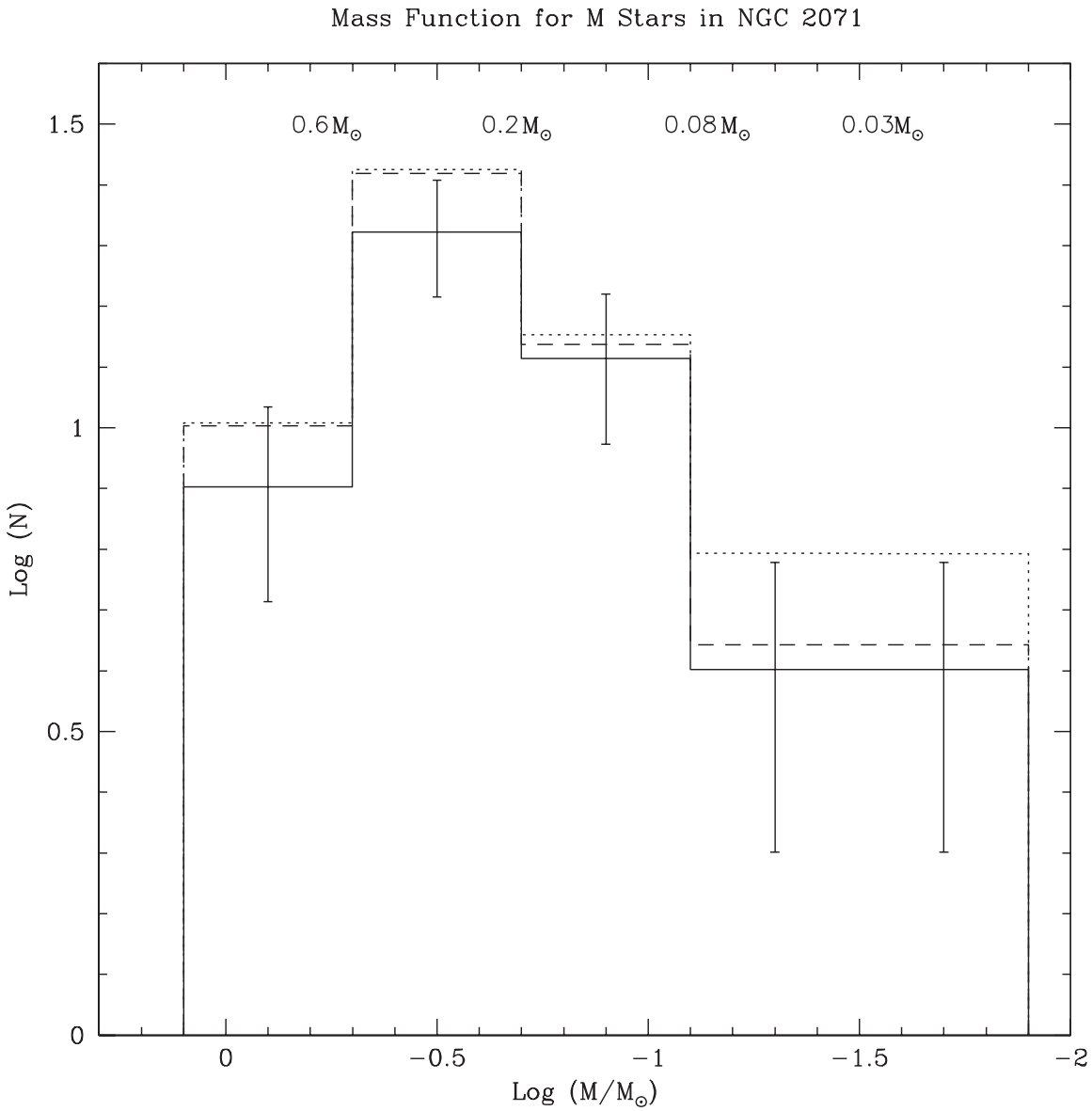

Figure 5–23. Mass function for M stars in NGC 2071. The solid line is the uncorrected, purely spectroscopic mass function for all classified members of NGC 2071. The dashed line is the spectroscopic mass function corrected for magnitude incompleteness in the range from $11.0<K<12.5$ and the dotted line has been corrected for magnitude incompletenes in the range $9.5<K<16.5$. Error bars shown are Poisson errors.

bringing the stellar total to 75. This yields an R_{ss} for NGC 2071 of 9/75 or 0.12±0.04. Note that neither R_{ss} derived here includes a correction for incomplete bins below K=15.0 (NGC 2068) or K=14.5 (NGC 2071), as it is highly uncertain whether missed sources in these bins are cluster members or background objects (in keeping with the discussion in the previous section. The implications of both possibilities along with a comparison of R_{ss} values for other young clusters can be found in the next chapter.

5.6 Summary

This Chapter presents FLAMINGOS photometry and spectroscopy for 100 M-type objects in the young Orion clusters NGC 2068 and NGC 2071. Sources were first classified based solely on their spectra. Photometry was then used to calculate extinctions and bolometric luminosities, which when combined with the spectral types allowed for the construction of H-R diagrams for both clusters. Membership status of all sources was assessed and masses and ages were inferred with the assistance of pre-main sequence evolutionary models for all confirmed cluster members.

The final membership sample in NGC 2068 contains 42 M-type sources with spectral types ranging from M1.25 to M9.00 and masses ranging from 0.02 to 0.68 $M_{\odot}$. For NGC 2071, the final membership sample contains 50 objects with spectral types ranging from M1.0 to M9.0, corresponding to a mass range of 0.02-0.82 $M_{\odot}$. The H-R diagrams for the clusters indicate that both NGC 2068 and NGC 2071 are extremely young: using the PMS tracks of D'Antona & Mazzitelli (1997) the median age of M stars in NGC 2068 is 0.9 Myr with a range from 0.6-1.2 Myr, as indicated by the standard error of the median; the median age for NGC 2071 is 0.4 Myr with a range from 0.3-0.6 Myr. These values are consistent with median ages $<$1 Myr as derived from the models of Chabrier et al. (2000).

The photometry was used to compile K-band luminosity functions for both clusters. These KLFs were corrected for background sources and then used to assess the completeness of the final membership samples in each cluster. Incorporating the bright spectra

of Hernandez (2006), the final incompleteness corrections were small, with many of the bins having completeness fractions of 90-100%. The resultant mass functions both rise to broad peaks around 0.2-0.5 $M_{\odot}$, however, the IMF for NGC 2068 remains flat throughout the substellar regime while that of NGC 2071 exhibits a relative brown dwarf defecit. The corresponding values of R_{ss}, the ratio of brown dwarfs to stars, illustrate the magnitude of this defecit, with an R_{ss} of 0.23$\pm$0.06 for NGC 2068 and an R_{ss} of 0.12$\pm$0.04 for NGC 2071. The implications of these results will be discussed in the next chapter.

CHAPTER 6
LOW MASS STARS IN YOUNG CLUSTERS: IMPLICATIONS FOR BROWN DWARF FORMATION

In the previous two Chapters I have presented results from a survey of young M stars in the three most populous clusters in Orion B, focusing specifically on the detailed characteristics of the substellar populations. In this Chapter, I combine my results with the current body of observational work in other young, low mass star forming regions in order to examine the viability of the current theories of brown dwarf formation.

6.1 Models of Brown Dwarf Formation

Recall that classical star formation theory predicts that the minimum mass for the collapse of a fragment within a molecular cloud is the thermal Jeans mass:

$$M_J \simeq \left(\frac{5kT}{G\mu m_{H_2}}\right)^{3/2} \left(\frac{4}{3}\pi\rho_0\right)^{-1/2}, \tag{6.1}$$

where T is the cloud temperature, μ is the mean molecular weight, m_{H_2} is the mass of a hydrogen molecule, ρ_0 is the gas density (which equals $n_{H_2}m_{H_2}$), and k and G are the Boltzmann and gravitational constants (Jeans, 1902; Spitzer, 1978). For a typical star-forming molecular cloud, the temperature and number density (n_{H_2}) are on the order of 10K and $10^5 \mathrm{cm}^{-3}$, respectively, resulting in an average Jeans mass of $\simeq 2.3 M_\odot$. This clearly contradicts the relatively large numbers of low mass stars and brown dwarfs observed, illustrating the problem with classical theory. In an effort to surmount this obstacle, many authors have recently proposed new theories of low mass star and brown dwarf formation. Broadly, they include four main mechanisms: turbulent fragmentation of molecular cloud cores, ejection of protostellar embryos from unstable multiple systems, the collision of protostellar disks, and photoerosion of pre-stellar cores. For the remainder of this section, I summarize each of these models in turn. In the following

sections I examine the model predictions in context of the observational work, ultimately placing constraints on the most likely methods of brown dwarf formation.

Turbulent Fragmentation: The minimum mass discussed above results from linear density perturbations in a molecular cloud offsetting the balance between gravity and thermal pressure, thus causing the collapse of a cloud core (Jeans, 1902). However, the gas density and velocity structure of star-forming clouds are highly nonlinear (recall, for example, the clumpy structure of Orion B as seen in the CS map of Lada et al. (1991a) shown in Figure 2–12) due to the presence of supersonic turbulence (e.g. Padoan & Nordlund, 2002, and references therein). The turbulent flow has extremely high kinetic energy, leading to a large network of shocked gas throughout the cloud. These shocks compress the cloud material, creating regions with very high local densities. If the density of a given region is larger than its local critical density it will collapse, irrespective of the average Jeans mass of the cloud. Consequently, dense cores of any size can form in a turbulent cloud.

Padoan & Nordlund (2004) investigated the possibility that brown dwarfs are formed directly via turbulent fragmentation. They computed both an upper limit to the brown dwarf mass fraction (assuming brown dwarfs only arise from turbulent fragmentation) and the analytical mass distribution of collapsing cores in a turbulent cloud, varying both the gas density and the sound speed (which is density-dependent). Their analysis shows that for higher values of gas density and sound speed, the core distribution peaks towards lower masses and the relative contribution of brown dwarfs to the IMF increases.

Embryo-Ejection: First proposed by Reipurth & Clarke (2001), the embryo-ejection model for brown dwarf formation postulates that stars are born in unstable multiple systems of small protostellar embryos, all gaining mass from a shared reservoir of gas. Brown dwarfs are formed when accretion is prematurely terminated due to dynamical ejection from the system.

Bate et al. (2002) and Bate & Bonnell (2005) have run two identical hydrodynamical simulations of the collapse and fragmentation of turbulent molecular clouds, differing only in the density of the two clouds. In their models, three quarters of the brown dwarfs form within gravitationally unstable circumstellar disks. The disk fragments interact and those destined to become brown dwarfs are ejected within 10^4-10^5 Myr. The remaining brown dwarfs initially form from isolated fragments of dense molecular gas but quickly fall into unstable multiple systems and are subsequently ejected before they can accrete to stellar mass. Comparing the results of the two calculations, their accretion/ejection model in a turbulent cloud predicts that the main variation of the IMF in different star forming environments is the location of the peak mass. In addition, they find that the denser cloud produces a higher proportion of brown dwarfs. Finally, large disks (radii $\geq$10 AU) have difficulty surviving the ejection process, with a frequency no higher than 5 percent.

Kroupa & Bouvier (2003) have also modelled the formation of brown dwarfs via embryo-ejection using N-body simulations. Their model predicts that the ejections occur within a few system dynamical times ($\tau \sim 1.6 \times 10^4$ yr) and the resultant distribution of ejection velocities contains a high velocity tail for brown dwarfs. In addition, large disks are not expected to survive the ejection process. Finally, they predict that assuming that the production of brown dwarfs is solely due to embryo-ejection and that this ejection occurs in the same manner for different environments, the total number brown dwarfs per star in a given star forming region should be invariate.

Disk Collisions: A third proposed mechanism is the formation of brown dwarfs induced by the collision of massive protostellar disks (e.g. Lin et al., 1998). In this scenario, tidal interactions between two protostars with massive circumstellar disks result in the formation of a tidal tail. This tail becomes gravitationally unstable and collapses to form a substellar object which is subsequently ejected from the system as the tail disperses on a timescale of $\sim 5 \times 10^3$ yr after the original collision. Brown dwarfs formed in this

manner are expected to have significant ejection velocities and not expected to maintain circumstellar disks.

Photoerosion: The fourth commonly discussed process for the formation of low mass stars and brown dwarfs is the photoerosion of prestellar cores by radiation from massive (OB) stars (Hester et al., 1996; Whitworth & Zinnecker, 2004). In this case, a dense, stellar mass core is overrun by an HII region. The ambient Lyman continuum radiation drives an ionziation front into the core, eroding it from the outside and applying an external pressure which causes the core to collapse. The final mass of the object is then determined by a competition between accretion onto the central protostar and the erosion of material at the boundary.

Kroupa & Bouvier (2003) and Whitworth & Zinnecker (2004) have examined analytical models of brown dwarf formation via photoerosion of prestellar cores and both authors find that photoevaporation of accretion envelopes can significantly affect the IMF near and below the substellar boundary in the immediate vicinity of ionizing stars (e.g. within the HII region). In addition, Whitworth & Zinnecker (2004) note that the effectiveness of this process implies that any intermediate-mass protostars in the region must have been well on their way to formation before the OB stars turned on. Neither model makes any predictions regarding the survival of circumstellar disks, however, logic dictates that the same environment which is hostile to protostellar accretion envelopes will also act to erode disk material.

6.2 Observational Constraints

6.2.1 Substellar Disk Frequencies

As part of the effort to characterize the low mass populations of NGC 2024, NGC 2068,and NGC 2071, I have used the $H-K$ colors and spectral types of all classified brown dwarfs to assess the amount of infrared excess (IRX) present in each object. (Remember that the presence of an IRX is conventionally taken as an indicator of emission from a warm circumstellar disk.) In this manner I derive a substellar disk

fraction for NGC 2024 of 39%±15% (Chapter 4, §4.5.4), and substellar disk fractions of 40%±11% and 25%±20% for NGC 2068 and NGC 2071, respectively (Chapter 5, §5.5.4).

Referring to the discussion of brown dwarf disks in Chapter 4, although the errors are large, the substellar excess fractions for all three Orion B clusters are consistent with the excess fractions found for other young star forming regions such as the Trapezium, Chamaeleon I, and IC 348. In addition, recent modelling of spectral energy distributions constructed from Spitzer data in IC 348 show that ∼42% of brown dwarfs in that region are surrounded by optically thick, primordial disks (Lada et al., 2006), which is again consistent with the inferred disk fractions derived in this thesis. Finally, the substellar disk fractions found here are in good agreement with recent work on the accretion properties of brown dwarfs.

Since the first definitive detection of active accretion in a substellar object in Taurus (Muzerolle et al., 2000), many brown dwarfs have been found to possess accretion disks (e.g. Jayawardhana et al., 2003; Natta et al., 2004; Muzerolle et al., 2005; Allers et al., 2006). Further, in 1-3 Myr old regions such as ρ Oph, Taurus, Chameleon I, and IC 348, the typical fraction of substellar accretors is 30-60% (Mohanty et al., 2005), consistent with my conclusion that 40-50% of brown dwarfs in the Orion B clusters are likely surrounded by circum(sub)stellar disks (see the discussion above and that in Chapter 4).

The detection of a significant disk fraction for young brown dwarfs places an important constraint on their formation mechanism. Recall from Chapter 1 that hydrogen-burning stars gain much of their mass through the accretion of material from a circum-stellar disk. The presence of accretion disks around substellar objects as well implies a certain level of uniformity in the overall formation process and provides a significant challenge for the embryo-ejection and disk collision models of formation, neither of which are expected to create brown dwarfs with significant disks. Indeed, the simulations of Bate et al. (2002); Bate & Bonnell (2005) show a mere ∼5% frequency of ejected

brown dwarfs having disks with radii $>$ 10 AU. However, these results are consistent with models of turbulent fragmentation where low mass objects are able to maintain significant disks.

6.2.2 Initial Mass Functions

In Chapters 4 and 5 I have derived the M star initial mass functions (IMFs) for NGC 2024, NGC 2068, and NGC 2071 (left-hand panels of Figure 6–1). All three mass functions rise to similar peaks in the vicinity of 0.2-0.3$M_{\odot}$, however, their behavior below the stellar/substellar boundary is quite different; the mass function for NGC 2024 drops at the brown dwarf limit but exhibits a modest secondary peak at $\simeq$0.03$M_{\odot}$while the mass function for NGC 2068 begins a slow decline around 0.2$M_{\odot}$which extends beyond the completeness limit of 0.035$M_{\odot}$. The mass function for NGC 2071 shows a sharp drop at the brown dwarf limit and contains only minimally populated bins beyond this point.

Low mass IMFs have been constructed for a number of other young star forming regions and in some cases their behavior is quite similar to the IMFs presented here. The right-hand panels of Figure 6–1 show the most recent spectroscopically derived mass functions for the $\sim$1 Myr Trapezium cluster in the Orion A molecular cloud (adapted from Slesnick et al. (2004)), the $\sim$2 Myr IC 348 cluster in Perseus (adapted from Luhman et al. (2003b)), and the 1-2 Myr Taurus star forming region (adapted from Luhman (2004)). Note that both IC 348 and the Trapezium are examples of the clustered mode of star formation, similar to the Orion B clusters and characterized by relatively high stellar and gas densities. In comparison, Taurus is an example of the isolated or distributed mode of star formation, occuring in a number of low density stellar aggregates widely spread throughout the Taurus-Auriga molecular cloud. The Trapezium IMF rises to a maximum at $\simeq$0.2$M_{\odot}$ before declining at the hydrogen-burning limit (HBL), in good agreement with the peaks of the Orion B IMFs and consistent with additional photometric and spectroscopic studies of the Trapezium (Hillenbrand & Carpenter, 2000; Luhman,

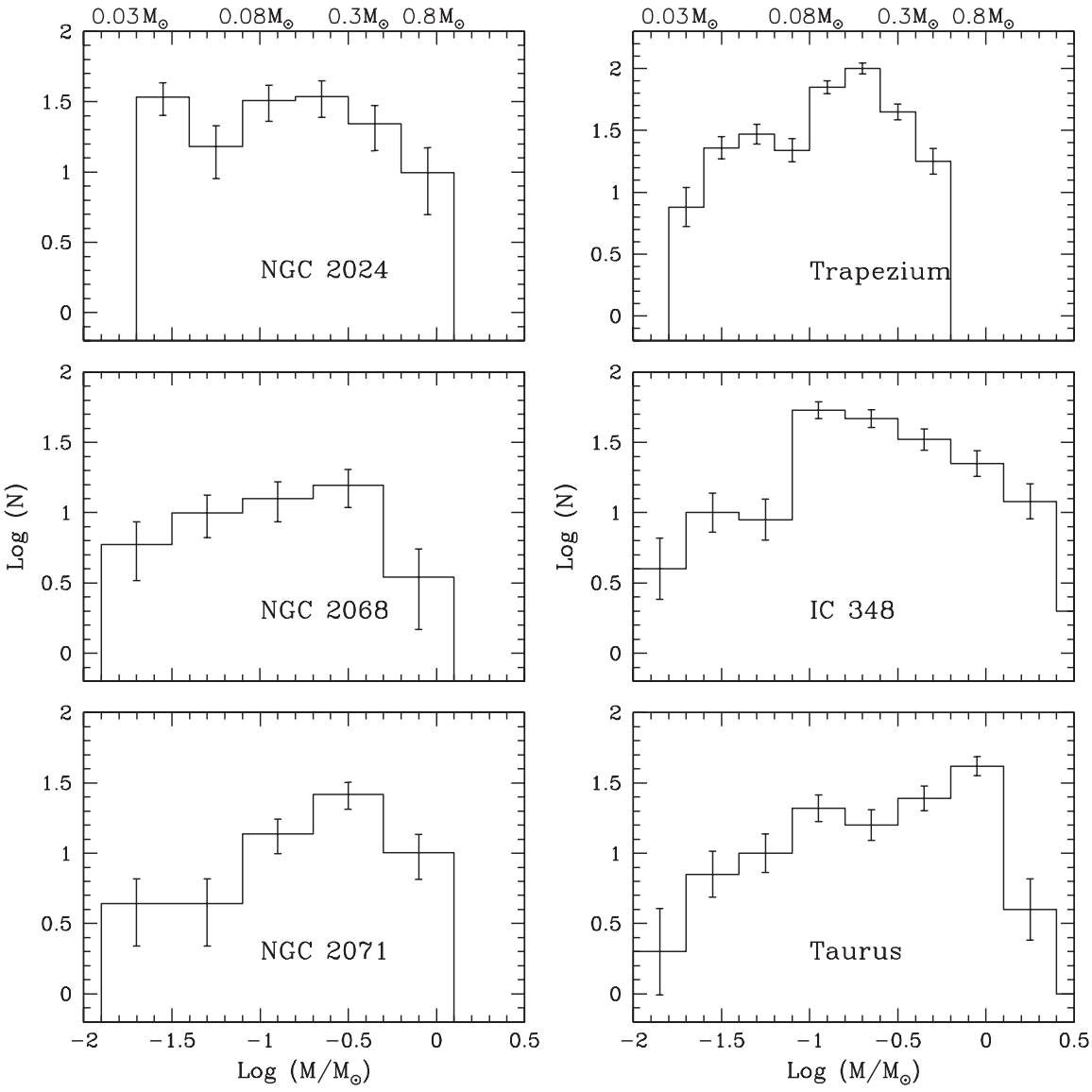

Figure 6–1. Initial mass functions of young clusters. The left-hand panels show the completeness-corrected mass functions derived in Chapters 4 and 5 for NGC 2024, NGC 2068, and NGC 2071. The right-hand panels show the IMFs for the ONC/Trapezium region (adapted from Slesnick et al. (2004), IC 348 (adapted from Luhman et al. (2003b), and the Taurus star forming region (adapted from Luhman (2004)).

2000; Muench et al., 2002; Lucas et al., 2005). The IC 348 IMF peaks at a slightly lower value ($\simeq 0.1 M_{\odot}$) than the Orion clusters before falling off relatively sharply at the HBL (Luhman et al., 2003b; Muench et al., 2003), similar to the sharp drop seen in the NGC 2071 IMF. On the other hand, the mass function derived for Taurus rises more sharply to a significantly higher maximum of 0.8-0.9$M_{\odot}$ and exhibits a much slower decline into the substellar regime (Briceño et al., 2002; Luhman et al., 2003a; Luhman, 2004).

Briceño et al. (2002) and Luhman et al. (2003b) offer the explanation that the differences between the peak mass of the Taurus IMF and the IMFs of the Trapezium and IC 348 may reflect a disparity among the local Jeans masses. The results from this dissertation support this theory as do the models of turbulent fragmentation described in §6.1. Simulations by Padoan & Nordlund (2002, 2004) and Bate & Bonnell (2005) find that while the mass distribution for star forming cores appears to be independent of environment for masses larger than a solar mass, the shape of the mass function for subsolar masses is dependent on the gas density and the level of turbulence in the cloud. Specifically, for higher gas densities (and thus increased turbulence), the IMF should peak at lower masses. In Figure 6–2 I plot the distribution of IMF peak masses shown in Figure 6–1 against the column density of hydrogen detected in each region (Table 6–2). With the exception of IC 348, the overall trend is in agreement with the model predictions, leading further weight to the idea that brown dwarfs form via turbulent fragmentation.

The observed variations in the substellar IMF are more challenging to explain. Both Muench et al. (2002) and Slesnick et al. (2004) cite a possible secondary peak below the HBL in the Trapezium IMF, similar to the result found in this thesis for NGC 2024. However, the locations of their respective peaks differ both from each other and the secondary peak I detect for NGC 2024 ($\sim$0.05 $M_{\odot}$ for Slesnick et al., $\sim$0.025 $M_{\odot}$ for Muench et al., as compared to $\sim$0.035 $M_{\odot}$ for NGC 2024). If these peaks are real features in the mass functions, they may indicate a break in formation mechanism for low mass objects (Muench et al., 2002). On the other hand, they may be artifacts introduced

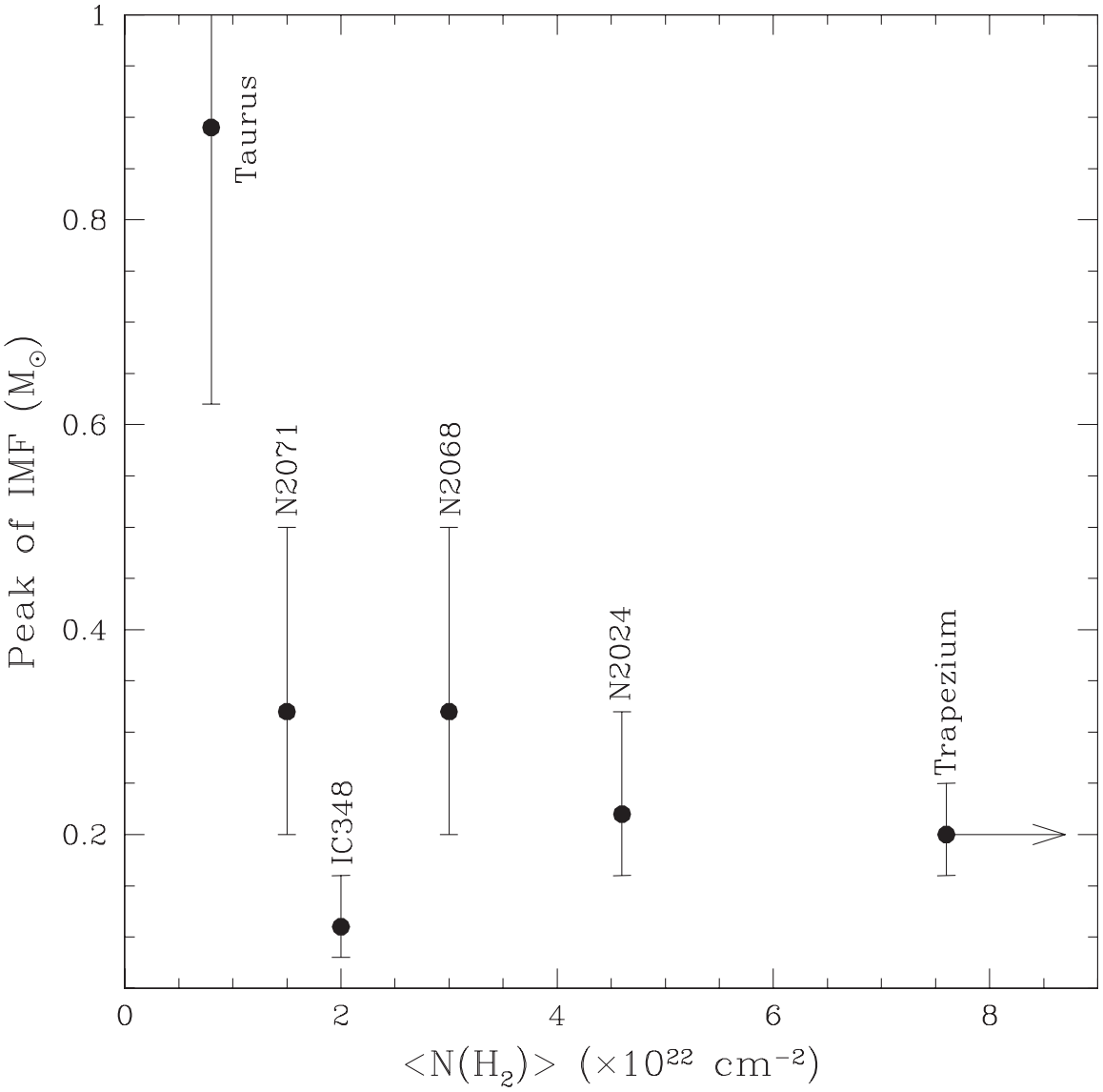

Figure 6–2. IMF peaks versus gas density for mass functions shown in Figure 6–1. Error bars are simply reflective of the bin widths used in each region. References for the column density of hydrogen (shown on the x-axis) can be found in Table 6–2.

by the mass-luminosity relation for brown dwarfs and not a true reflection of the mass function itself (Muench et al., 2003). In addition, as discussed in §4.5.5 and §5.5.5.3, the exact shape of the substellar mass function can be influenced by binning, particularly when dealing with small number statistics (as in NGC 2071 for example). Consequently, accurate inferences regarding the significance of the substellar populations in these clusters is better left to a more robust quantity such as the ratio of brown dwarfs to stars, discussed below.

6.2.3 The Abundance of Brown Dwarfs

Recall from Chapter 4 that in order to facillitate quantitative comparisons between the low mass IMFs of different regions, Briceño et al. (2002) defined the quantity R_{ss} to be the ratio of brown dwarfs ($0.02 \leq M/M_{\odot} \leq 0.08$) to stars ($0.08 \leq M/M_{\odot} \leq 10$). In the same vein, I have computed the R_{ss} for the Orion B clusters studied in this thesis: R_{ss}=0.30±0.05 for NGC 2024, R_{ss}=0.23±0.06 for NGC 2068, and R_{ss}=0.12±0.04 for NGC 2071. The values of NGC 2024 and NGC 2071 clearly differ significantly, with far fewer brown dwarfs in NGC 2071 than in NGC 2024. The R_{ss} for NGC 2068 falls in between; a trend that is reflected by the shapes of all three substellar mass functions shown in the left-hand panels of Figure 6–1.

The ratio of brown dwarfs to stars has been calculated for the star forming regions discussed in the previous section, also with a variety of results. In the Trapezium, Slesnick et al. (2004) find R_{ss}=0.20, which is slightly lower than the value of R_{ss}=0.26±0.04 found by Luhman (2000). Slesnick et al. (2004) attribute this variation to the difference between spectroscopic and photometric IMFs, however, I contend that the different R_{ss} values are likely caused by the use of different evolutionary models. Slesnick et al. (2004) employed the pre-main sequence models of D'Antona & Mazzitelli (1997) to derive masses whereas Luhman (2000) employed the model isochrones of the Lyon group (Baraffe et al., 1998 and Chabrier et al., 2000). I have recomputed the Trapezium R_{ss} using the data of Slesnick et al. (2004) with the Lyon models and find a higher value of

Table 6–1. Abundances of Brown Dwarfs in Young Star Forming Regions

Region	$R_{ss} = \frac{N(0.02-0.08 M_{\odot})}{N(0.08-10 M_{\odot})}$	Reference
Taurus.....	0.17±0.04	1,2
IC 348.....	0.12±0.03	3
NGC 2071.....	0.12±0.04	4
NGC 2068.....	0.23±0.06	4
NGC 2024.....	0.30±0.05	4
Trapezium.....	0.30±0.05	4,5

References. — (1) Luhman (2006); (2) Guieu et al. (2006); (3) Luhman et al. (2003b); (4) this work; (5) Slesnick et al. (2004).

R_{ss}=0.30±0.05, in excellent agreement with my result for NGC 2024. Similarly, looking at the H-R diagrams in Figures 4–6, 5–8, and 5–9, it is clear that had I chosen to employ the DM97 models I would have counted fewer brown dwarfs, leading to lower values of R_{ss} for each cluster. These results bring up an interesting point - namely that exact values of R_{ss} are clearly dependent on the choice of evolutionary models. Thus, if we wish to examine the relative proportions of stars and brown dwarfs from region to region, it is important to compare results derived from the same set of PMS tracks. To remain consistent in the ensuing discussion, from this point forward I will discuss only those values derived using the Lyon models.

Table 6–1 lists the most recent spectroscopically derived R_{ss} values for the three Orion B clusters, the Trapezium, IC 348, and Taurus. Note that the R_{ss} for the Trapezium is the recalculation described above, using the data from Slesnick et al. (2004) with the Lyon group models. In addition, the value presented for Taurus warrants some discussion. Originally, in their studies of the Taurus aggregates, Briceño et al. (2002) and Luhman et al. (2003b) calculated a slightly lower value of 0.14±0.04 for the R_{ss}. As surveys of Taurus have been expanded beyond the aggregate radii, the corresponding ratio of brown dwarfs to stars has also increased. Luhman (2004) combined optical imaging

and spectroscopy with infrared photometry from 2MASS to find R_{ss}=0.18±0.04) for a 12.4 deg^2 area. More recently, Guieu et al. (2006, hereafter G06) completed an optical survey covering ∼28 deg^2, finding 12 new brown dwarfs in the region and an updated R_{ss} of 0.23±0.05. However, shortly thereafter, Luhman (2006, hereafter L06) completed a search for brown dwarfs in the entire 225 deg^2 area of Taurus and found that 6 of the new brown dwarfs found by Guieu et al. in fact had spectral types earlier than M6 and thus were not substellar. L06 recalculated the R_{ss} of G06 with the updated classifications and derived a lower value of R_{ss}=0.17±0.04; this is the value presented in Table 6–1. It is important to note that L06 does not attempt to calculate R_{ss} for his entire survey, citing significant incompleteness in the spectral type range from M2-M6. Further, he notes that his revision of the G06 result may still not be an accurate representation of the Taurus population due to significant incompleteness at M4-M6 (33% complete) and ≥M6 (63% complete). Thus, it is most likely that an R_{ss} of 0.17 for Taurus is an *upper limit* to the true value.

Looking at Table 6–1, the abundances of brown dwarfs in IC 348 and NGC 2071 are consistent with each other and significantly lower than those of NGC 2024 or the Trapezium. In light of the comments above, it is also probable that the R_{ss} for Taurus is consistent with the low values of NGC 2071 and IC 348 rather than the higher R_{ss} of NGC 2024 and the Trapezium. It is unclear where to place the R_{ss} for NGC 2068. However, as can be seen from Figure 5–20, the largest amount of incompleteness in the survey of NGC 2068 occurs in the magnitude range $11.0<K<13.0$, with 27/43 or 63% of sources present in the spectroscopic sample. At an age of ∼1 Myr, this corresponds to a mass range of 0.3-0.08$M_\odot$ (spectral types ∼M4-M6), just above the substellar limit. For comparison, the bins from $13.0<K<15.0$ are all >95% complete. Thus, as for Taurus, it is likely that the current calculation of R_{ss} for NGC 2068 is an overestimate due to incompleteness in the spectroscopic sample just above the HBL.

Table 6–2. Physical Properties of Young Star Forming Regions

Region	N(H_2)[a] (cm^{-2})	Stellar Density[b] (stars/pc^3)	Cluster Mass[c] ($M_\odot$)	Earliest Spectral Type[d]
Taurus	0.8	10	13	B9
IC 348	2.0	159	160	B5
NGC 2071	1.5	130	60	B2.5
NGC 2068	3.0	130	110	B2
NGC 2024	4.6	537	180	O9
Trapezium	$>$7.6	1616	413	O7

[a]Column density of hydrogen as indicated by the $C^{18}O$ observations of Aoyama et al. 2001 (NGC 2024, NGC 2068, NGC 2071), Hatchell et al. 2005 (IC 348), Wilson et al. 1999 (Trapezium), and Onishi et al. 1998 (Taurus).

[b]Masses of the young clusters are taken from Lada & Lada (2003). The corresponding references for Taurus is Gomez et al. (1993).

[c]Stellar densities for the young clusters were calculated by taking the cluster centers listed in Lada & Lada (2003) and using FLAMINGOS photometry of each region to count the number of sources in a 0.5 pc radius down to $K \leq 15.0$. The stellar density of the Taurus aggregates was taken from Gomez et al. (1993).

[d]The spectral type of the most massive star in each region, taken from Bik et al. 2003 (NGC 2024), Strom et al. 1975 (NGC 2068, NGC 2071), Luhman et al. 2003b (IC 348), van Altena et al. 1988 (Trapezium), and Strom & Strom 1994 (Taurus).

These results indicate that there are fewer brown dwarfs in IC 348, NGC 2071, Taurus, and possibly NGC 2068 as compared to NGC 2024 and the Trapezium. A natural conclusion to draw is therefore that the brown dwarf formation process is not universal but depends on the star forming environment. To test this hypothesis, I now investigate the correlation between the R_{ss} and the local physical conditions in each star forming region.

Table 6–2 presents various physical properties for the regions discussed above, including gas column density, local stellar density, total mass, and the spectral type of the earliest (i.e. most massive) star in each region. Figures 6–3 to 6–6 show the relationship of each of these parameters to the R_{ss}. It should be noted that while the gas column density, total mass, and spectral types for each region were taken directly from the literature, the stellar densities for the young clusters were calculated in a self-consistent manner using photometry from the FLAMINGOS GMC survey. Cluster centers were

obtained from Lada & Lada (2003) and the number of sources to $K \leq 15.0$ contained within a 0.5 pc radius of the center were tallied and used to compute the volume density. In this way, it is assured that the relative stellar densities of each region are correct.

Figure 6–3 presents the relationship between the hydrogen column density and the R_{ss}. Generally, the regions with lower gas densities have fewer brown dwarfs, consistent with the predictions of the turbulent fragmentation models (Padoan & Nordlund, 2004; Bate & Bonnell, 2005). However, not all points fit the trend. If we take the datum for Taurus at face value, IC 348 and NGC 2071 appear to have a defecit of brown dwarfs compared to Taurus and NGC 2024 has an excess. Even if we take into account the relatively large error bars and consider the Taurus and NGC 2068 values as upper limits, brown dwarf formation arising solely from turbulent fragmentation cannot quite explain why the abundances of brown dwarfs in NGC 2024 and the Trapezium appear to be the same, given the large variation in their respective core densities.

Figure 6–4 shows the R_{ss} as a function of the stellar density in stars/pc^3. The trend is not as clear in this figure as compared to Figure 6–3, however, if we take the Taurus and NGC 2068 points as upper limits, the plot may indicate that there is a stellar density threshold above which young clusters either produce more brown dwarfs or retain them as ejected embryos caught in the larger gravitational potential of the denser clusters, as suggested by Kroupa & Bouvier (2003). In the first case, if more brown dwarfs are actually produced, it may be that the dependence of the R_{ss} on stellar density is simply a reflection of the relationship between stellar and gas densities (e.g. Lada et al., 1991a) and brown dwarf formation is again tied to the Jeans mass of each region. In the second case, if the effect is due to the retention of a larger number of brown dwarfs in denser regions, we might then expect to see a dependence of the R_{ss} on the total mass of each region.

Figures 6–5 shows the R_{ss} as a function the total cluster (or aggregate) mass in solar masses. There does not appear to be a significant correlation. If embryo-ejection is the dominant mode of brown dwarf formation and if the model behaves similarly in

each region (e.g. Kroupa & Bouvier, 2003), we might expect to see larger brown dwarf abundances in the more massive clusters as their larger gravitational potentials would make it harder for the ejected objects to escape, however, this doesn't seem to be the case.

Figure 6–6 shows the R_{ss} as a function of the spectral type of the earliest star in each region. As with the plot for gas density, there appears to be a general trend in the data: the regions containing massive stars have larger numbers of brown dwarfs. If we assume that the true R_{ss} for Taurus and NGC 2068 (the two regions depicted as upper limits) are smaller than depicted, it is also possible that the correlation is a step function. In this case, the regions with O stars are differentiated from those without. This is consistent with the photoerosion models of brown dwarf formation where substellar objects form when their accretion envelopes are prematurely eroded by the strong ionizing radiation of massive stars in an HII region.

There is some additional evidence that photoionization of prestellar cores is a likely explanation for the excess of brown dwarfs in the Trapezium and NGC 2024. Of the star forming regions discussed in this Chapter, only NGC 2024 and the Trapezium are affiliated with HII regions. In the Trapezium, the Orion Nebula is excited by the 5 Trapezium stars themselves, which range in spectral type from 07V-B0.5V. Disk accretion rates in the vicinity of these objects have been found to be lower than average (Robberto et al., 2004). The ionizing source for the HII region associated with NGC 2024 (the Flame Nebula) has recently been identified as IRS2b, an O8V-B2V star located in the core of the cluster (cf. Figure 4–7) and at the center of the radio continuum radiation field (Bik et al., 2003). Bik et al. (2003) note that IRS2b is more likely to be late O than early B. In addition, NGC 2024 also contains IRS2, a candidate early B star (Lenorzer et al., 2004) and seven compact dust condensations that are likely massive protostars (Mezger et al., 1988). Finally, recent analysis of archival Chandra data by Ezoe et al. (2006) has uncovered diffuse X-ray emission emanating from the region. The center of the X-ray emission coincides with the nine sources described above; the authors conclude that

the energy source for the emission is likely shocks generated by the accumulated stellar winds of young massive sources.

If photoevaporation of accretion envelopes is the dominant mode of substellar formation, we may expect to observe a higher density of brown dwarfs in regions closest to the ionizing source(s). Figure 6–7 shows the spatial distribution of brown dwarfs in NGC 2024 with the radio continuum contours of Barnes et al. (1989) outlining the HII region. While it is true that the majority of the brown dwarfs (15/23) do fall within the boundaries of the ionization front, the region also encompassess most of our stellar sources. Unfortunately the current survey does not have the statistics to conclusively test this theory, thus I defer further discussion to future work and simply note that photoevaporation of protostellar cores remains a viable option for brown dwarf formation in regions with massive stars.

6.3 Overall Implications for Brown Dwarf Formation

In this Chapter I have examined the most common scenarios put forth to explain the formation of low mass stars and brown dwarfs and placed them in the context of my results for the low mass populations of NGC 2024, NGC 2068, and NGC 2071 and published work on Taurus, the Trapezium, and IC 348. The key points are as follows:

- The detection of significant substellar disk fractions in all three clusters is consistent with current findings for other young star forming regions and likely precludes embryo-ejection or protostellar disk collisions as the dominant modes of formation for brown dwarfs. Rather it would appear that low mass objects are able to form as direct analogs to their more massive counterparts, employing disk accretion to attain their final mass.
- The characteristic mass of the IMFs for all young clusters studied are reasonably consistent with one another (0.1-0.3$M_{\odot}$) and significantly different from the Taurus star forming region (peak mass $\simeq$0.8$M_{\odot}$). An examination of the dependence of the peak mass on the local hydrogen column density revealed a general trend

where the regions with higher gas densities have lower characteristic masses. Numerical simulations of the fragmentation of a turbulent molecular cloud support this conjecture, with the characteristic mass being sensitively dependent on the local gas density and the sound speed.

- The relative abundances of stars and brown dwarfs in the star forming regions considered are generally consistent with formation models involving the fragmentation and collapse of a turbulent molecular cloud, however, when invoked alone, these models cannot acccount for the excess of brown dwarfs in NGC 2024. On the other hand, given that NGC 2024 is the only known region of massive star formation in Orion B, it is possible that the relatively large number of brown dwarfs in the cluster is caused by more massive pre-stellar cores being overrun by the ionizing radiation of the HII region.

In summary, based on the work presented in this dissertation, I conclude that the observations are most consistent with mechanisms of low mass star and brown dwarf formation employing turbulent fragmentation, similar to the classical paradigm for the fragmentation, collapse, and accretion of a proto-stellar core. In addition, in regions of massive star formation, the photoevaporation of the proto-stellar cores may also play a role and act to increase the number of brown dwarfs produced above the numbers expected from simple fragmentation models alone. Brown dwarf formation solely via ejected stellar embryos or disk instabilities does not appear to be supported by the data.

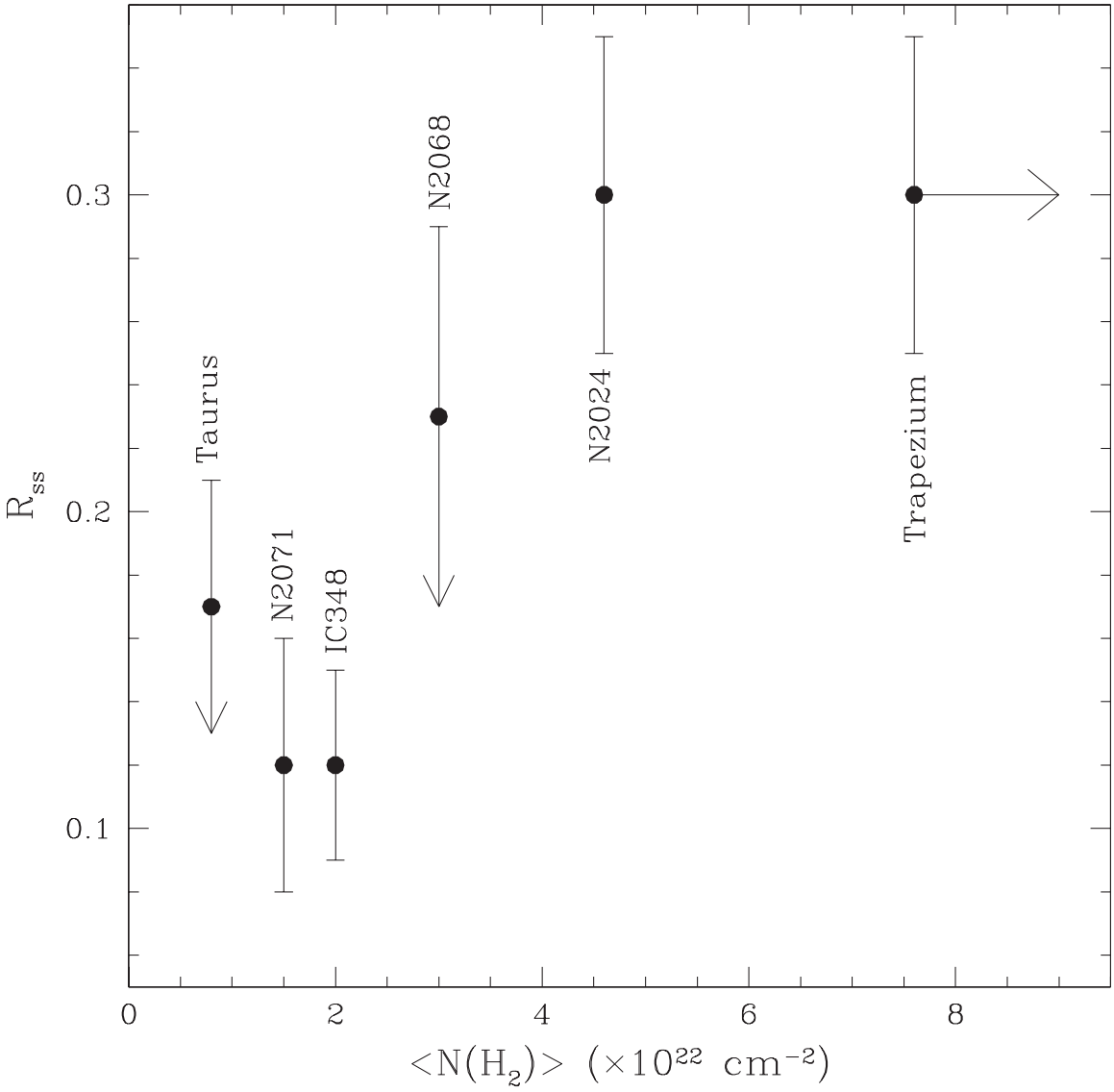

Figure 6–3. R_{ss} versus gas density plotted for Taurus, IC 348, NGC 2024, NGC 2068, NGC 2071 and the Trapezium. The x-axis is the average column density of molecular hydrogen as inferred from the $C^{18}O$ data. The y-axis is the R_{ss} for each region as listed in Table 6–1. Note that the value for the Trapezium is a lower limit.

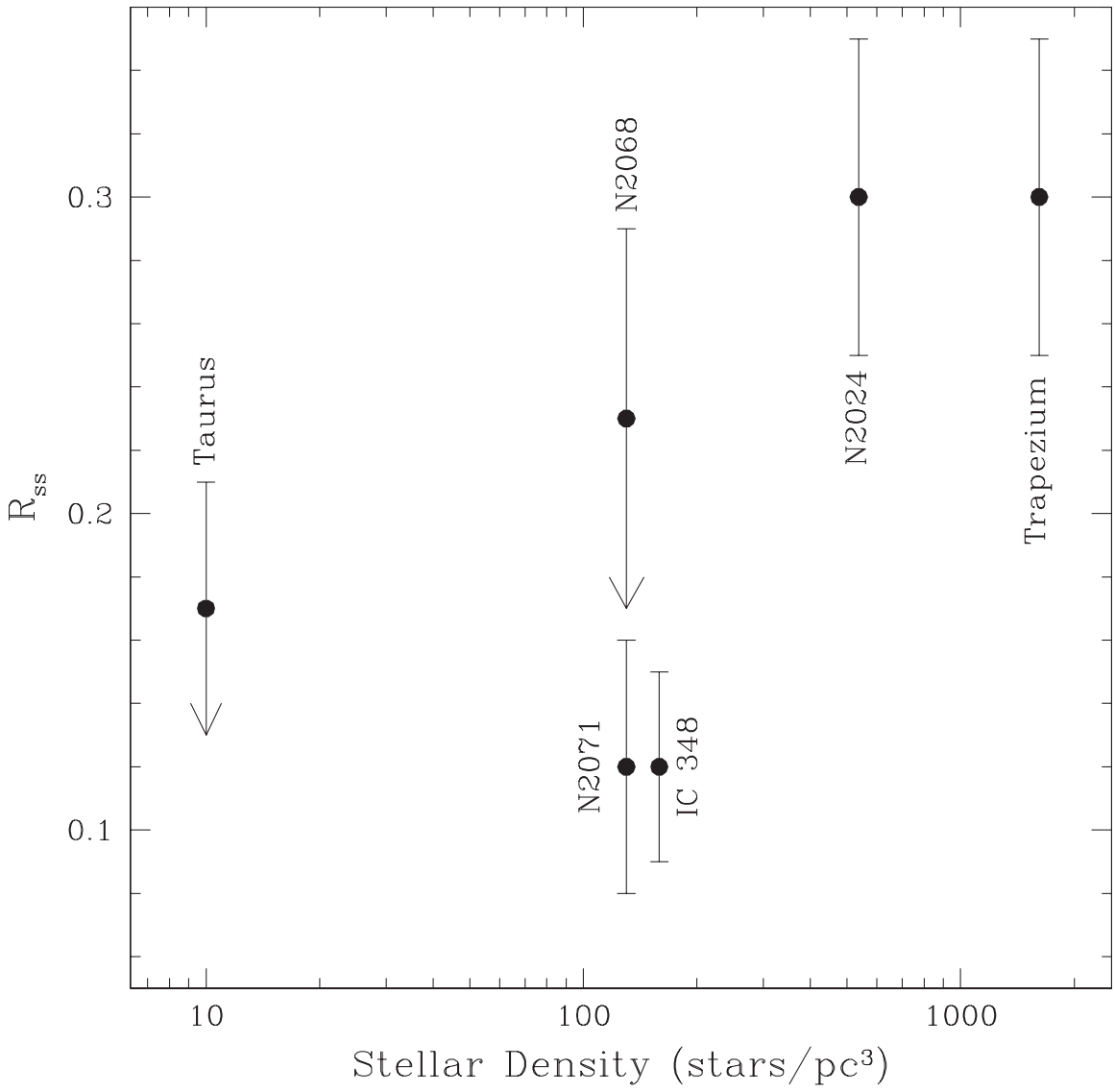

Figure 6–4. R_{ss} versus stellar density plotted for Taurus, IC 348, NGC 2024, NGC 2068, NGC 2071 and the Trapezium. The x-axis is the average stellar density in stars/pc^3. The y-axis is the R_{ss} for each region as listed in Table 6–1.

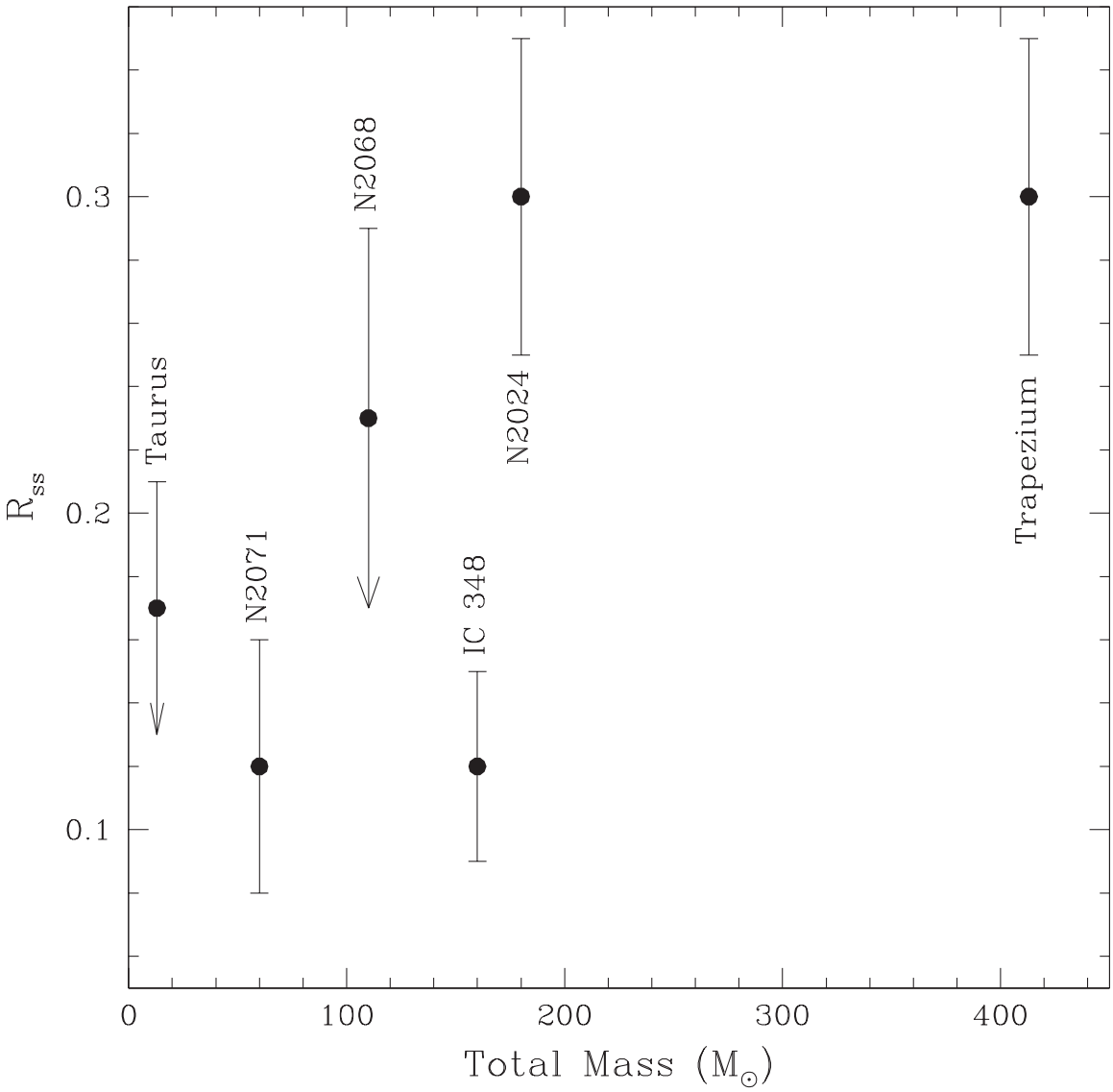

Figure 6–5. R_{ss} versus total mass shown for Taurus, IC 348, NGC 2024, NGC 2068, NGC 2071 and the Trapezium. The x-axis shows the mass in units of solar masses. The y-axis is the R_{ss} for each region as listed in Table 6–1. Note that the mass shown for Taurus is the typical mass of one of the aggregates.

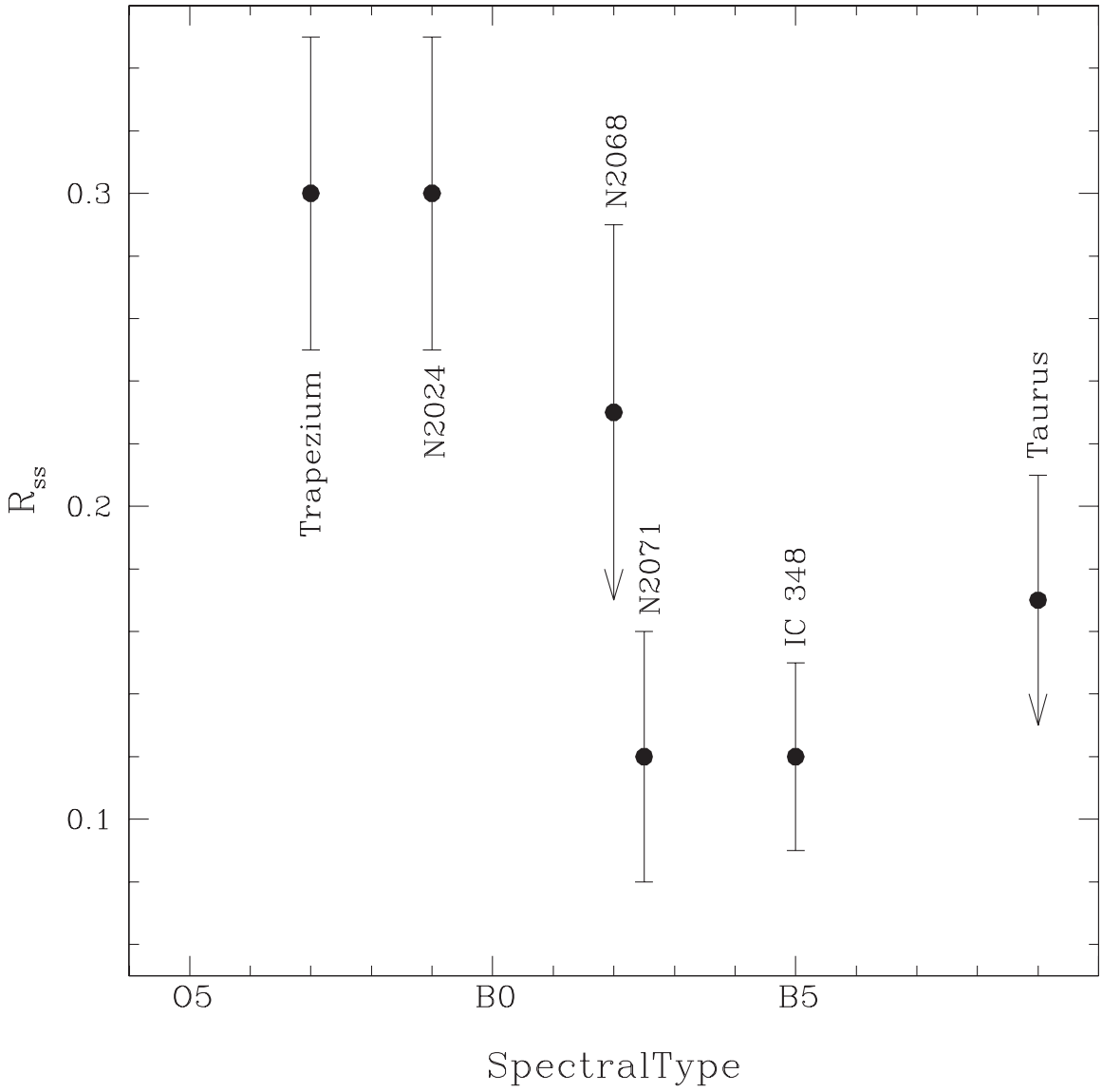

Figure 6–6. R_{ss} versus spectral type of the earliest (i.e. most massive) star for Taurus, IC 348, NGC 2024, NGC 2068, NGC 2071, and the Trapezium. The x-axis plots the numerical spectral type and the y-axis is the R_{ss} for each region as listed in Table 6–1.

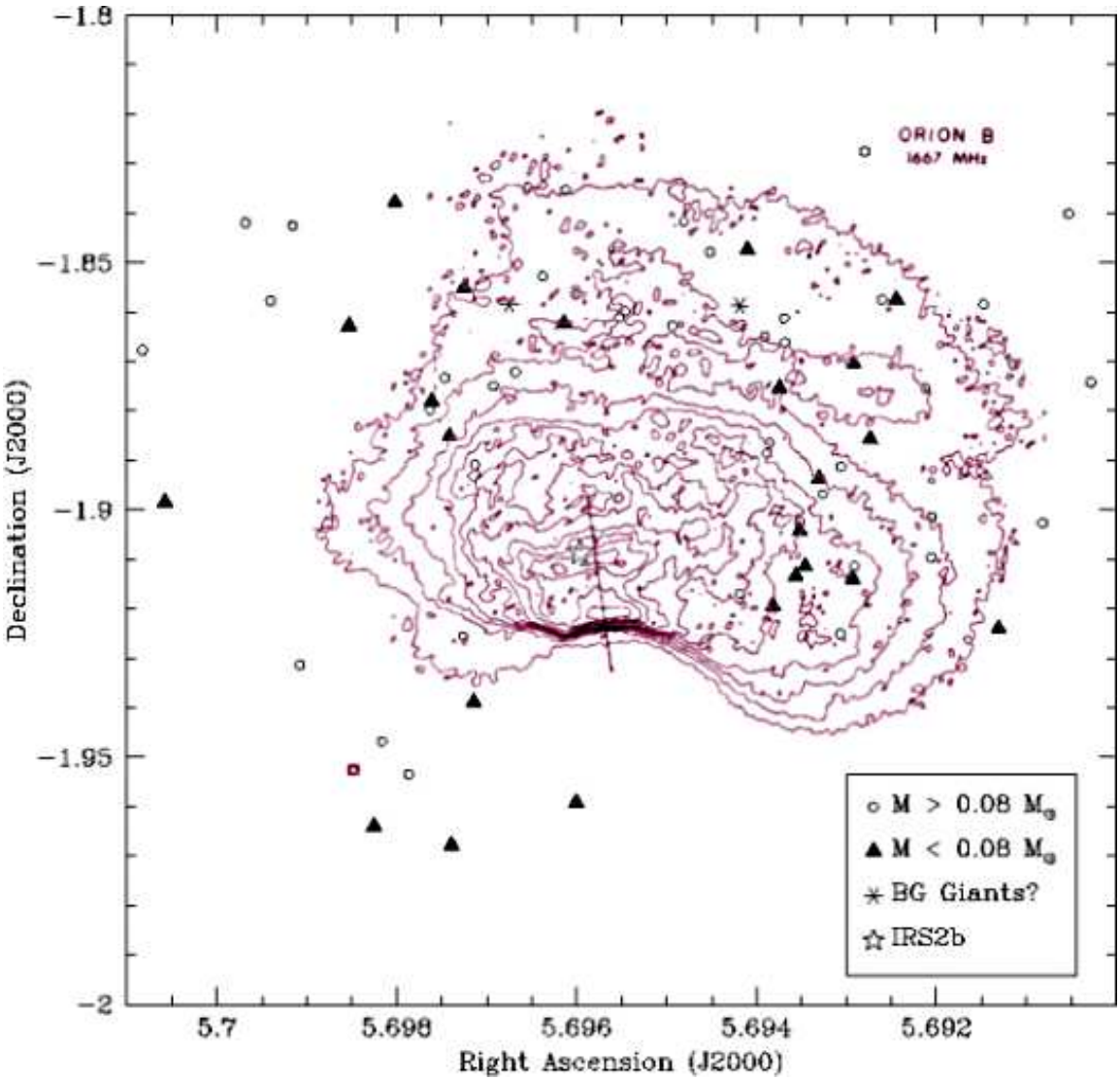

Figure 6–7. Distribution of brown dwarfs in NGC 2024 relative to the HII region. Open circles are the stars and filled triangles are the brown dwarfs. The purple contours show the 1667 MHz radio continuum emission detected by Barnes et al. (1989). The resolution of the radio map is 4″.

CHAPTER 7
THE STAR-FORMING HISTORY OF ORION

In Chapters 4 and 5 I have used FLAMINGOS photometry and spectroscopy to derive median ages for the low mass populations of three young clusters in Orion B. Steinhauer et al. (2006) have also employed FLAMINGOS data to derive a median age for the Trapezium cluster in exactly the same manner as I have done here. In this final chapter, I combine these data with published work on the Orion OB association to examine the star-forming history of the region.

The Orion OB association, Ori OB1, has long been known to be a large region that is actively forming massive stars. Blaauw (1964) identified four major subgroups in the area which differ vastly in both age and amount of ambient gas and dust. Ori OB1a and 1b are largely located away from the molecular clouds with no ambient molecular material and were estimated by (Blaauw, 1991) to be older, with ages ranging from 7-10 Myr. Ori OB1c is in the foreground of the Orion A cloud with an original age estimate (by Blaauw) of $\sim$3 Myr. Ori OB1d is the young Trapezium cluster, still embedded in Orion A and estimated by many authors to be $<$1 Myr. Figure 7–1 shows the spatial relationship of the Orion A and B molecular clouds (indicated by the CO contours of Maddalena et al. 1986) to the association Ori OB1 and its subgroups 1a, 1b, 1c and the Trapezium.

In his review, Blaauw (1991) postulates that the star formation in the region began with Ori OB1a and proceeded in a sequential fashion, with 1b and 1c responsible for triggering star formation events in the Orion B and A clouds, respectively. I now examine this hypothesis in light of the new ages determined for the low mass populations of both the Orion embedded clusters and the OB association subgroups.

Table 7–1 lists the newly derived ages for the clusters studied in this dissertation along with ages for the Trapezium and subgroups 1a, 1b, and 1c. As mentioned above,

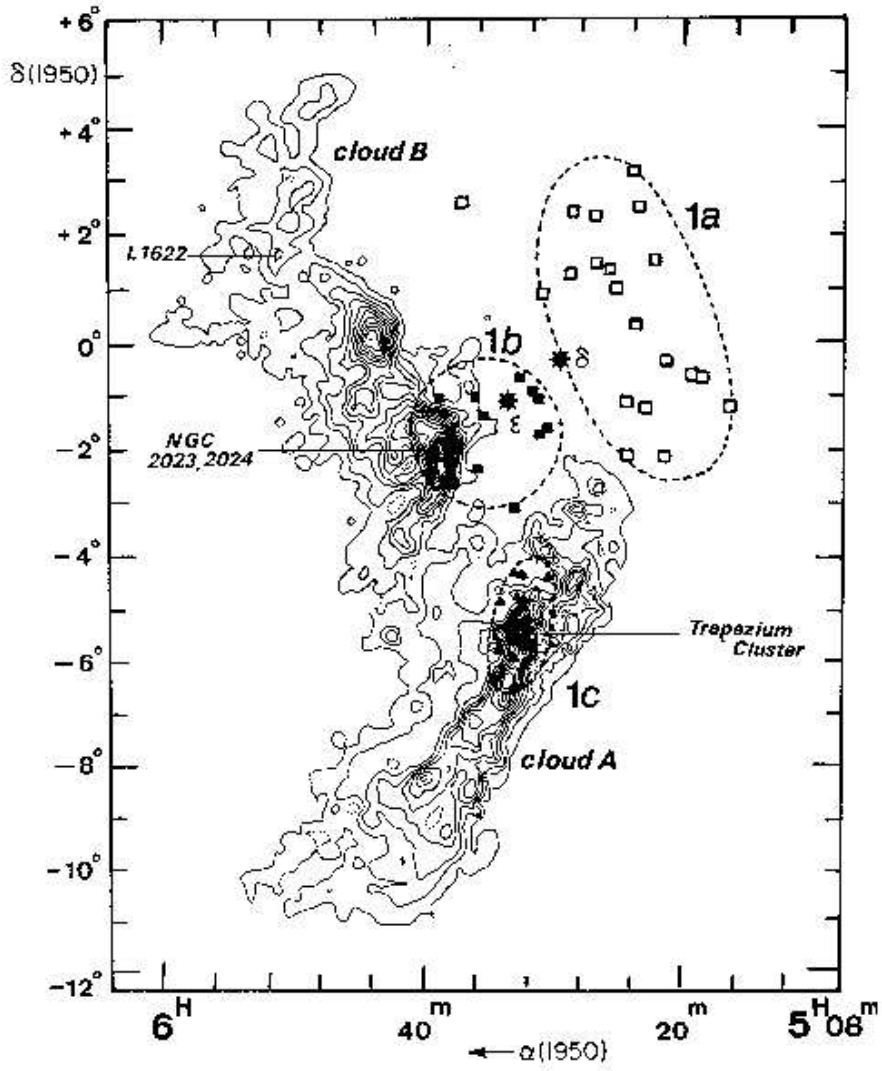

Figure 7–1. Molecular clouds in Orion and their relationship to the Orion OB1 association and its subgroups. Figure from Blaauw (1991).

the age of the Trapezium is also derived from a study of low mass stars in the region (Steinhauer et al., 2006). The ages of subgroups 1a and 1b were obtained through the spectroscopic identification of ∼200 new low mass ($0.1\,M_{\odot} < M < 0.9\,M_{\odot}$) members of the OB association (Briceño et al., 2005). The age for subgroup 1c is based on isochrone fitting in color-magnitude diagrams of members identified via proper motions (Brown et al., 1994). Thus, with the exception of OB1c, all of the ages under consideration here are based on the low mass populations of each region.

Table 7–1. Ages of Star-Forming Regions in Orion

Region	R.A. (degrees)	Dec. (degrees)	Age (Myr)	Age Error (Myr)	Reference
NGC 2024	85.42750	-1.89611	0.5	0.1	1
NGC 2068	86.67417	0.10583	0.9	0.3	1
NGC 2071	86.79167	0.32194	0.4	0.2	1
Trapezium	83.81833	-5.38972	0.2	0.1	2
Ori OB1c	83.86667	-5.26889	4.6	2.0	3
Ori OB1b	84.38333	-1.67111	5.0	1.0	4
Ori OB1a	81.64167	0.44194	8.5	1.5	4

References. — (1) This work; (2) Steinhauer et al. (2006); (3) Brown et al. (1994); (4) Briceño et al. (2005).

Figure 7–2 shows a histogram of ages for the regions discussed above. Based on this diagram, it would appear that there have been three distinct episodes of star formation in Orion. The oldest region is subgroup 1a at $\sim$8.5 Myr, followed by subgroups 1b and 1c at $\sim$5 Myr and finally the young clusters embedded in the clouds, which all have ages $<$1 Myr. It is interesting to note (1) that all star formation in the clouds appears to be occuring simultaneously and (2) that while all four of the youngest regions remain deeply enshrouded in their natal clouds, the intermediate-aged subgroups are partially to mostly removed from the cloud material and Ori OB1a shows no evidence for any remaining molecular gas. This implies that cloud lifetimes must be less than 8-10 Myr, with most of the molecular material dispersing on even smaller timescales ($\tau \lesssim 5$ Myr).

Finally, comparing Figures 7–1 and 7–2 it does appear that star formation in Orion is proceeding radially away from subgroup 1a. The most massive star in OB1a is δ Ori, an O9.5 giant estimated to be $45 M_{\odot}$ (Brown et al., 1994). Figure 7–3 shows the age of each region as a function of the angular distance (in degrees) from δ Ori, calculated using the coordinates listed in Table 7–1. With the exception of OB1c (whose age was determined in a far different manner than all other ages under discussion), there does seem to be a correlation between age and position relative to δ Ori. Note that this result should be

taken as tentative since this analysis does not incorporate the physical distance to each region as there are large uncertainties in these measurements.

In conclusion, the observed trend in age as a function of position and the trimodal distribution of ages for the region is in agreement with Blaauw's initial hypothesis that star formation in Orion is proceeding sequentially. The trigger for the first star formation event remains unknown but is likely one or more supernova explosions in the initial OB association.

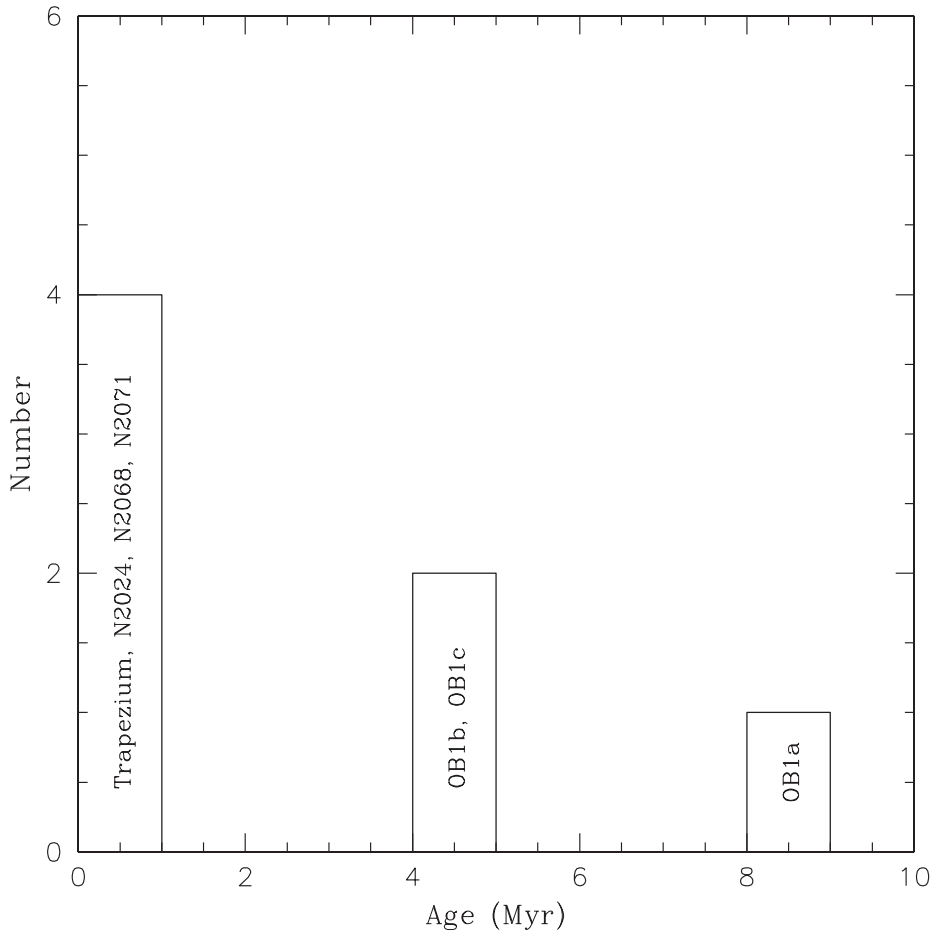

Figure 7–2. Histogram of ages for a range of star-forming regions in Orion. The exact ages, errors, and references for these regions can be found in Table 7–1.

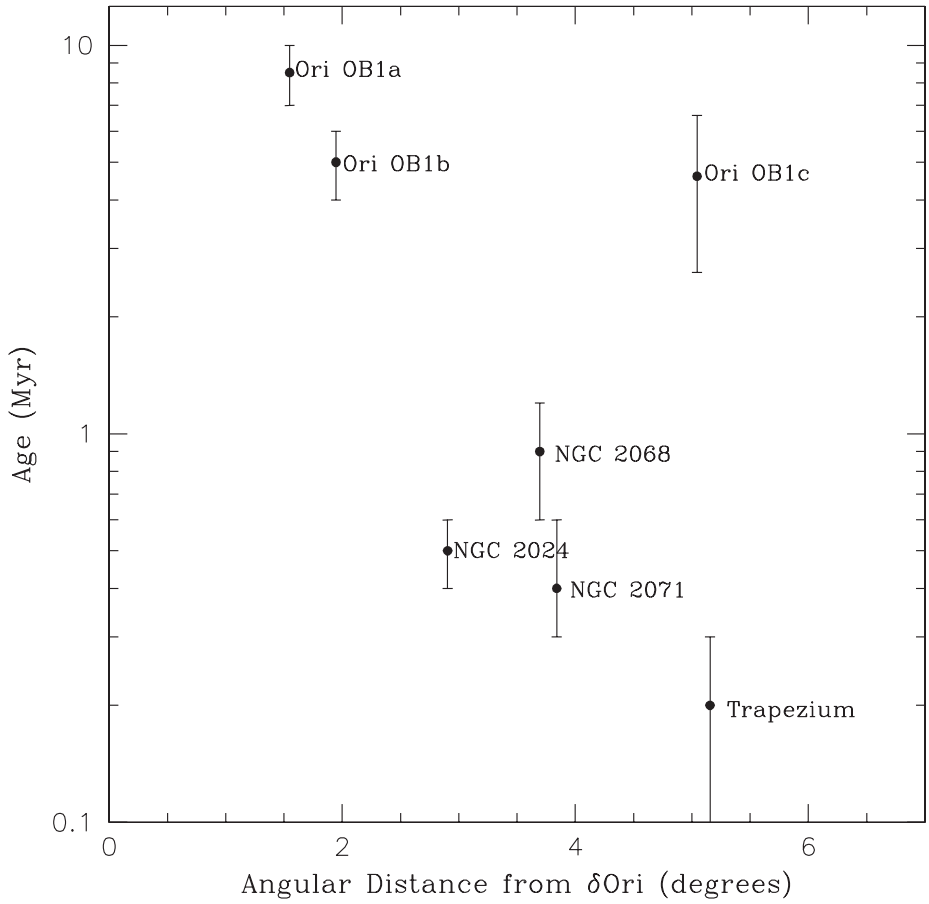

Figure 7–3. Age versus angular distance (in degrees) from δ Ori for star-forming regions in Orion.

CHAPTER 8
FUTURE WORK

For my dissertation, I have completed a near-infared imaging and spectroscopic survey of low mass star forming regions in the Orion B molecular cloud in an attempt to place constraints on the mechanisms responsible for brown dwarf formation. The data set includes J, H, and K-band photometry of a large area ($\sim$6 square degrees) of the cloud and spectra of $\sim$200 M stars in the three most populous regions of ongoing star formation: the young embedded clusters NGC 2024, NGC 2068, and NGC 2071. By combining the photometry and spectroscopy, I have determined masses and ages for M stars in each cluster and estimated median ages for each population. Analysis of these data show that:

1. Young brown dwarfs are prevalent throughout Orion B.
2. Significant numbers of brown dwarfs (40-50%) in Orion B are likely surrounded by circumsubstellar disks.
3. The mass functions of the Orion B clusters are similar to each other above the hydrogen-burning limit but vary significantly at substellar masses. In addition, the IMF peaks appear to be somewhat dependent on the local gas density.
4. The ratio of brown dwarfs to stars is not invariant but appears to depend on certain physical properties of the star-forming environment, including the local gas density, stellar density, and the presence or absence of hot massive stars.

These results indicate that brown dwarf formation is not universal but instead is dependent on the local star-forming conditions. The models which best fit the observations are those involving the turbulent fragmentation of low mass cloud cores, the photoerosion of a prestellar core by ionizing radiation from a massive star, or a combination of

both. The data do not favor the formation of significant numbers of brown dwarfs via embryo-ejection or protostellar disk collisions.

The Orion B data presented here have helped place powerful contraints on the possible mechanisms of low mass star and brown dwarf formation. However, there exists the potential for many more in-depth studies which may strengthen the conclusions. For example, a common source of uncertainty in both the mass functions and R_{ss} values presented here occurs in the correction for incompleteness. Following the precedent of Luhman et al. (2003b) in IC 348 and Luhman (2006) in Taurus, one possible solution is to obtain a spectrum of every source in the photometric KLF. This would remove the need for a completeness correction, thereby reducing the uncertainty in the final IMF. In addition, increasing the sample size will allow for smaller bins in the IMF, potentially revealing additional structure below the stellar/substellar boundary.

Another limitation to the data is the lack of spatial completeness in each cluster. As discussed in the previous chapter, radial searches for brown dwarfs in the vicinity of HII regions may prove fruitful in determining the importance of photoerosion as a mechanism for brown dwarf formation. Additional constraints for this model may also be provided by a study of the accretion rates of low mass sources in NGC 2024, similar to the work done by Robberto et al. (2004) in the Trapezium.

Finally, all spectra presented here are in young clusters. In order to further investigate the effect of environment on the brown dwarf IMF, it would be interesting to examine the distributed brown dwarf population in Orion B. A systematic spectroscopic study of M stars in the core regions of Lada et al. (1991a), the small cluster NGC 2023, and the general cloud population will provide new data points and possibly reveal additional functional dependencies of the R_{ss} and characteristic mass, allowing us to better understand the mysterious brown dwarf formation process.

APPENDIX A
IMAGING SURVEY: OBSERVING LOG AND SURVEY STATISTICS

This appendix contains data and statistics for the FLAMINGOS/Orion B imaging survey, described fully in Chapter 2. All information presented here is for the *final* selection of fields only; data are not presented for all observations of every field.

Table A–1 contains the observing log for the fields chosen for final photometry. Table A–2 presents the final photometric scatter measurements by band for each field, *after* application of the zero point correction. Table A–3 presents the luminosity function peaks by band for each field. Note that these values are taken as our 90% completeness limits.

Table A–1. Orion B Imaging Observing Log

ID	R.A. (J2000)	Dec. (J2000)	Obs. Date	Filter	Exp. Time (seconds)	$N_{exposures}$	Total Exp. Time (seconds)	Airmass	Seeing (″)
01	05:41:31.99	-01:54:16.0	2001 Dec 18	H	35	9	315	1.227	1.93
01	05:41:31.99	-01:54:16.0	2001 Dec 18	J	35	9	315	1.260	1.98
01	05:41:31.99	-01:54:16.0	2001 Dec 18	K	35	8	280	1.247	1.91
02	05:40:11.99	-01:54:16.0	2001 Dec 18	H	35	7	245	1.220	1.77
02	05:40:11.99	-01:54:16.0	2001 Dec 18	J	35	9	315	1.242	1.86
02	05:40:11.99	-01:54:16.0	2001 Dec 18	K	35	8	280	1.280	1.69
03	05:40:11.99	-01:34:16.0	2001 Dec 18	H	35	7	245	1.209	1.79
03	05:40:11.99	-01:34:16.0	2001 Dec 18	J	35	9	315	1.221	1.92
03	05:40:11.99	-01:34:16.0	2001 Dec 18	K	35	8	280	1.302	1.66
04	05:41:31.99	-01:34:16.0	2001 Dec 18	H	35	9	315	1.201	2.02
04	05:41:31.99	-01:34:16.0	2001 Dec 18	J	35	9	315	1.214	1.99
04	05:41:31.99	-01:34:16.0	2001 Dec 18	K	35	9	315	1.320	1.63
05	05:42:51.99	-01:34:16.0	2001 Dec 18	H	35	9	315	1.199	2.00

Table A–1—Continued

ID	R.A. (J2000)	Dec. (J2000)	Obs. Date	Filter	Exp. Time (seconds)	$N_{exposures}$	Total Exp. Time (seconds)	Airmass	Seeing (″)
05	05:42:51.99	-01:34:16.0	2001 Dec 18	J	35	9	315	1.206	2.03
05	05:42:51.99	-01:34:16.0	2001 Dec 18	K	35	9	315	1.343	1.67
06	05:44:11.99	-01:34:16.0	2001 Dec 18	H	35	9	315	1.200	2.04
06	05:44:11.99	-01:34:16.0	2001 Dec 18	J	35	9	315	1.203	2.01
06	05:44:11.99	-01:34:16.0	2001 Dec 18	K	35	9	315	1.370	1.66
07	05:45:31.99	-01:34:16.0	2001 Dec 18	H	35	8	280	1.449	1.88
07	05:45:31.99	-01:34:16.0	2001 Dec 18	J	35	9	315	1.493	1.80
07	05:45:31.99	-01:34:16.0	2001 Dec 18	K	35	8	280	1.410	1.62
08	05:46:51.99	-01:34:16.0	2001 Dec 20	H	35	9	315	1.238	1.85
08	05:46:51.99	-01:34:16.0	2001 Dec 20	J	35	7	245	1.254	1.85
08	05:46:51.99	-01:34:16.0	2001 Dec 20	K	35	9	315	1.244	1.73
09	05:42:51.99	-01:54:16.0	2001 Dec 20	H	35	9	315	1.237	1.81
09	05:42:49.99	-01:53:46.0	2001 Dec 20	J	35	8	280	1.283	1.80

Table A–1—Continued

ID	R.A. (J2000)	Dec. (J2000)	Obs. Date	Filter	Exp. Time (seconds)	$N_{exposures}$	Total Exp. Time (seconds)	Airmass	Seeing (″)
09	05:42:51.99	-01:54:16.0	2001 Dec 20	K	35	9	315	1.229	1.81
10	05:44:11.99	-01:54:16.0	2001 Dec 20	H	35	7	245	1.223	1.90
10	05:44:12.10	-01:54:16.0	2001 Dec 20	J	35	9	315	1.307	1.77
10	05:44:11.99	-01:54:16.0	2001 Dec 20	K	35	9	315	1.221	1.86
11	05:45:31.99	-01:54:16.0	2001 Dec 20	H	35	9	315	1.215	1.86
11	05:45:31.99	-01:54:16.0	2001 Dec 20	J	35	9	315	1.327	1.77
11	05:45:31.99	-01:54:16.0	2001 Dec 20	K	35	8	280	1.215	1.83
12	05:46:51.99	-01:54:16.0	2001 Dec 20	H	35	8	280	1.209	1.92
12	05:46:51.99	-01:54:16.0	2001 Dec 20	J	35	9	315	1.350	1.70
12	05:46:51.99	-01:54:16.0	2001 Dec 20	K	35	8	280	1.210	1.97
13	05:40:11.99	-02:14:16.0	2001 Dec 20	H	35	9	315	1.213	1.85
13	05:40:11.99	-02:14:16.0	2001 Dec 20	J	35	9	315	1.412	1.75
13	05:40:11.99	-02:14:16.0	2001 Dec 20	K	35	9	315	1.209	1.83

Table A–1—Continued

ID	R.A. (J2000)	Dec. (J2000)	Obs. Date	Filter	Exp. Time (seconds)	$N_{exposures}$	Total Exp. Time (seconds)	Airmass	Seeing ($''$)
14	05:41:31.99	-02:14:16.0	2001 Dec 20	H	35	9	315	1.209	1.97
14	05:41:31.99	-02:14:16.0	2001 Dec 20	J	35	9	315	1.444	1.80
14	05:41:31.99	-02:14:16.0	2001 Dec 20	K	35	6	210	1.208	1.95
15	05:42:51.99	-02:14:16.0	2002 Feb 01	H	35	9	315	1.213	2.05
15	05:42:51.99	-02:14:16.0	2002 Feb 01	J	35	9	315	1.342	1.96
15	05:42:51.99	-02:14:16.0	2002 Feb 01	K	35	9	315	1.209	2.03
16	05:44:11.99	-02:14:16.0	2002 Feb 01	H	35	9	315	1.219	1.99
16	05:44:11.99	-02:14:16.0	2002 Feb 01	J	35	9	315	1.325	1.97
16	05:44:11.99	-02:14:16.0	2002 Feb 01	K	35	9	315	1.209	2.01
17	05:45:31.99	-02:14:16.0	2002 Jan 05	H	35	7	245	1.338	1.70
17	05:45:31.99	-02:14:16.0	2002 Jan 07	J	35	8	280	1.263	1.81
17	05:45:31.99	-02:14:16.0	2002 Jan 05	K	35	5	175	1.224	2.16
18	05:46:51.99	-02:14:16.0	2002 Jan 05	H	35	9	315	1.312	1.81

Table A–1—Continued

ID	R.A. (J2000)	Dec. (J2000)	Obs. Date	Filter	Exp. Time (seconds)	$N_{exposures}$	Total Exp. Time (seconds)	Airmass	Seeing (″)
18	05:46:51.99	-02:14:16.0	2002 Jan 07	J	35	9	315	1.251	1.75
18	05:46:51.99	-02:14:16.0	2002 Jan 05	K	35	9	315	1.219	2.29
19	05:40:11.99	-02:34:16.0	2002 Jan 05	H	35	7	245	1.312	1.78
19	05:40:11.99	-02:34:16.0	2002 Jan 07	J	35	7	245	1.236	1.83
19	05:40:11.99	-02:34:16.0	2002 Jan 05	K	35	9	315	1.214	2.50
20	05:41:31.99	-02:34:16.0	2001 Dec 24	H	35	9	315	1.426	2.41
20	05:41:31.99	-02:34:16.0	2002 Jan 05	H	35	5	175	1.222	2.23
20	05:41:31.99	-02:34:16.0	2001 Dec 24	J	35	9	315	1.467	2.54
20	05:41:31.99	-02:34:16.0	2001 Dec 24	K	35	9	315	1.327	2.17
21	05:42:51.99	-02:34:16.0	2001 Dec 24	H	35	9	315	1.385	2.23
21	05:42:47.99	-02:35:16.0	2001 Dec 24	J	35	6	210	1.512	2.36
21	05:42:51.99	-02:34:16.0	2001 Dec 24	K	35	9	315	1.352	2.28
22	05:44:11.99	-02:34:16.0	2002 Jan 07	H	35	9	315	1.326	1.93

Table A–1—Continued

ID	R.A. (J2000)	Dec. (J2000)	Obs. Date	Filter	Exp. Time (seconds)	$N_{exposures}$	Total Exp. Time (seconds)	Airmass	Seeing ($''$)
22	05:44:11.99	-02:34:16.0	2002 Jan 07	J	35	8	280	1.217	1.75
22	05:44:11.99	-02:34:16.0	2002 Jan 07	K	35	9	315	1.290	1.74
22	05:44:11.99	-02:34:16.0	2002 Jan 15	K	40	9	360	1.240	1.96
23	05:45:31.99	-02:34:16.0	2002 Jan 07	H	35	9	315	1.346	1.98
23	05:45:31.99	-02:34:16.0	2002 Jan 07	J	35	9	315	1.214	1.81
23	05:45:31.99	-02:34:16.0	2002 Jan 07	K	35	9	315	1.255	1.86
24	05:46:51.99	-02:34:16.0	2002 Jan 12	H	35	7	245	1.355	2.22
24	05:46:51.99	-02:34:16.0	2002 Jan 07	J	35	9	315	1.213	1.70
24	05:46:51.99	-02:34:16.0	2002 Jan 07	K	35	9	315	1.236	1.89
25	05:40:11.99	-01:14:16.0	2002 Feb 01	H	35	9	315	1.421	2.19
25	05:40:11.99	-01:14:16.0	2002 Feb 01	J	35	8	280	1.485	2.21
25	05:40:11.99	-01:14:16.0	2002 Jan 07	K	35	9	315	1.214	1.93
26	05:41:31.99	-01:14:16.0	2002 Jan 13	H	35	7	245	1.255	1.73

Table A–1—Continued

ID	R.A. (J2000)	Dec. (J2000)	Obs. Date	Filter	Exp. Time (seconds)	$N_{exposures}$	Total Exp. Time (seconds)	Airmass	Seeing (″)
26	05:41:31.99	-01:14:16.0	2002 Jan 13	J	35	9	315	1.272	1.73
26	05:41:31.99	-01:14:16.0	2002 Jan 13	K	35	9	315	1.233	1.58
27	05:42:51.99	-01:14:16.0	2002 Jan 13	H	35	9	315	1.239	1.72
27	05:42:51.99	-01:14:16.0	2002 Jan 13	J	35	6	210	1.288	1.69
27	05:42:51.99	-01:14:16.0	2002 Jan 13	K	35	9	315	1.223	1.59
28	05:44:11.99	-01:14:16.0	2002 Jan 13	H	35	9	315	1.225	1.69
28	05:44:07.99	-01:13:16.0	2002 Jan 13	J	35	7	245	1.312	1.72
28	05:44:11.99	-01:14:16.0	2002 Jan 13	K	35	9	315	1.214	1.63
29	05:45:31.99	-01:14:16.0	2002 Jan 20	H	35	9	315	1.427	2.05
29	05:45:31.99	-01:14:16.0	2002 Jan 20	J	35	9	315	1.468	1.90
29	05:45:31.99	-01:14:16.0	2002 Jan 20	K	35	9	315	1.239	1.79
30	05:46:51.99	-01:14:16.0	2002 Jan 20	H	35	9	315	1.388	2.50
30	05:46:51.99	-01:14:16.0	2002 Jan 20	J	35	9	315	1.506	1.88

Table A–1—Continued

ID	R.A. (J2000)	Dec. (J2000)	Obs. Date	Filter	Exp. Time (seconds)	$N_{exposures}$	Total Exp. Time (seconds)	Airmass	Seeing ($''$)
30	05:46:51.99	-01:14:16.0	2002 Jan 20	K	35	9	315	1.251	1.75
31	05:45:15.00	+00:07:48.0	2002 Jan 13	H	35	9	315	1.195	1.79
31	05:45:15.00	+00:07:48.0	2002 Jan 13	J	35	9	315	1.308	1.60
31	05:45:15.00	+00:07:48.0	2002 Jan 13	K	35	9	315	1.189	1.73
32	05:45:50.00	-00:13:48.0	2002 Jan 20	H	35	9	315	1.344	1.85
32	05:45:50.00	-00:13:48.0	2002 Jan 20	J	35	9	315	1.539	1.87
32	05:45:50.00	-00:13:48.0	2002 Jan 20	K	35	9	315	1.255	1.76
33	05:47:10.00	-00:13:48.0	2002 Jan 20	H	35	9	315	1.313	2.26
33	05:47:10.00	-00:13:48.0	2002 Jan 20	J	35	9	315	1.583	1.91
33	05:47:10.00	-00:13:48.0	2002 Jan 20	K	35	14	490	1.271	1.69
34	05:46:35.00	+00:07:48.0	2002 Jan 13	H	35	14	490	1.183	1.81
34	05:46:35.00	+00:07:48.0	2002 Jan 13	J	35	9	315	1.334	1.66
34	05:46:35.00	+00:07:48.0	2002 Jan 13	K	35	9	315	1.183	1.88

Table A–1—Continued

ID	R.A. (J2000)	Dec. (J2000)	Obs. Date	Filter	Exp. Time (seconds)	$N_{exposures}$	Total Exp. Time (seconds)	Airmass	Seeing ($''$)
35	05:47:55.00	+00:07:48.0	2002 Jan 21	H	35	9	315	1.274	1.76
35	05:47:55.00	+00:07:48.0	2002 Jan 21	J	35	8	280	1.410	1.88
35	05:47:51.00	+00:08:48.0	2002 Jan 21	K	35	8	280	1.182	1.72
36	05:47:55.00	+00:27:48.0	2002 Jan 21	H	35	7	245	1.251	2.09
36	05:47:55.00	+00:27:48.0	2002 Jan 21	J	35	9	315	1.441	2.00
36	05:47:55.00	+00:27:48.0	2002 Jan 21	K	35	9	315	1.175	1.75
37	05:46:35.00	+00:27:48.0	2002 Jan 13	H	35	9	315	1.175	2.04
37	05:46:35.00	+00:27:48.0	2002 Jan 13	J	35	9	315	1.368	1.77
37	05:46:35.00	+00:27:48.0	2002 Jan 13	K	35	9	315	1.174	2.02
38	05:45:15.00	+00:27:48.0	2002 Jan 21	H	35	9	315	1.224	1.84
38	05:45:15.00	+00:27:48.0	2002 Jan 21	J	35	7	245	1.543	2.09
38	05:45:15.00	+00:27:48.0	2002 Jan 21	K	35	7	245	1.173	1.75
39	05:45:11.00	+00:46:48.0	2002 Jan 21	H	35	6	210	1.211	1.82

Table A–1—Continued

ID	R.A. (J2000)	Dec. (J2000)	Obs. Date	Filter	Exp. Time (seconds)	$N_{exposures}$	Total Exp. Time (seconds)	Airmass	Seeing ($''$)
39	05:45:15.00	+00:47:48.0	2002 Jan 21	J	35	9	315	1.581	2.11
39	05:45:15.00	+00:47:48.0	2002 Jan 21	K	35	9	315	1.170	1.76
40	05:46:35.00	+00:47:48.0	2002 Jan 21	H	35	9	315	1.194	1.65
40	05:46:35.00	+00:47:48.0	2002 Jan 21	J	35	9	315	1.632	2.12
40	05:46:35.00	+00:47:48.0	2002 Jan 21	K	35	9	315	1.173	1.72
41	05:47:55.00	+00:47:48.0	2002 Jan 21	H	35	9	315	1.184	1.81
41	05:47:55.00	+00:47:48.0	2002 Jan 21	J	35	9	315	1.687	2.28
41	05:47:55.00	+00:47:48.0	2002 Jan 21	K	35	9	315	1.177	1.71
42	05:47:08.00	-00:33:18.0	2002 Jan 19	H	35	8	280	1.221	2.08
42	05:47:10.00	-00:33:48.0	2002 Jan 19	J	35	9	315	1.268	1.84
42	05:47:10.00	-00:33:48.0	2002 Jan 19	K	35	10	350	1.262	1.84
43	05:45:50.00	-00:33:48.0	2002 Jan 19	H	35	14	490	1.212	2.02
43	05:45:50.00	-00:33:48.0	2002 Jan 19	J	35	6	210	1.292	2.40

Table A–1—Continued

ID	R.A. (J2000)	Dec. (J2000)	Obs. Date	Filter	Exp. Time (seconds)	$N_{exposures}$	Total Exp. Time (seconds)	Airmass	Seeing (″)
43	05:45:50.00	-00:33:48.0	2002 Jan 19	K	35	9	315	1.222	1.87
44	05:45:50.00	-00:53:48.0	2002 Jan 19	H	35	9	315	1.208	1.93
44	05:45:50.00	-00:53:48.0	2002 Jan 19	J	35	9	315	1.314	1.91
44	05:45:50.00	-00:53:48.0	2002 Jan 19	K	35	9	315	1.212	1.89
45	05:47:10.00	-00:53:48.0	2002 Jan 19	H	35	9	315	1.198	2.02
45	05:47:10.00	-00:53:48.0	2002 Jan 19	J	35	9	315	1.337	1.81
45	05:47:10.00	-00:53:48.0	2002 Jan 19	K	35	9	315	1.204	2.03
56	05:43:53.99	-03:14:16.0	2002 Jan 19	H	35	9	315	1.228	1.96
56	05:43:53.99	-03:14:16.0	2002 Jan 19	J	35	9	315	1.421	1.88
56	05:43:53.99	-03:14:16.0	2002 Jan 19	K	35	9	315	1.228	2.06
57	05:43:53.99	-03:34:16.0	2002 Jan 19	H	35	9	315	1.230	1.88
57	05:43:53.99	-03:34:16.0	2002 Jan 19	J	35	9	315	1.463	1.93
57	05:43:53.99	-03:34:16.0	2002 Jan 19	K	35	7	245	1.228	1.90

Table A–1—Continued

ID	R.A. (J2000)	Dec. (J2000)	Obs. Date	Filter	Exp. Time (seconds)	$N_{exposures}$	Total Exp. Time (seconds)	Airmass	Seeing ($''$)
58	05:45:13.99	-03:34:16.0	2002 Jan 19	H	35	9	315	1.651	2.16
58	05:45:13.99	-03:34:16.0	2002 Jan 19	J	35	9	315	1.497	2.00
58	05:45:13.99	-03:34:16.0	2002 Jan 19	K	35	8	280	1.862	2.48
59	05:45:13.99	-03:54:16.0	2002 Jan 19	H	35	9	315	1.604	2.11
59	05:45:13.99	-03:54:16.0	2002 Jan 19	J	35	9	315	1.547	2.04
59	05:45:13.99	-03:54:16.0	2002 Jan 19	K	35	7	245	1.792	2.34
n2071	05:47:08.00	+00:19:55.0	2002 Dec 31	H	35	9	315	1.176	1.76
n2071	05:47:08.00	+00:19:55.0	2002 Dec 31	J	35	9	315	1.180	1.73
n2071	05:47:08.00	+00:19:55.0	2002 Dec 31	K	35	9	315	1.174	1.82
gap1	05:47:15.00	-00:03:48.0	2003 Nov 20	H	35	9	315	1.182	1.71
gap1	05:47:15.00	-00:03:48.0	2003 Nov 20	J	35	9	315	1.441	1.78
gap1	05:47:15.00	-00:03:48.0	2003 Nov 20	K	35	9	315	1.350	1.75
gap2	05:45:55.00	-00:03:48.0	2003 Nov 20	H	35	9	315	1.179	1.69

Table A–1—Continued

ID	R.A. (J2000)	Dec. (J2000)	Obs. Date	Filter	Exp. Time (seconds)	$N_{exposures}$	Total Exp. Time (seconds)	Airmass	Seeing (″)
gap2	05:45:55.00	-00:03:48.0	2003 Nov 20	J	35	9	315	1.362	1.74
gap2	05:45:55.00	-00:03:48.0	2003 Nov 20	K	35	9	315	1.412	1.72
gap3	05:45:55.00	+00:17:48.0	2003 Nov 20	H	35	9	315	1.176	1.77
gap3	05:45:55.00	+00:17:48.0	2003 Nov 20	J	35	9	315	1.309	1.72
gap3	05:45:55.00	+00:17:48.0	2003 Nov 20	K	35	9	315	1.446	1.71
gap4	05:42:12.00	-01:44:16.0	2003 Nov 20	H	35	9	315	1.206	1.69
gap4	05:42:12.00	-01:44:16.0	2003 Nov 20	J	35	9	315	1.304	1.70
gap4	05:42:12.00	-01:44:16.0	2003 Nov 20	K	35	9	315	1.553	1.71
gap5	05:40:52.00	-01:44:16.0	2003 Nov 20	H	35	9	315	1.216	2.23
gap5	05:40:52.00	-01:44:16.0	2003 Nov 20	J	35	9	315	1.256	1.72
gap5	05:40:52.00	-01:44:16.0	2003 Nov 20	K	35	9	315	1.627	1.78
cf1	05:58:00.00	-04:56:00.0	2004 Jan 27	H	35	9	315	1.585	1.87
cf1	05:58:00.00	-04:56:00.0	2004 Jan 27	J	35	9	315	1.429	2.01

Table A–1—Continued

ID	R.A. (J2000)	Dec. (J2000)	Obs. Date	Filter	Exp. Time (seconds)	$N_{exposures}$	Total Exp. Time (seconds)	Airmass	Seeing ($''$)
cf1	05:58:00.00	-04:56:00.0	2004 Jan 27	K	35	9	315	1.397	1.89
cf2	05:48:00.00	-04:56:00.0	2004 Jan 27	H	35	9	315	1.487	1.99
cf2	05:48:00.00	-04:56:00.0	2004 Jan 27	J	35	9	315	1.422	2.16
cf2	05:48:00.00	-04:56:00.0	2004 Jan 27	K	35	9	315	1.346	1.93
cf3	05:41:13.00	-03:06:00.0	2003 Nov 20	H	35	9	315	1.206	1.58
cf3	05:41:13.00	-03:06:00.0	2003 Nov 20	J	35	9	315	1.468	1.75
cf3	05:41:13.00	-03:06:00.0	2003 Nov 21	K	35	9	315	1.169	1.93
cf4	05:41:16.00	-02:36:00.0	2003 Nov 20	H	35	9	315	1.238	1.57
cf4	05:41:16.00	-02:36:00.0	2003 Nov 20	J	35	9	315	1.423	1.72
cf4	05:41:16.00	-02:36:00.0	2003 Nov 21	K	35	9	315	1.164	1.84
cf5	05:58:00.00	-02:00:00.0	2004 Dec 16	H	35	13	455	1.236	1.71
cf5	05:58:00.00	-02:00:00.0	2004 Dec 16	J	35	13	455	1.269	1.72
cf5	05:58:00.00	-02:00:00.0	2004 Nov 20	K	35	9	315	1.543	1.73

Table A–1—Continued

ID	R.A. (J2000)	Dec. (J2000)	Obs. Date	Filter	Exp. Time (seconds)	$N_{exposures}$	Total Exp. Time (seconds)	Airmass	Seeing ($''$)
cf6	05:58:00.00	-02:30:00.0	2004 Dec 16	H	35	13	455	1.220	1.74
cf6	05:58:00.00	-02:30:00.0	2004 Dec 16	J	35	13	455	1.287	1.75
cf6	05:58:00.00	-02:30:00.0	2004 Nov 20	K	35	9	315	1.501	1.75
cf7	05:41:00.00	-03:36:00.0	2004 Dec 16	H	35	13	455	1.153	1.76
cf7	05:41:00.00	-03:36:00.0	2004 Dec 16	J	35	13	455	1.275	1.76
cf7	05:41:00.00	-03:36:00.0	2004 Nov 20	K	35	9	315	1.460	1.76

Table A–2. Mean Photometric Scatter by Field

Field	σ_J	σ_H	σ_K	Comments
01	0.10	0.09	0.11	NGC 2024
02	0.05	0.05	0.04	
03	0.05	0.03	0.04	
04	0.05	0.05	0.05	
05	0.05	0.05	0.05	
06	0.05	0.04	0.05	
07	0.04	0.04	0.05	
08	0.05	0.04	0.04	
09	0.04	0.04	0.06	
10	0.06	0.05	0.04	
11	0.05	0.05	0.04	
12	0.04	0.05	0.05	
13	0.05	0.04	0.04	
14	0.05	0.07	0.06	NGC 2023
15	0.06	0.05	0.06	
16	0.06	0.06	0.07	
17	0.04	0.04	0.04	
18	0.04	0.04	0.11	
19	0.05	0.04	0.08	
20	0.06	0.04	0.04	
21	0.05	0.07	0.05	
22	0.04	0.05	0.04	
23	0.05	0.04	0.05	
24	0.05	0.04	0.04	
25	0.04	0.04	0.03	
26	0.05	0.05	0.04	
27	0.06	0.04	0.04	
28	0.06	0.05	0.05	
29	0.05	0.04	0.05	
30	0.04	0.04	0.04	
31	0.06	0.04	0.04	
32	0.04	0.04	0.05	
33	0.05	0.04	0.04	
34	0.07	0.07	0.06	NGC 2068
35	0.04	0.04	0.05	
36	0.05	0.05	0.06	
37	0.06	0.06	0.07	NGC 2071

Table A–2—Continued

Field	σ_J	σ_H	σ_K	Comments
38	0.04	0.04	0.03	
39	0.04	0.04	0.04	
40	0.04	0.04	0.04	
41	0.04	0.04	0.06	
42	0.05	0.04	0.04	
43	0.06	0.04	0.04	
44	0.04	0.05	0.04	
45	0.05	0.04	0.04	
56	0.04	0.04	0.04	
57	0.06	0.04	0.04	
58	0.04	0.04	0.05	
59	0.04	0.04	0.05	
n2071	0.10	0.08	0.08	NGC 2071
g1	0.10	0.09	0.08	NGC 2024
g2	0.08	0.08	0.10	NGC 2024
g3	0.10	0.09	0.08	NGC 2024
g4	0.11	0.09	0.12	NGC 2024
g5	0.10	0.07	0.08	

Table A–3. Luminosity Function Peaks by Field

Field	$J_{LF\,peak}$	$H_{LF\,peak}$	$K_{LF\,peak}$
01	18.25	17.25	16.50
02	18.75	18.25	17.75
03	18.25	18.25	17.75
04	18.25	17.75	17.25
05	18.50	18.00	17.75
06	18.75	18.00	17.50
07	18.50	18.00	17.50
08	18.50	18.25	17.50
09	18.50	18.50	17.75
10	19.00	18.25	17.50
11	18.75	18.25	17.25
12	18.75	18.00	17.50
13	19.00	18.50	17.50
14	19.00	18.50	17.75
15	18.50	17.75	17.50
16	18.50	17.75	17.50
17	18.50	18.25	17.50
18	18.50	18.00	17.50
19	18.50	18.00	17.50
20	18.25	17.75	17.50
21	18.25	17.75	17.50
22	18.50	17.75	17.50
23	18.25	17.75	17.25
24	18.50	17.75	17.25
25	18.50	17.50	17.25
26	18.50	18.00	17.75
27	18.75	18.25	17.75
28	18.75	18.50	17.50
29	18.50	17.75	17.75
30	18.50	17.75	17.75
31	18.75	18.25	17.50
32	18.50	18.00	17.75
33	18.25	17.75	18.00
34	19.00	18.50	17.75
35	18.25	18.00	17.50
36	18.50	17.75	17.75
37	19.00	18.25	17.50

Table A–3—Continued

Field	$J_{LF\,peak}$	$H_{LF\,peak}$	$K_{LF\,peak}$
38	18.25	17.75	17.75
39	18.25	17.50	17.50
40	18.25	18.00	17.75
41	18.00	17.75	17.75
42	18.50	17.50	17.50
43	18.00	18.00	17.25
44	18.50	17.75	17.00
45	18.50	17.50	17.00
56	18.50	18.00	16.75
57	18.75	18.00	17.50
58	18.25	17.75	17.25
59	18.25	17.75	17.25
g1	18.75	18.50	17.75
g2	19.00	18.50	18.00
g3	19.00	18.50	17.75
g4	19.00	18.50	17.75
g5	19.00	18.25	17.75
n2071	19.25	18.75	18.00

APPENDIX B
SPECTROSCOPIC SURVEY: OBSERVING LOG

This appendix contains a table listing all slit masks with classifiable spectra used in the FLAMINGOS spectroscopic survey of Orion B. Masks are organized first by region and then by observation date and listings include the telescope used, individual and total exposure times, and target selection criteria for the mask.

A complete description of the spectroscopic survey can be found in Chapter 2, §2.4.

Table B–1. FLAMINGOS/Orion B Spectroscopic Observing Log

Region[a]	Mask ID	Telescope	Obs. Date	t_{exp}	N_{exp}	Total t_{exp}	Target Selection Criteria
02 (NGC 2071)	n2071f21	2.1m	2003 Nov 28	300s	10	3000s	*K* magnitude
”	n2071f22	2.1m	2003 Dec 01	300s	12	3600s	*K* magnitude
”	oc34mf1a	4m	2003 Dec 11	300s	22	6600s	IRX sources
”	oc44mf11	4m	2003 Dec 11	300s	8	2400s	IRX sources
”	oc34mf2a	4m	2004 Jan 06	300s	24	7200s	IRX sources
”	oc44mf31	4m	2004 Jan 07	300s	22	6600s	IRX sources
”	n2071a2	4m	2004 Nov 26	300s	12	3600s	*H* magnitude
”	n2071a4	4m	2004 Dec 03	300s	16	4800s	*H* magnitude
”	n2071a21	2.1m	2004 Dec 20	300s	12	3600s	*H* magnitude
”	n2071a6	4m	2005 Dec 17	300s	14	4200s	*H* magnitude
”	n2071a3	4m	2005 Dec 20	300s	16	4800s	*H* magnitude
”	n2071a5	4m	2005 Dec 21	300s	8	2400s	*H* magnitude
04 (NGC 2068)	ob4nm1	4m	2003 Jan 15	600s	4	2400s	BD candidates
”	”	”	”	300s	8	2400s	”
”	n2068f11	2.1m	2003 Nov 30	300s	12	3600s	*K* magnitude
”	n2068f21	2.1m	2003 Nov 30	300s	12	3600s	*K* magnitude
”	n2068a1	4m	2004 Dec 01	300s	8	2400s	*H* magnitude
”	n2068a2	4m	2004 Dec 02	300s	12	3600s	*H* magnitude
”	n2068a4	4m	2004 Dec 03	300s	12	3600s	*H* magnitude
”	n2068a31	2.1m	2004 Dec 14	300s	12	3600s	*H* magnitude
06 (LBS 23)	ob6bd1	4m	2003 Jan 23	600s	8	4800s	BD candidates
”	ob64m11	4m	2004 Jan 03	300s	12	3600s	IRX sources
”	ob64m21	4m	2004 Jan 05	300s	11	3300s	IRX sources
08 (LBS 29,30)	ob84m11	4m	2004 Jan 06	300s	12	3600s	IRX sources
09 (LBS 31,32)	ob94m11	4m	2004 Jan 03	300s	6	1800s	IRX sources

Table B–1—Continued

Region[a]	Mask ID	Telescope	Obs. Date	t_{exp}	N_{exp}	Total t_{exp}	Target Selection Criteria
10 (NGC 2024)	n2024bd1	4m	2003 Jan 19	600s	8	4800s	BD candidates
”	n2024f31	2.1m	2003 Nov 29	300s	14	4200s	*K* magnitude
”	oc24mf11	4m	2003 Dec 06	300s	8	2400s	IRX sources
”	oc24mf21	4m	2003 Dec 10	300s	13	3900s	IRX souces
”	n2024b2	4m	2004 Dec 01	300s	10	3000s	*H* magnitude
”	n2024b3	4m	2004 Dec 01	300s	10	3000s	*H* magnitude
13	ob13off1	4m	2003 Jan 23	300s	8	2400s	BD candidates

[a]Regions listed here correspond to those in Figure 2–12 and Table 2–1

REFERENCES

Ali, B., Sellgren, K., Depoy, D. L., Carr, J. S., Gatley, I., Merrill, K. M., & Lada, E. 1998, in ASP Conf. Ser. 154: Cool Stars, Stellar Systems, and the Sun, ed. R. A. Donahue & J. A. Bookbinder, 1663

Allers, K. N., Kessler-Silacci, J. E., Cieza, L. A., & Jaffe, D. T. 2006, ApJ, 644, 364

Anthony-Twarog, B. J. 1982, AJ, 87, 1213

Aoyama, H., Mizuno, N., Yamamoto, H., Onishi, T., Mizuno, A., & Fukui, Y. 2001, PASJ, 53, 1053

Baraffe, I., Chabrier, G., Allard, F., & Hauschildt, P. H. 1998, A&A, 337, 403

Barnes, P. J., Crutcher, R. M., Bieging, J. H., Storey, J. W. V., & Willner, S. P. 1989, ApJ, 342, 883

Bate, M. R. & Bonnell, I. A. 2005, MNRAS, 356, 1201

Bate, M. R., Bonnell, I. A., & Bromm, V. 2002, MNRAS, 332, L65

Bertin, E. & Arnouts, S. 1996, A&AS, 117, 393

Bessell, M. S. & Brett, J. M. 1988, PASP, 100, 1134

Bik, A., Lenorzer, A., Kaper, L., Comerón, F., Waters, L. B. F. M., de Koter, A., & Hanson, M. M. 2003, A&A, 404, 249

Blaauw, A. 1964, ARA&A, 2, 213

Blaauw, A. 1991, in NATO ASIC Proc. 342: The Physics of Star Formation and Early Stellar Evolution, ed. C. J. Lada & N. D. Kylafis, 125–+

Bohlin, R. C., Savage, B. D., & Drake, J. F. 1978, ApJ, 224, 132

Briceño, C., Calvet, N., Hernández, J., Vivas, A. K., Hartmann, L., Downes, J. J., & Berlind, P. 2005, AJ, 129, 907

Briceño, C., Luhman, K. L., Hartmann, L., Stauffer, J. R., & Kirkpatrick, J. D. 2002, ApJ, 580, 317

Brown, A. G. A., de Geus, E. J., & de Zeeuw, P. T. 1994, A&A, 289, 101

Burrows, A., Marley, M., Hubbard, W. B., Lunine, J. I., Guillot, T., Saumon, D., Freedman, R., Sudarsky, D., & Sharp, C. 1997, ApJ, 491, 856

Carpenter, J. M. 2000, AJ, 120, 3139

Chabrier, G. 2002, ApJ, 567, 304

Chabrier, G., Baraffe, I., Allard, F., & Hauschildt, P. 2000, ApJ, 542, 464

Cohen, J. G., Persson, S. E., Elias, J. H., & Frogel, J. A. 1981, ApJ, 249, 481

Comeron, F., Rieke, G. H., & Rieke, M. J. 1996, ApJ, 473, 294

Cushing, M. C., Rayner, J. T., & Vacca, W. D. 2005, ApJ, 623, 1115

Dahn, C. C., Harris, H. C., Vrba, F. J., Guetter, H. H., Canzian, B., Henden, A. A., Levine, S. E., Luginbuhl, C. B., Monet, A. K. B., Monet, D. G., Pier, J. R., Stone, R. C., Walker, R. L., Burgasser, A. J., Gizis, J. E., Kirkpatrick, J. D., Liebert, J., & Reid, I. N. 2002, AJ, 124, 1170

D'Antona, F. & Mazzitelli, I. 1997, Memorie della Societa Astronomica Italiana, 68, 807

Delfosse, X., Tinney, C. G., Forveille, T., Epchtein, N., Bertin, E., Borsenberger, J., Copet, E., de Batz, B., Fouque, P., Kimeswenger, S., Le Bertre, T., Lacombe, F., Rouan, D., & Tiphene, D. 1997, A&A, 327, L25

Elston, R. 1998, in Proc. SPIE Vol. 3354, p. 404-413, Infrared Astronomical Instrumentation, Albert M. Fowler; Ed., ed. A. M. Fowler, 404–413

Elston, R., Raines, S. N., Hanna, K. T., Hon, D. B., Julian, J., Horrobin, M., Harmer, C. F. W., & Epps, H. W. 2003, in Instrument Design and Performance for Optical/Infrared Ground-based Telescopes. Edited by Iye, Masanori; Moorwood, Alan F. M. Proceedings of the SPIE, Volume 4841, pp. 1611-1624 (2003)., ed. M. Iye & A. F. M. Moorwood, 1611–1624

Epchtein, N., de Batz, B., Copet, E., Fouque, P., Lacombe, F., Le Bertre, T., Mamon, G., Rouan, D., Tiphene, D., Burton, W. B., Deul, E., Habing, H., Boersenberger, J., Dennefeld, M., Omont, A., Renault, J. C., Rocca-Volmerange, B., Kimeswenger, S., Appenzeller, I., Bender, R., Forveille, T., Garzon, F., Hron, J., Persi, P., Ferrari-Toniolo, M., & Vauglin, I. 1994, Ap&SS, 217, 3

Ezoe, Y., Kokubun, M., Makishima, K., Sekimoto, Y., & Matsuzaki, K. 2006, ApJ, 649, L123

Gomez, M., Hartmann, L., Kenyon, S. J., & Hewett, R. 1993, AJ, 105, 1927

Gorlova, N. I., Meyer, M. R., Rieke, G. H., & Liebert, J. 2003, ApJ, 593, 1074

Guieu, S., Dougados, C., Monin, J.-L., Magnier, E., & Martín, E. L. 2006, A&A, 446, 485

Haisch, Jr., K. E., Lada, E. A., & Lada, C. J. 2000, AJ, 120, 1396

Haro, G. & Moreno, A. 1953, Boletin de los Observatorios Tonantzintla y Tacubaya, 1, 11

Hatchell, J., Richer, J. S., Fuller, G. A., Qualtrough, C. J., Ladd, E. F., & Chandler, C. J. 2005, A&A, 440, 151

Hepburn, N., Hagen, J. P., & McClain, E. F. 1954, Proceedings of the IRE, 42, 1811

Herbig, G. H. 1998, ApJ, 497, 736

Herbig, G. H. & Kuhi, L. V. 1963, ApJ, 137, 398

Hernandez, A. K. 2006, in preparation

Hester, J. J., Scowen, P. A., Sankrit, R., Lauer, T. R., Ajhar, E. A., Baum, W. A., Code, A., Currie, D. G., Danielson, G. E., Ewald, S. P., Faber, S. M., Grillmair, C. J., Groth, E. J., Holtzman, J. A., Hunter, D. A., Kristian, J., Light, R. M., Lynds, C. R., Monet, D. G., O'Neil, Jr., E. J., Shaya, E. J., Seidelmann, K. P., & Westphal, J. A. 1996, AJ, 111, 2349

Hillenbrand, L. A. & Carpenter, J. M. 2000, ApJ, 540, 236

Jayawardhana, R., Mohanty, S., & Basri, G. 2003, ApJ, 592, 282

Jeans, J. H. 1902, Royal Society of London Philosophical Transactions Series A, 199, 1

Johnstone, D., Fich, M., Mitchell, G. F., & Moriarty-Schieven, G. 2001, ApJ, 559, 307

Jones, H. R. A., Longmore, A. J., Jameson, R. F., & Mountain, C. M. 1994, MNRAS, 267, 413

Jones, H. R. A., Pavlenko, Y., Viti, S., & Tennyson, J. 2002, MNRAS, 330, 675

Kirkpatrick, J. D., Reid, I. N., Liebert, J., Cutri, R. M., Nelson, B., Beichman, C. A., Dahn, C. C., Monet, D. G., Gizis, J. E., & Skrutskie, M. F. 1999, ApJ, 519, 802

Kroupa, P., Aarseth, S., & Hurley, J. 2001, MNRAS, 321, 699

Kroupa, P. & Bouvier, J. 2003, MNRAS, 346, 369

Kruegel, E., Thum, C., Pankonin, V., & Martin-Pintado, J. 1982, A&AS, 48, 345

Kumar, S. S. 1963, ApJ, 137, 1121

Lada, C. J. 2005, Progress of Theoretical Physics Supplement, 158, 1

Lada, C. J. & Lada, E. A. 2003, ARA&A, 41, 57

Lada, C. J., Lada, E. A., Clemens, D. P., & Bally, J. 1994, ApJ, 429, 694

Lada, C. J., Muench, A. A., Lada, E. A., & Alves, J. F. 2004, AJ, 128, 1254

Lada, C. J., Muench, A. A., Luhman, K. L., Allen, L., Hartmann, L., Megeath, T., Myers, P., Fazio, G., Wood, K., Muzerolle, J., Rieke, G., Siegler, N., & Young, E. 2006, AJ, 131, 1574

Lada, E. A., Bally, J., & Stark, A. A. 1991a, ApJ, 368, 432

Lada, E. A., Evans, II, N. J., Depoy, D. L., & Gatley, I. 1991b, ApJ, 371, 171

Lada, E. A., Evans, II, N. J., & Falgarone, E. 1997, ApJ, 488, 286

Lancon, A. & Rocca-Volmerange, B. 1992, A&AS, 96, 593

Larson, R. B. 1995, MNRAS, 272, 213

Leggett, S. K. 1992, ApJS, 82, 351

Leggett, S. K., Allard, F., Berriman, G., Dahn, C. C., & Hauschildt, P. H. 1996, ApJS, 104, 117

Leggett, S. K., Allard, F., Geballe, T. R., Hauschildt, P. H., & Schweitzer, A. 2001, ApJ, 548, 908

Leggett, S. K., Geballe, T. R., Fan, X., Schneider, D. P., Gunn, J. E., Lupton, R. H., Knapp, G. R., Strauss, M. A., McDaniel, A., Golimowski, D. A., Henry, T. J., Peng, E., Tsvetanov, Z. I., Uomoto, A., Zheng, W., Hill, G. J., Ramsey, L. W., Anderson, S. F., Annis, J. A., Bahcall, N. A., Brinkmann, J., Chen, B., Csabai, I., Fukugita, M., Hennessy, G. S., Hindsley, R. B., Ivezić, Ž., Lamb, D. Q., Munn, J. A., Pier, J. R., Schlegel, D. J., Smith, J. A., Stoughton, C., Thakar, A. R., & York, D. G. 2000, ApJ, 536, L35

Lenorzer, A., Bik, A., de Koter, A., Kurtz, S. E., Waters, L. B. F. M., Kaper, L., Jones, C. E., & Geballe, T. R. 2004, A&A, 414, 245

Lin, D. N. C., Laughlin, G., Bodenheimer, P., & Rozyczka, M. 1998, Science, 281, 2025

Liu, M. C., Najita, J., & Tokunaga, A. T. 2003, ApJ, 585, 372

Lucas, P. W., Roche, P. F., Allard, F., & Hauschildt, P. H. 2001, MNRAS, 326, 695

Lucas, P. W., Roche, P. F., & Tamura, M. 2005, MNRAS, 361, 211

Luhman, K. L. 1999, ApJ, 525, 466

—. 2000, ApJ, 544, 1044

—. 2004, ApJ, 617, 1216

—. 2006, ApJ, 645, 676

Luhman, K. L., Briceño, C., Stauffer, J. R., Hartmann, L., Barrado y Navascués, D., & Caldwell, N. 2003a, ApJ, 590, 348

Luhman, K. L., Lada, E. A., Muench, A. A., & Elston, R. J. 2005a, ApJ, 618, 810

Luhman, K. L., Rieke, G. H., Young, E. T., Cotera, A. S., Chen, H., Rieke, M. J., Schneider, G., & Thompson, R. I. 2000, ApJ, 540, 1016

Luhman, K. L., Stauffer, J. R., & Mamajek, E. E. 2005b, ApJ, 628, L69

Luhman, K. L., Stauffer, J. R., Muench, A. A., Rieke, G. H., Lada, E. A., Bouvier, J., & Lada, C. J. 2003b, ApJ, 593, 1093

Lynds, B. T. 1962, ApJS, 7, 1

Maddalena, R. J., Morris, M., Moscowitz, J., & Thaddeus, P. 1986, ApJ, 303, 375

Massey, P. 1998, in ASP Conf. Ser. 142: The Stellar Initial Mass Function (38th Herstmonceux Conference), ed. G. Gilmore & D. Howell, 17

McGovern, M. R., Kirkpatrick, J. D., McLean, I. S., Burgasser, A. J., Prato, L., & Lowrance, P. J. 2004, ApJ, 600, 1020

McLean, I. S., McGovern, M. R., Burgasser, A. J., Kirkpatrick, J. D., Prato, L., & Kim, S. S. 2003, ApJ, 596, 561

Meyer, M. R. 1996, Ph.D. Thesis

Meyer, M. R., Calvet, N., & Hillenbrand, L. A. 1997, AJ, 114, 288

Mezger, P. G., Chini, R., Kreysa, E., Wink, J. E., & Salter, C. J. 1988, A&A, 191, 44

Mitchell, G. F., Johnstone, D., Moriarty-Schieven, G., Fich, M., & Tothill, N. F. H. 2001, ApJ, 556, 215

Mohanty, S., Jayawardhana, R., & Basri, G. 2005, ApJ, 626, 498

Muench, A. A., Alves, J., Lada, C. J., & Lada, E. A. 2001, ApJ, 558, L51

Muench, A. A., Lada, E. A., Lada, C. J., & Alves, J. 2002, ApJ, 573, 366

Muench, A. A., Lada, E. A., Lada, C. J., Elston, R. J., Alves, J. F., Horrobin, M., Huard, T. H., Levine, J. L., Raines, S. N., & Román-Zúñiga, C. 2003, AJ, 125, 2029

Muzerolle, J., Briceño, C., Calvet, N., Hartmann, L., Hillenbrand, L., & Gullbring, E. 2000, ApJ, 545, L141

Muzerolle, J., Luhman, K. L., Briceño, C., Hartmann, L., & Calvet, N. 2005, ApJ, 625, 906

Nakajima, T., Oppenheimer, B. R., Kulkarni, S. R., Golimowski, D. A., Matthews, K., & Durrance, S. T. 1995, Nature, 378, 463

Natta, A., Testi, L., Muzerolle, J., Randich, S., Comerón, F., & Persi, P. 2004, A&A, 424, 603

Newberry, M. V. 1991, PASP, 103, 122

Onishi, T., Mizuno, A., Kawamura, A., Ogawa, H., & Fukui, Y. 1998, ApJ, 502, 296

Oppenheimer, B. R., Kulkarni, S. R., Matthews, K., & Nakajima, T. 1995, Science, 270, 1478

Padoan, P. & Nordlund, Å. 2002, ApJ, 576, 870

—. 2004, ApJ, 617, 559

Porras, A., Christopher, M., Allen, L., Di Francesco, J., Megeath, S. T., & Myers, P. C. 2003, AJ, 126, 1916

Reid, I. N., Burgasser, A. J., Cruz, K. L., Kirkpatrick, J. D., & Gizis, J. E. 2001, AJ, 121, 1710

Reid, I. N., Kirkpatrick, J. D., Liebert, J., Burrows, A., Gizis, J. E., Burgasser, A., Dahn, C. C., Monet, D., Cutri, R., Beichman, C. A., & Skrutskie, M. 1999, ApJ, 521, 613

Reipurth, B. & Clarke, C. 2001, AJ, 122, 432

Robberto, M., Song, J., Mora Carrillo, G., Beckwith, S. V. W., Makidon, R. B., & Panagia, N. 2004, ApJ, 606, 952

Román-Zúñiga, C. G. 2006, Ph.D. Thesis

Salpeter, E. E. 1955, ApJ, 121, 161

Shu, F. H. 1977, ApJ, 214, 488

Shu, F. H., Adams, F. C., & Lizano, S. 1987, ARA&A, 25, 23

Skrutskie, M. F., Schneider, S. E., Stiening, R., Strom, S. E., Weinberg, M. D., Beichman, C., Chester, T., Cutri, R., Lonsdale, C., Elias, J., Elston, R., Capps, R., Carpenter, J., Huchra, J., Liebert, J., Monet, D., Price, S., & Seitzer, P. 1997, in ASSL Vol. 210: The Impact of Large Scale Near-IR Sky Surveys, ed. F. Garzon, N. Epchtein, A. Omont, B. Burton, & P. Persi, 25

Slesnick, C. L., Hillenbrand, L. A., & Carpenter, J. M. 2004, ApJ, 610, 1045

Spitzer, L. 1978, Physical processes in the interstellar medium (New York Wiley-Interscience, 1978. 333 p.)

Steinhauer, A., Levine, J. L., & Lada, E. A. 2006, in preparation

Stetson, P. B. 1987, PASP, 99, 191

Strom, K. M. & Strom, S. E. 1994, ApJ, 424, 237

Strom, K. M., Strom, S. E., Carrasco, L., & Vrba, F. J. 1975, ApJ, 196, 489

Tucker, K. D., Kutner, M. L., & Thaddeus, P. 1973, ApJ, 186, L13

van Altena, W. F., Lee, J. T., Lee, J.-F., Lu, P. K., & Upgren, A. R. 1988, AJ, 95, 1744

White, R. J., Ghez, A. M., Reid, I. N., & Schultz, G. 1999, ApJ, 520, 811

Whitworth, A. P. & Zinnecker, H. 2004, A&A, 427, 299

Wilking, B. A., Greene, T. P., & Meyer, M. R. 1999, AJ, 117, 469

Wilking, B. A., Meyer, M. R., Greene, T. P., Mikhail, A., & Carlson, G. 2004, AJ, 127, 1131

Wilson, T. L., Mauersberger, R., Gensheimer, P. D., Muders, D., & Bieging, J. H. 1999, ApJ, 525, 343

York, D. G., Adelman, J., Anderson, Jr., J. E., Anderson, S. F., Annis, J., Bahcall, N. A., Bakken, J. A., Barkhouser, R., Bastian, S., Berman, E., Boroski, W. N., Bracker, S., Briegel, C., Briggs, J. W., Brinkmann, J., Brunner, R., Burles, S., Carey, L., Carr, M. A., Castander, F. J., Chen, B., Colestock, P. L., Connolly, A. J., Crocker, J. H., Csabai, I., Czarapata, P. C., Davis, J. E., Doi, M., Dombeck, T., Eisenstein, D., Ellman, N., Elms, B. R., Evans, M. L., Fan, X., Federwitz, G. R., Fiscelli, L., Friedman, S., Frieman, J. A., Fukugita, M., Gillespie, B., Gunn, J. E., Gurbani, V. K., de Haas, E., Haldeman, M., Harris, F. H., Hayes, J., Heckman, T. M., Hennessy, G. S., Hindsley, R. B., Holm, S., Holmgren, D. J., Huang, C.-h., Hull, C., Husby, D., Ichikawa, S.-I., Ichikawa, T., Ivezić, Ž., Kent, S., Kim, R. S. J., Kinney, E., Klaene, M., Kleinman, A. N., Kleinman, S., Knapp, G. R., Korienek, J., Kron, R. G., Kunszt, P. Z., Lamb, D. Q., Lee, B., Leger, R. F., Limmongkol, S., Lindenmeyer, C., Long, D. C., Loomis, C., Loveday, J., Lucinio, R., Lupton, R. H., MacKinnon, B., Mannery, E. J., Mantsch, P. M., Margon, B., McGehee, P., McKay, T. A., Meiksin, A., Merelli, A., Monet, D. G., Munn, J. A., Narayanan, V. K., Nash, T., Neilsen, E., Neswold, R., Newberg, H. J., Nichol, R. C., Nicinski, T., Nonino, M., Okada, N., Okamura, S., Ostriker, J. P., Owen, R., Pauls, A. G., Peoples, J., Peterson, R. L., Petravick, D., Pier, J. R., Pope, A., Pordes, R., Prosapio, A., Rechenmacher, R., Quinn, T. R., Richards, G. T., Richmond, M. W., Rivetta, C. H., Rockosi, C. M., Ruthmansdorfer, K., Sandford, D., Schlegel, D. J., Schneider, D. P., Sekiguchi, M., Sergey, G., Shimasaku, K., Siegmund, W. A., Smee, S., Smith, J. A., Snedden, S., Stone, R., Stoughton, C., Strauss, M. A., Stubbs, C., SubbaRao, M., Szalay, A. S., Szapudi, I., Szokoly, G. P., Thakar, A. R., Tremonti, C., Tucker, D. L., Uomoto, A., Vanden Berk, D., Vogeley, M. S., Waddell, P., Wang, S.-i., Watanabe, M., Weinberg, D. H., Yanny, B., & Yasuda, N. 2000, AJ, 120, 1579

BIOGRAPHICAL SKETCH

Joanna Lisa Levine was born on December 3, 1975 in Leuven, Belgium. After spending the first few months of her life in this wonderful country, planting the seeds for a lifelong appreciation of waffles, chocolate, and fruity Lambic beer, she relocated with her parents to New York. Living in Brooklyn for three years taught her that she should always root for all New York sports teams (at least if she wanted Dad to be in a good mood). Joanna then moved to Port Chester, NY where she acquired a younger sister and finally to Worcester, Massachusetts where she acquired a younger brother and her own room.

In Worcester, at age 6, Joanna took her first ballet class and immediately fell in love. At age 9, Joanna looked through her first telescope and after catching a glimpse of Jupiter, decided that it would be more fun to go sleep in the car. She did however spend many hours watching Star Trek with her father, slowly fostering an interest in the mysteries of space. After spending the next 7 years at the Performing Arts School of Worcester and Walnut Hill School for the Arts, pursuing her dream to become a ballerina, a knee injury temporarily sidelined our young hero. Rather than dancing during the summer of 1992, Joanna went off to Astronomy Camp in Tucson, AZ where, after her first taste of “real” astronomy, she decided to become an astronomer.

After graduation from Walnut Hill, Joanna attended college at the University of Massachusetts at Amherst. She briefly entertained the idea of double-majoring in physics and dance but upon finding that the university inconveniently scheduled physics labs during ballet class, Joanna settled on solely studying physics. Although the large red failing marks on every single one of her freshman year physics exams could have been a deterrent, Joanna stubbornly persevered. Her efforts were rewarded during her junior

year when Joanna *finally* received her first ”A” on a physics exam and was awarded the spring 1996 “Physics Book Award” - a large handbook of Chemistry and Physics which has been collecting dust ever since.

During the summer of 1996 Joanna traveled to Flagstaff, AZ and spent 10 weeks working with Dr. Stephen Tegler on the primoridal surfaces of Kuiper Belt objects. This research stimulated her interest in the formation of solar systems (ours and others) and taught her more than she ever wanted to know about photometry (knowledge that will haunt her forever). Finally, at the end of the summer, Steve encouraged Joanna to apply to the University of Florida and for that she will always be grateful.

Joanna graduated from UMASS in May 1997 with a B.S. in Physics and moved to sunny Gainesville, FL. There she began working with Elizabeth Lada who taught her all about star formation and the true meaning of the phrase “statistically significant.” After an unmentionable number of years (long enough for the Gators to win a National Championship *in basketball*), Joanna defended her dissertation and is now pondering what to do next. Her time at Florida was priceless - she met the love of her life, Timothy B. Spahr, and made many close friends along the way. Most importantly, during the tail end of her graduate career Joanna found her way back to dance, spending much time dancing with Alora Haynes, Alberto Alonso, Sonia Calero-Alonso, and the Dance Theatre of Santa Fe Community College. Joanna is now hoping to find a job that will allow her to balance the science of dance with the art of science. In the meantime, if you are reading this and hiring, feel free to contact her.